

The University of New South Wales
School of Mechanical and Manufacturing
Engineering

A Study of Inverted Wings with Endplates
in Ground Effect

David Ricapito

Master of Engineering

May 2007

Supervisor: Dr Tracie Barber

Originality Statement

‘I hereby declare that this submission is my own work and to the best of my knowledge it contains no materials previously published or written by another person, or substantial proportions of material which have been accepted for the award of any other degree or diploma at UNSW or any other educational institution, except where due acknowledgement is made in the thesis. Any contribution made to the research by others, with whom I have worked at UNSW or elsewhere, is explicitly acknowledged in the thesis. I also declare that the intellectual content of this thesis is the product of my own work, except to the extent that assistance from others in the project’s design and conception or in style, presentation and linguistic expression is acknowledged.’

ABSTRACT

An inverted wing with various endplate configurations was investigated at two different angles of incidence. A moving ground was designed and constructed for use in the UNSW T1 wind tunnel. The test cases were investigated in ground effect using the moving ground. Measurements and observations were obtained using laser sheet flow visualisation and laser doppler anemometry. Computational fluid dynamics models of the test cases were run to gain further understanding of the flow field generated when using inverted wings with endplates. The computational fluid dynamics models correlated well to the experimental results.

DECLARATION

I the undersigned, hereby declare that I am the sole author of this work and that any content from other sources has been acknowledged and fully cited.

David Ricapito

ACKNOWLEDGEMENTS

I would like to thank Dr Tracie Barber for her continual support, guidance, input and just plain common sense throughout the degree. Also I would like to thank Alex Litvak for his help and support in the labs. I would not have finished the moving ground without the help from Sam Diasinos and Chris Beves, and for keeping the wind tunnel working and getting the LDA to work.

And finally thanks to my family for their support and understanding!

CONTENTS

ABSTRACT	III
DECLARATION	IV
ACKNOWLEDGEMENTS	V
CONTENTS	VI
LIST OF FIGURES	X
LIST OF TABLES	XVII
NOMENCLATURE	XVIII
1. INTRODUCTION	1
1.1 Topic	2
1.1.1 Problem Definition.....	3
1.2 Literature Review.....	3
1.3 Aims and Objectives of Research	6
1.4 Thesis Structure and Methodology	6
1.6 Summary	7
2. MOVING GROUND	8
2.1 Chapter Overview	9
2.2 Practicality and Use of a Moving Ground.....	9
2.3 Moving Ground Design and Construction	10
2.4 Moving Ground Development	13
2.5 Summary	16
3. WIND TUNNEL TEST CASES	17

3.1	Chapter Overview	18
3.2	Wind Tunnel Test Facilities	18
3.3	Endplates	19
3.4	Flow Visualisation	22
3.5	Laser Doppler Anemometry.....	23
3.6	Summary	25
4.	COMPUTATIONAL FLUID DYNAMICS.....	26
4.1	Chapter Overview	27
4.2	Introduction.....	27
4.3	Computational Fluid Dynamics Domain	29
4.4	Grid Generation.....	31
4.5	Turbulence Models	33
4.6	Validation and Verification.....	34
4.7	Data Collection	35
4.8	Summary	36
5.	RESULTS	37
5.1	Chapter Overview	38
5.2	Flow Visualisation	38
5.2.1	Vortex Patterns for 6° Incidence without Endplates	39
5.2.2	Vortex Patterns for 6° Incidence at h = 10.....	41
5.2.3	Vortex Patterns for 6° Incidence at h = 20.....	47
5.2.4	Vortex Patterns for 10° Incidence without Endplates	55
5.2.5	Vortex Patterns for 10° Incidence at h = 10.....	57
5.2.6	Vortex Patterns for 10° Incidence at h = 20.....	62
5.2.7	Summary for Flow Visualisation Results	70
5.3	Computational Fluid Dynamics	70
5.3.1	C _L and C _D for 6deg-h10 Cases	71
5.3.2	C _L and C _D for 6deg-h15 Cases	71
5.3.3	C _L and C _D for 6deg-h20 Cases	71
5.3.4	C _L and C _D for 6deg-h40 Cases	72

5.3.5	C_L and C_D for 10deg-h10 Cases	72
5.3.6	C_L and C_D for 10deg-h15 Cases	73
5.3.7	C_L and C_D for 10deg-h20 Cases	73
5.3.8	Comparison of C_L and C_D for All Test Cases	81
5.4	Laser Doppler Anemometry.....	84
5.5	Summary	90
6.	DISCUSSION	91
6.1	Chapter Overview	92
6.2	Moving Ground.....	92
6.2.1	Material Choice for the Moving Ground	92
6.2.2	Moving Ground Drive System.....	93
6.2.3	Possible Causes of Error in the Moving Ground	94
6.3	Flow Visualisation	95
6.3.1	Flow Visualisation Technique.....	95
6.3.2	Flow Visualisation Observations	96
6.3.3	Possible Causes of Error in Flow Visualisation Experiments.....	97
6.4	Computational Fluid Dynamics	98
6.4.1	Test Case Choice and Generation	98
6.4.2	Boundary Conditions	99
6.4.3	Static Pressures and Vortex Paths	105
6.4.4	Possible Causes for Error in the Computational Fluid Dynamics Results.	107
6.5	Laser Doppler Anemometry.....	108
6.5.1	Limitations of Laser Doppler Anemometry Experiments.....	108
6.5.2	Possible Causes of Error in Laser Doppler Anemometry Experiments.....	109
6.6	Comparisons and Observations.....	109
6.6.1	Experiments, Simulation and Analysis Techniques.....	109
6.6.2	Comparing Results	110
6.6.3	Observations.....	111
6.6.4	Scale Effects.....	111
7.	CONCLUSION.....	117

7.1 Conclusion	118
7.2 Suggestions for Future Work	118
BIBLIOGRAPHY	120
Bibliography.....	121
APPENDICES	123
Appendix A: CFD Test Case Details	124
Appendix B: Static Pressure Contours on Wing Suction Surface.....	128
Appendix C: Drawings for Perspex Moving Ground Parts	147

LIST OF FIGURES

Figure 1: Modern open wheel racing car front wing with endplates	2
Figure 2: Inverted wings with endplates used in drag racing.....	3
Figure 3: Air velocity profiles with wing near ground	9
Figure 4: Test Section Basic Dimensions	11
Figure 5: Computer model of moving ground assembly and test section air volume.....	12
Figure 6: Moving ground during belt adjustment	14
Figure 7: Copper wire locations.....	15
Figure 8: Typical test case	19
Figure 9: Endplate sizes for wind tunnel tests (mm).....	20
Figure 10: Example endplate configuration (mm).....	21
Figure 11: Flow visualisation example	22
Figure 12: Image planes at various distances behind wing and endplate	23
Figure 13: Laser Doppler anemometry measurement example	24
Figure 14: CFD domain in 3D	29
Figure 15: Dimensions of CFD Domain.....	30
Figure 16: Adapted mesh example.....	33
Figure 17: 6deg-h20 with plane at 0.267c.....	39
Figure 18: 6deg-h20 with plane at 1.333c.....	40
Figure 19: 6deg-h20 with plane at 2.667c.....	40
Figure 20: 6deg-h10-A-m4 with plane at 0.067c.....	41
Figure 21: 6deg-h10-A-m4 with plane at 0.267c.....	42
Figure 22: 6deg-h10-A-m4 with plane at 1.333c.....	42
Figure 23: 6deg-h10-A-m4 with plane at 2.667c.....	43
Figure 24: 6deg-h10-B-m4 with plane at 0.067c	43
Figure 25: 6deg-h10-B-m4 with plane at 0.267c	44
Figure 26: 6deg-h10-C-m4 with plane at 0.067c	44
Figure 27: 6deg-h10-C-m4 with plane at 0.267c	45

Figure 28: 6deg-h10-C-m4 with plane at 1.333c	45
Figure 29: 6deg-h10-C-m4 with plane at 2.667c	46
Figure 30: 6deg-h10-D-m4 with plane at 0.067c	46
Figure 31: 6deg-h20-A-m14 with plane at 0.067c	47
Figure 32: 6deg-h20-A-m14 with plane at 0.267c	48
Figure 33: 6deg-h20-A-m14 with plane at 1.333c	48
Figure 34: 6deg-h20-A-m14 with plane at 2.667c	49
Figure 35: 6deg-h20-B-m14 with plane at 0.067c	49
Figure 36: 6deg-h20-B-m14 with plane at 0.267c	50
Figure 37: 6deg-h20-B-m14 with plane at 1.333c	50
Figure 38: 6deg-h20-B-m14 with plane at 2.667c	51
Figure 39: 6deg-h20-C-m14 with plane at 0.067c	51
Figure 40: 6deg-h20-C-m14 with plane at 0.267c	52
Figure 41: 6deg-h20-C-m14 with plane at 1.333c	52
Figure 42: 6deg-h20-C-m14 with plane at 2.667c	53
Figure 43: 6deg-h20-D-m14 with plane at 0.067c	53
Figure 44: 6deg-h20-D-m14 with plane at 0.267	54
Figure 45: 6deg-h20-D-m14 with plane at 1.333c	54
Figure 46: 10deg-h10 with plane at 0.067c	55
Figure 47: 10deg-h10 with plane at 0.267c	56
Figure 48: 10deg-h10 with plane at 1.333c	56
Figure 49: 10deg-h10 with plane at 2.667c	57
Figure 50: 10deg-h10-A-m4 with plane at 0.267c	58
Figure 51: 10deg-h10-A-m4 with plane at 1.333c	58
Figure 52: 10deg-h10-B-m4 with plane at 0.267c	59
Figure 53: 10deg-h10-C-m4 with plane at 0.067c	59
Figure 54: 10deg-h10-C-m4 with plane at 0.267c	60
Figure 55: 10deg-h10-C-m4 with plane at 1.333c	60
Figure 56: 10deg-h10-D-m4 with plane at 0.067c	61
Figure 57: 10deg-h10-D-m4 with plane at 1.333c	61
Figure 58: 10deg-h20-A-m14 with plane at 0.067c	63

Figure 59: 10deg-h20-A-m14 with plane at 1.333c	63
Figure 60: 10deg-h20-A-m14 with plane at 2.667c	64
Figure 61: 10deg-h20-B-m14 with plane at 0.067c	64
Figure 62: 10deg-h20-B-m14 with plane at 0.267c	65
Figure 63: 10deg-h20-B-m14 with plane at 1.333c	65
Figure 64: 10deg-h20-B-m14 with plane at 2.667c	66
Figure 65: 10deg-h20-C-m14 with plane at 0.267c	66
Figure 66: 10deg-h20-C-m14 with plane at 1.333c	67
Figure 67: 10deg-h20-C-m14 with plane at 2.667c	67
Figure 68: 10deg-h20-D-m14 with plane at 0.067c	68
Figure 69: 10deg-h20-D-m14 with plane at 0.267c	68
Figure 70: 10deg-h20-D-m14 with plane at 1.333c	69
Figure 71: 10deg-h20-D-m14 with plane at 2.667c	69
Figure 72: 6deg-h10 cases C_L values ($h/c = 0.07$)	74
Figure 73: 6deg-h10 cases C_D values ($h/c = 0.07$)	74
Figure 74: 6deg-h15 cases C_L Values ($h/c = 0.13$)	75
Figure 75: 6deg-h15 cases C_D Values ($h/c = 0.13$)	75
Figure 76: 6deg-h20 cases C_L Values ($h/c = 0.20$)	76
Figure 77: 6deg-h20 cases C_D Values ($h/c = 0.20$)	76
Figure 78: 6deg-h40 cases C_L Values ($h/c = 0.47$)	77
Figure 79: 6deg-h40 cases C_D Values ($h/c = 0.47$)	77
Figure 80: 10deg-h10 cases C_L Values ($h/c = 0.08$)	78
Figure 81: 10deg-h10 cases C_D Values ($h/c = 0.08$)	78
Figure 82: 10deg-h15 cases C_L Values ($h/c = 0.15$)	79
Figure 83: 10deg-h15 cases C_D Values ($h/c = 0.15$)	79
Figure 84: 10deg-h20 cases C_L Values ($h/c = 0.21$)	80
Figure 85: 10deg-h20 cases C_D Values ($h/c = 0.21$)	80
Figure 86: C_L comparison for Angle of Incidence and Height Cases	82
Figure 87: C_D comparison for Angle of Incidence and Height Cases	83
Figure 88: C_L/C_D comparison for Angle of Incidence and Height Cases	83
Figure 89: LDA velocity contours for case 10deg-h20-C-m14 at 0.067c (ms^{-1})	86

Figure 90: LDA velocity contours for case 10deg-h20-C-m14 at 0.067c with vectors (ms ⁻¹)	86
.....	
Figure 91: LDA velocity contours for case 10deg-h20-C-m14 at 0.267c (ms ⁻¹)	87
Figure 92: LDA velocity contours for case 10deg-h20-C-m14 at 0.267c with vectors (ms ⁻¹)	87
.....	
Figure 93: LDA velocity contours for case 10deg-h20-C-m14 at 1.333c (ms ⁻¹)	88
Figure 94: LDA velocity contours for case 10deg-h20-C-m14 at 1.333c with vectors (ms ⁻¹)	88
.....	
Figure 95: LDA velocity contours for case 10deg-h20-C-m14 at 2.667c (ms ⁻¹)	89
Figure 96: LDA velocity contours for case 10deg-h20-C-m14 at 2.667c with vectors (ms ⁻¹)	89
.....	
Figure 97: Velocity contours for 10deg-h20-C-m14 at 0.067c (ms ⁻¹)	101
Figure 98: Velocity contours for symmetrical 10deg-h20-C-m14 at 0.067c (ms ⁻¹)	101
Figure 99: Velocity contours for 10deg-h20-C-m14 at 0.267c (ms ⁻¹)	102
Figure 100: Velocity contours for symmetrical 10deg-h20-C-m14 at 0.267c (ms ⁻¹)	102
Figure 101: Velocity contours for 10deg-h20-C-m14 at 1.333c (ms ⁻¹)	102
Figure 102: Velocity contours for symmetrical 10deg-h20-C-m14 at 1.333c (ms ⁻¹)	103
Figure 103: Velocity contours for 10deg-h20-C-m14 at 2.667c (ms ⁻¹)	103
Figure 104: Velocity contours for symmetrical 10deg-h20-C-m14 at 2.667c (ms ⁻¹)	103
Figure 105: Upper and Lower Vortex path for 10deg-h20-C-m14, velocity path lines (ms ⁻¹)	104
.....	
Figure 106: Upper and Lower Vortex path for symmetrical 10deg-h20-C-m14, velocity path lines (ms ⁻¹)	104
.....	
Figure 107: Suction surface static pressure contour plot for 10deg-h20-C-m14 (Pa)	104
Figure 108: Suction surface static pressure contour plot for symmetrical 10deg-h20-C-m14 (Pa)	105
.....	
Figure 109: LDA velocity contours in 3D for 10deg-h20-C-m14	112
Figure 110: CFD velocity contours in 3D for 10deg-h20-C-m14	112
Figure 111: Comparison of 10deg-h20-C-m14 case at plane at 0.267c	113
Figure 112: Comparison of 10deg-h20-C-m14 case at plane at 1.333c	113
Figure 113: Comparison of 10deg-h20-C-m14 case at plane at 2.667c	114

Figure 114: Velocity vector plots for LDA and CFD at 0.067c.....	114
Figure 115 Velocity vector plots for LDA and CFD at 0.267c.....	115
Figure 116: Velocity vector plots for LDA and CFD at 1.333c.....	115
Figure 117: Velocity vector plots for LDA and CFD at 2.667c.....	115
Figure 118: Flow swapping sides of endplate for case 4412-10deg-h10-D-m5 (units are particle ID)	116
Figure B1: Suction surface static pressure contours for 6deg-h10-A-m2 (Pa)	128
Figure B2: Suction surface static pressure contours for 6deg-h10-A-m4 (Pa)	128
Figure B3: Suction surface static pressure contours for 6deg-h10-B-m2 (Pa)	129
Figure B4: Suction surface static pressure contours for 6deg-h10-B-m4 (Pa)	129
Figure B5: Suction surface static pressure contours for 6deg-h10-C-m2 (Pa)	129
Figure B6: Suction surface static pressure contours for 6deg-h10-C-m4 (Pa)	130
Figure B7: Suction surface static pressure contours for 6deg-h10-D-m2 (Pa)	130
Figure B8: Suction surface static pressure contours for 6deg-h10-D-m4 (Pa)	130
Figure B9: Suction surface static pressure contours for 6deg-h15-A-m4 (Pa)	131
Figure B10: Suction surface static pressure contours for 6deg-h15-A-m9 (Pa)	131
Figure B11 Suction surface static pressure contours for 6deg-h15-B-m4 (Pa)	131
Figure B12: Suction surface static pressure contours for 6deg-h15-B-m9 (Pa)	132
Figure B13: Suction surface static pressure contours for 6deg-h15-C-m4 (Pa)	132
Figure B14: Suction surface static pressure contours for 6deg-h15-C-m9 (Pa)	132
Figure B15: Suction surface static pressure contours for 6deg-h15-D-m4 (Pa)	133
Figure B16: Suction surface static pressure contours for 6deg-h15-D-m9 (Pa)	133
Figure B17: Suction surface static pressure contours for 6deg-h20-A-m9 (Pa)	133
Figure B18: Suction surface static pressure contours for 6deg-h20-A-m14 (Pa)	134
Figure B19: Suction surface static pressure contours for 6deg-h20-B-m9 (Pa)	134
Figure B20: Suction surface static pressure contours for 6deg-h20-B-m14 (Pa)	134
Figure B21: Suction surface static pressure contours for 6deg-h20-C-m9 (Pa)	135
Figure B22: Suction surface static pressure contours for 6deg-h20-C-m14 (Pa)	135
Figure B23: Suction surface static pressure contours for 6deg-h20-D-m9 (Pa)	135
Figure B24: Suction surface static pressure contours for 6deg-h20-D-m14 (Pa)	136
Figure B25: Suction surface static pressure contours for 6deg-h40-A-m28 (Pa)	136

Figure B26: Suction surface static pressure contours for 6deg-h40-A-m34 (Pa)	136
Figure B27: Suction surface static pressure contours for 6deg-h40-B-m28 (Pa)	137
Figure B28: Suction surface static pressure contours for 6deg-h40-B-m34 (Pa)	137
Figure B29: Suction surface static pressure contours for 6deg-h40-C-m10 (Pa)	137
Figure B30: Suction surface static pressure contours for 6deg-h40-C-m34 (Pa)	138
Figure B31: Suction surface static pressure contours for 6deg-h40-D-m10 (Pa)	138
Figure B32: Suction surface static pressure contours for 6deg-h40-D-m34 (Pa)	138
Figure B33: Suction surface static pressure contours for 10deg-h10-A-m4 (Pa)	139
Figure B34: Suction surface static pressure contours for 10deg-h10-A-m5 (Pa)	139
Figure B35: Suction surface static pressure contours for 10deg-h10-B-m4 (Pa)	139
Figure B36: Suction surface static pressure contours for 10deg-h10-B-m5 (Pa)	140
Figure B37: Suction surface static pressure contours for 10deg-h10-C-m4 (Pa)	140
Figure B38: Suction surface static pressure contours for 10deg-h10-C-m5 (Pa)	140
Figure B39: Suction surface static pressure contours for 10deg-h10-D-m4 (Pa)	141
Figure B40: Suction surface static pressure contours for 10deg-h10-D-m5 (Pa)	141
Figure B41: Suction surface static pressure contours for 10deg-h15-A-m9 (Pa)	141
Figure B42: Suction surface static pressure contours for 10deg-h15-A-m10 (Pa)	142
Figure B43: Suction surface static pressure contours for 10deg-h15-B-m9 (Pa)	142
Figure B44: Suction surface static pressure contours for 10deg-h15-B-m10 (Pa)	142
Figure B45: Suction surface static pressure contours for 10deg-h15-C-m9 (Pa)	143
Figure B46: Suction surface static pressure contours for 10deg-h15-C-m10 (Pa)	143
Figure B47: Suction surface static pressure contours for 10deg-h15-D-m9 (Pa)	143
Figure B48: Suction surface static pressure contours for 10deg-h15-D-m10 (Pa)	144
Figure B49: Suction surface static pressure contours for 10deg-h20-A-m14 (Pa)	144
Figure B50: Suction surface static pressure contours for 10deg-h20-B-m14 (Pa)	144
Figure B51: Suction surface static pressure contours for 10deg-h20-C-m14 (Pa)	145
Figure B52: Suction surface static pressure contours for 10deg-h20-D-m14 (Pa)	145
Figure B53: Suction surface static pressure contours for 6deg-no endplate (Pa)	145
Figure B54: Suction surface static pressure contours for 10deg no endplate (Pa).....	146
Figure C1: Moving ground drawing MVG1	147
Figure C2: Moving ground drawing MVG2	148

Figure C3: Moving ground drawing MVG3	149
Figure C4: Moving ground drawing MVG4	150
Figure C5: Moving ground drawing MVG5	151
Figure C6: Moving ground drawing MVG6	152
Figure C7: Moving ground drawing MVG7	153
Figure C8: Moving ground drawing MVG8	154
Figure C9: Moving ground drawing MVG9	155
Figure C10: Moving ground drawing MVG10	156
Figure C11: Moving ground drawing MVG11	157

LIST OF TABLES

Table 1: Endplate details.....	20
Table 2: Height / Chord ratios.....	21
Table 3: Flow visualisation test case statistics.....	38
Table 4: Maximum and minimum C_L , C_D and C_L/C_D values for each case set	82
Table 5: Endplate configuration, height vs case number	82
Table A1: Test case details	124
Table A2: CFD test case statistics.....	126
Table A3: C_L , C_D and C_L/C_D values from CFD	127

NOMENCLATURE

SYMBOL	MEANING	UNITS
AR	Aspect Ratio	-
c	wing chord length	mm
C_D	Drag coefficient ($D/\frac{1}{2} \rho V^2 S$)	-
C_L	Lift coefficient ($L/\frac{1}{2} \rho V^2 S$)	-
D	Drag	N
e	Internal energy	J
h	Height of wing above ground	mm
he	Height of endplate above ground	mm
L	Lift	N
P	Pressure	Pa
Re	Reynolds number	-
S	Wing area	m^2
\dot{q}	Heat transfer coefficient	$Jm^{-2}s^{-1}$
U_∞	Free stream velocity	ms^{-1}
\mathbf{V}	Vector velocity	ms^{-1}
x, y, z	Cartesian axes	-
α	Angle of incidence	degrees
f_x	x component of body force	N
f_y	y component of body force	N
f_z	z component of body force	N
$k-\varepsilon$	Turbulence model	-
ρ	Density	kgm^{-3}
τ_{xx}	x component of normal force in x direction	N
τ_{xy}	y component of shear force on x - y plane	N
τ_{xz}	z component of shear force on x - z plane	N

τ_{yx}	x component of shear force on y - x plane	N
τ_{yy}	y component of normal force in y direction	N
τ_{yz}	z component of shear force on y - z plane	N
τ_{zx}	x component of shear force on z - x plane	N
τ_{zy}	y component of shear force on z - y plane	N
τ_{zz}	z component of normal force in z direction	N
u	x component of velocity	ms^{-1}
v	y component of velocity	ms^{-1}
w	z component of velocity	ms^{-1}

1. INTRODUCTION

1.1 Topic

Inverted wings were first used on a racing car in 1966 in the CanAm (Canadian-American Challenge Cup) series, on the Chaparral 2E racing car. Following the success on this innovative aerodynamic aid, the use of inverted wings quickly spread throughout the automotive racing world. Inverted wings generate downforce by creating a suction force on the surface of the wing closest to the road.

Many aerodynamic developments have dramatically improved the performance of racing cars, from series such as the open wheel type: Formula 1, A1 and Indy cars, to hill climb series and even drag racing. Figure 1 (own picture) shows an example of a modern inverted wing with endplate in motor sport. The particular component which will be investigated is the front wing with endplates on open wheel type racing cars. The front wing of modern open wheel racing cars predominantly function in ground effect, producing up to 30% of the total downforce of the vehicle [1]. Even for racing cars where cornering speeds are of no concern, the maximum possible downforce is necessary to help transmit enormous power from the wheels to the ground with speeds in excess of 500kmh^{-1} , as in Top Fuel drag racing vehicles, see figure 2 (own picture).



Figure 1: Modern open wheel racing car front wing with endplates



Figure 2: Inverted wings with endplates used in drag racing

The front wing plays an important role in the aerodynamic performance since the majority of the flow around the car is governed by the geometry of the front wing. Much research has been performed by racing teams and racing car manufacturers, but this data remains a closely guarded secret, as every team is aiming for a competitive edge.

1.1.1 Problem Definition

Many shapes and sizes of endplates are used in motor sport, gaining an understanding of the effects from various endplate configurations will contribute to the knowledge of complex airflows generated and needed in high performance motor sport.

1.2 Literature Review

Originally racing cars relied on tyre performance alone for cornering at high speeds, the use of inverted wings and other aerodynamic devices has increased the performance to the levels seen today. Before the use of aerodynamic downforce, the lateral acceleration of a racing vehicle was around 1g, with the introduction and development of aerodynamic downforce the lateral acceleration rapidly increased to around 4g [2], a level where the drivers are subjected to very high loads. The vehicle designers would certainly be pleased with this performance, but the drivers will definitely become the limiting factor for car cornering speeds.

Modelling and simulating racing car style inverted wings, that is, low aspect ratio inverted wings close to the ground, requires equal consideration on ground detail as well as

wing detail. It has been regularly documented [3] that a moving ground, that is, where the ground is moving at the same velocity as the free stream, is the most accurate representation of real life applications. Other methods [3] [6] [14] for simulating the ground have been studied, these include a symmetrical model, using two identical wings opposite each other with the imaginary mid plane acting as the ground. Theoretical and computational studies have used a slip boundary condition, where the shear stresses are set at zero at the ground plane. And the most basic is using a stationary ground to represent the ground. The main problem with using a stationary ground for ground effect analyses is the boundary layer growth along the test section. As the boundary layer grows in thickness, the flow around the inverted wing is affected, due to loss of momentum of the airflow close to the ground.

A two-dimensional study [3] shows that a NACA4412 airfoil (not inverted) with h/c less than 0.1, the C_L value can vary by as much as 30% with respect when using a stationary and moving ground. The C_D can vary by as much as 20% in the same conditions. The problem of boundary layer growth led to the use of various techniques of removing the boundary along the stationary test section ground [4]. These techniques include suction systems and air injection systems, but may change the pressure gradient in the test section [5].

Ground effect in normal wing configurations, that is, the suction surface up, was noticed first by pilots when they flew aircraft close to the ground. Pilots observed an increase in lift and forward pitching moment. The increase in lift causes an increase in the slope of the wing lift curve, the increase in forward pitching moment is caused by the reduction of downwash acting on the tail [7]. The wingtip vortices generated in free stream flow are caused by the air 'spilling' from the high pressure surface to the low pressure surface [16]. Numerous theorems have been developed to study the phenomenon of vortical flows.

The effects of endplates on a wing in free stream flow showed that the area and shape of an endplate can have an effect on the C_L and C_D values. The airfoil section was a NACA 641A412, with an $AR = 4$ [10].

The performance of racing cars using inverted wings in ground effect, also suffer from performance changes. The front wing operates in ground effect, and the wake generated by the front wing dictates the flow around the rest of the vehicle [8]. The

stiffness of the suspension can impact on the downforce, as the car travels faster, the higher the downforce and the higher the compression of the suspension, at slower speeds the suspension is under less load and the car could ride higher, therefore altering the ground effect on the front wing.

Studies of the performance of a single element inverted wing (Section LS(1)-0413 MOD) in ground effect have shown that as the wing approaches the ground the C_L increases until a $h/c = 0.082$ [9]. It was found that as the wing approaches the ground the wake increases, therefore increasing the drag.

A typical simple front wing consists of a single element wing and flat endplate attached to the wing tips. A study [11] shows that when an inverted wing with endplates is positioned near the ground, the tip vortices and flow separation on the suction surface. The vortex was noted to decrease in intensity the lower the h/c , until a h/c with maximum C_L where the vortex breaks down completely. The emphasis of the study was on the lower vortex generated by the suction surface / endplate region. Endplates used in racing cars can increase the downforce by as much as 30% compared to not using endplates on inverted wings [15]. A study [17] comparing variable wing height to fixed endplate height shows that the maximum downforce is obtained when the wing is close to the ground, that is, with a ground clearance of 22% rather than 29%.

The path of vortices change with varying wing angles of incidence and height. A study [12] into the movement of wingtip vortices generated by a Gottingen 723 wing (not inverted) shows that as the wing is located closer to the ground the vortex path moves laterally outwards away from the wingtip. A study of an inverted wing with a NACA4412 section investigated the movement of the vortex laterally [13]. Cases ranged from $h/c = 1$ to $h/c = 0.1$ and the trend was the vortex moved laterally inwards as h/c was lower.

Simulating the flow around the generic front wing with endplates using a CFD solver presents choices and problems. 2D or 3D simulation, developing the geometry and choosing the correct, or most suitable turbulence model. Many studies have been performed for ground effect analysis, with different solutions for different cases.

A study [3] used the RNG $k-\epsilon$ turbulence model to investigate the flow of a NACA4412 airfoil shows that there are errors in the final solution, the C_L error is around 3% and C_D error around 11%. Another 2D study by Zerihan [9] compares two turbulence models to experimental results. The turbulence models were the Spalart-Allmaras one

equation model and Menter $k-\omega$ model. The $k-\omega$ turbulence model was found to produce a larger boundary layer, therefore producing incorrect results when the wing was close to the ground, while the Spalart-Allmaras turbulence model produces a C_L that was slightly more than the experimental results.

Moryossef and Levy [18] investigated the difference between modelling inviscid and viscous flows, it was found that the viscous turbulence model predicted the surface pressure coefficient more accurately than the inviscid model. A inviscid turbulence model is suitable for wing heights over $h/c = 0.5$, and for very small h/c values the viscous effects cannot be ignored.

The $k-\varepsilon$ turbulence models have been found to produce incorrect pressure coefficients at stagnation points [19], which will lead to incorrect C_L and C_D values, as found in other studies. A Reynolds Stress transport Model (RSM) was found to produce more accurate stagnation pressures. The downside of the increase in accuracy is the increase in CPU time necessary [19] [28].

A study of vortex shedding [20] used a Shear-Stress Transport (SST) $\varepsilon - SST$ turbulence model. This model is acceptable for use where some flow separation is expected.

An series of laser Doppler anemometry experiments was conducted by Zerihan [9], these experiments were conducted on an inverted wing with endplates.

1.3 Aims and Objectives of Research

The aims and objectives of this thesis are to:

- Help develop, design and construct a suitable moving ground system for the University of New South Wales T1 wind tunnel.
- Examine the flow fields generated by inverted wings with endplates in ground effect, using experimental and computational techniques.

1.4 Thesis Structure and Methodology

The thesis is split into the following sections:

- Moving ground development and design.

- Describing the wind tunnel test facilities
- Perform basic flow visualisation experiments to help choose turbulence model
- Test cases examined
- Flow visualisation cases
- Computational fluid dynamics cases
- Laser doppler anemometry cases
- Results comparison
- Causes of error
- Discussion of results

1.6 Summary

Much research has been undertaken on inverted wings in ground effect, but there is a limited knowledge base in regards to the effects of inverted wings using different endplates in ground effect. Looking at the motor sport industry, it is obvious from the technological advances over the years that research is performed, but unfortunately from a public research perspective, that knowledge remains proprietary to those companies.

The flow fields generated by inverted wings with endplates are interesting and complex, with many unknowns. The use of laser Doppler anemometry and flow visualisation are important tools as they are both non-intrusive and provide a large amount of detail on the flow structures. Public information or published studies on this topic was very limited, the details on computational fluid dynamics studies and laser Doppler anemometry experiments was limited. This thesis uses experimental and computational techniques available at the time to help build the knowledge base and expose details in the complex flow structure that merits further investigation.

2. MOVING GROUND

2.1 Chapter Overview

This chapter discusses the importance of using a moving ground in ground effect aerodynamics, the design, construction, development and testing of the moving ground. Section 2.2 describes the importance of the moving ground. Section 2.3 describes the design and construction. Section 2.4 discusses the issues during the development of the moving ground.

2.2 Practicality and Use of a Moving Ground

In order to study inverted wings in ground effect, a wind tunnel with a moving ground is necessary. In wind tunnels with stationary walls, the velocity profile is not constant across the test section, a boundary layer is present, and grows in thickness along the length of the entire tunnel. In the case of studying normal or inverted wings close to a surface, simulating ground for example, the velocity profile of the air between the wing and the surface, the 'ground' does not represent this same case in reality. In a wind tunnel with stationary walls, the wing and ground are both stationary, and the air moving relative to both. Where as in reality the wing is moving and the ground and air (to an extent) is stationary.

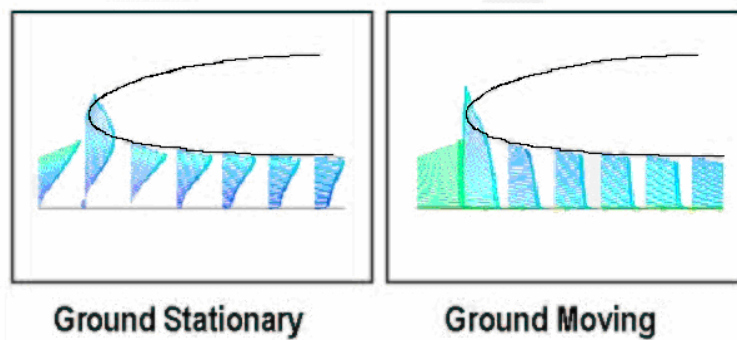


Figure 3: Air velocity profiles with wing near ground

Figure 3 [13] illustrates the air velocity profiles when the ground and wing are stationary, with air moving (left) and when the air and ground are moving relative to the wing. Using a stationary 'ground' presents many problems when investigating the air flow

around and downstream of the wing, incorrect pressure distributions will result from disrupted flow from the boundary layer, any wake and vortices will also be affected.

A typical moving ground installation in a wind tunnel consists of a flexible belt, wrapped around 2 primary rollers and other rollers for tension control and alignment. The speed of the belt matches the free stream velocity in the test section. Moving grounds are used in many various sized wind tunnels, some which are capable of testing full size vehicles use multiple belts.

The size of the wind tunnel and the tests which are desired dictate the size and speed of the moving ground, and the larger and faster the moving ground, the more complex the system. Cooling systems and other control systems also grow in complexity.

Various methods for removing the boundary layer before the belt and test section include, suction systems before the test section, the boundary layer is sucked through many small holes in the wind tunnel ground. Suction systems along the test section, many holes along the length of the test section remove the boundary layer along the entire length. The test section can be raised to allow the developed boundary layer to pass underneath, either vented to atmosphere or rejoining the wind tunnel flow behind the test section. A combination of these methods are also used [4]. The simplest method is to allow the boundary layer to pass underneath the test section.

2.3 Moving Ground Design and Construction

The wind tunnel air volume was designed by Sam Diasinos. The air flow geometry was modelled in CATIATM v5 and simulated using FluentTM. The test section air volume was used as a “negative”, and the moving ground structure was modelled to fit around the air volume. The length of the moving belt was designed approximately 1000mm in length, and the width approximately 230mm. The actual test section tapered from 232mm to 227mm. A duct to pass the boundary layer beneath the test section limited the space for the moving ground structure. Figure 4 shows the test section air volume. The basic requirements for the moving ground were: the maximum belt velocity must equal the maximum free stream velocity – 15ms^{-1} , driven externally, the original power source was an angle grinder motor.

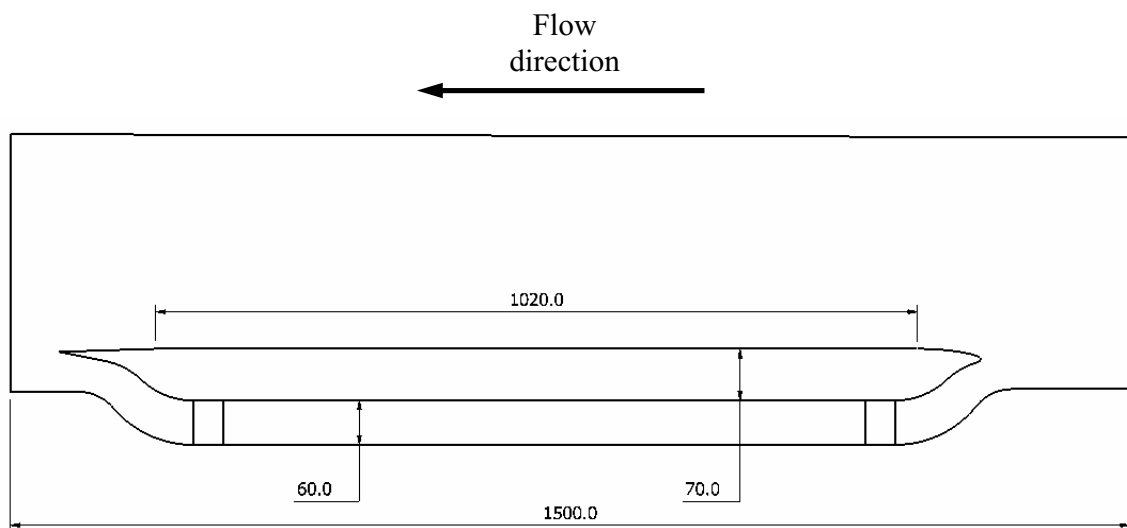


Figure 4: Test Section Basic Dimensions

The basic mechanisms needed to be fitted, these include the front and rear rollers, and the tension roller. The front and rear rollers were supported by 8mm roller bearings, position fixed. The tension roller height variable to maintain belt tension and also to help the tracking of the belt. The structure was designed such that belt access was provided, and the provision to remove the moving ground as a whole assembly from the wind tunnel if needed.

The front and rear rollers were salvaged from an older moving ground, they were also acrylic, with diameters of 50mm. The tension roller was manufactured from aluminium and the diameter was 22mm. The tension roller diameter needed to be less than the main rollers to allow the height to be adjusted. Arms manufactured from sheet stainless steel held the roller and allowed the height to be adjusted via “swinging and locking” the arms at different positions.

The main walls and supports were designed using clear acrylic, manufacturing limits were noted and compromises made to allow for the manufacture and assembly of the parts. Figure 5 is a computer model (modelled using Inventor™ CAD software). The drawings for the Perspex parts are shown in Appendix C.

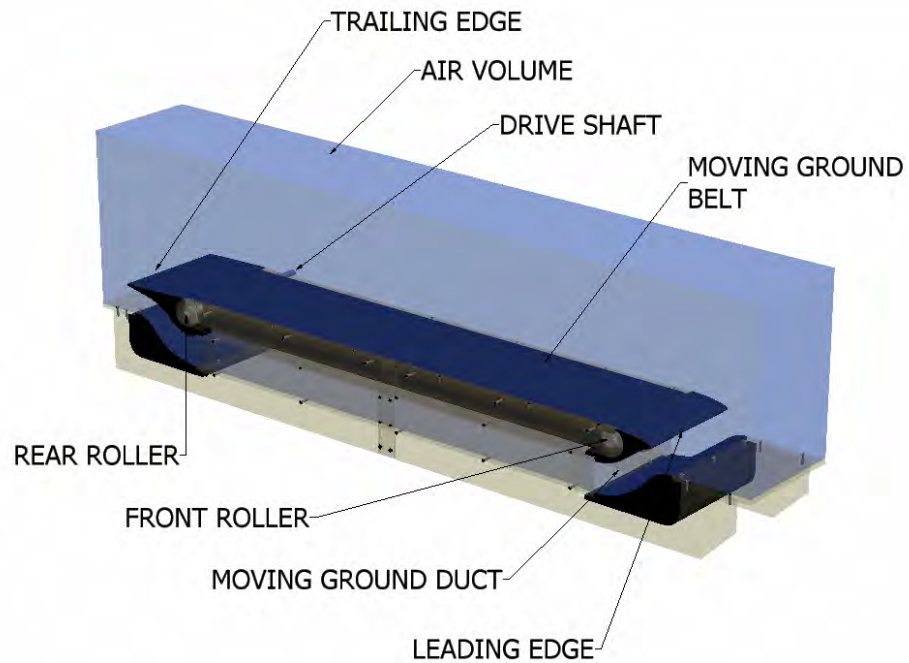


Figure 5: Computer model of moving ground assembly and test section air volume

The leading and trailing edge parts were originally designed as single parts each, manufacturing restrictions led to these parts being manufactured in slices, each 25mm wide. These slices were glued together using PVA wood glue and sanded down to a suitable surface finish.

Several options were planned for the belt itself, including a clear thin sheet of polycarbonate. The first prototype belt constructed was made from 1.5mm EPDM insertion rubber, joined using Urethane Bond and a thin fabric approximately 100mm wide across the join. Care was taken to ensure that the belt was straight. Unfortunately the first prototype belt was not joined straight, and resulted in the belt wobbling as it travelled. A second belt of similar material and construction was more successful. The polycarbonate option was quickly dismissed after an initial attempt, although flexible around the rollers, it was intolerant to any crowning on the main rollers, and creating a thin and smooth join was problematic.

A stand was constructed to hold the angle grinder motor and a drive shaft using a flexible coupling connecting the drive (rear) roller. The angle grinder was originally used as it provided the torque and rpm necessary to drive the belt, it was also variable speed controlled.

2.4 Moving Ground Development

During the first runs of the moving ground, problems were noted. Before assembling the entire wind tunnel, the moving ground was set up separately and test run until the function was satisfactory. The following is a list of the problems observed:

- Belt drifting to opposite sides when running at different speeds
- Belt not remaining flat near drive (rear) roller at higher speeds
- Belt speed not constant
- Flexible drive failing
- Static charge build up
- Belt join failure

When varying the belt speed i.e. increasing from a low to high speed, it was noted that the belt would drift from one side of the moving ground bed to the other. Although calibrating the belt position at a particular speed was possible, calibration was impossible across a range of speeds. The drift was a result of two main issues, the belt was not perfectly straight and the rollers were ‘flat’.

The original rollers which were salvaged from previous moving ground had ‘flat’ cylindrical surfaces, where as crown is needed Crown is a feature on a roller where the centre of the roller has a larger diameter than the edges. New rollers were designed with crown by Diasinos, S. and were made from aluminium, the exact alloy and temper were not known as they were manufactured from spare pieces from the workshop. Aluminium was chosen as one of the acrylic rollers cracked near the bearing counter bore.

Before the new rollers were installed, crown was improvised on the acrylic rollers by wrapping a layer of masking tape around the drive roller. When the roller was mounted, the moving ground speed was ramped up to approximately 10ms^{-1} , the tracking was studied, and if the belt drifted to one side, the roller was removed and the tape position changed. This was a very time consuming process as each iteration was around 20 minutes. A very small adjustment in the tape position caused the belt to drift to either side. The belt position was steady at various speeds after many attempts. Figure 6 shows the moving ground belt and drive during the alignment process.

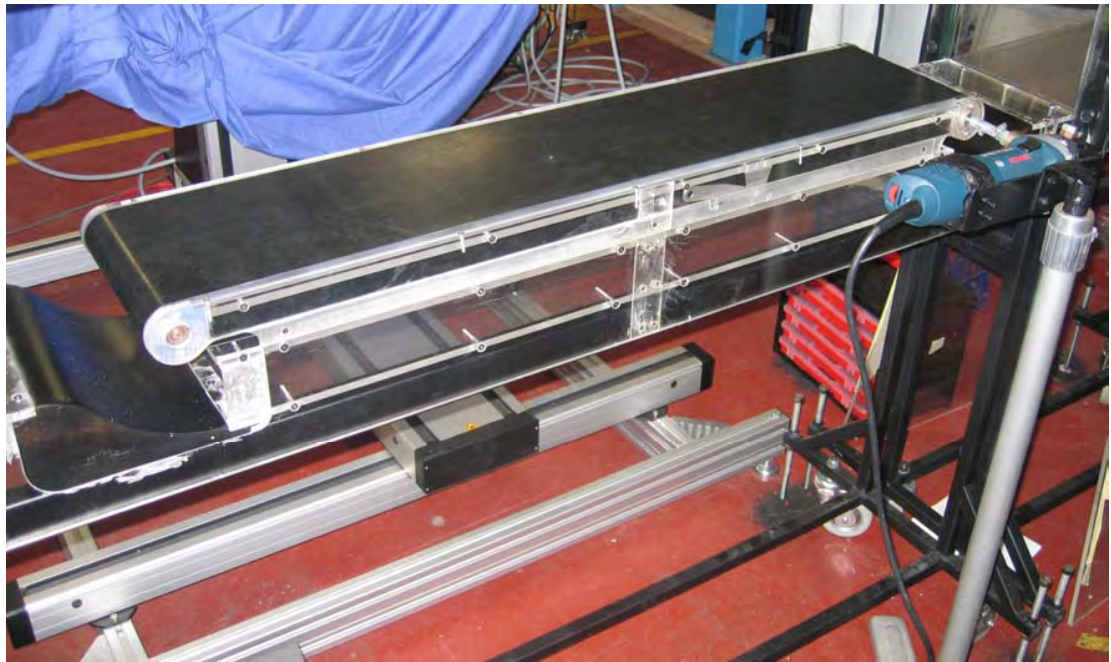


Figure 6: Moving ground during belt adjustment

Once confident with the belt position, the speed was ramped up to higher speeds ($\sim 15\text{ms}^{-1}$). Another issue was that at higher speeds the belt deflected near the drive roller. The belt bulged above the moving ground bed just before the drive roller, the height of the bulge was approximately 10mm. This would become an obstacle in the wind tunnel, although at the rear of the test section, the flow upstream of the bulge would be affected.

The tension roller was adjusted to apply maximum tension on the belt, but at the higher speeds, the bulge still remained. The tension roller mountings were modified. With the higher tension, there was no bulge, but the drifting returned. Adjusting the crown (tape) on the roller was now relatively easy, it did not take long to fix that problem.

The first flexible drive was too flexible, it was made using pipe clamps and a nylon reinforced air hose. After prolonged moving ground use, the hose needed changing. A solution was to source a thicker tube. A thicker, heavier nylon reinforced hose was used. This version was more durable and resisted sudden changes torque from belt loads, such as when increasing and decreasing speed.

After the above issues were fixed, the moving ground was tested in the wind tunnel. Initial tests were carried out with an empty test section. Smoke visualisation was carried out by Diasinos, S., to assist in verifying the CFD model of the tunnel [13]. Initial observations were promising, the boundary layer flowed underneath the moving ground as predicted.

During extended periods of running, the frictional load on the belt increased gradually, this was noted via the different sound pitch from the motor, occasionally the belt would almost stop, as the motor did not have sufficient torque to overcome the frictional force on the belt. It was not clear at first what was creating the variable frictional force, as the moving ground ran smoothly some days, and seemingly under heavy load other days. It was discovered that the friction was caused by a creation of a static charge on the belt, virtually sticking the belt to the acrylic belt bed. Also when the moving ground was run initially the weather was warm and humid, but as the weather cooled and humidity dropped, the frictional force increased, rendering the moving ground useless.

The acrylic belt bed was replaced by a sheet of PTFE, this reduced the frictional force on the belt, but did not eliminate it, as the belt was in contact with other parts. The next idea was to mount multiple thin copper wires on the top of the belt bed and under the belt. Three wires were fixed in position as shown in figure 7, and the ends of each wire joined and earthed.

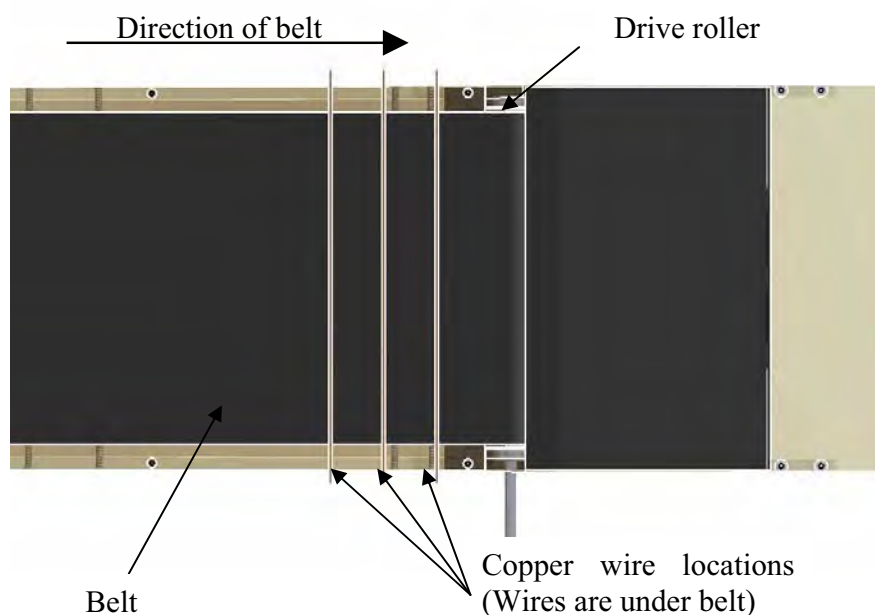


Figure 7: Copper wire locations

On a cool dry day, there was sufficient static charge build up, that when the collector wires were removed from earth and brought close to an earthing object, small sparks would jump across the air gap. Static charge was created, but as long as the copper

connector wires were earthed, there was no build-up and subsequent increase in friction. Another location where static charge was observed was around the front roller bearings and acrylic surfaces near the bearings. During laser sheet visualisation experiments, with a dark room, a faint blue glow was observed around the mentioned areas, upon close inspection many very small sparks were continuously jumping across the joints in the moving ground parts. This did not effect the performance of the moving ground, but never the less, an interesting observation and quite disturbing when first noticed.

After many hours of use, the belt join started to fail. Since this was one of the prototype belts, it lasted longer than expected. Diasinos, S., sourced a professionally made belt, similar to belts used in food production conveyors.

The moving ground worked well, but after much use the structure started to wear and break, as the parts were made from acrylic. The idea of a clear moving ground was novel, but impractical, as it was not reliable. The rolling ground rollers and supporting structure were eventually replaced by an aluminium frame. The newer reliable aluminium frame based moving ground was used for the CFD verification of the moving ground design, and all flow visualisation and LDA experiments.

2.5 Summary

From the initial design of the moving ground, much development took place to ensure that the moving ground was reliable and accurate. Reliability was important as many hours of experiments took place, and accuracy of speed was needed to maintain constant speed during both flow visualisation and LDA experiments.

3. WIND TUNNEL TEST CASES

3.1 Chapter Overview

This chapter covers the wind tunnel facilities available for experimentation, the endplates and endplate configurations, flow visualisation techniques and LDA experiments.

3.2 Wind Tunnel Test Facilities

The wind tunnel used for all experiments was the UNSW T1 wind tunnel with 235mm x 440mm test section (232mm x 290mm with moving ground installed). This tunnel was specifically designed for studying ground effect. The clear acrylic walls allow use of flow visualisation and laser measurement techniques, including LDA (Laser Doppler Anemometry) and PIV (Particle Image Velocimetry). These techniques were possible using laser beams and laser sheets, and viewing, photographing and video recording the highlighted sections [13]. The test section has a width of 235mm and height of 440mm [13]. The tunnel is powered by a Donaldson Torit 10kW vacuum box, and the maximum free stream velocity is 15ms^{-1} . The moving ground belt has a width of 200mm and a flat length of 1000mm. The left wall has mounting facilities for various wing sections and a single wheel, the wing height and angle of attack can be changed with the wing remaining in the tunnel. The wing can be mounted normal or inverted, and the wing tip at the mid-plane of the tunnel or simulating 2D flow by mounting the wing spanning the tunnel. There were no facilities to measure forces or moments acting on the wing.

The wing section was made from clear acrylic, to allow a laser sheet to pass through and illuminate the seeded air below the wing, although the light would refract through curved objects, the majority of the underside would be illuminated. The endplates used were made from clear 1mm thick polycarbonate sheet, and attached to the wingtip using 3M double sided tape.

The wing section used was NACA4412, with a chord length of 75mm, with a corresponding maximum thickness of 9.3mm, the section geometry was taken from [23]. This section was being used for other ground effect studies, continued use of this section would provide a larger knowledge pool on ground effect based around the NACA4412. Testing was carried out at 10ms^{-1} , due to moving ground speed limitations and also was to match other work which was carried out previously and currently. The corresponding

Reynolds number (Re) is 53.3×10^3 (see section 6.5.4). Figure 8 shows a typical test case with an inverted NACA4412 airfoil with an endplate attached.



Figure 8: Typical test case

The wind velocity was measured using a Betz manometer with a Pitot static tube inserted into the test section, without obstructing the flow near the wing and endplate. Initially the moving ground speed was measured using a hand held tachometer, which had both an optical sensor for measuring the frequency of a passing marker, and a roller to hold against the belt.

3.3 Endplates

The choice of endplates was limited to four versions, all rectangular. From studying numerous images from books, magazines and the internet, a large variety of endplate shapes are used, from basic rectangular, to complex trapezoidal shapes with extra protrusions. For the scope of this thesis, it was decided to use simple rectangular shapes, as a basis for the study of inverted wings with endplates. A study [17] looks at endplates with various features, this study was CFD based and presented no experimental results.

Four endplate sizes were chosen for wind tunnel and CFD analysis. Using one wing section (NACA 4412) with the four endplate sizes, a myriad of combinations was possible.

The first step was to limit the number of cases for investigation, this process was repeated several times during the course of the research, as the information obtained became a huge database. The endplates investigated are based around the endplates used on inverted front wings on racing vehicles.

Different motor sport fields use different regulations to define the aerodynamic devices allowed for use on racing cars, that is, the size and shape of front wing elements are not limited, to an extent. Therefore the scope of this study will include four arbitrary endplates of different areas and aspect ratios. Figure 9 shows the four endplates used in the wind tunnel tests. Table 1 shows the corresponding length, height, aspect ratio and area for the endplates.

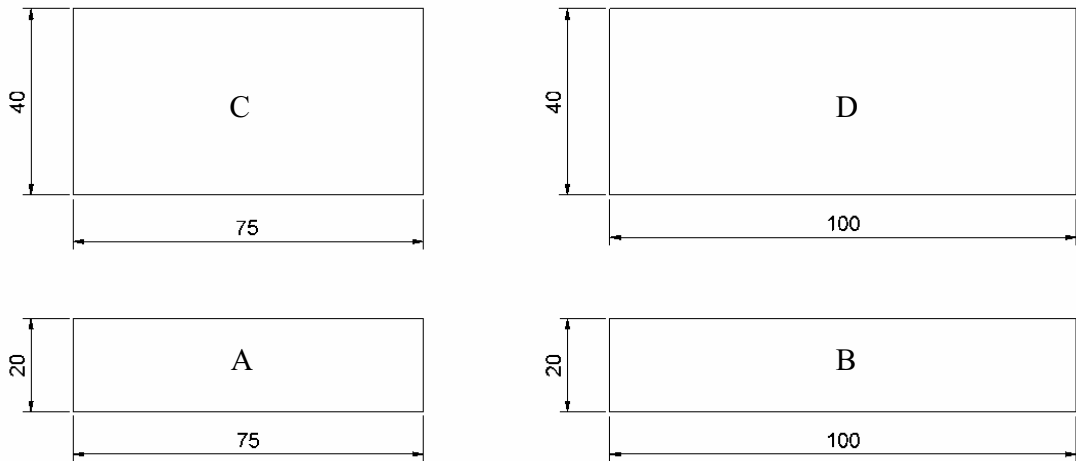


Figure 9: Endplate sizes for wind tunnel tests (mm)

Endplate details				
Name	Length	Height	AR	Area
	(mm)	(mm)		(mm ²)
A	75	20	3.75	1500
B	100	20	5	2000
C	75	40	1.88	3000
D	100	40	2.5	4000

Table 1: Endplate details

The endplates were manufactured from 1mm thick clear polycarbonate. The sharp edges were removed, and the edge faces left as flat as possible, this was to help with running CFD cases, as any curved surfaces on the edges of the endplates would present numerous problems when meshing. No airfoil sections were used for the endplates, as an airfoil shape would affect the pressure distributions and velocity profiles near the wing and endplate join. Ease of manufacture and assembly was another small reason for the flat endplates. The double sided tape used for attaching the endplates allowed for quick change over during experiments, and did not require any protruding features from the thin endplate surfaces for mounting purposes.

An example endplate assembly is shown in figure 10, the endplate dimensions are arbitrary. For all the test cases, the endplates were located longitudinally an equal distance from the leading and trailing edges of the wing, 'h' depicts the minimum height of the wing surface above the ground, ' α ' is the angle of incidence and 'he' is the minimum height of the endplate above the ground.

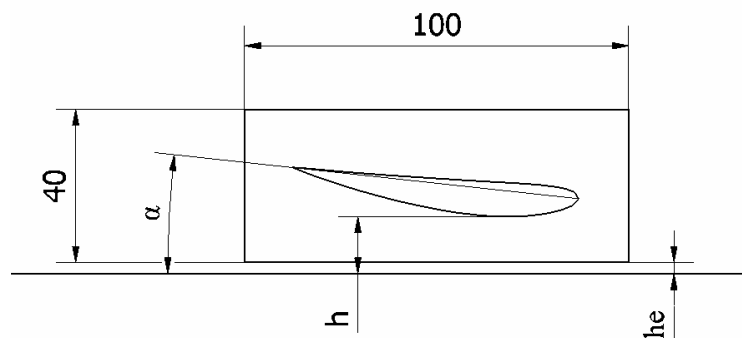


Figure 10: Example endplate configuration (mm)

Table 2 shows the corresponding height/chord (h/c) ratios for the test cases.

Height/Chord Ratios				
h	5	10	15	30
h/c	0.07	0.13	0.2	0.4

Table 2: Height / Chord ratios

3.4 Flow Visualisation

Flow visualisation is an indispensable tool when studying fluid flow. It allows us to see the flow, and to break down the whole picture into sections that make it easier to study and record. Flow visualisation techniques can aid with CFD simulations, such as highlighting 2D planes in 3D flows and comparing the two results.

A simple and very effective method of flow visualisation is to use a laser sheet to highlight a 2D plane in the wind tunnel. A 25mW Helium-Neon laser was used to create a sheet of light, which was movable to any desired position. A second laser sheet generated by a laser diode was used to highlight the endplate. This allowed the plane of interest to be referenced to the wing and endplate, and to highlight which endplate is attached to the wing. Flow seeding was generated using a fog machine. The amount of fog and the location and direction of the fog jet needed fine tuning until just the right amount was drawn through the tunnel in the right region. Too much fog and the flow was a blur, and too little and the flow detail was indistinguishable from other light interference.

Figure 11 shows an example of using two laser sheets to record flow patterns.

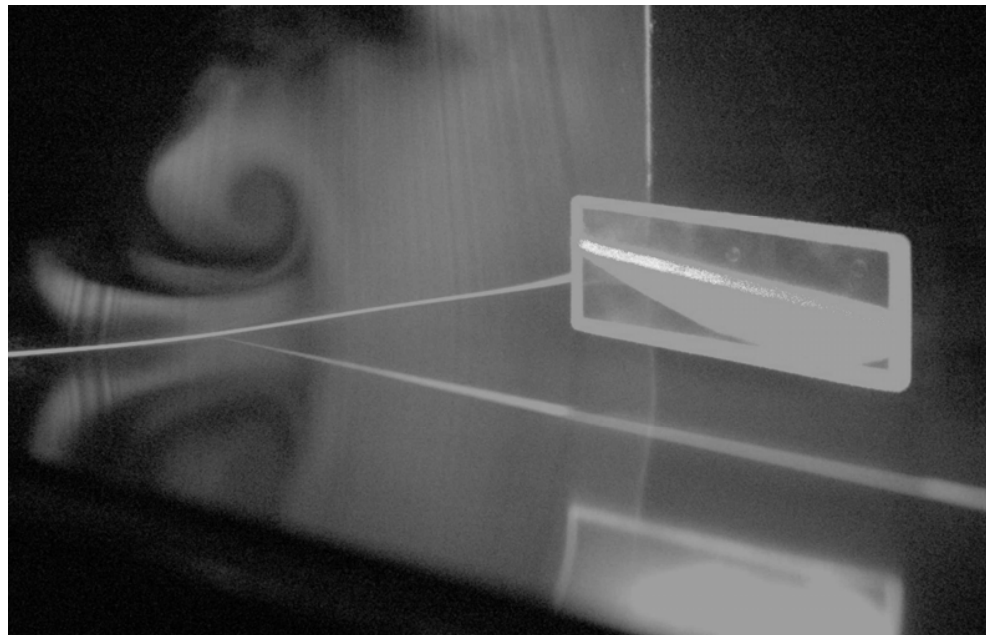


Figure 11: Flow visualisation example

To study the vortices generated, the plane was always across the wind tunnel, perpendicular to the free stream flow. The reference laser was fixed for each case and the

plane was located at four displacements behind the endplate rear edge. The four distances were 5mm (0.067c), 20mm (0.267c), 100mm (1.333c) and 200mm (2.667c). Figure 12 shows the planes at the corresponding distances behind the endplate rear edge.

A Nikon D70 digital SLR camera with 18 – 55mm lens was used for still image recording. The camera was mounted on a tripod and the ISO setting was 1600ASA film equivalent. The aperture was fixed at f4.5. A 1 gigabyte memory card was used. A Canon Ixus 400 “point and shoot” digital camera was used for movie recording of the test cases. Obtaining acceptable images was challenging, thousands of images were captured of the different test case combinations, yielding approximately 1% usable images. Many test cases were repeated until there were enough photos to ‘describe’ the flow.

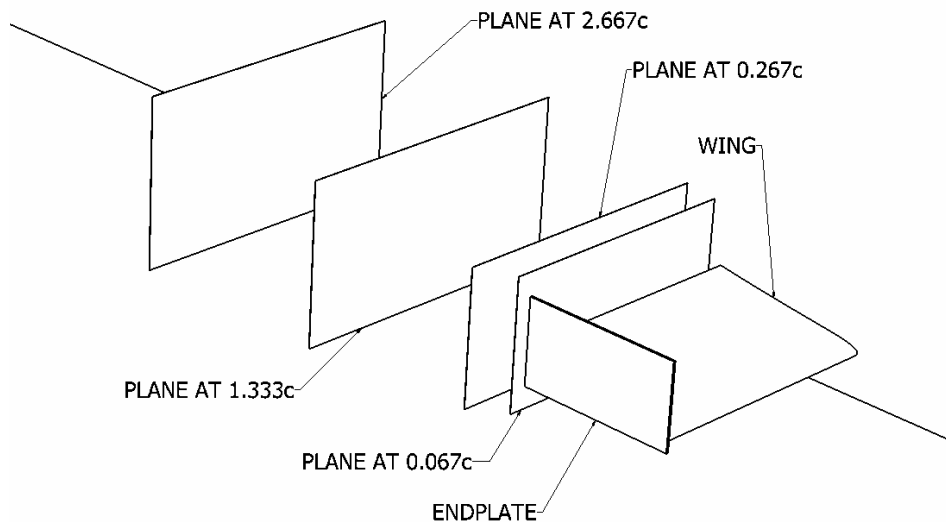


Figure 12: Image planes at various distances behind wing and endplate

3.5 Laser Doppler Anemometry

In an extension to flow visualisation, laser Doppler anemometry (LDA) is a non-intrusive measurement method for the airflow around the wing and endplate. LDA can measure and display the velocity and turbulence in Cartesian and vector form. Measurements are made in points only, to measure the velocity profile in a plane, a 2D grid of points is generated for the motion, to measure the velocity profile in a volume, a 3D grid of points is generated.

The LDA systems uses a Dantec 5W Argon-ion laser, with the beam split into three component pairs, green, blue and purple. The beams are focused in a point, the point of measurement, the interference pattern is analysed and displayed in the users preferred style. Generally a vector plot of a 2D plane is displayed real time, that is, as each measurement is taken for a particular point, the vector is plotted.

The flow during LDA measurements is seeded with a mist of vegetable oil, as the LDA system needs spherical (preferred) particles to create the interference patterns. A number of samples is required per point, a rough guide was at least 2000 samples per point. The samples are sorted statistically and the mean value is recorded for each component for point.

The time to count 2000 samples is affected by the quality of the seeding, therefore a limit of 30 seconds recording for each point is set, otherwise the experiment will take a very long time. The results can be set to record the velocity, or velocity and turbulence. Recording the turbulence requires more accurate sampling and therefore an increase in sample time. Turbulence levels were not recorded due to time constraints.

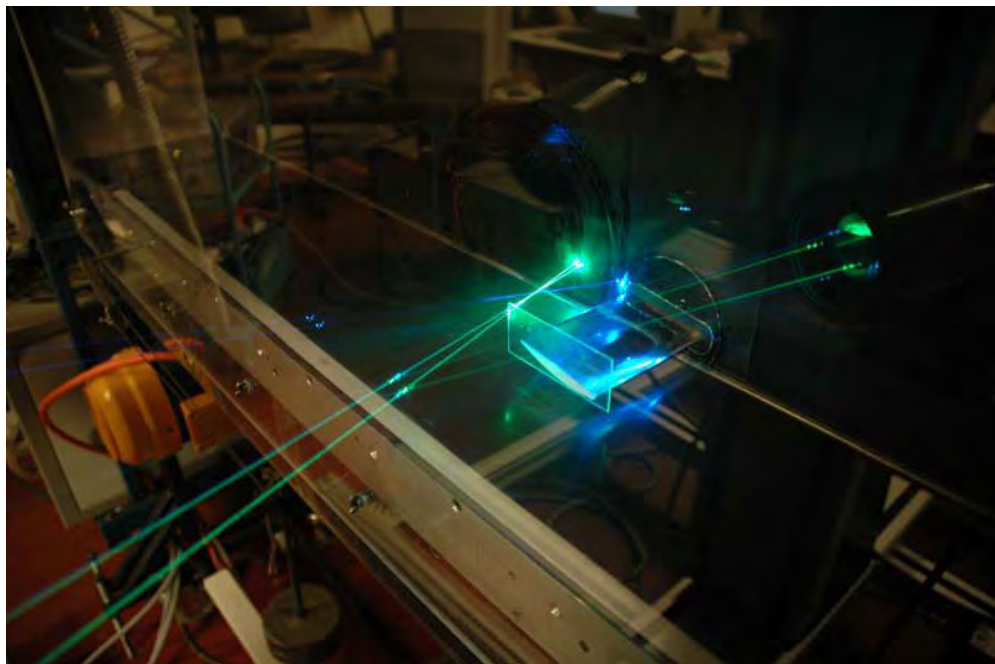


Figure 13: Laser Doppler anemometry measurement example

Figure 13 shows an example LDA measurement with a typical test case. From studying flow visualisation and CFD results, the area of interest can be narrowed down to

reduce the size of the grid of measurement points, and the areas of greater interest can be measured with a very fine grid. There was no set standard for LDA measurements, therefore the grid sizes depended more on the time available per experiment rather than recording the most accurate results possible.

3.6 Summary

This chapter described the experimental aspects of the work, including the endplates and endplate configurations. The wind tunnel and moving ground configuration, wing style and endplate sizes were specified. These experiments were also analysed using CFD. The next chapter describes the computational simulation methods and test case choice and generation.

4. COMPUTATIONAL FLUID DYNAMICS

4.1 Chapter Overview

To assist the understanding of the flow structure of inverted wings, CFD simulations were vital, this chapter describes the CFD simulation methods chosen. Section 4.2 briefly outlines the ‘nature’ of CFD, section 4.3 describes the domain and test cases chosen, section 4.4 describes the grid generation techniques, section 4.5 explains the turbulence modelling, section 4.6 describes the validation and verification and section 4.7 describes how the data was collected and sorted.

4.2 Introduction

Computational fluid dynamics (CFD) has developed rapidly in the last few decades to provide an extra tool for studying fluid flow. Developed primarily for the aerospace industry, CFD has become a common tool to use along side wind tunnels in automotive applications. Wind tunnels and CFD are both simulators, analog and digital respectively [4]. From a high level view, using wind tunnels the results are produced relatively quickly once the model is setup, results can be obtained while the tunnel is running, and recorded for processing. Using CFD the results can be saved for future reference and investigation.

Looking closer at the advantageous of CFD, the fluid flow can be analysed in high detail in areas otherwise not accessible in a wind tunnel model, such as turbulence levels inside or under model parts.

The quality of the CFD results depends greatly on the model used, such as grid quality and boundary conditions, these will be explained in following sections. To obtain high quality results, much time is needed to create the model, and powerful computers are needed to solve the model. The larger the model, the longer the time required to solve.

The conservation form of the governing equations is given by [21]:

$$\frac{\partial U}{\partial t} + \frac{\partial F}{\partial x} + \frac{\partial G}{\partial y} + \frac{\partial H}{\partial z} = J \quad (1)$$

Where:

$$U = \left\{ \begin{array}{l} \rho \\ \rho u \\ \rho v \\ \rho w \\ \rho \left(e + \frac{V^2}{2} \right) \end{array} \right\} \quad (2)$$

$$F = \left\{ \begin{array}{l} \rho u \\ \rho u^2 + p - \tau_{xx} \\ \rho uv - \tau_{xy} \\ \rho wu - \tau_{xz} \\ \rho \left(e + \frac{V^2}{2} \right) u + pu - k \frac{\partial T}{\partial x} - u\tau_{xx} - v\tau_{xy} - w\tau_{xz} \end{array} \right\} \quad (3)$$

$$G = \left\{ \begin{array}{l} \rho v \\ \rho uv - \tau_{yx} \\ \rho v^2 + p - \tau_{yy} \\ \rho wv - \tau_{yz} \\ \rho \left(e + \frac{V^2}{2} \right) v + pv - k \frac{\partial T}{\partial y} - u\tau_{yx} - v\tau_{yy} - w\tau_{yz} \end{array} \right\} \quad (4)$$

$$H = \left\{ \begin{array}{l} \rho w \\ \rho uw - \tau_{zx} \\ \rho vw - \tau_{zy} \\ \rho w^2 + p - \tau_{zz} \\ \rho \left(e + \frac{V^2}{2} \right) w + pw - k \frac{\partial T}{\partial z} - u\tau_{zx} - v\tau_{zy} - w\tau_{zz} \end{array} \right\} \quad (5)$$

$$J = \left\{ \begin{array}{l} 0 \\ \rho f_x \\ \rho f_y \\ \rho f_z \\ \rho (uf_x + vf_y + wf_z) + p\dot{q} \end{array} \right\} \quad (6)$$

The CFD code used was Fluent™ 6.1. Fluent™ has various turbulence models available. Choosing the best turbulence model for a particular case is important, as each turbulence model can predict different effects, depending on the expected flow pattern. It is also a time consideration since the more complex turbulence models require more computational time and power.

4.3 Computational Fluid Dynamics Domain

The domain chosen for the CFD analysis is a simplified wind tunnel model. The intention of the CFD analysis is to perform ‘digital’ wind tunnel tests along side the physical wind tunnel tests. Features of the physical wind tunnel such as the taper, belt width and Pitot static tube were not modelled, as it was decided that they would create complexities in mesh generation and flow calculation.

The full wind tunnel 3D model was exported from CATIA™ v5 into step format, then imported into Inventor 7. The final domain chosen limits are: the vertical plane from the front of the moving ground as the inlet, the vertical plane from the rear of the moving ground as the outlet, the walls and the moving ground. Figure 14 shows an example of the CFD domain in 3D, figure 15 shows the CFD domain dimensions. The taper was removed from the CFD domain as it caused mesh generation errors. In the actual tunnel, the moving ground belt is 200mm wide, where as the tunnel is wider with taper. The belt thickness creates a step on the longitudinal edges of the tunnel ground, these features were ignored, as they also created unnecessary meshing problems. The Pitot static tube was not modelled for the same reasons of removing insignificant and unnecessary complexity from the CFD domain.

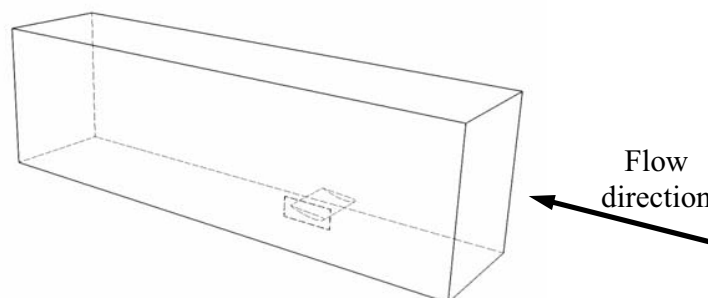


Figure 14: CFD domain in 3D

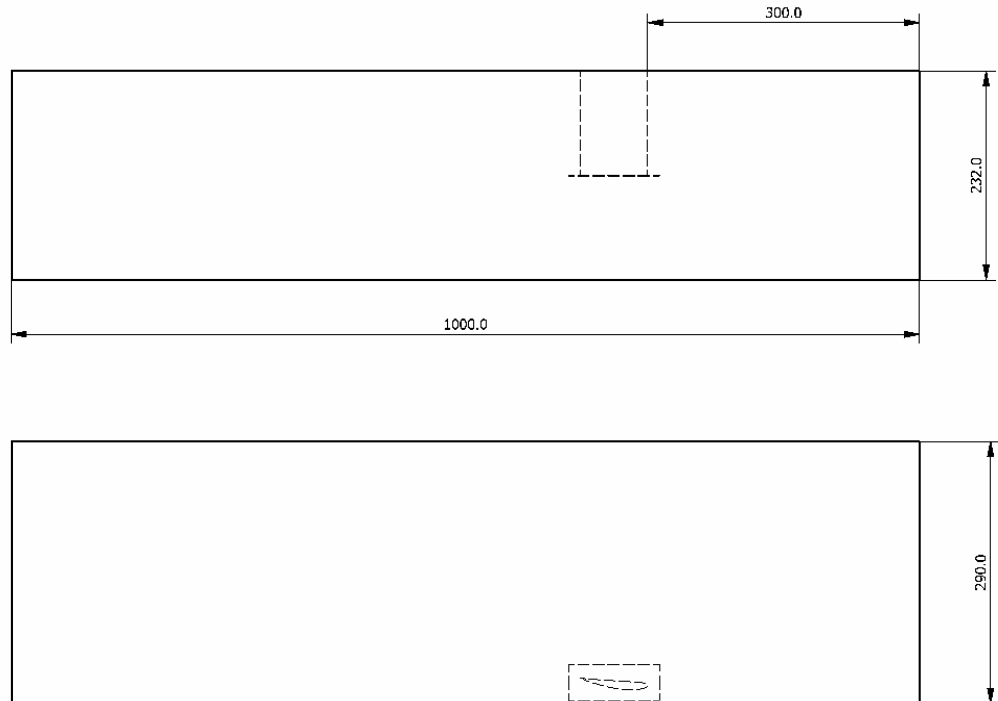


Figure 15: Dimensions of CFD Domain

As many test cases needed to be studied as possible, various heights, angles of attack and endplate combinations needed to be modelled. The endplate choice, as described in section 3.3 was used to simulate the general shapes and ratios found on motor sport vehicles. The two angles of incidence were chosen (after an initial three, including 2°), as the wings on motor sport vehicles use variable angles of incidence. After initial CFD simulations it was determined that time allowed for fifty six cases to be studied for comparison purposes. The fifty six cases comprised of two angles of incidence, three height combinations for both angles of incidence, an extra height, relatively higher than the other sets, with extreme endplate positions. The steps were chosen on the basis that motor sport vehicles use stepped positions for adjusting the front wings, therefore limiting the options. The 6° cases at $h = 40$ were added for use as a comparison at heights which are less affected by ground effect [9]. The 10° cases at $h = 20$ used only four cases, as insufficient space was available for any meaning endplate height difference. An additional number of cases were used for technique and grid adaptation studies.

The two angles of attack, 6° and 10° were used, cases with a 2° angle of attack were initially trialled but various meshing problems could not be overcome as a large wing

surface area was very close to the moving ground, and the mesh quality needed was not attainable, this will be discussed in section 4.4.

One free stream velocity of 10ms^{-1} was used for all test cases, as this was the general limit of the wind tunnel equipment. Therefore the moving ground velocity was set to 10ms^{-1} . The inlet was set as a velocity inlet with a free stream velocity set to 10ms^{-1} . At the time of initial test case simulations, the actual wind tunnel turbulence level was unknown, therefore a turbulence level of 1% was assumed. The outlet was set as an outflow. The walls, wing and endplate surfaces were set as stationary walls.

Table A1 in Appendix A shows the combinations of test cases used for the CFD analysis.

4.4 Grid Generation

To help grid generation for a large number of models studied, a ‘standard’ meshing scheme was developed. This was to decrease the meshing time and eventual adaptation issues for many cases with similar geometry.

Two separate computers were used to perform the grid generation and CFD analysis, they had Pentium 4 3GHz processors, 2Gb RAM, one computer with a 64Mb video card the other with a 128Mb video card, various external hard drives were used for data storage. Gambit™ 2.2.30 was used to generate the grids (meshes). The geometry was imported from a 3D step file, the edges, surfaces and volume were meshed accordingly.

An ideal mesh is fully structured, with eventual conformal adaptation. The geometry of an endplate attached to an inverted wing needs relatively long time to generate a structured mesh. Since many test cases needed to be modelled, and time was limited, an unstructured mesh was chosen for the volume for all cases. A structured mesh was used for most surfaces. Some surfaces had an odd number of sides, such as the surface which joined the underside of the wing to the inside of the endplate – the endplate surface converged to points on the leading and trailing edge of the wing, which provided many errors in generating a structured mesh, such as the cell aspect ratio being too large. Surfaces where each edge had different numbers of nodes needed an unstructured mesh.

The average mesh size prior to adaptation was approximately 1,000,000 cells. The time to generate each mesh was approximately 30 minutes, this does not include the time to model each domain in the 3D modelling software.

When using an unstructured mesh, the cells away from surfaces and edges tended to be very large in comparison, this would cause problems in the quality of the flow, especially in areas where the flow would be expected to be turbulent, changing directions rapidly or where a vortex is expected (or unexpected). Therefore a method was developed to adapt the mesh prior to flow initialisation. This method will be described later in this section.

The domain features chosen dictate the boundary conditions needed for the CFD model, these boundary conditions are applied using GambitTM, after all surfaces and the volume meshed. Experience was needed in splitting the features into surfaces needed for CFD result extraction, that is, which parts of the endplate can have different labels, allowing the results to be displayed clearer in FluentTM. This function can be applied in FluentTM, but for ease of model generation and maintaining ‘standard’ model features, it was performed in GambitTM.

Each model was saved in GambitTM with an according file name, for back-up use, and the mesh itself was exported from GambitTM, in mesh format. Before the mesh was ready for use in FluentTM, a quick grid check was carried out on every model, to check for irregularities or errors in the grid, which would create errors in the CFD solution. The mesh was smoothed using the ‘Smooth’ function, minimum skewness was set at 0.3 and 30 smoothing iterations were applied. The gradient of the cell volumes were also checked. These features help remove *“rapid changes in cell volume between adjacent cells”*, which can *“translate into larger truncation errors”* [22].

From initial mesh and model trials, a technique for adapting the mesh was needed, to decrease the time needed to obtain results and to provide a ‘standard’ mesh to compare results. Using the grid adaptation function in FluentTM, a cylindrical volume extending from the inlet to approximately 200mm behind the endplate was adapted. Hanging node adaptation was used. The region between the endplate and moving ground and the region behind the endplate is of importance as this is where vortices are expected to form.

Figure 16 shows an example of an adapted mesh before initialisation. Only the surfaces of the moving ground, wing and endplate are shown for clarity.

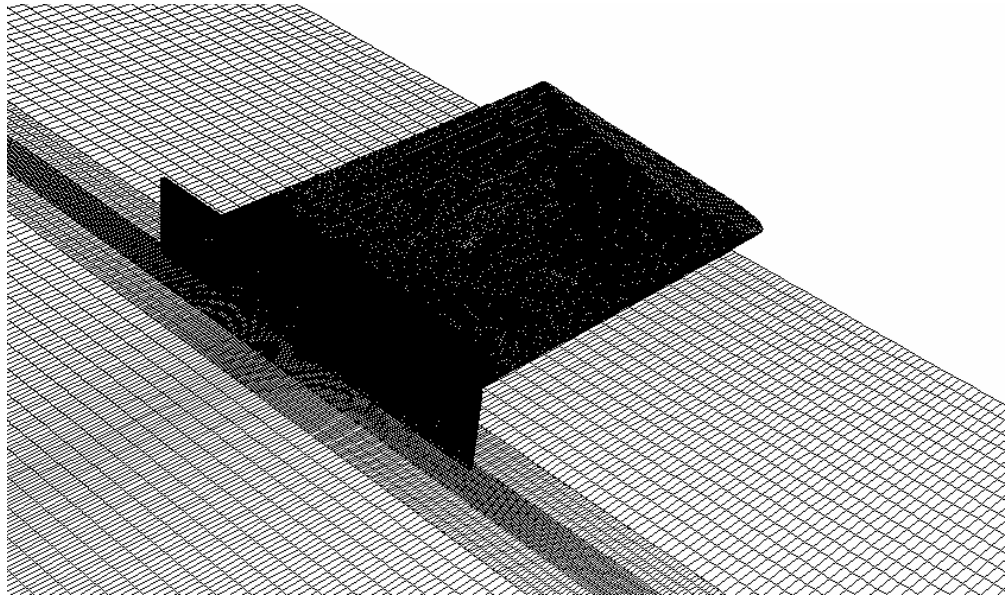


Figure 16: Adapted mesh example

For the cases studied, the average final mesh size was 1,874,500 cells, the minimum was 1,485,436 cells and the maximum was 2,106,766 cells. The number of cells for each case was relative to the size of the endplate, the larger the endplate, the more cells needed. The maximum was found to be the largest possible mesh used with the chosen turbulence model.

4.5 Turbulence Models

Choosing a turbulence model for a particular simulation can vary the results, or the detail of the results. For the cases studied, a turbulence model which can accommodate for some swirl was needed. After initial flow visualisation experiments on a single case (10deg-h20-C-m14) and trials using various turbulence models, considering time constraints and based on published work [3] [22] [27], the Renormalization group theory (RNG) $k-\varepsilon$ turbulence model was chosen. After studying the flow visualisation results, it was decided that this turbulence model predicted the flow with sufficient confidence and accuracy for data comparison purposes.

Features of the RNG $k-\varepsilon$ turbulence model [22] are:

- The RNG model has an additional term in its ε equation that significantly improves the accuracy for rapidly strained flows.
- The effect of swirl on turbulence is included in the RNG model, enhancing accuracy for swirling flows
- The RNG theory provides an analytical formula for turbulent Prandtl numbers, while the standard k - ε model uses user-specified, constant values.
- While the standard k - ε model is a high-Reynolds-number model, the RNG theory provides an analytically-derived differential formula for effective viscosity that accounts for low-Reynolds-number effects. Effective use of this feature does, however, depend on an appropriate treatment of the near-wall region.

The computational power available also limited the choice of turbulence models. Time being an unavoidable factor also contributed to the decision to run all cases for investigation with the RNG k - ε turbulence model. The average time for acceptable convergence was approximately 24 – 36 hours, each case. The RSM turbulence model did not provide benefits as the unstructured mesh quality did not allow for greater flow detail development available with this turbulence model [28]. It was noted that none of the trialled CFD simulations predicted the relative strength and path of the upper vortex. The convergence time using the RSM turbulence model was approximately 36 – 48 hours, including a mesh with less cells, as more memory is needed for this turbulence model. This would have essentially doubled the time to complete the test cases, as each case was loaded and saved every two days, instead of the majority of cases which took 24 hours.

Maintaining the scope of the thesis, which was to investigate many endplate and wing configurations, the previously proven RNG k - ε turbulence model was sufficient for data comparison. With any CFD analysis, the turbulence model contributes to a percentage of the accuracy, the quality of the mesh is a contributing factor also. It was decided that the highest possible accuracy was traded-off for a sufficiently accurate broader investigation.

4.6 Validation and Verification

The validation and verification of the CFD models was not straight forward, without any numerical data to check the CFD results, the only option was to use the initial flow

visualisation results to compare to the CFD results. The LDA system was not in operation. The case used for initial comparison was case 10deg-h20-C-m14.

In order to help with all aspects of the analysis techniques, the geometry of the endplate was simplified, allowing a very close geometric reproduction when meshing, therefore removing most geometric errors. The wind tunnel turbulence level was not known initially, some error was expected, but since the test cases were run at a relatively low Reynolds number, inlet turbulence levels from 0% to 5% did not effect the flow pattern. Again, this was an observation of the CFD results, as no numerical data was available to compare.

The domain was chosen to represent as much of the wind tunnel as possible, that is, the width, height and length matched the physical test section. The taper and belt step were ignored to aid in mesh generation.

Without any numerical data, a grid convergence test was not possible, as there were no means to check and compare C_L , or C_D values from the physical model in the wind tunnel to the CFD results. After many CFD simulations with various mesh sizes, it was found that finer the mesh, the more detail it captured. The mesh quality was checked after initial generation and adaptation, to ensure no elements exceeded the recommended skewness and aspect ration levels. Using hanging nodes during adaptation may have introduced errors, but this was the only option when refining the grid to capture flow details.

Generally speaking, the more convergence of the mass residual the more accurate the CFD results, for the given data. Using a RNG $k-\varepsilon$ turbulence model, the mass residual is the most important. The average convergence level for all the test cases was 1.7×10^{-5} , refer to Table A2 for full list of convergence levels for corresponding cases. Ideally 1×10^{-6} is the aim, but errors due to grid quality, grid adaptation and the turbulence model prevented this limited being reached, again, the highest quality was traded off for more data to gain a 'bigger picture'.

4.7 Data Collection

The CFD models generated a large amount of data, choosing the most appropriate and valuable aspects was important. Firstly the comparison to flow visualisation results and

LDA results (the LDA system was only available at the end of the thesis) was the most important, as these not only added to the overall picture of the flow, but helped validate the CFD analysis. Extracting C_L or C_D values was important to quantify the differences of the test cases.

Streamlines and surface pressure distributions helped visualise the flow. Limits on the detail of the streamlines were caused by computational power limitations – if too many streamlines are requested, the computers crashed.

4.8 Summary

The CFD simulations were carried out to obtain a large variety of flow structures. The methods used were described throughout the chapter, the domain generation and grid strategy, test case choice and turbulence model choice explained. Examining the results proved more difficult than expected but acceptable methods were developed.

5. RESULTS

5.1 Chapter Overview

This chapter presents the results obtained from the flow visualisation experiments, CFD simulations and LDA experiments. Section 5.2 presents the flow visualisation results, section 5.3 presents and discusses the CFD results and section 5.4 presents and discusses the LDA results.

5.2 Flow Visualisation

The flow visualisation experiments were carried out on a few of the test cases specified in chapter 4.2. The following test cases have flow visualisation results presented, as they provide a wide range of different flow fields:

CASE NAME	ANGLE OF INCIDENCE	HEIGHT OF LEADING EDGE	HEIGHT OF ENDPLATE	h/c	ENDPLATE A/R
	(degrees)	(mm)	(mm)		
6deg-h10-A-m4	6	10	4	0.07	3.75
6deg-h10-B-m4	6	10	4	0.07	5
6deg-h10-C-m4	6	10	4	0.07	1.88
6deg-h10-D-m4	6	10	4	0.07	2.5
6deg-h20-A-m14	6	20	14	0.20	3.75
6deg-h20-B-m14	6	20	14	0.20	5
6deg-h20-C-m14	6	20	14	0.20	1.88
6deg-h20-D-m14	6	20	14	0.20	2.5
10deg-h10-A-m4	10	10	4	0.08	3.75
10deg-h10-B-m4	10	10	4	0.08	5
10deg-h10-C-m4	10	10	4	0.08	1.88
10deg-h10-D-m4	10	10	4	0.08	2.5
10deg-h20-A-m14	10	20	14	0.21	3.75
10deg-h20-B-m14	10	20	14	0.21	5
10deg-h20-C-m14	10	20	14	0.21	1.88
10deg-h20-D-m14	10	20	14	0.21	2.5
6deg-h20	6	20	N/A	0.20	N/A
10deg-h10	10	10	N/A	0.08	N/A

Table 3: Flow visualisation test case statistics

The key to the test case names is as follows: '6deg' or '10deg' indicates the angle of incidence of the wing, 'h10' or 'h20' indicates the height of the wing above the ground. A, B, C, or D indicates the endplate and 'm4' or 'm14' indicates the height of the endplate above the ground. Two cases (6deg-h20 and 10deg-h10) have been included to provide a comparison between the flow patterns produced on similar cases without endplates. For most of the cases presented in this section, the flow on four planes behind the endplate are shown, due to the randomness in trying to capture the flow, not all planes were 'captured' for the presented cases. All distances are specified in terms of the wing chord length (c) and measured from the trailing edge of the endplate. Table 3 shows the test case statistics for the flow visualisation experiments.

5.2.1 Vortex Patterns for 6° Incidence without Endplates

Figures 17 to 19 show the single vortex generated from an inverted wing without an endplate. The angle of incidence is 6° . The vortex is strong and well developed, as can be seen the photos. The trajectory is observed to move towards the wing root wall the further behind the wing it travels.

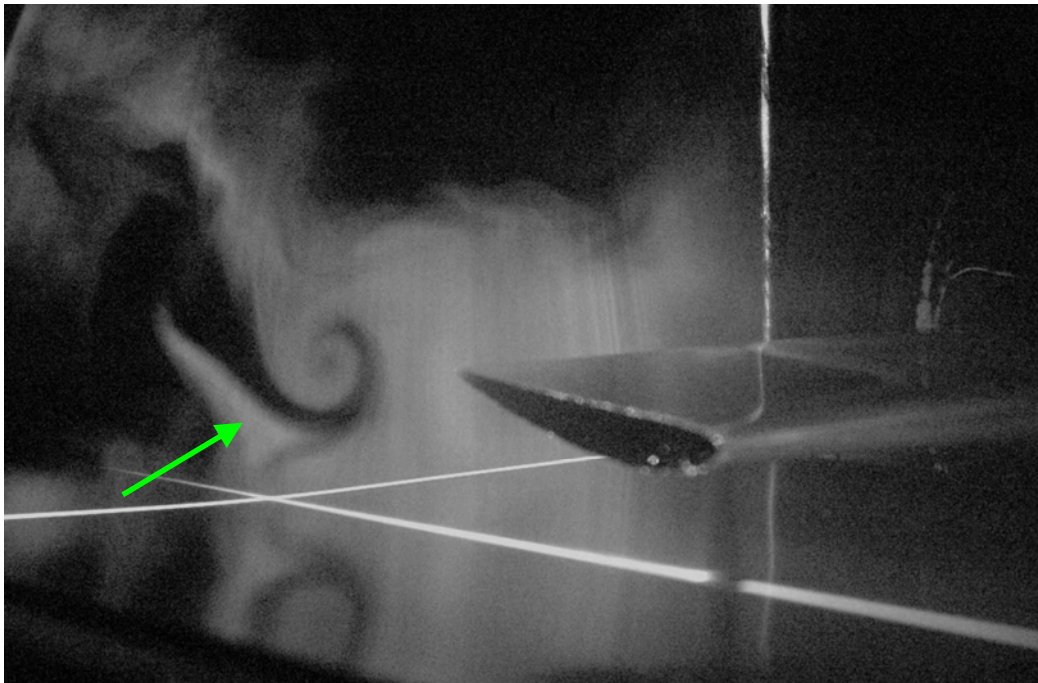


Figure 17: 6deg-h20 with plane at $0.267c$

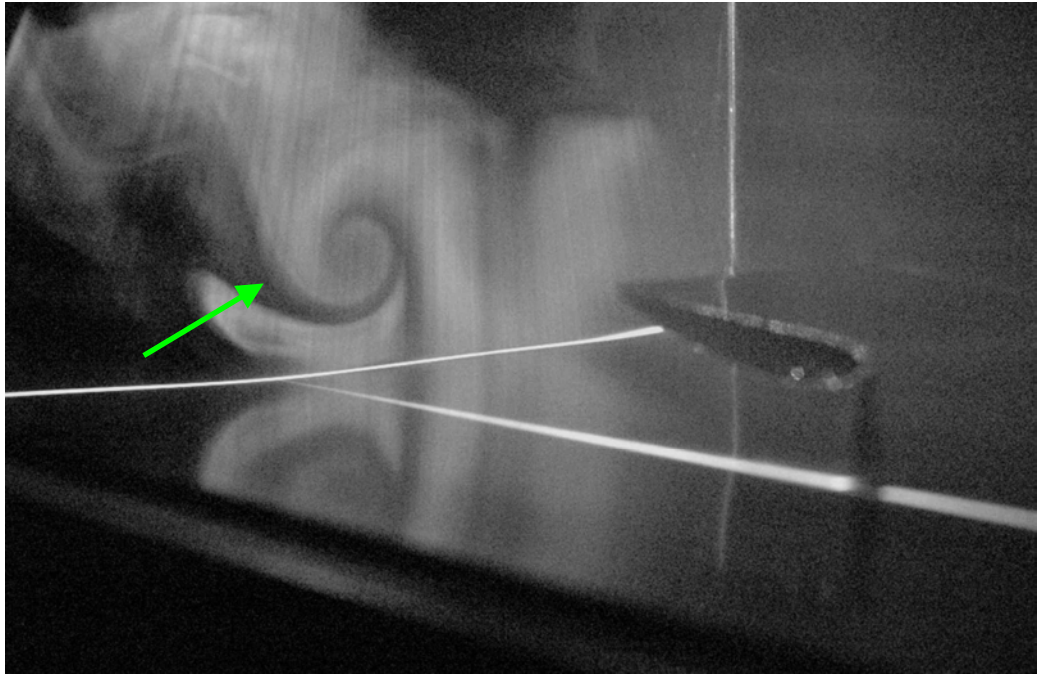


Figure 18: 6deg-h20 with plane at 1.333c

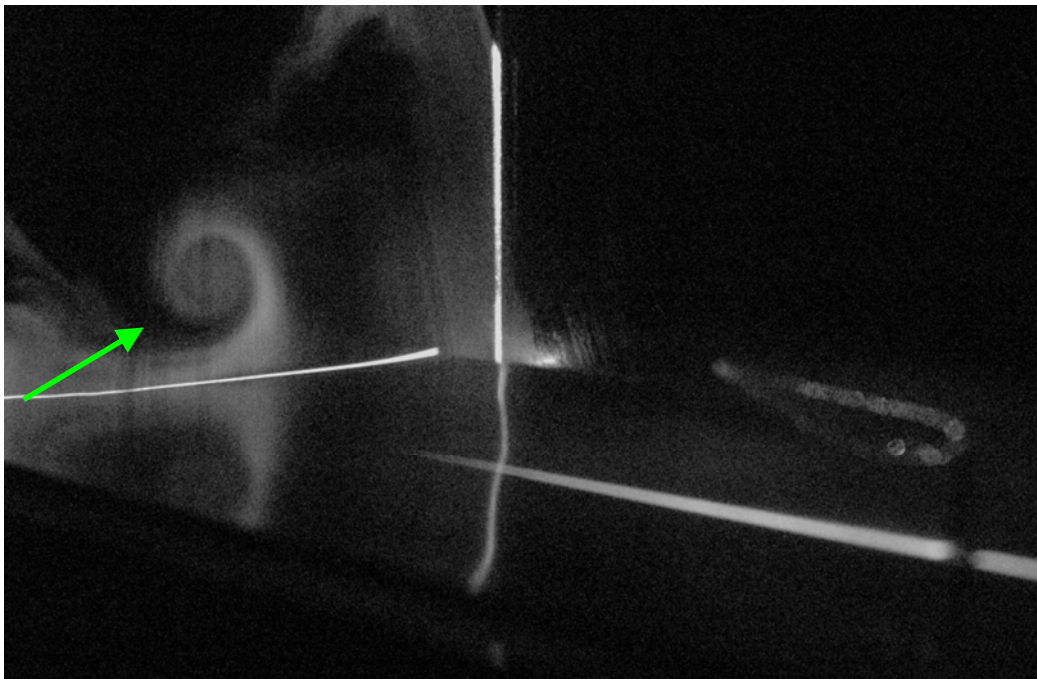


Figure 19: 6deg-h20 with plane at 2.667c

5.2.2 Vortex Patterns for 6° Incidence at $h = 10$

Looking at figures 20 to 23, a case where the wing and endplate is close to the ground, the vortex formed from the top of the endplate is rotating with a faster radial velocity. The weaker vortex formed from the lower endplate edge has blended with the upper vortex at a distance of $2.667c$, as can be seen in figure 23. The combined vortex has moved towards the wing root wall.

In figures 24 and 25, which used a longer endplate (B) with the same wing configuration, at a distance of $0.267c$ the two vortices are further apart than observed in figure 21.

In figures 26 to 28 both the upper and lower vortices are observed to be weak, and remain separated at a distance of $2.667c$. The lower vortex strength is apparently lower than the upper vortex, from observing the flow patterns.

Figure 29 shows the relatively weak vortices at a distance of $0.067c$ from the endplate. The vortices generated in this case were too weak to capture any usable images.

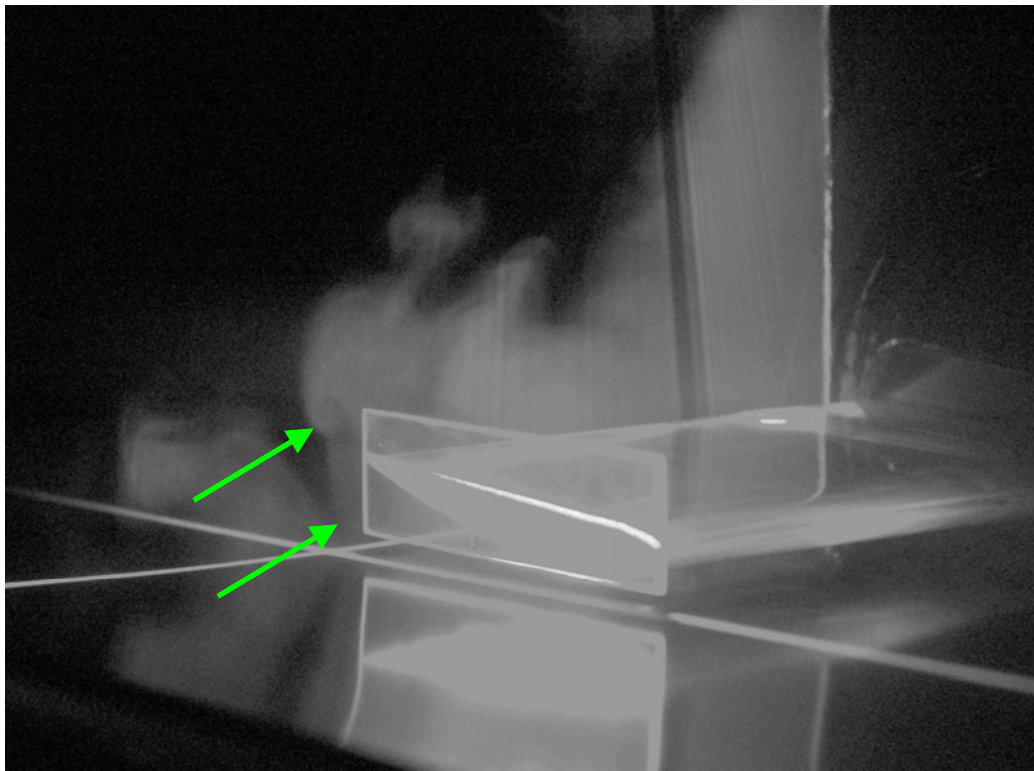


Figure 20: 6deg-h10-A-m4 with plane at $0.067c$

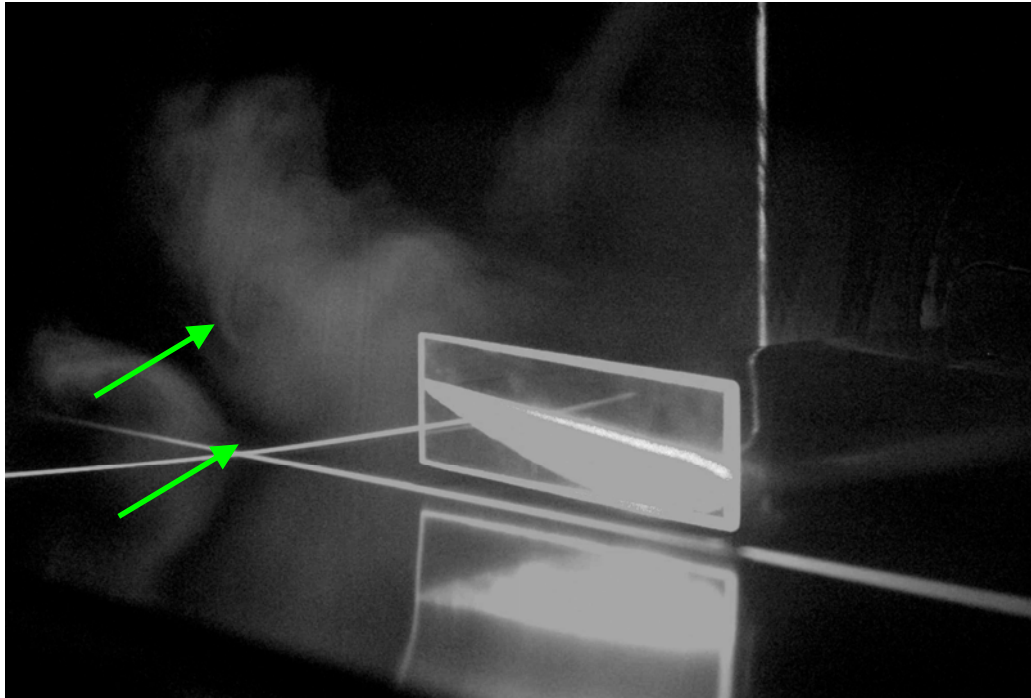


Figure 21: 6deg-h10-A-m4 with plane at 0.267c

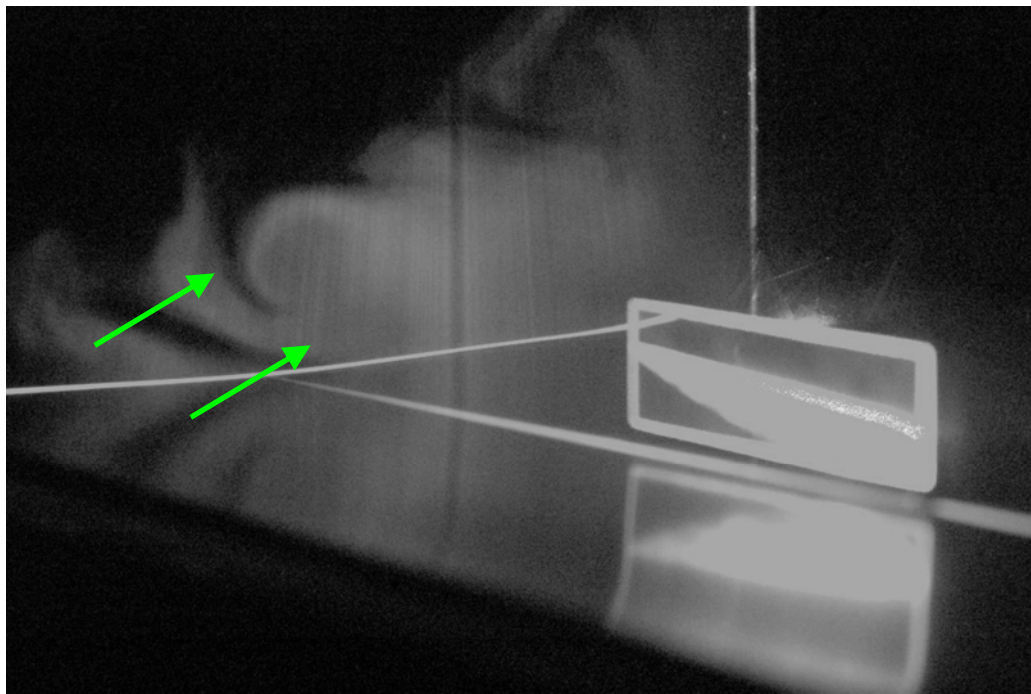


Figure 22: 6deg-h10-A-m4 with plane at 1.333c



Figure 23: 6deg-h10-A-m4 with plane at 2.667c

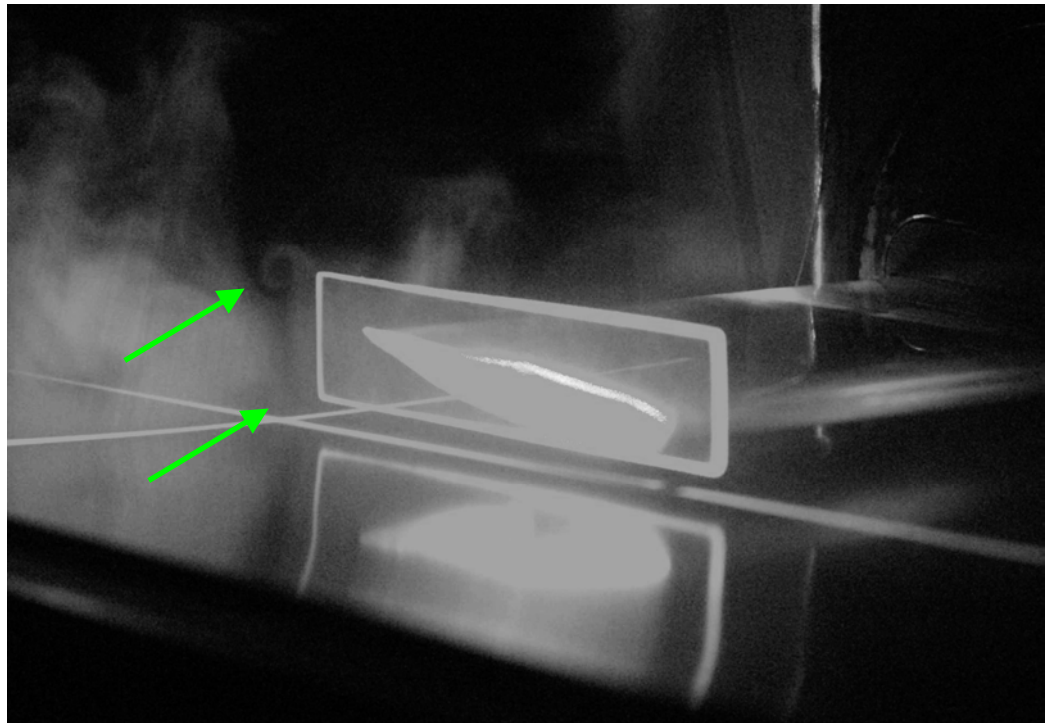


Figure 24: 6deg-h10-B-m4 with plane at 0.067c

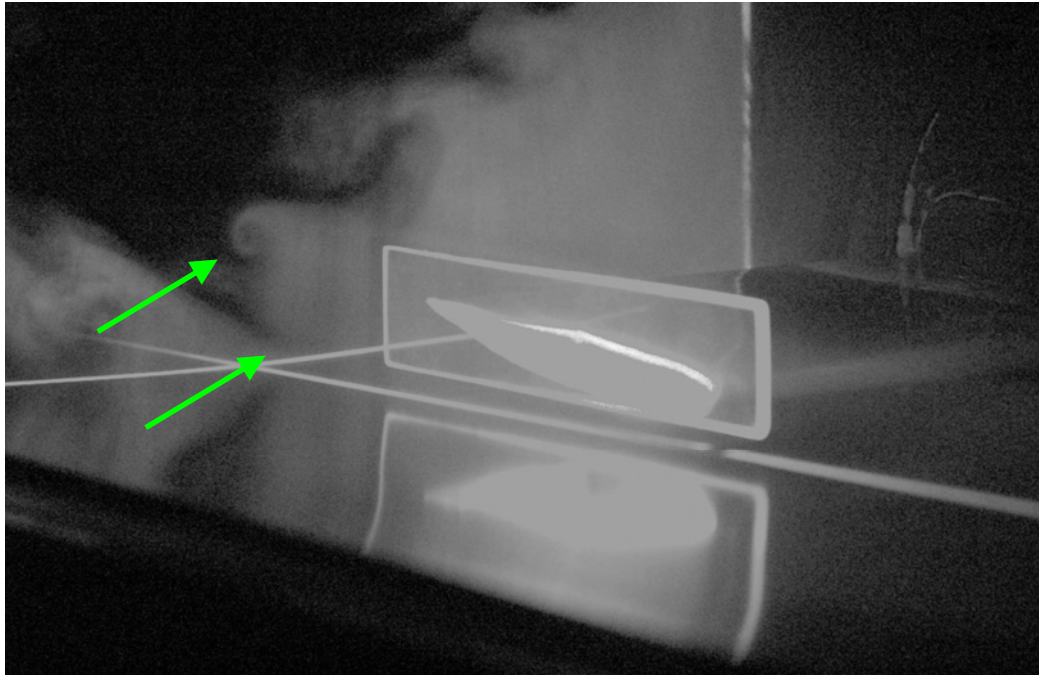


Figure 25: 6deg-h10-B-m4 with plane at 0.267c

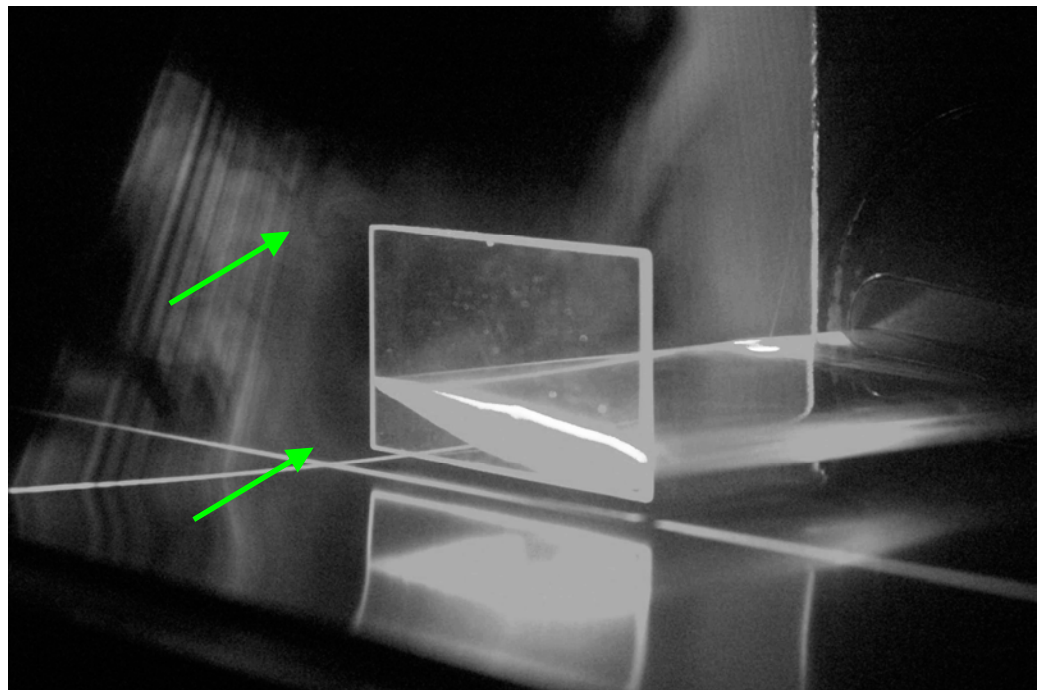


Figure 26: 6deg-h10-C-m4 with plane at 0.067c

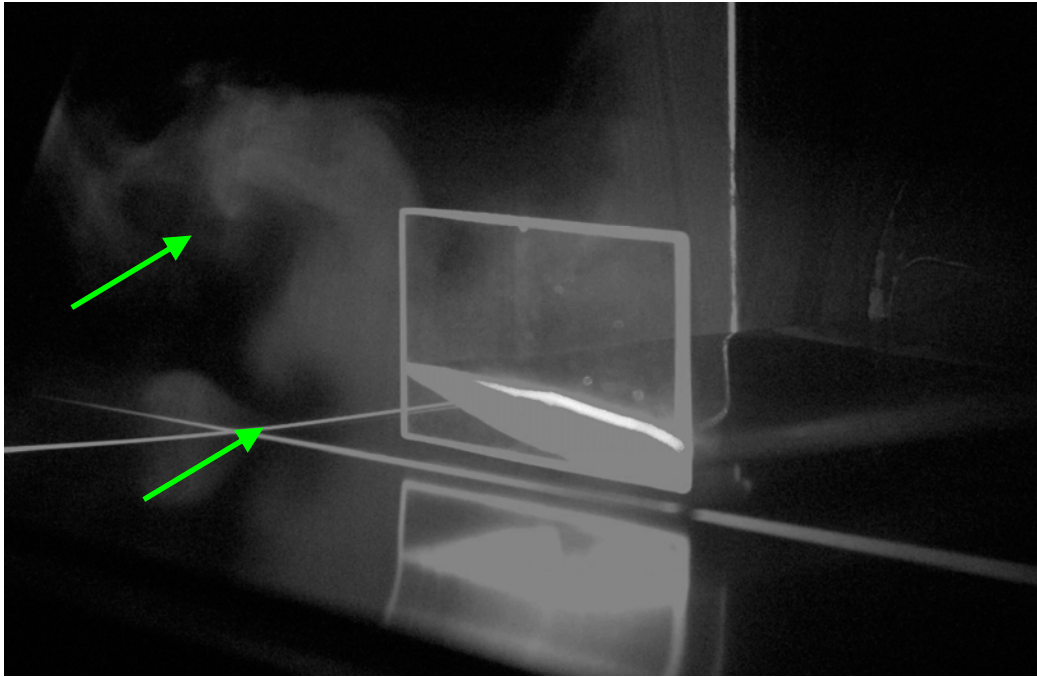


Figure 27: 6deg-h10-C-m4 with plane at 0.267c

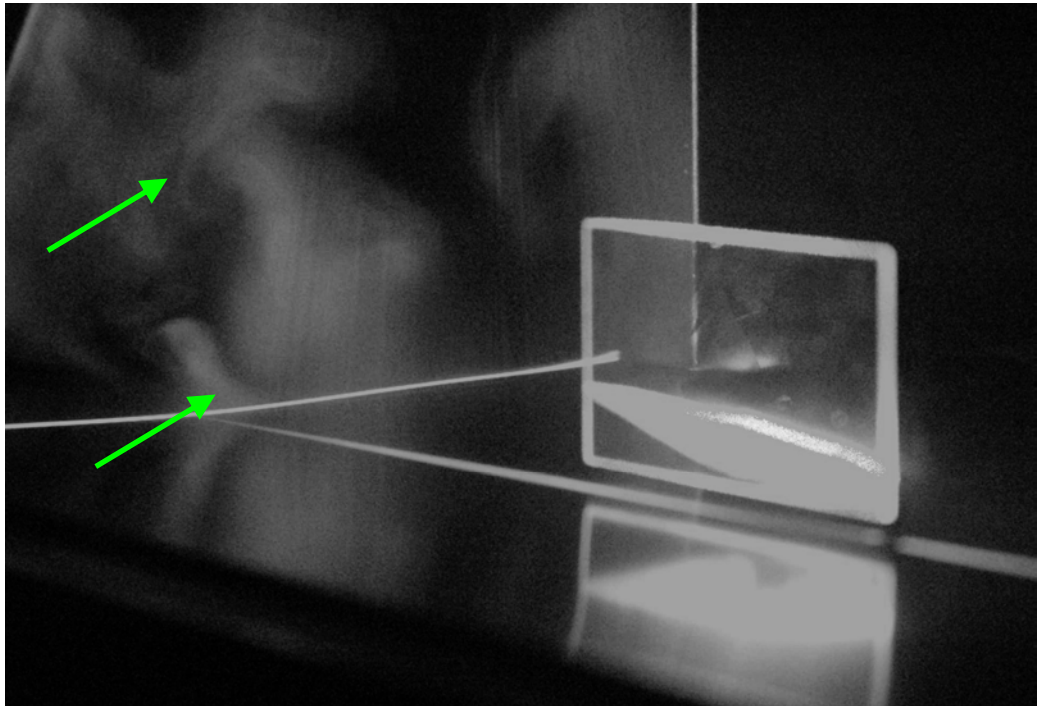


Figure 28: 6deg-h10-C-m4 with plane at 1.333c

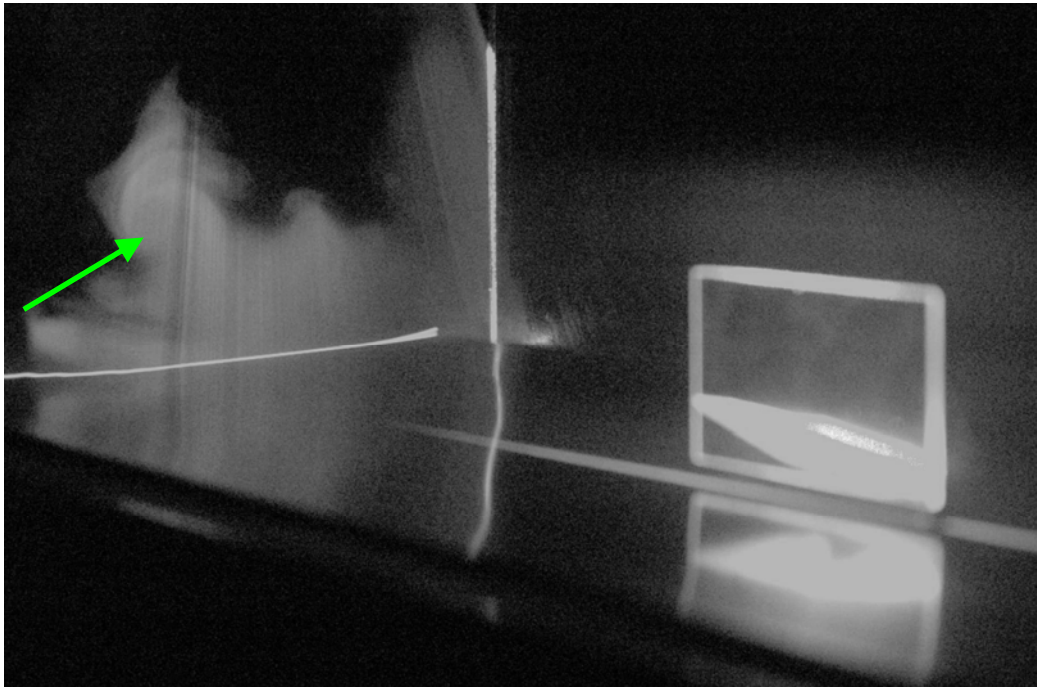


Figure 29: 6deg-h10-C-m4 with plane at 2.667c

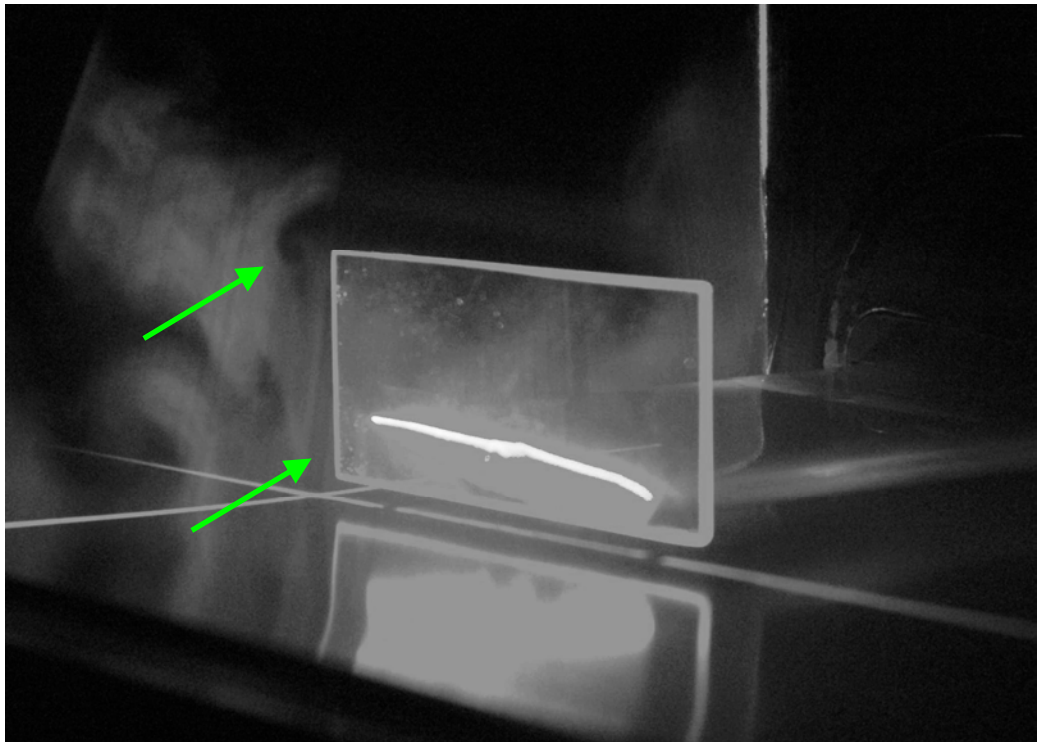


Figure 30: 6deg-h10-D-m4 with plane at 0.067c

5.2.3 Vortex Patterns for 6° Incidence at $h = 20$

Figures 31 to 34 with endplate A shows larger vortices formed than in figures 20 to 23, which is to be expected. At a distance of $0.067c$ two large distinct vortices are present, with the lower vortex slightly larger than the upper vortex. At $0.267c$ the vortices are appearing to merge and at a distance of $2.667c$ the vortices have combined.

Figures 35 to 38 with endplate B shows very strong upper and lower vortices at $0.067c$ and $0.267c$. At $0.267c$ the upper vortex is relatively strong and almost as large as the lower vortex. At $1.333c$ the two vortices have merged but are still distinct, and at $2.667c$ the vortices have merged.

Figures 39 to 42 show the vortices formed using endplate C. At $0.067c$ there are two distinct relatively small vortices. The two vortices remain separate relatively defined at $2.667c$.

Figures 43 to 45 show the vortices formed using endplate D. At the four distances observed, the vortices remain separate and well defined.

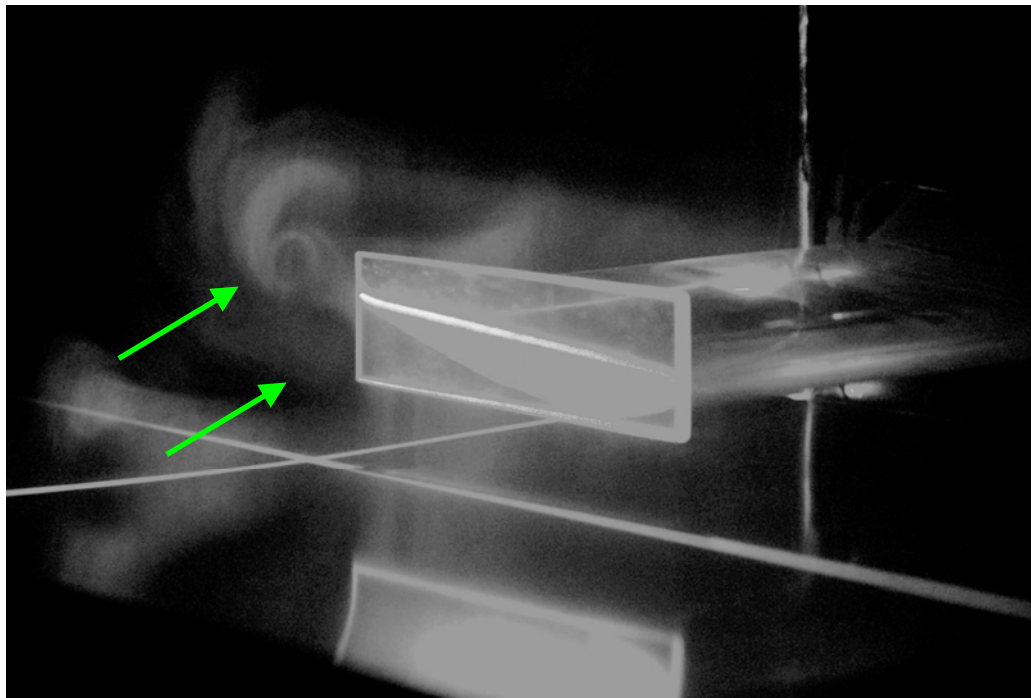


Figure 31: 6deg-h20-A-m14 with plane at $0.067c$

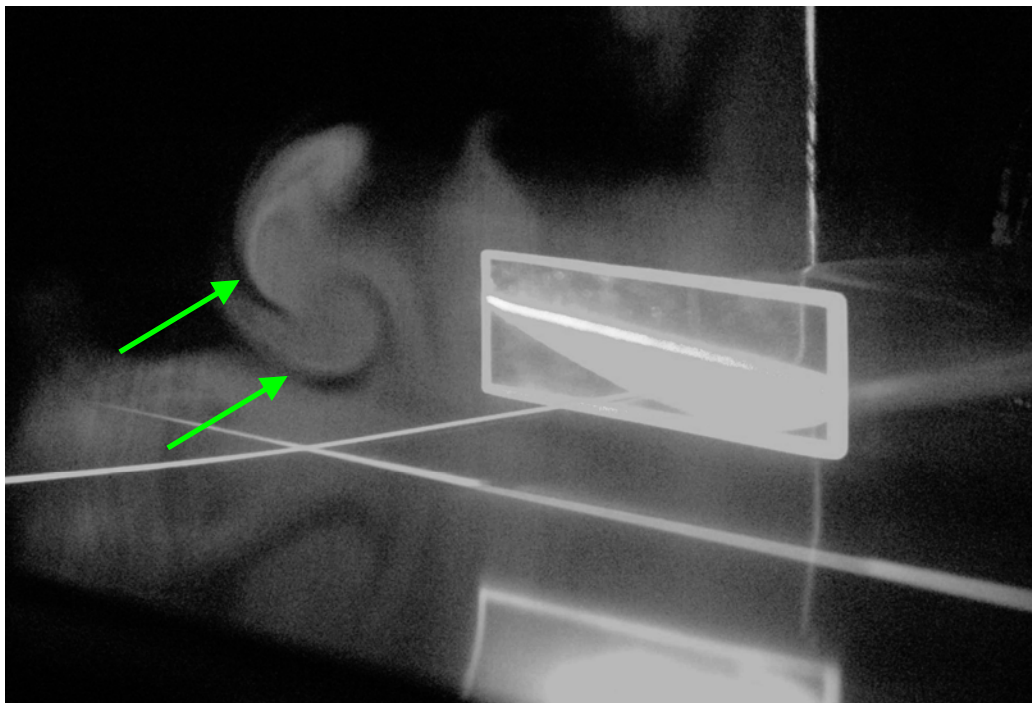


Figure 32: 6deg-h20-A-m14 with plane at 0.267c

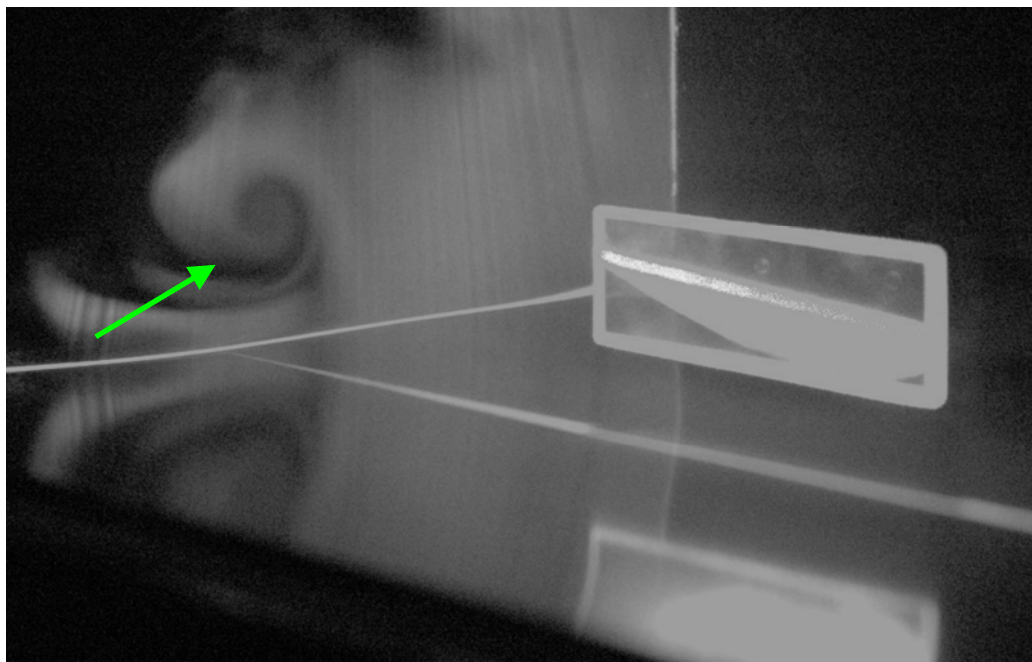


Figure 33: 6deg-h20-A-m14 with plane at 1.333c

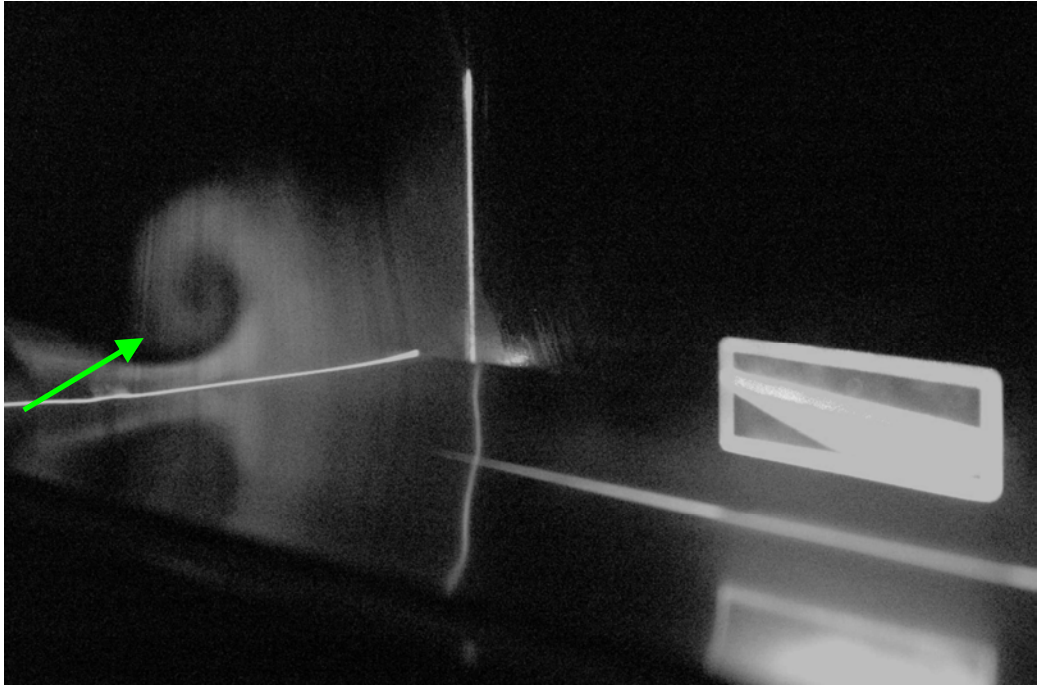


Figure 34: 6deg-h20-A-m14 with plane at 2.667c

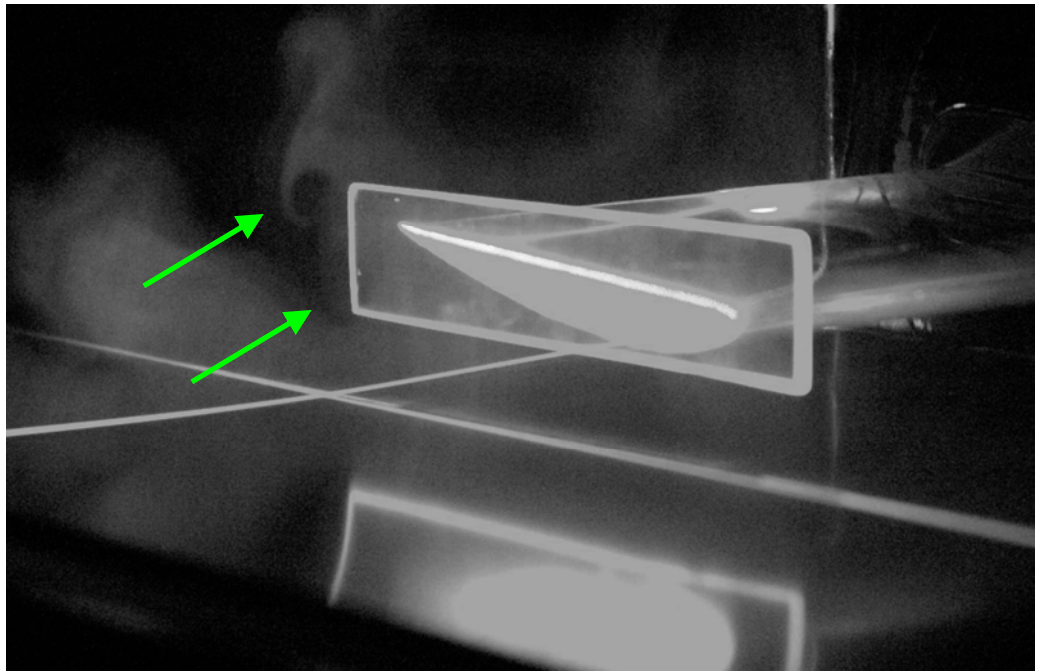


Figure 35: 6deg-h20-B-m14 with plane at 0.067c

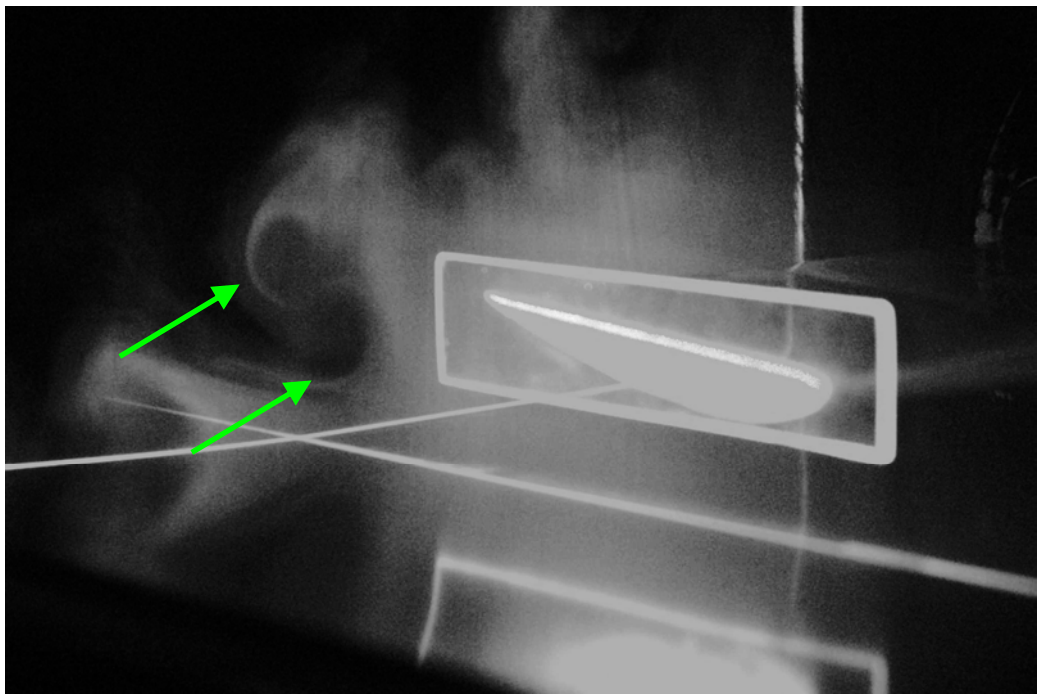


Figure 36: 6deg-h20-B-m14 with plane at 0.267c

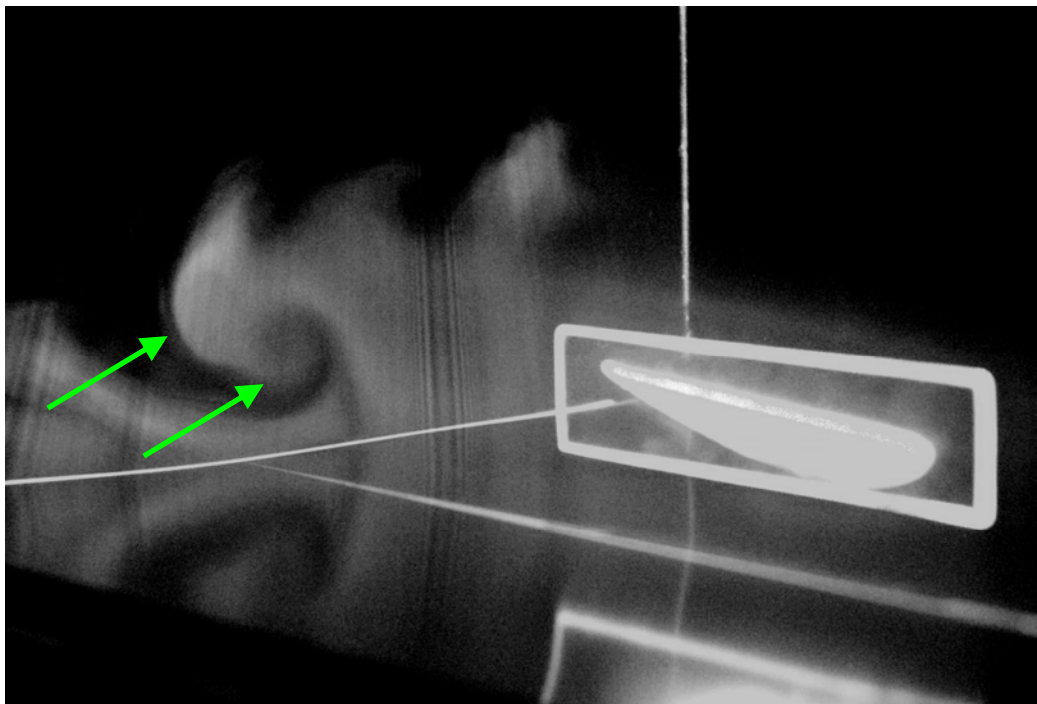


Figure 37: 6deg-h20-B-m14 with plane at 1.333c

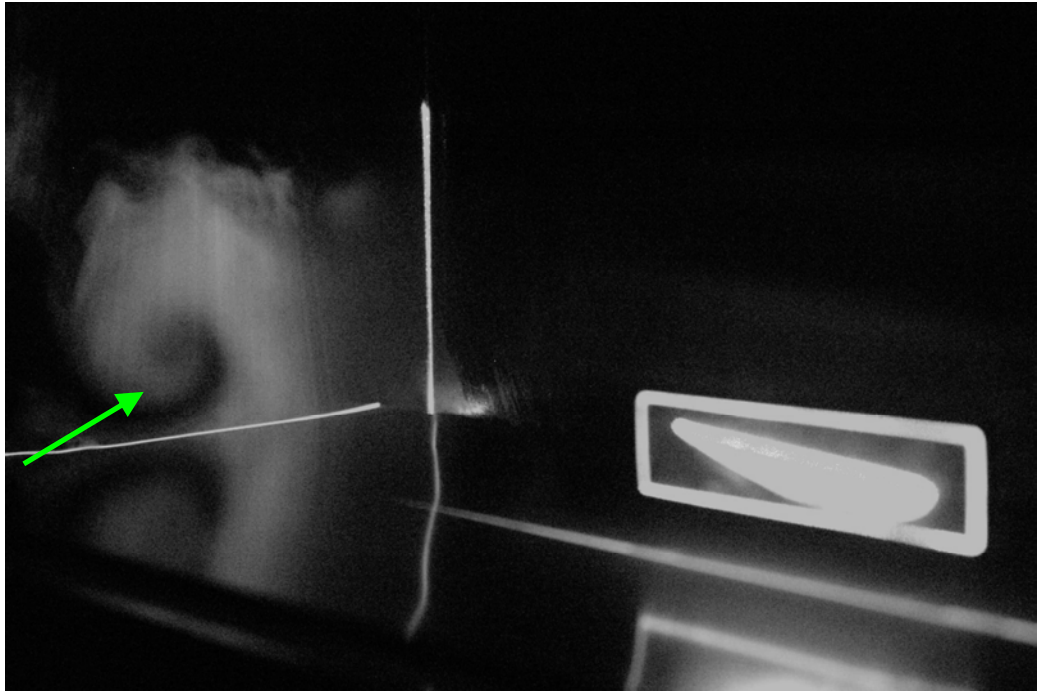


Figure 38: 6deg-h20-B-m14 with plane at 2.667c

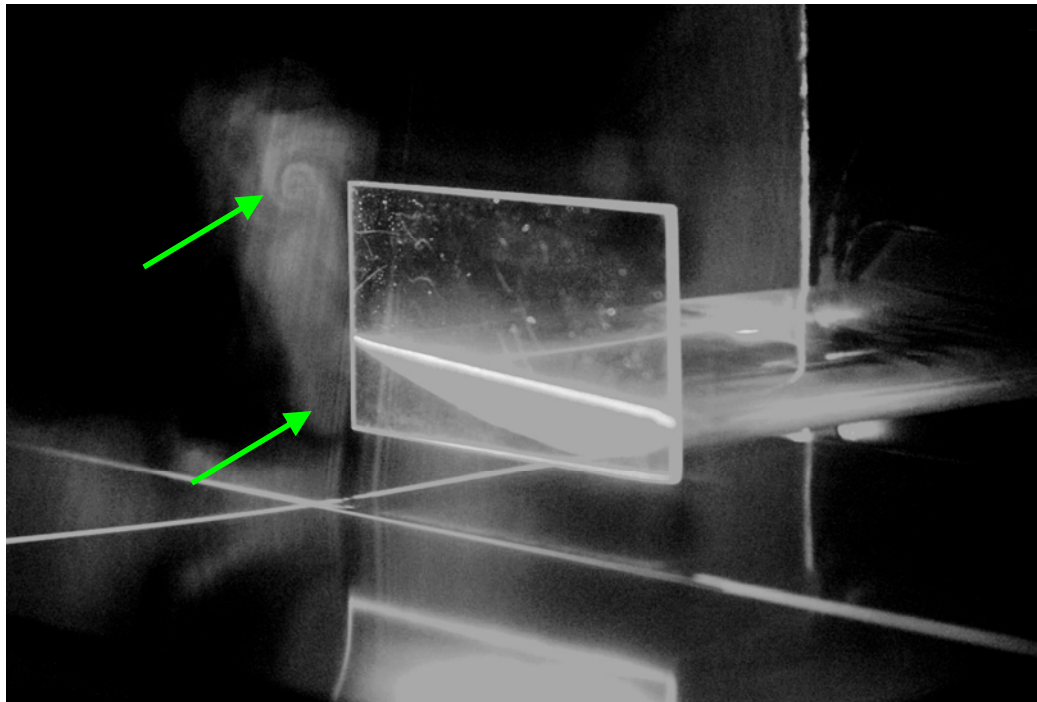


Figure 39: 6deg-h20-C-m14 with plane at 0.067c

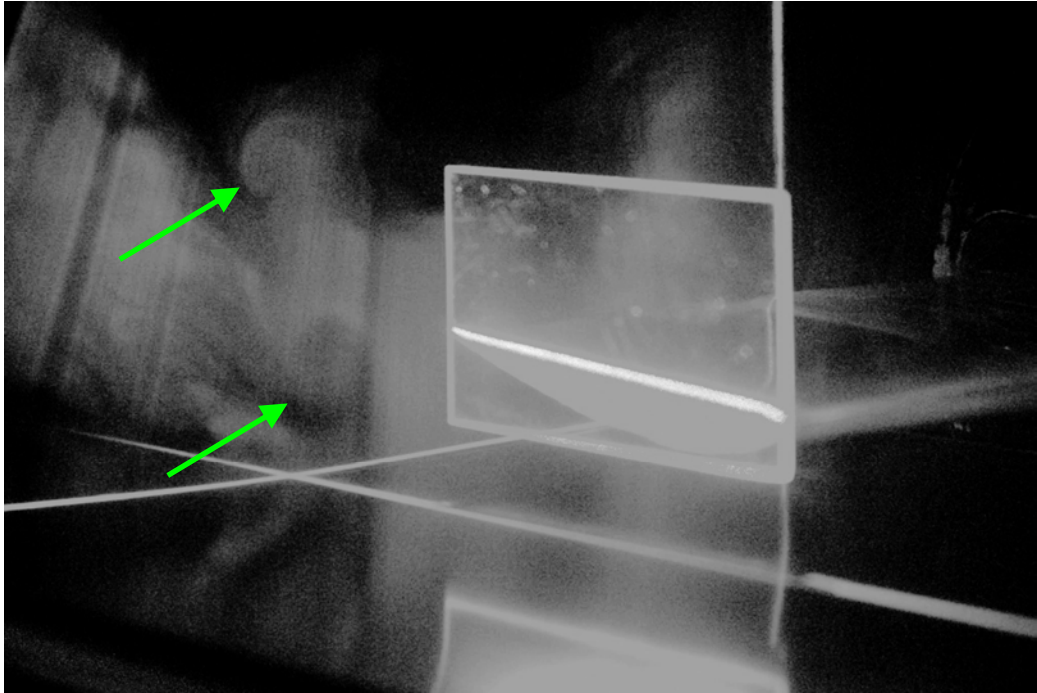


Figure 40: 6deg-h20-C-m14 with plane at 0.267c

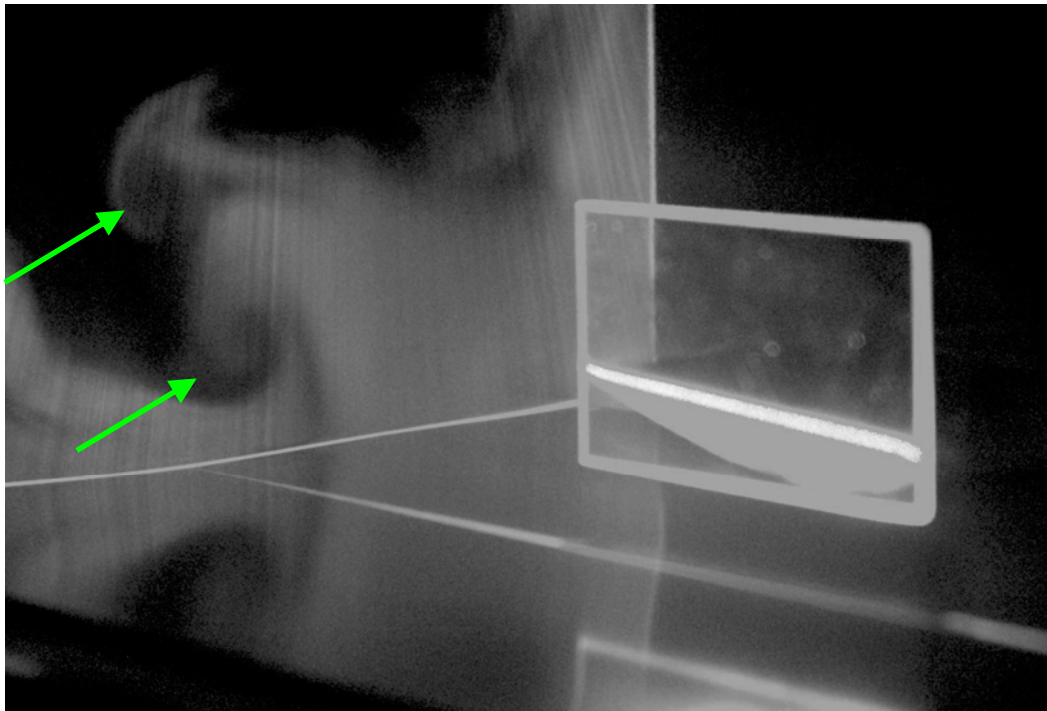


Figure 41: 6deg-h20-C-m14 with plane at 1.333c

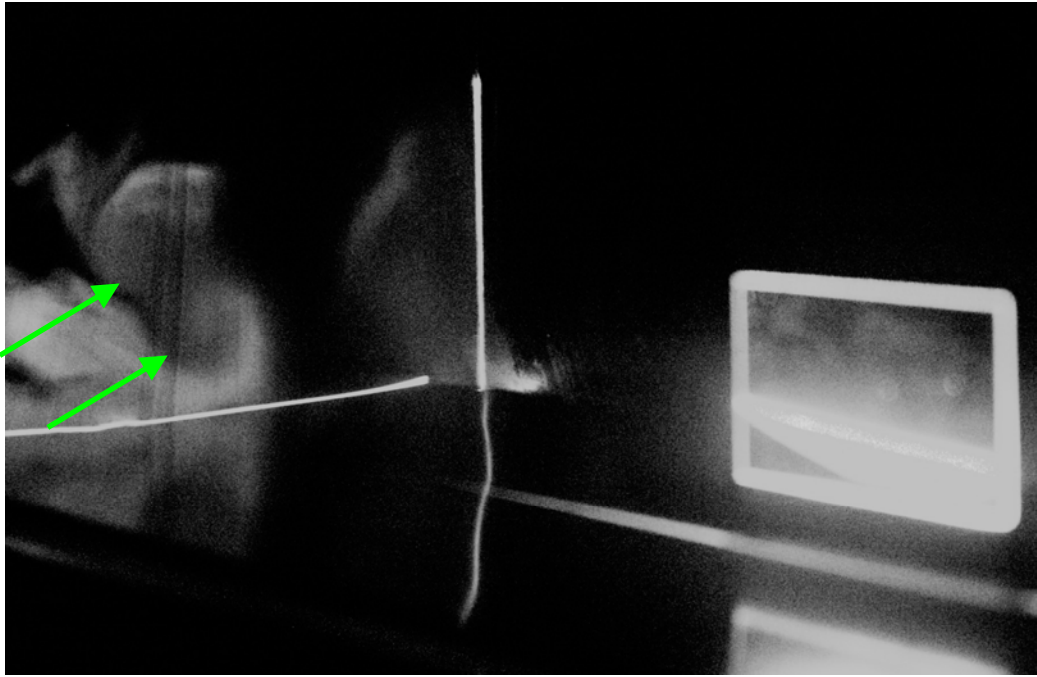


Figure 42: 6deg-h20-C-m14 with plane at 2.667c

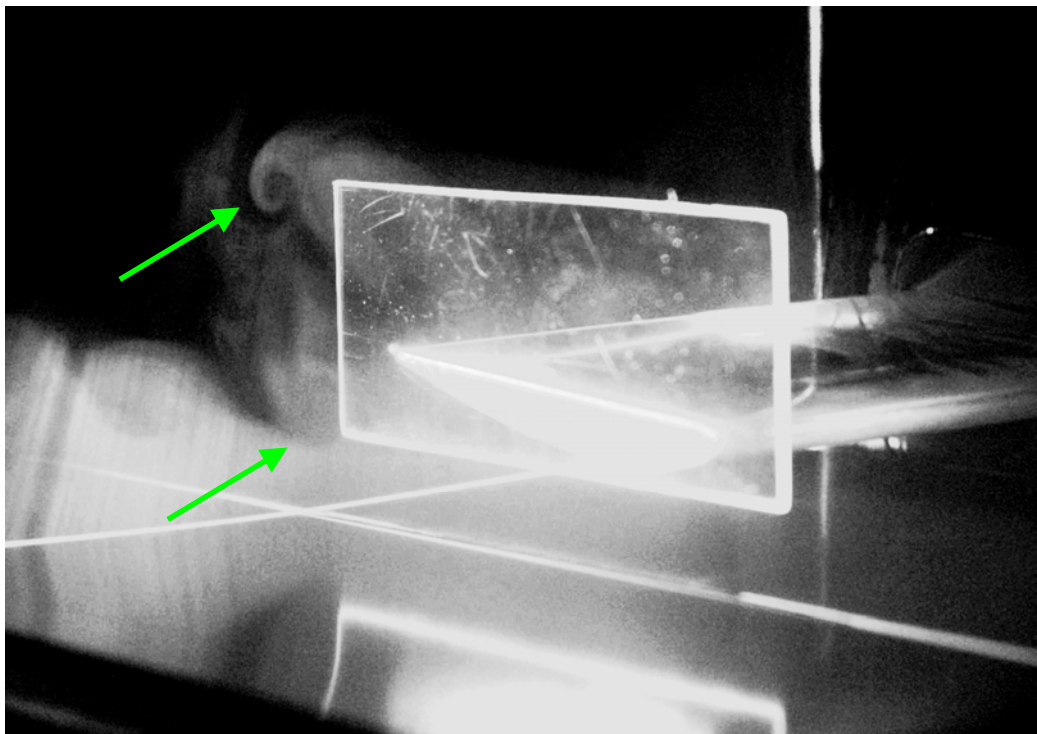


Figure 43: 6deg-h20-D-m14 with plane at 0.067c

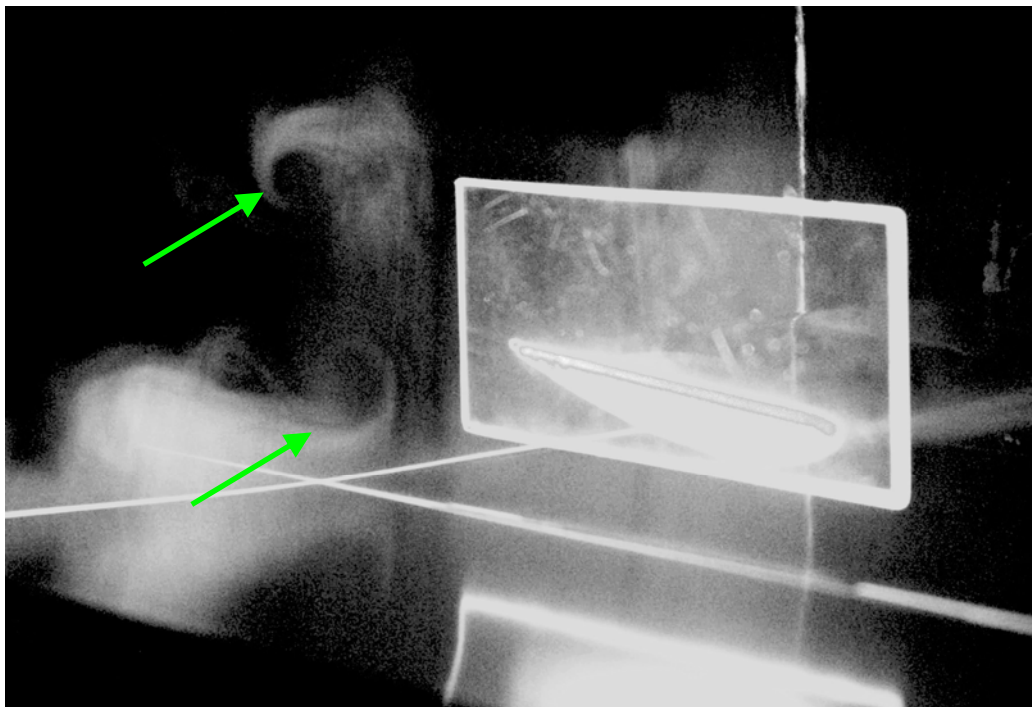


Figure 44: 6deg-h20-D-m14 with plane at 0.267

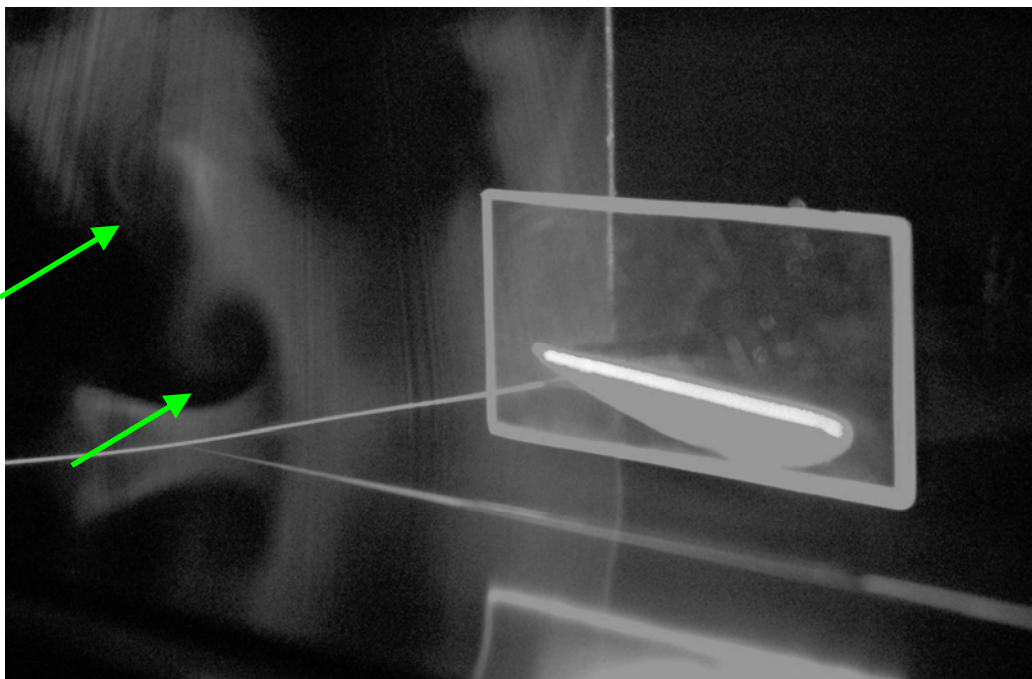


Figure 45: 6deg-h20-D-m14 with plane at 1.333c

5.2.4 Vortex Patterns for 10° Incidence without Endplates

Figures 46 to 49 show an inverted wing with an angle of incidence of 10° without an endplate. The vortex formed is strong and well defined, the trajectory of the vortex moves towards the wing root wall as it travels downstream. The vortex also appears to drop in height as it travels downstream.

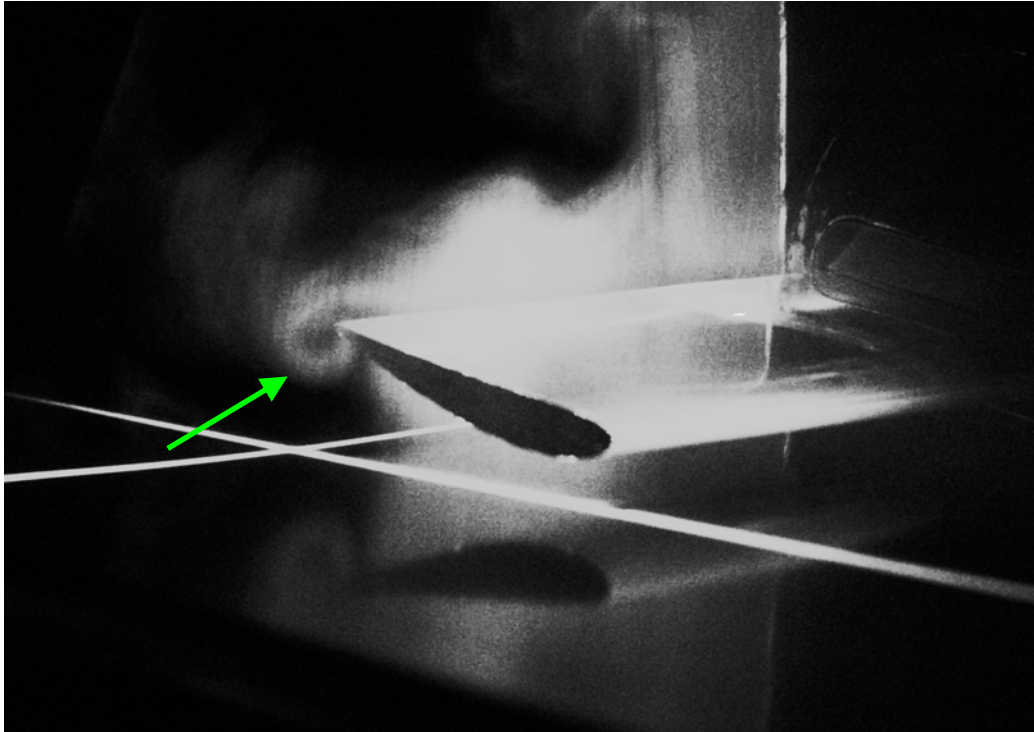


Figure 46: 10deg-h10 with plane at 0.067c

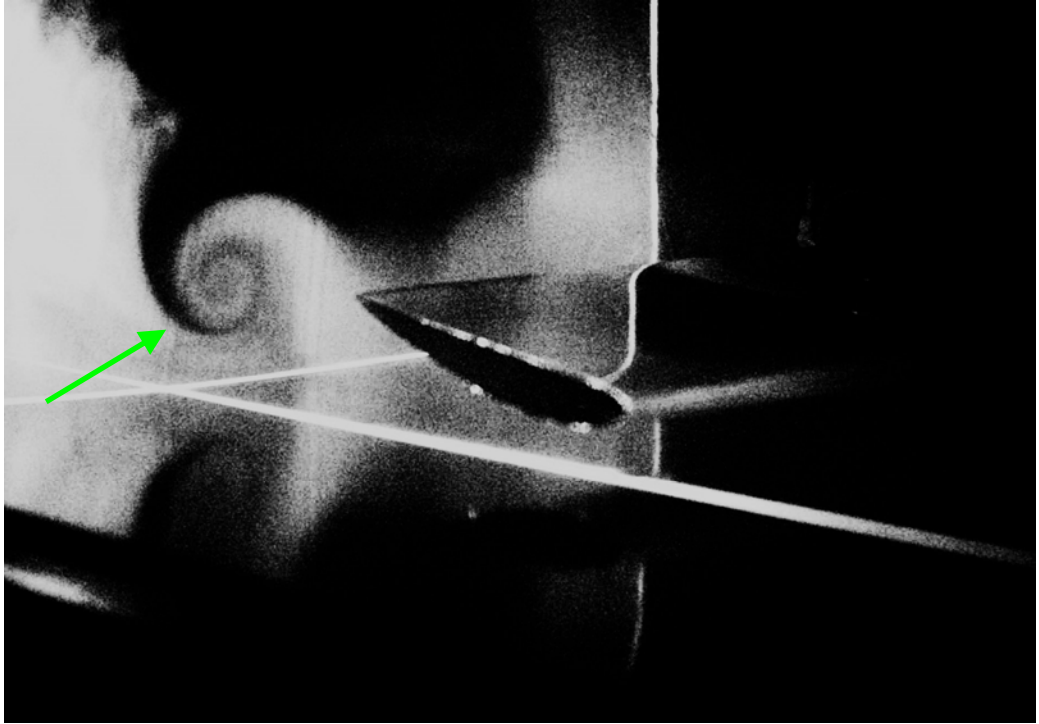


Figure 47: 10deg-h10 with plane at 0.267c

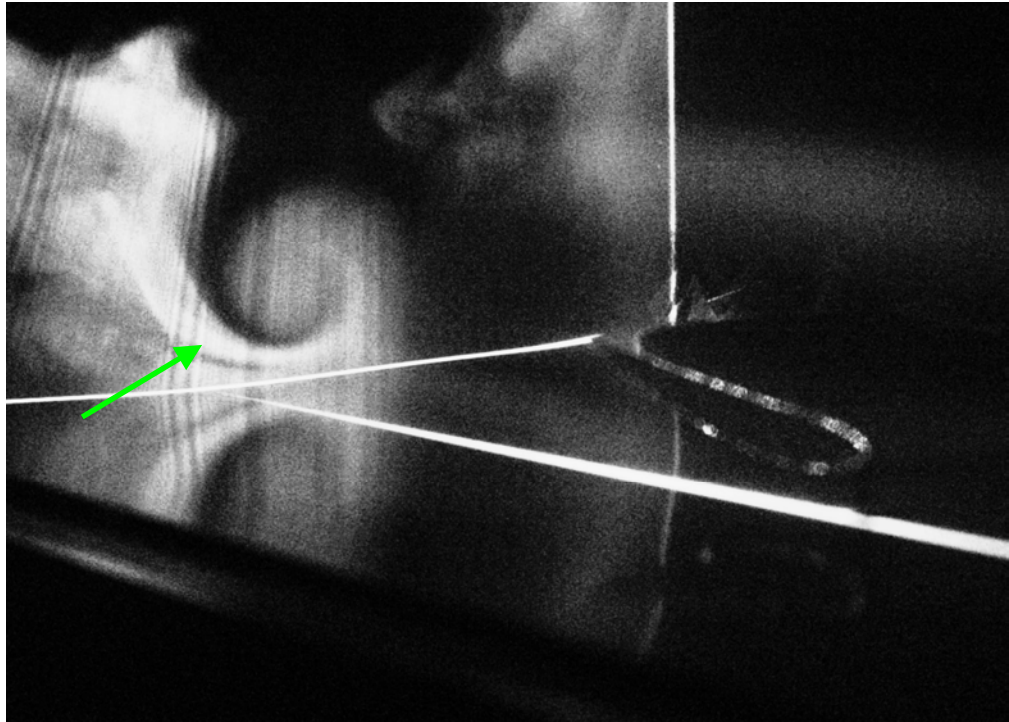


Figure 48: 10deg-h10 with plane at 1.333c

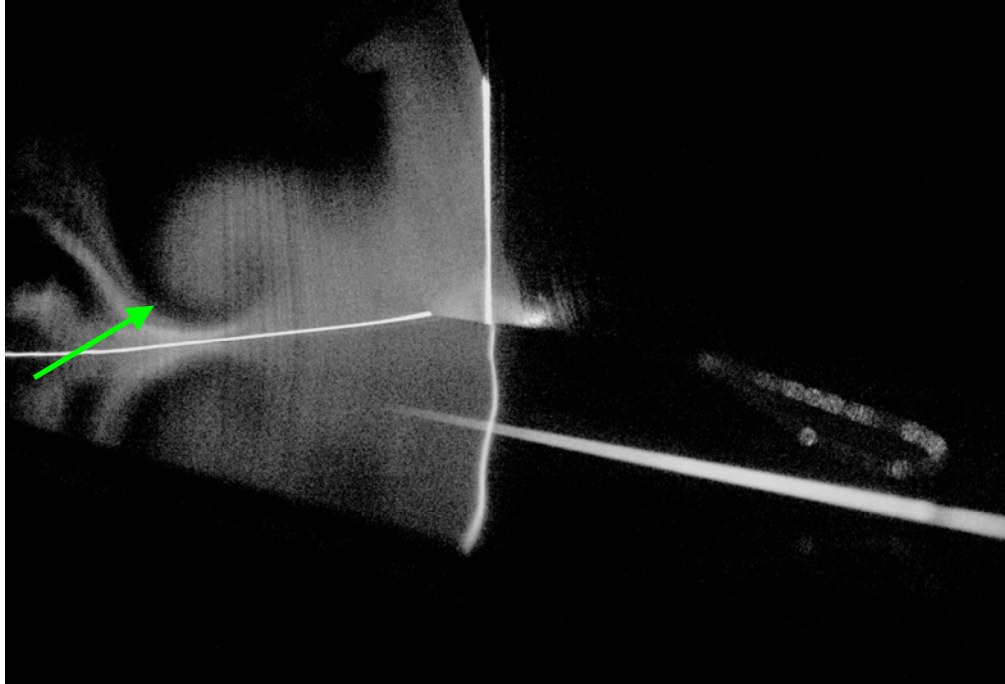


Figure 49: 10deg-h10 with plane at 2.667c

5.2.5 Vortex Patterns for 10° Incidence at $h = 10$

In figures 50 and 51, with endplate A, the upper and lower vortices appear similar sized at $0.067c$, although the upper vortex appears slightly more defined. In figure 51 the vortices have merged, although not completely. No other photos for this case were captured.

Figure 52 shows the vortices generated from endplate B at a distance of $0.267c$. Both vortices appear to be similar size at this distance. No other photos were captured for this case.

Figures 53 to 55 show the vortices formed off endplate C. At a distance of $0.067c$ the upper vortex appears to be stronger than the lower vortex, indicating a chance of wake, or turbulent flow on the lower wing surface near the endplate. In figures 54 and 55 the difference in vortex strength is more apparent as the swirl captured in the image in the upper vortex is much stronger and defined clearer.

In figures 56 and 57 endplate D is used, both vortices appear similar in size but not as strong as seen in figures 53 to 55. The lower vortex appears very weak, but oval in shape.

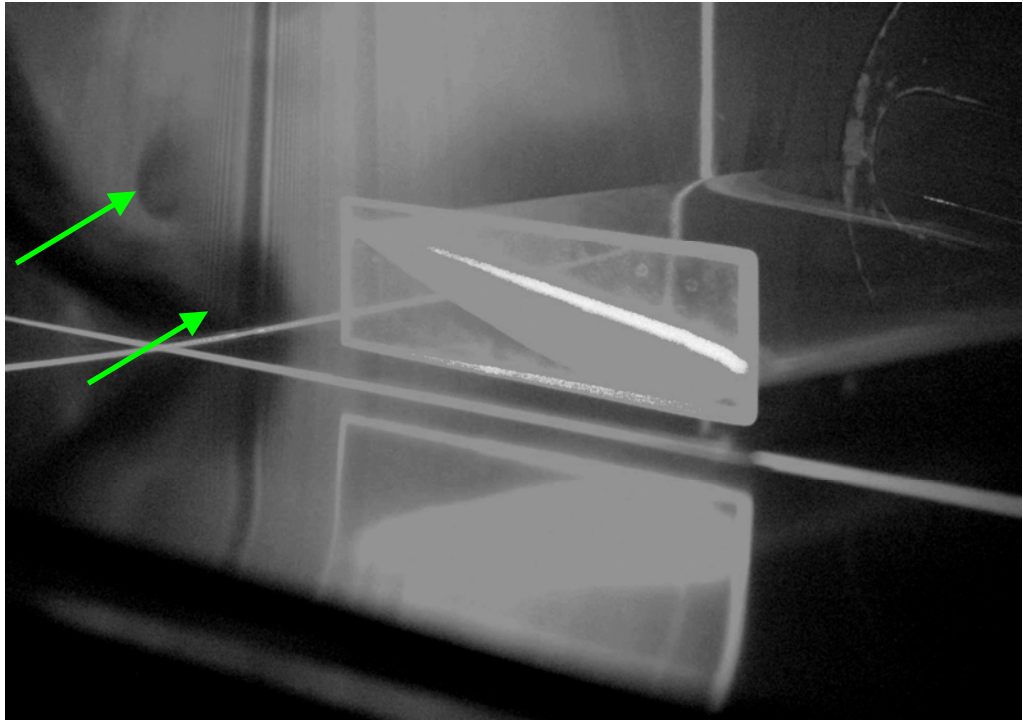


Figure 50: 10deg-h10-A-m4 with plane at 0.267c

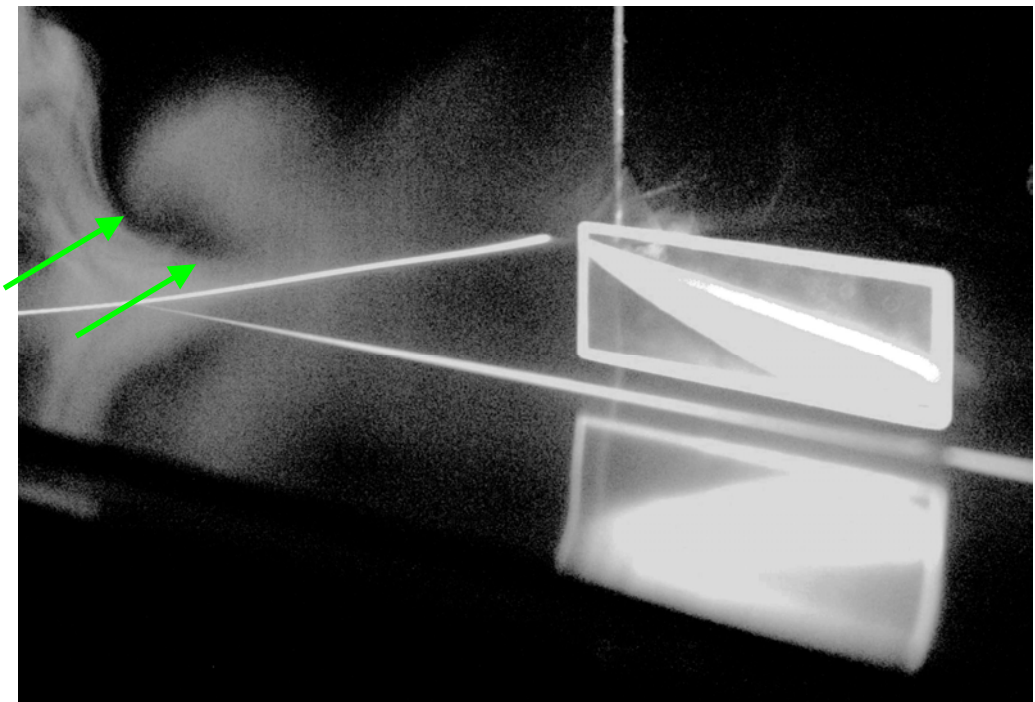


Figure 51: 10deg-h10-A-m4 with plane at 1.333c

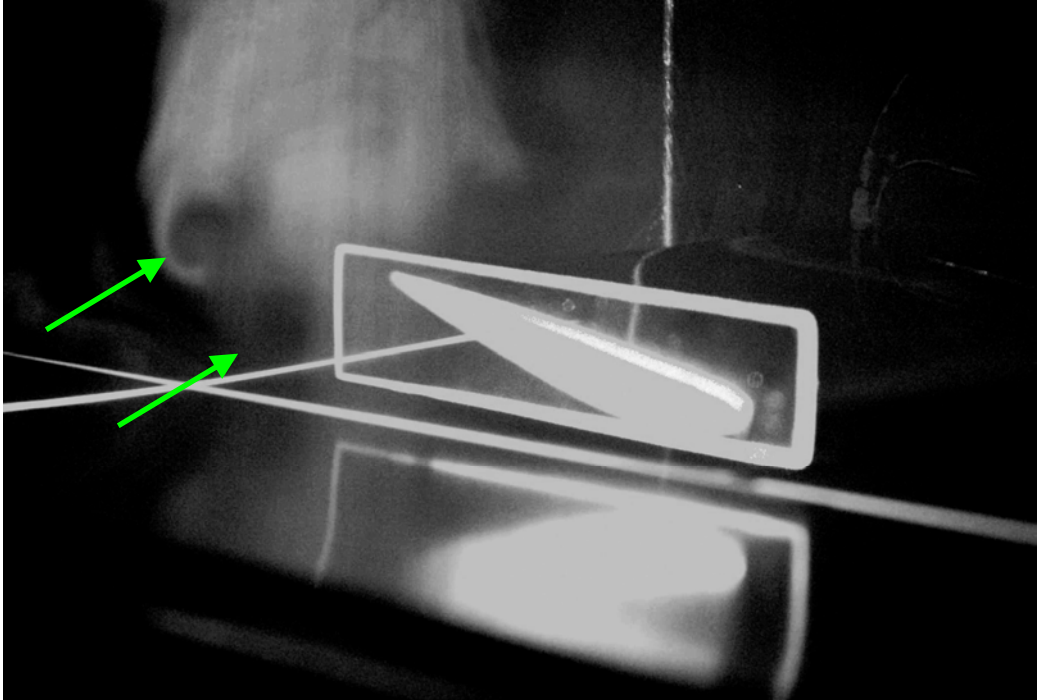


Figure 52: 10deg-h10-B-m4 with plane at 0.267c

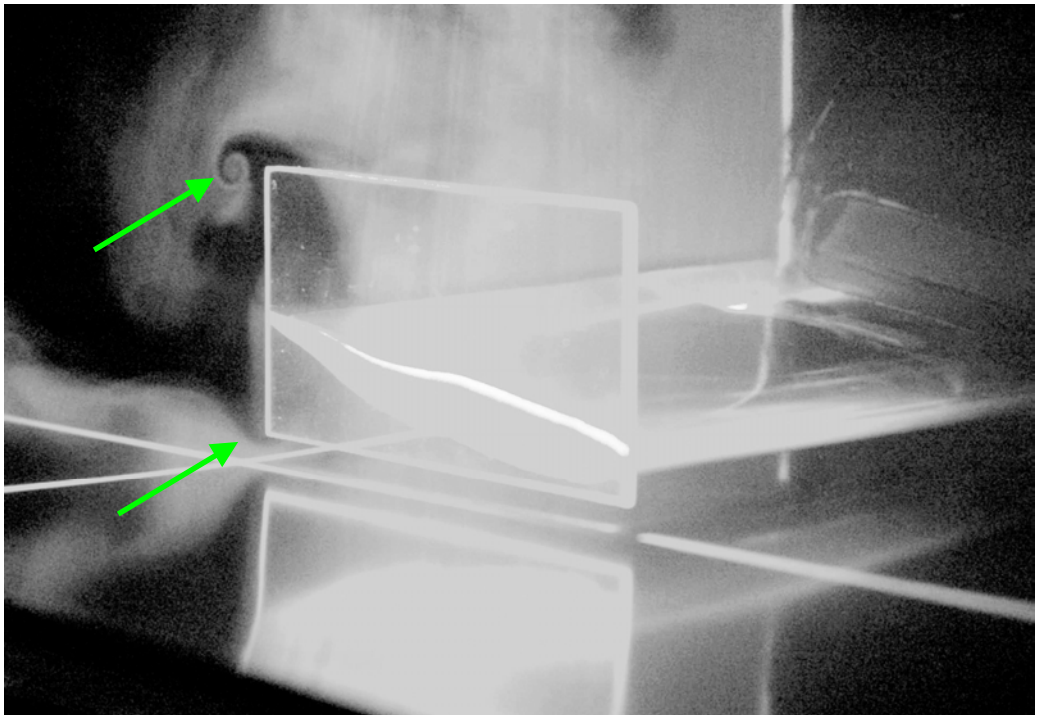


Figure 53: 10deg-h10-C-m4 with plane at 0.067c

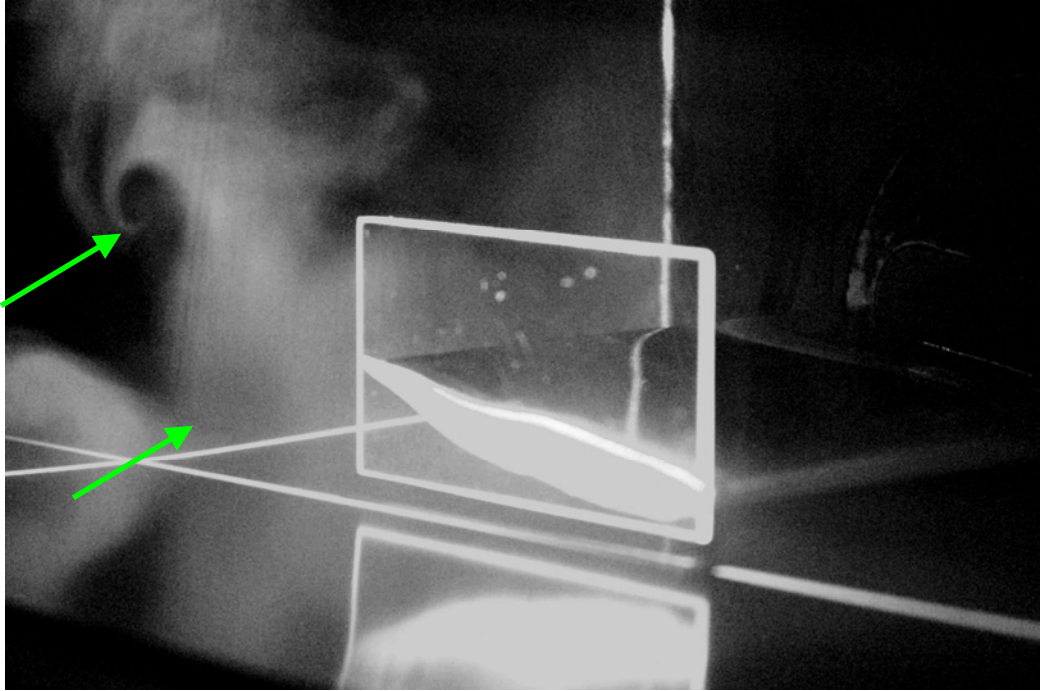


Figure 54: 10deg-h10-C-m4 with plane at 0.267c

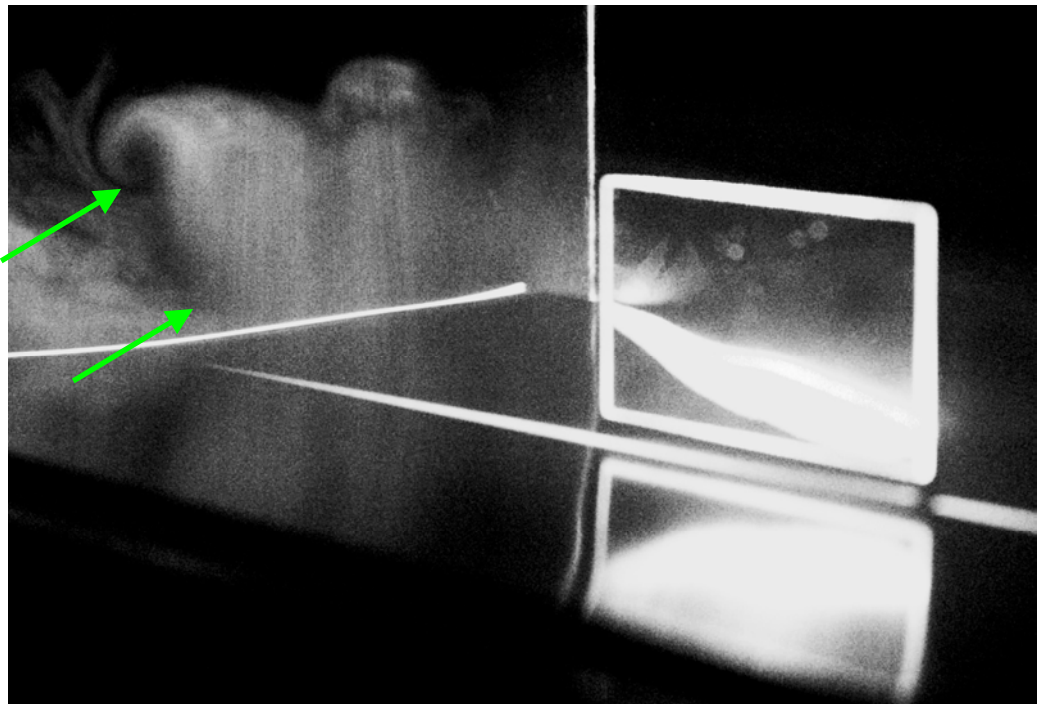


Figure 55: 10deg-h10-C-m4 with plane at 1.333c

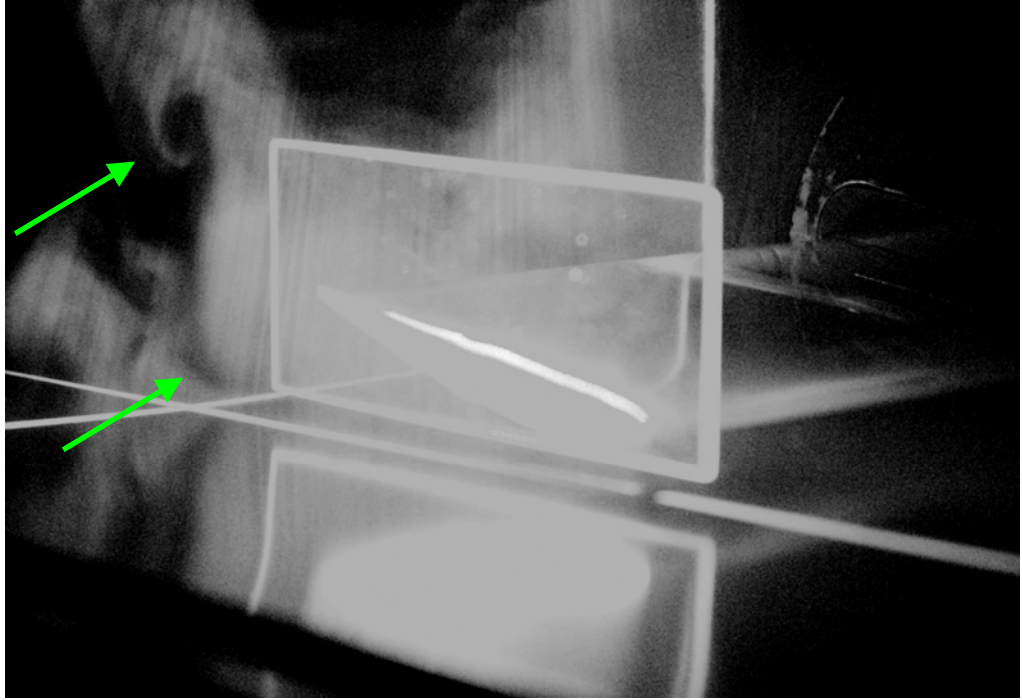


Figure 56: 10deg-h10-D-m4 with plane at 0.067c

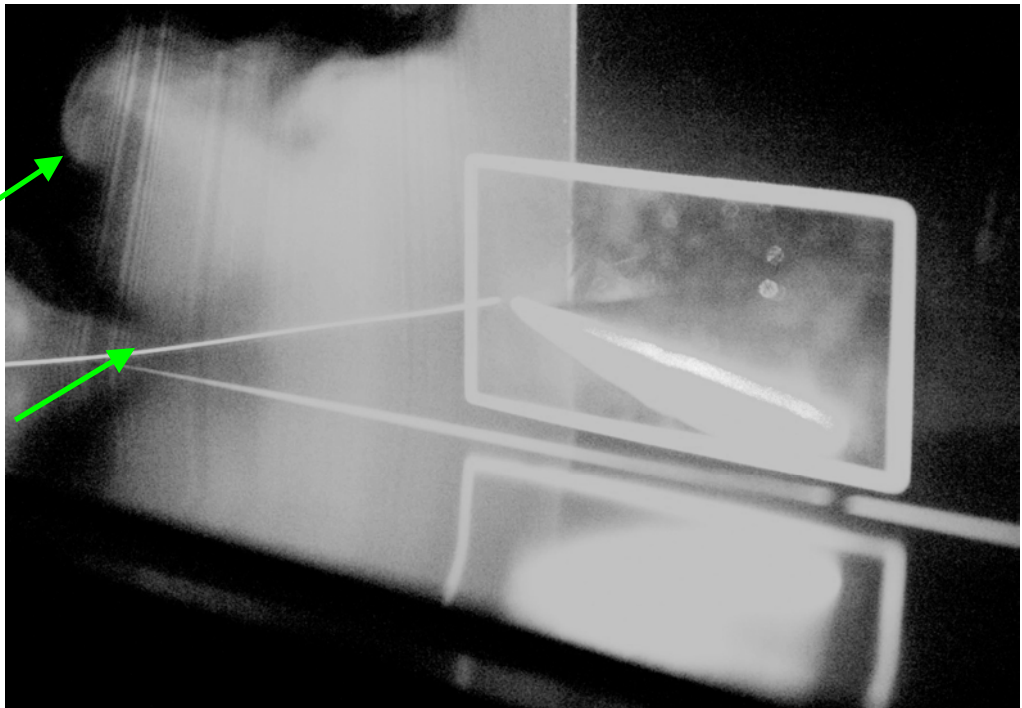


Figure 57: 10deg-h10-D-m4 with plane at 1.333c

5.2.6 Vortex Patterns for 10° Incidence at $h = 20$

Figures 58 to 60 show endplate A with a $h=20$ case, at a distance of $0.067c$ the lower vortex appears larger than the upper vortex but not as defined. In figure 59, at a distance of $1.333c$ the vortices have moved to be horizontally lined forming an oval or elliptical shaped flow. In figure 60, at a distance of $2.667c$, the two vortices appear to have joined, forming an unusually large vortex at that distance compared to other cases.

In figures 61 to 64 endplate B is used. In figure 61, at a distance of $0.067c$ both vortices are very strong and similar in size. In figure 62 the lower vortex appears slightly larger than the upper vortex. In figure 63 the two vortices are nearly lined horizontally, indicating that the upper vortex is moving lower, forming a larger oval shaped vortex. Figure 64 at $2.667c$ shows that the two vortices have merged.

Figures 65 to 67 show vortex formations of endplate C. In figure 65 at $0.267c$ the lower vortex appears larger than the upper vortex, both vortices are separated. In figure 66 the vortices appear similar in size, but separated. Figure 67 shows that the vortices have merged slightly, that is, the surrounding rotating flows have merged slightly. The lower vortex has moved towards the wing root wall and the upper vortex has moved downwards.

In figures 68 to 71 endplate D is used. In figures 69 and 70 the vortices are separate and well defined. In figure 71 the vortices have moved close together in similar fashion when endplate C is used, as shown in figure 67.

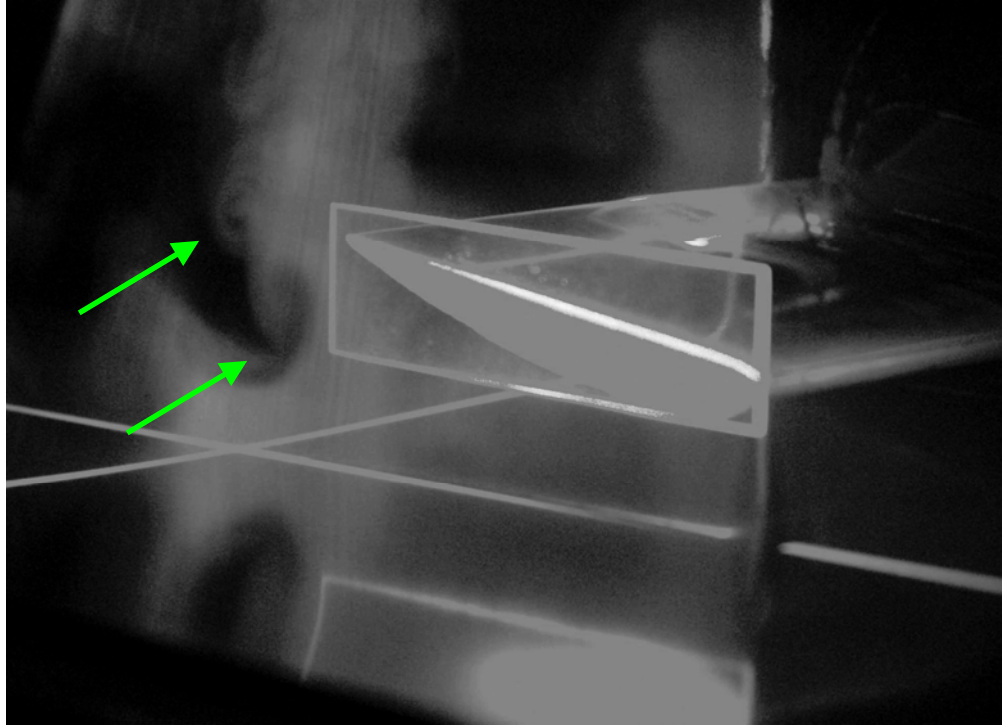


Figure 58: 10deg-h20-A-m14 with plane at 0.067c

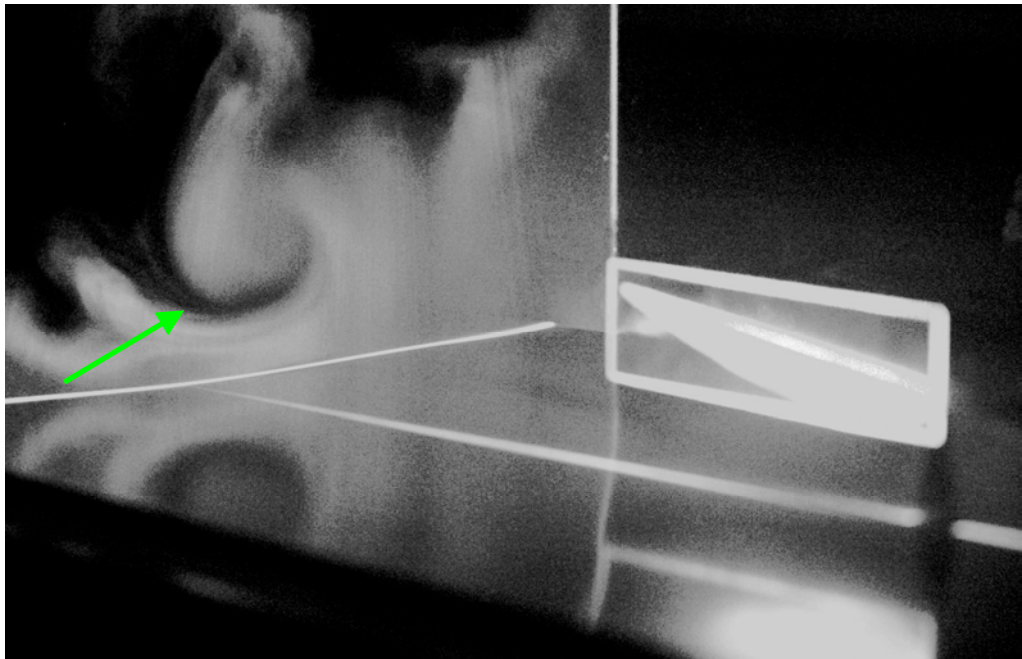


Figure 59: 10deg-h20-A-m14 with plane at 1.333c



Figure 60: 10deg-h20-A-m14 with plane at 2.667c

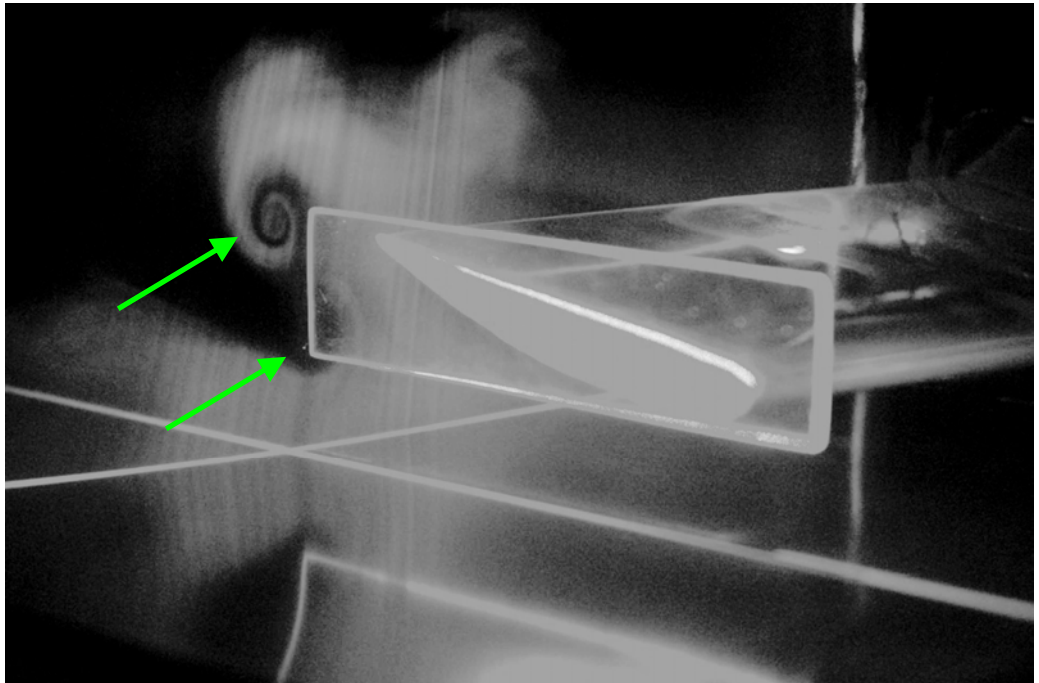


Figure 61: 10deg-h20-B-m14 with plane at 0.067c

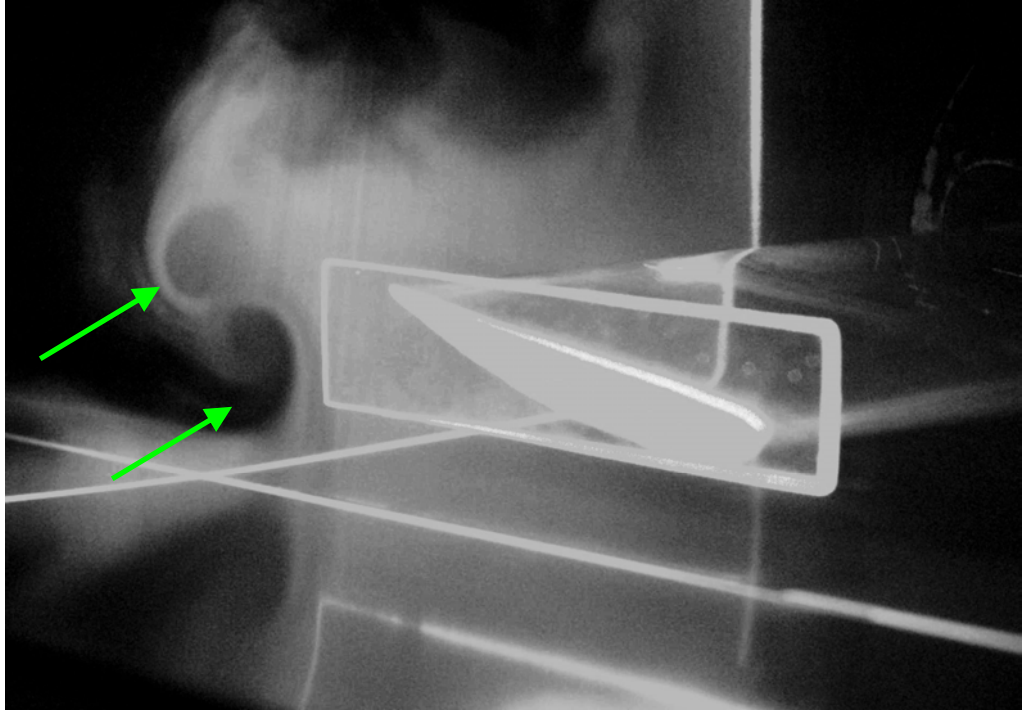


Figure 62: 10deg-h20-B-m14 with plane at 0.267c

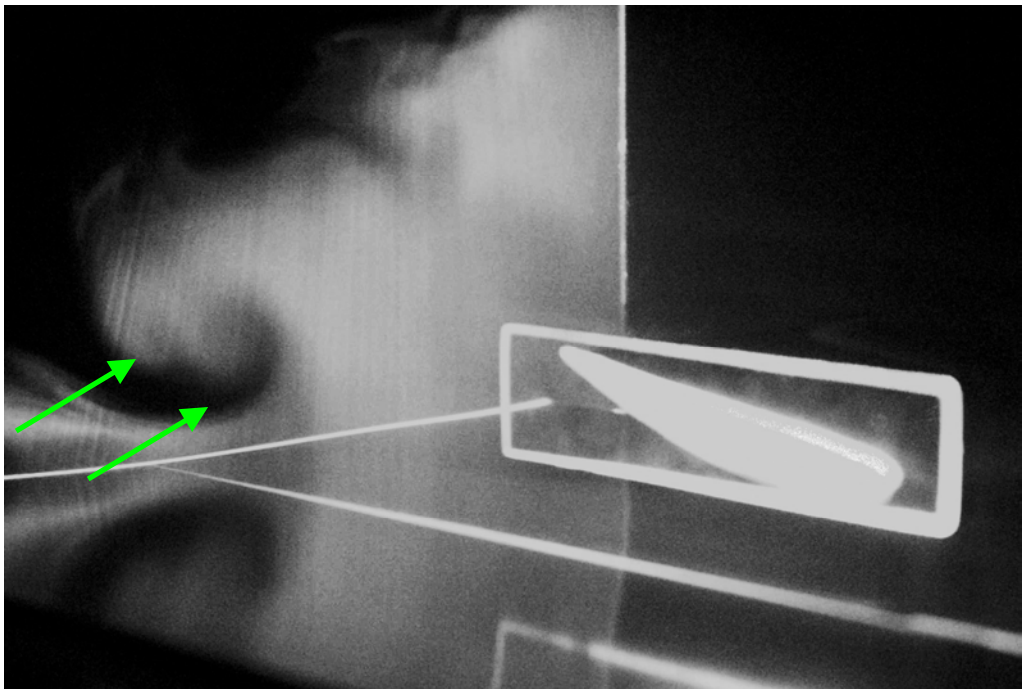


Figure 63: 10deg-h20-B-m14 with plane at 1.333c



Figure 64: 10deg-h20-B-m14 with plane at 2.667c

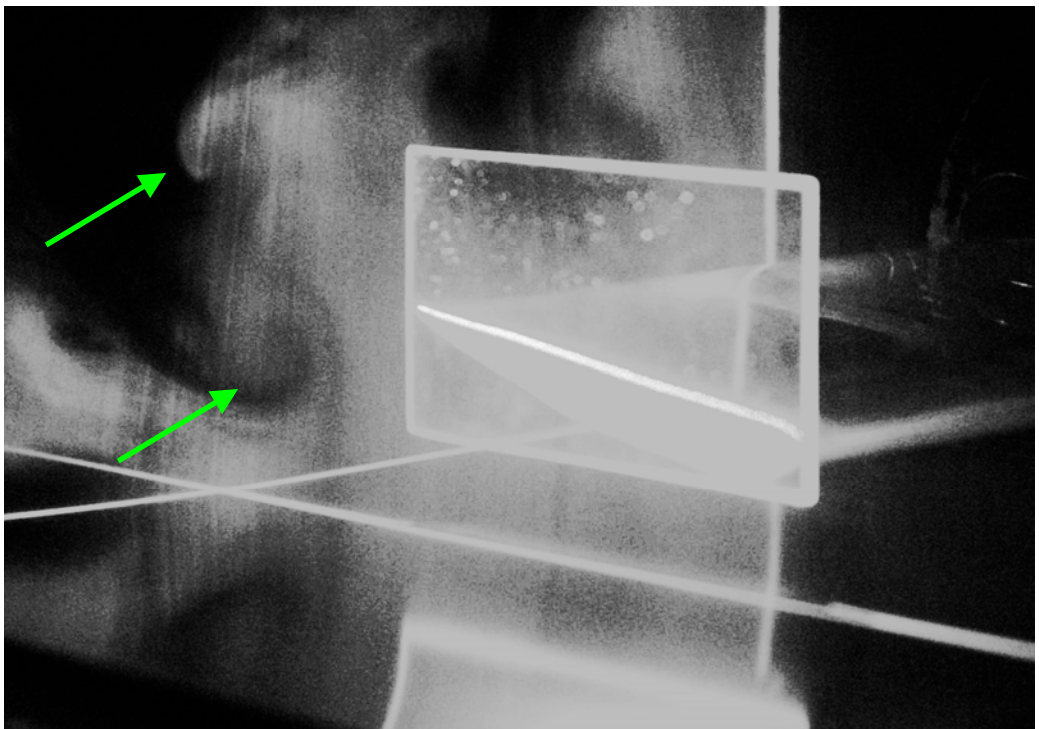


Figure 65: 10deg-h20-C-m14 with plane at 0.267c

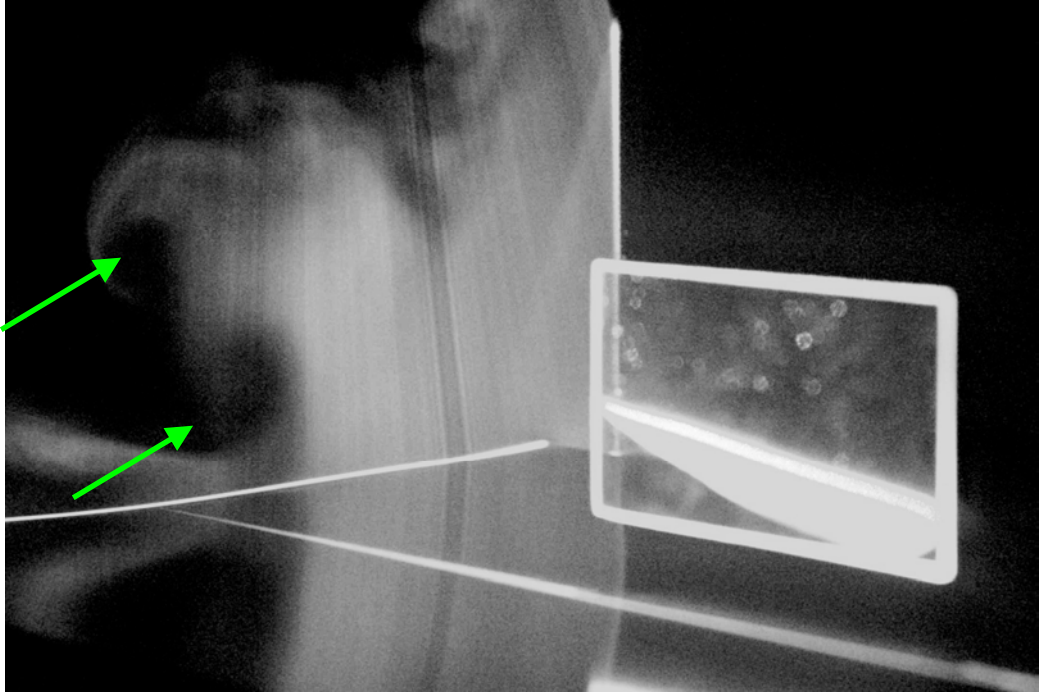


Figure 66: 10deg-h20-C-m14 with plane at 1.333c

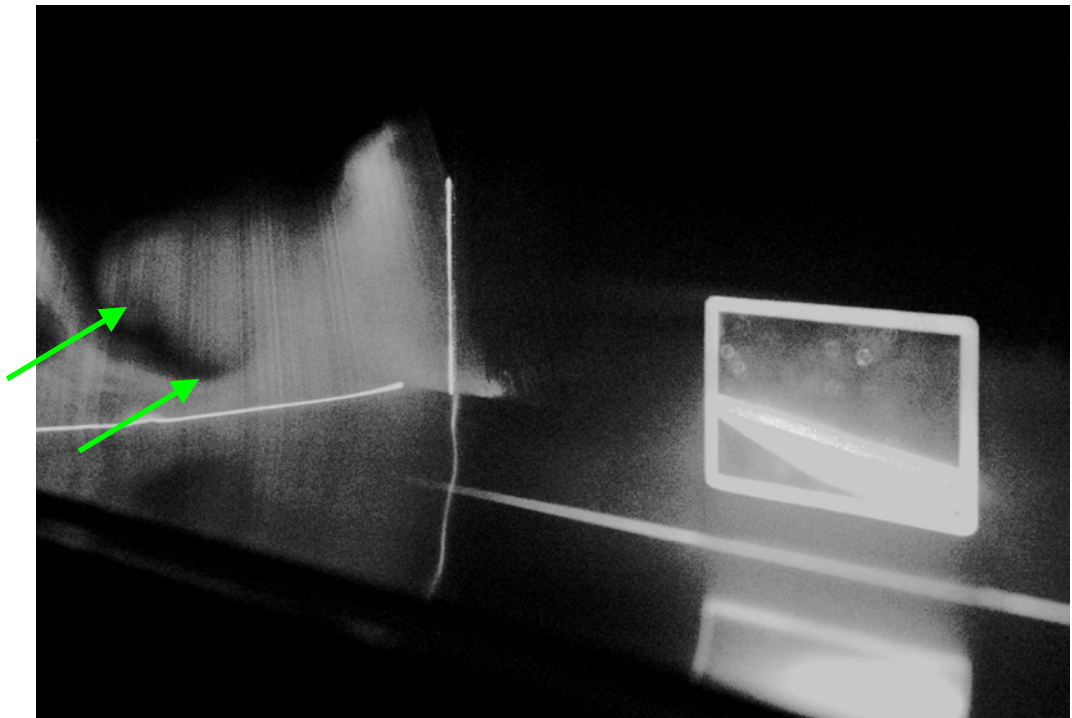


Figure 67: 10deg-h20-C-m14 with plane at 2.667c

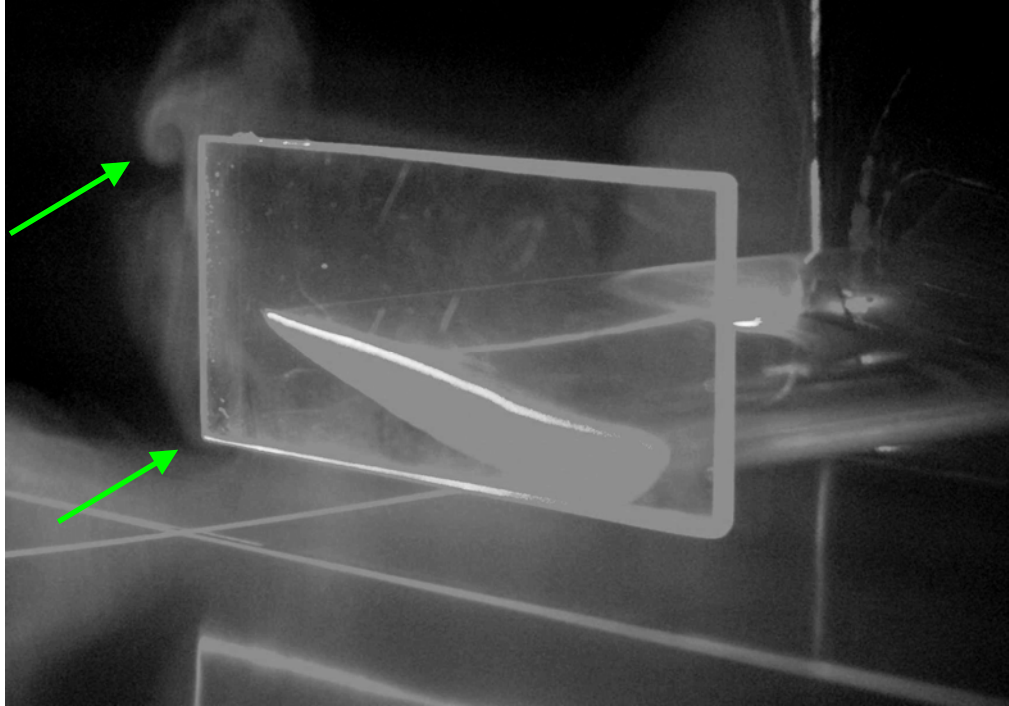


Figure 68: 10deg-h20-D-m14 with plane at 0.067c

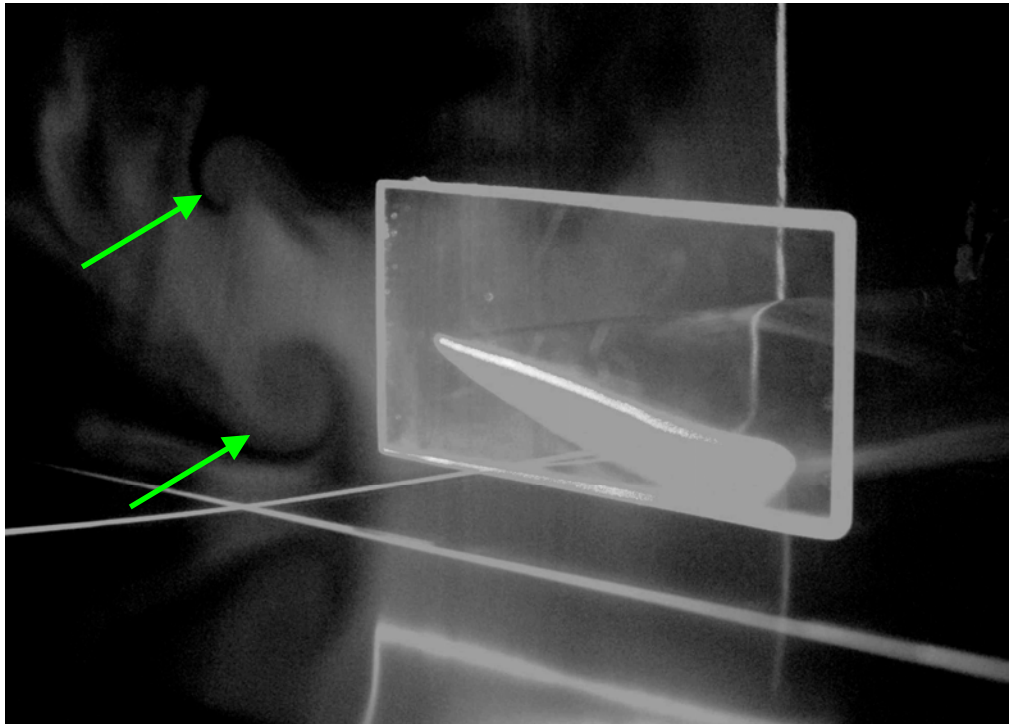


Figure 69: 10deg-h20-D-m14 with plane at 0.267c

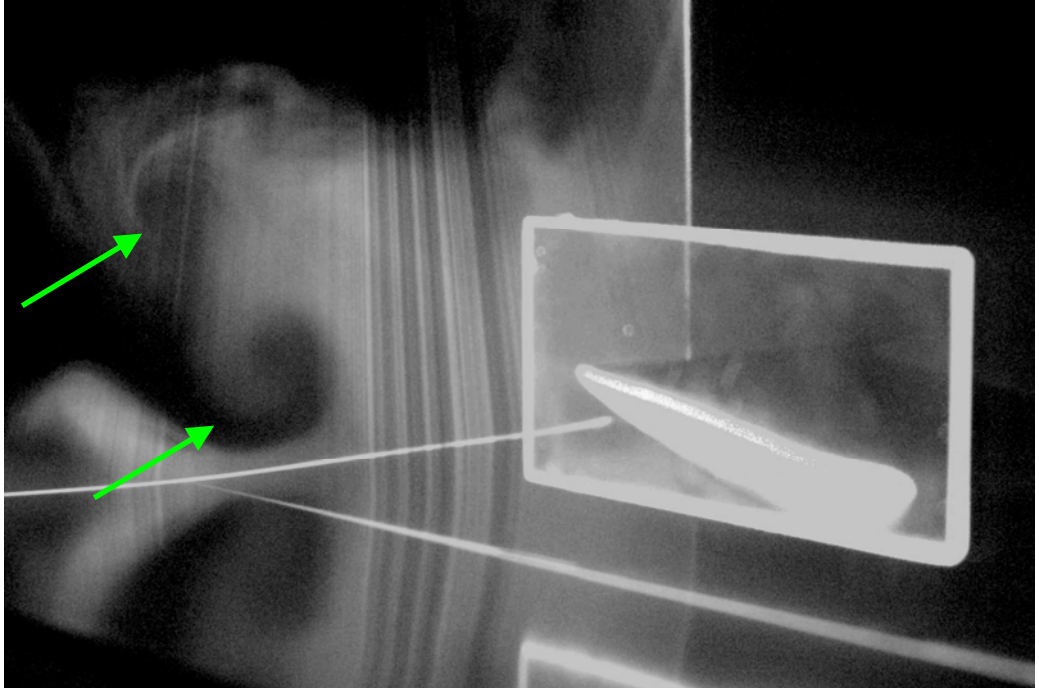


Figure 70: 10deg-h20-D-m14 with plane at 1.333c

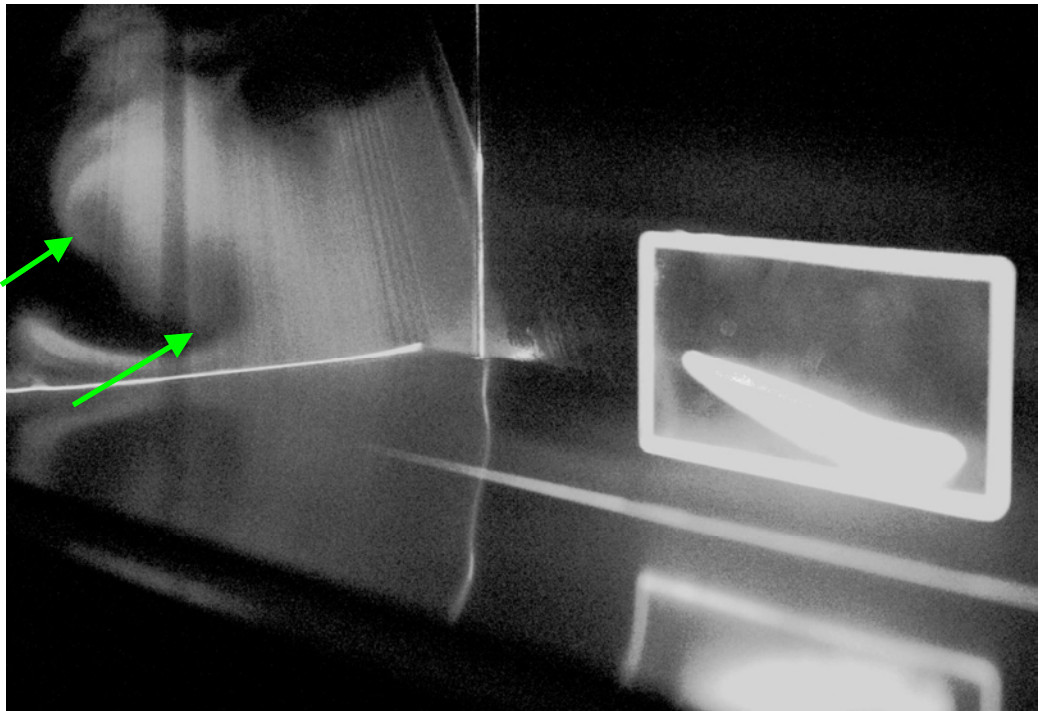


Figure 71: 10deg-h20-D-m14 with plane at 2.667c

5.2.7 Summary for Flow Visualisation Results

In summary, the vortices generated by the inverted wings without endplates are obviously different to the vortices generated by the inverted wings with endplates. The vortices generated by small endplates, A and B, at relatively high h/c , are large and similar in size and very close together, which appeared to merge at further distances, $2.667c$. The same conditions with endplates C and D produced two large vortices, further apart, but stay separated at further distances, $2.667c$. As the height, h/c , is reduced, the vortices appear to weaken, the upper vortices remain defined but reduced in size and the lower vortices are very weak, and almost indistinguishable from the surrounding flow. The further the distance behind the wing, the more detail in the vortex is visible, or its presence is more apparent. The cases with the endplates B and D, which extend in front and behind the wing produce more defined vortices for the same cases with endplates A and C.

5.3 Computational Fluid Dynamics

A complete list of the test cases simulated with CFD can be found in Table A1 in Appendix A. In figures 72 to 85, the C_L and C_D values are not corrected for any wake or wall effects. These are direct comparisons against different endplate configurations whilst maintaining constant wing height and incidence in each case set. From studying the CFD results, the wake and other interference effects were similar in size and value for each case set, and therefore not evaluated. Since the CFD simulations were modelling the physical experiments as closely as possible, direct comparisons could be made between the physical and simulated results. Any errors generated in each method are discussed in chapter 6. The CFD results will be compared to the flow visualisation and LDA results in section 6.6. The key to the test case names repeated from the Flow Visualisation section is as follows: '6deg' or '10deg' indicates the angle of incidence of the wing, 'h10' or 'h20' indicates the height of the wing above the ground. A, B, C, or D indicates the endplate and 'm4' or 'm14' indicates the height of the endplate above the ground.

5.3.1 C_L and C_D for 6deg-h10 Cases

The first group of results in figures 72 and 73 are the C_L and C_D values for the 6deg-h10 cases ($h/c = 0.07$) respectively. Endplates A and B with a height of 2mm produce the highest C_L , while the same endplates at a height of 4mm produce the lowest C_L values. With each endplate, the case with a height of 2mm produces a higher C_L than at 4mm. The C_L ranges from 1.044 to 0.973, giving a maximum difference of 0.071. The C_D values generally increase as the endplate area increases. For endplates A and B the C_D values are the highest with endplate heights of 2mm, which correspond to the highest C_L values. The high C_D could be caused by the induced drag for the high C_L cases. The C_D values range from 0.145 to 0.126, giving a maximum difference of 0.019.

5.3.2 C_L and C_D for 6deg-h15 Cases

Figures 74 and 75 are the C_L and C_D values for the 6deg-h15 cases ($h/c = 0.13$) respectively. Figure 74 clearly shows the difference in C_L values with the two heights, 4mm and 9mm. With 4mm endplate height, the C_L value is lowest for endplate B, and highest for endplate D, at a height of 9mm, where there is greater clearance for the air to spill underneath the endplates, the C_L values are almost constant, indicating a large amount of air spilling between the larger gap between the endplate and ground. The C_L ranges from 1.117 to 0.967, giving a maximum difference of 0.15. Figure 74 shows the drag increasing with endplate area and corresponding increase in lift. The C_D values range from 0.141 to 0.126, giving a maximum difference of 0.015.

5.3.3 C_L and C_D for 6deg-h20 Cases

Figures 76 and 77 are the C_L and C_D values for the 6deg-h20 cases ($h/c = 0.20$) respectively. Again, the C_L values show similar characteristics to the h10 and h15 cases, that is, the closer the endplate to the ground the higher the C_L . For this configuration (6deg-h20), and in particular the cases with endplate height of 14mm, there is a large jump from endplates A and B to endplates C and D. With the cases with endplate height of 9mm, the C_L values follow a similar trend to the h15 cases. The C_L values range from 0.998 to 0.908,

giving a maximum difference of 0.09. The C_D values also show similar stepped increases as observed in the h15 cases. The cases with an endplate height of 9mm have higher relative C_D values than the cases with an endplate height of 14mm. The C_D values range from 0.128 to 0.116, giving the maximum difference of 0.012.

5.3.4 C_L and C_D for 6deg-h40 Cases

Figures 78 and 79 are the C_L and C_D values for the 6deg-h40 cases ($h/c = 0.47$) respectively. At $h/c = 0.47$, the effects of ground effect are less apparent, as there is a relatively large decrease in C_L values across the range of cases. Across the cases with lowest endplate heights, endplates A and B have heights of 28mm, and endplates C and D have heights of 10mm, these configurations were chosen as they were the extreme positions of the endplates with respect to the available wingtip space, both upper and lower. With the wing at $h/c = 0.47$, the positions of the larger endplates closer to the ground increases the C_L values. Endplates C and D have the highest C_L values, 0.897 and 0.943 respectively. The C_L values range from 0.769 to 0.943. Figure 78 shows the C_D values, endplate D with 10mm height has the highest C_D value, which corresponds with the maximum C_L value. The C_D values range from 0.101 to 0.132.

5.3.5 C_L and C_D for 10deg-h10 Cases

Figures 80 and 81 are the C_L and C_D values for the 10deg-h10 ($h/c = 0.08$) cases respectively. With the higher angle of incidence, 10° , the C_L values are higher than at 6° . In similar trends to earlier cases, endplates A and B have higher C_L values when the endplates are closer to the ground. With endplates C and D, the C_L values decrease with the increase in endplate area, and the C_L values decrease with increase in endplate height. The C_L values range from 1.265 to 1.415. The C_D values are lower for endplates A and B than endplates C and D. This would be a result of the lower surface area, creating less skin friction. The C_D values for endplates C and D follow the same trend as the C_L values, therefore indicate that the induced drag is the main contributor, adding to the drag created by skin friction. The C_D values range from 0.181 to 0.193.

5.3.6 C_L and C_D for 10deg-h15 Cases

Figures 82 and 83 are the C_L and C_D values for the 10deg-h15 ($h/c = 0.15$) cases respectively. Endplates A and B follow similar trends with the cases with the endplate closer to the ground given higher C_L values. The cases with endplates C and D have C_L values that are the reverse of the trend. The two heights are 9mm and 10mm, yet the difference in C_L values is quite significant. The C_L values range from 1.185 to 1.244. The C_D values for endplates A and B are the lowest, which is a result of lower friction drag. The C_D values for endplates C and D are higher due to increased friction drag and increased induced drag. Looking at endplate C, there is a large difference in C_L of 0.058, and a relatively small difference in C_D of 0.0006, compared to endplate D with a C_L difference of 0.015 and C_D difference of 0.0004. The C_D values range from 0.175 to 0.187.

5.3.7 C_L and C_D for 10deg-h20 Cases

Figures 84 and 85 are the C_L and C_D values for the 10deg-h20 cases ($h/c = 0.21$) respectively. This case set has one endplate height, insufficient time was the factor for not obtaining the results for another endplate height. There is an obvious trend present in these cases, as the C_L value increases with increase in endplate size. The C_L values range from 1.199 to 1.296. The C_D values follow the same trend, increasing as the endplate size increases. The C_D values range from 0.168 to 0.178.

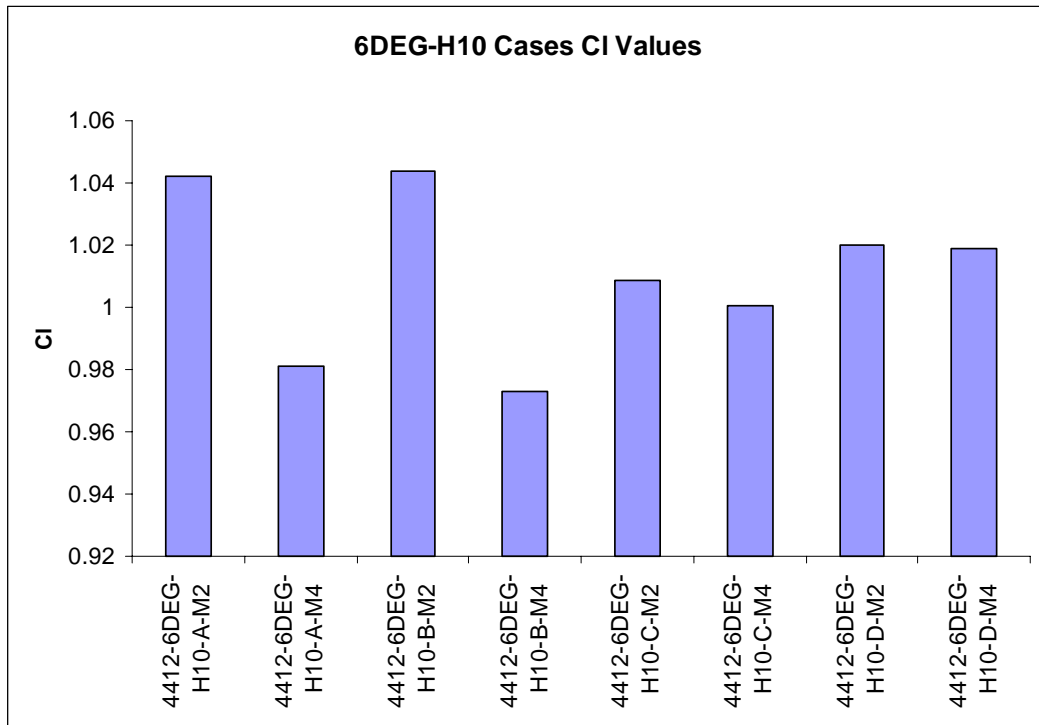


Figure 72: 6deg-h10 cases C_L values ($h/c = 0.07$)

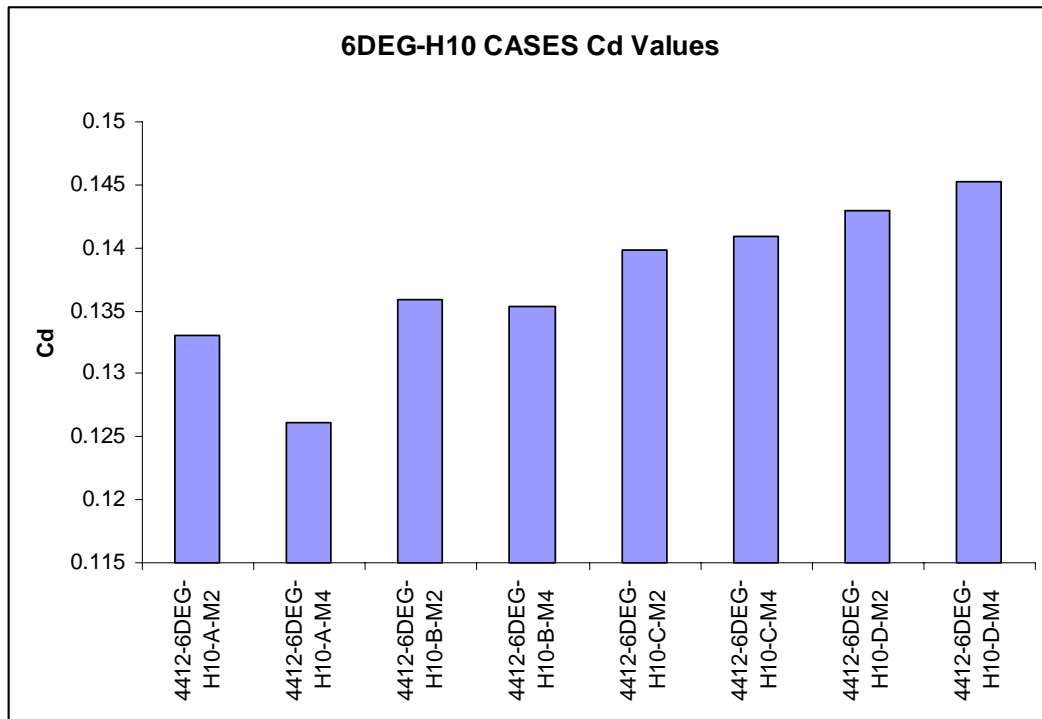


Figure 73: 6deg-h10 cases C_D values ($h/c = 0.07$)

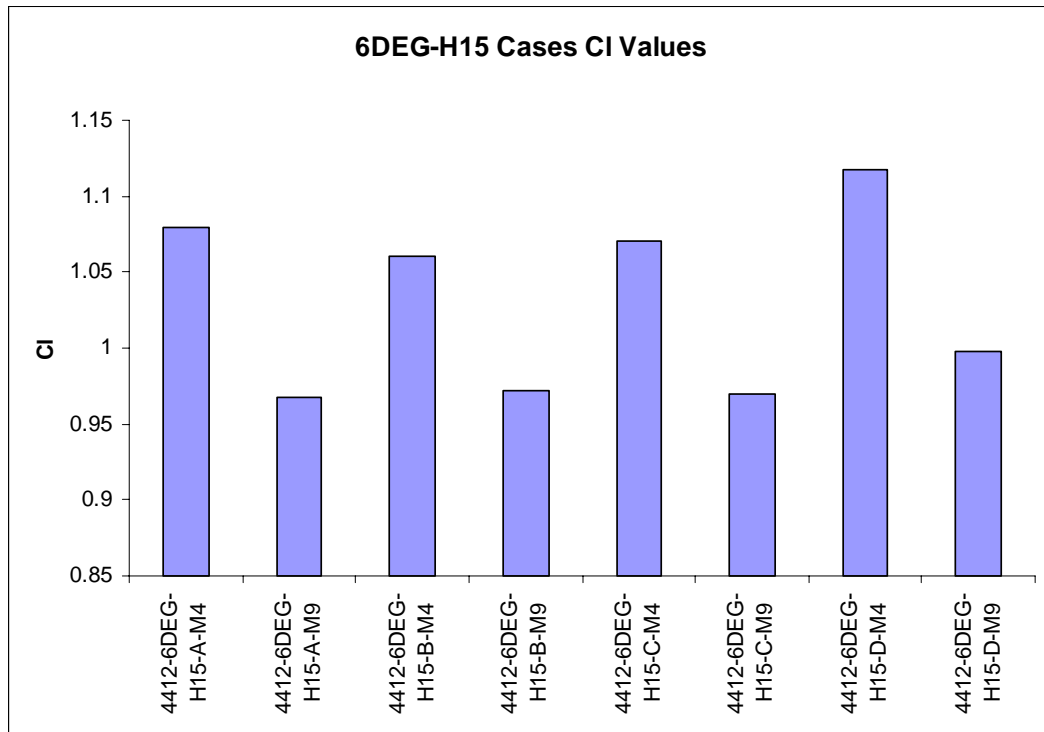


Figure 74: 6deg-h15 cases C_L Values ($h/c = 0.13$)

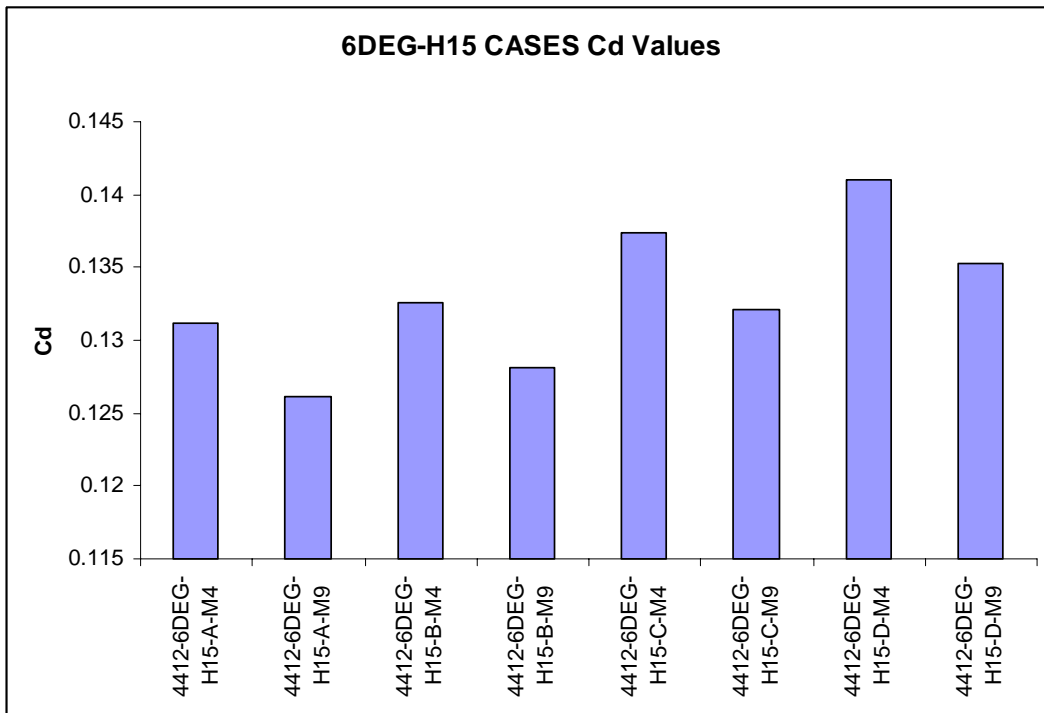


Figure 75: 6deg-h15 cases C_D Values ($h/c = 0.13$)

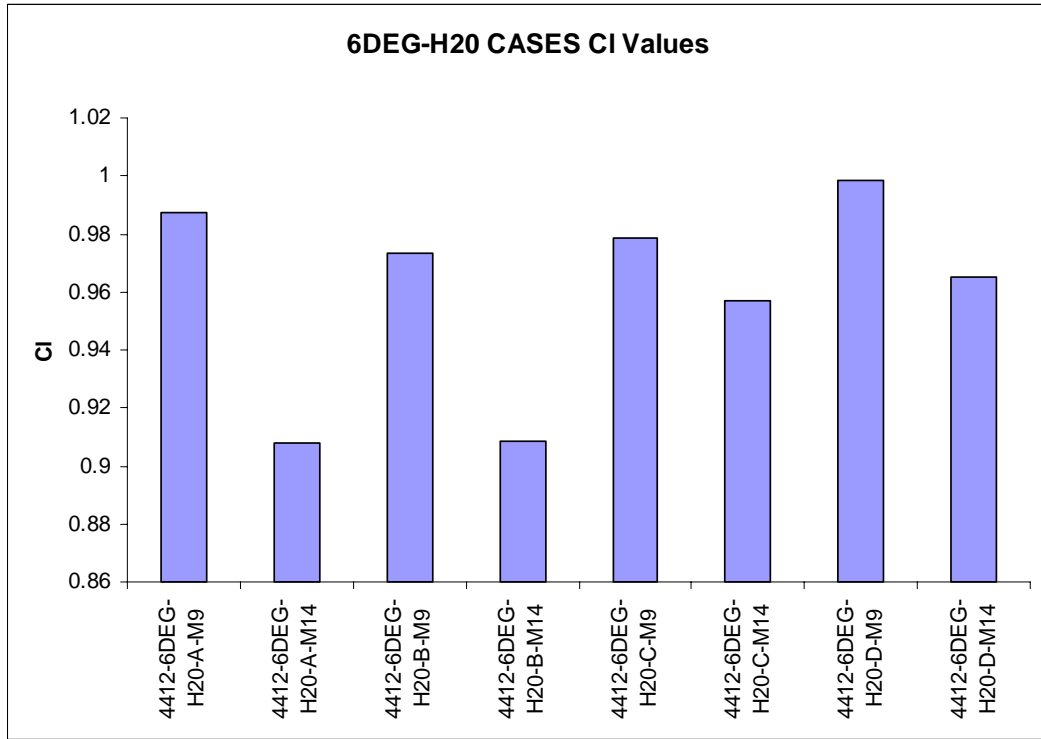


Figure 76: 6deg-h20 cases C_L Values ($h/c = 0.20$)

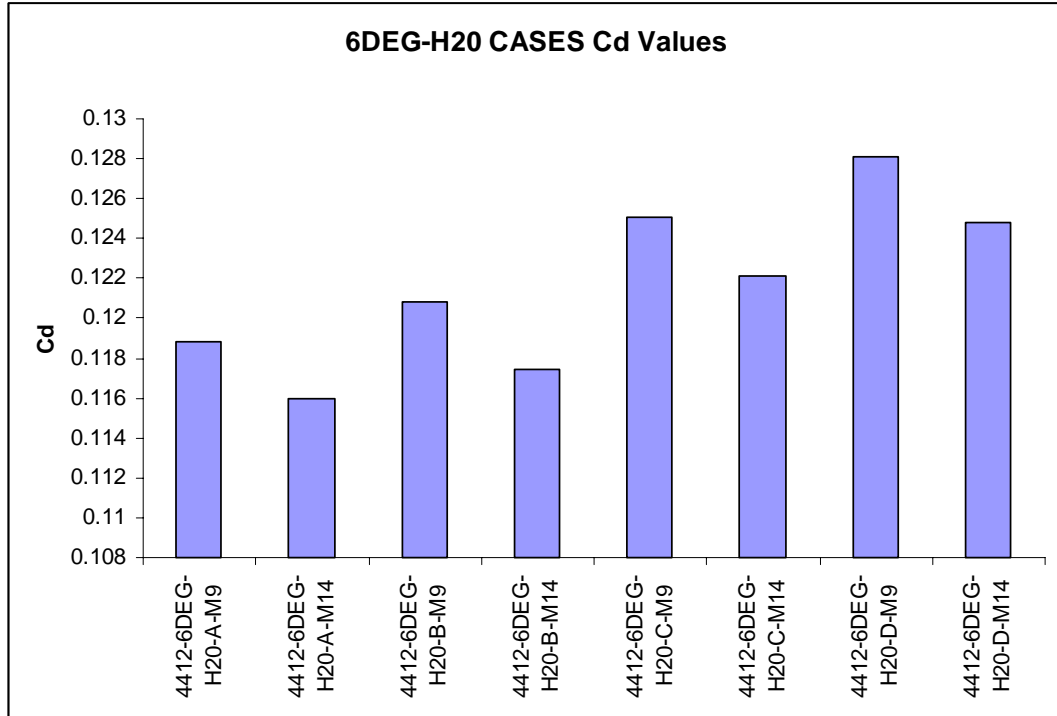


Figure 77: 6deg-h20 cases C_D Values ($h/c = 0.20$)

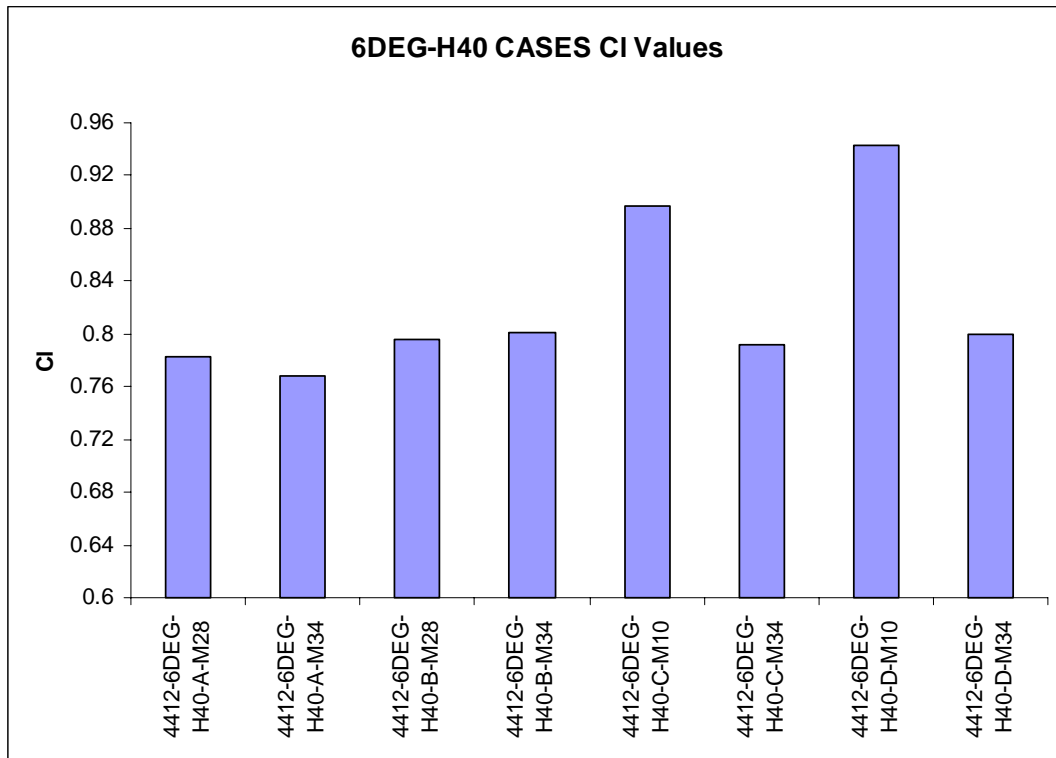


Figure 78: 6deg-h40 cases C_L Values ($h/c = 0.47$)

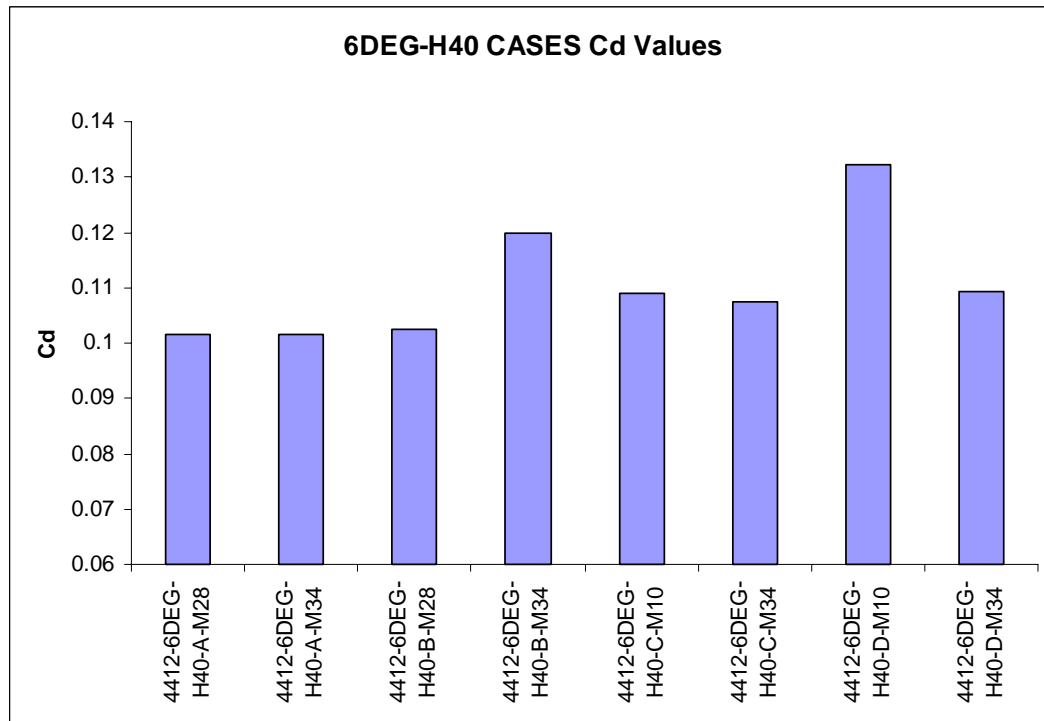


Figure 79: 6deg-h40 cases C_D Values ($h/c = 0.47$)

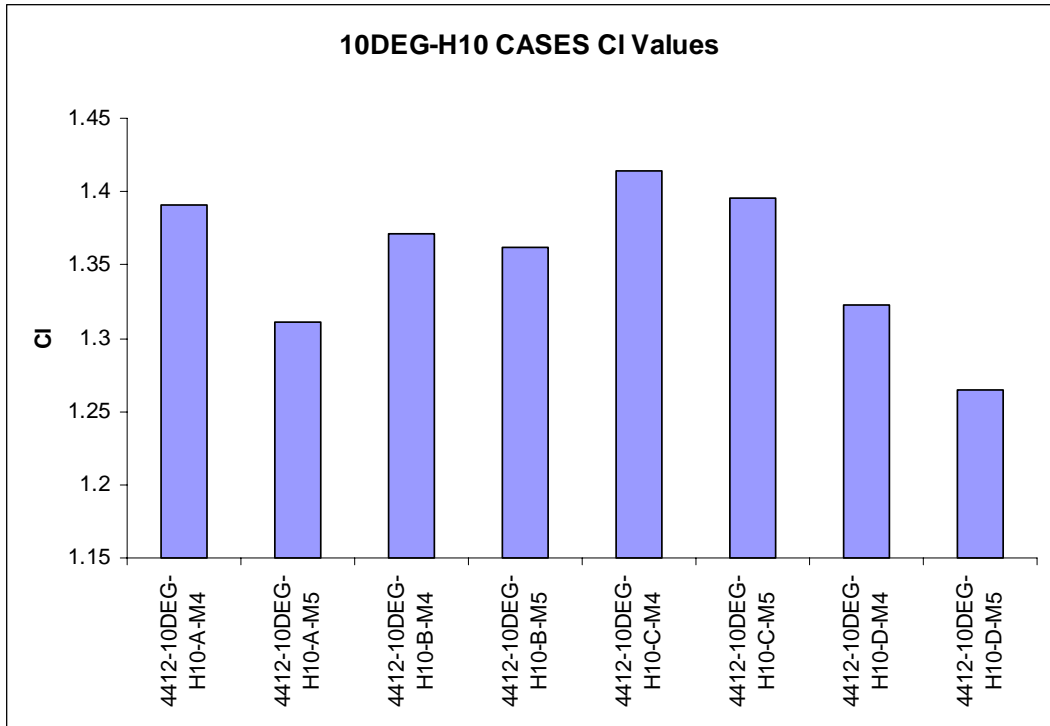


Figure 80: 10deg-h10 cases C_L Values ($h/c = 0.08$)

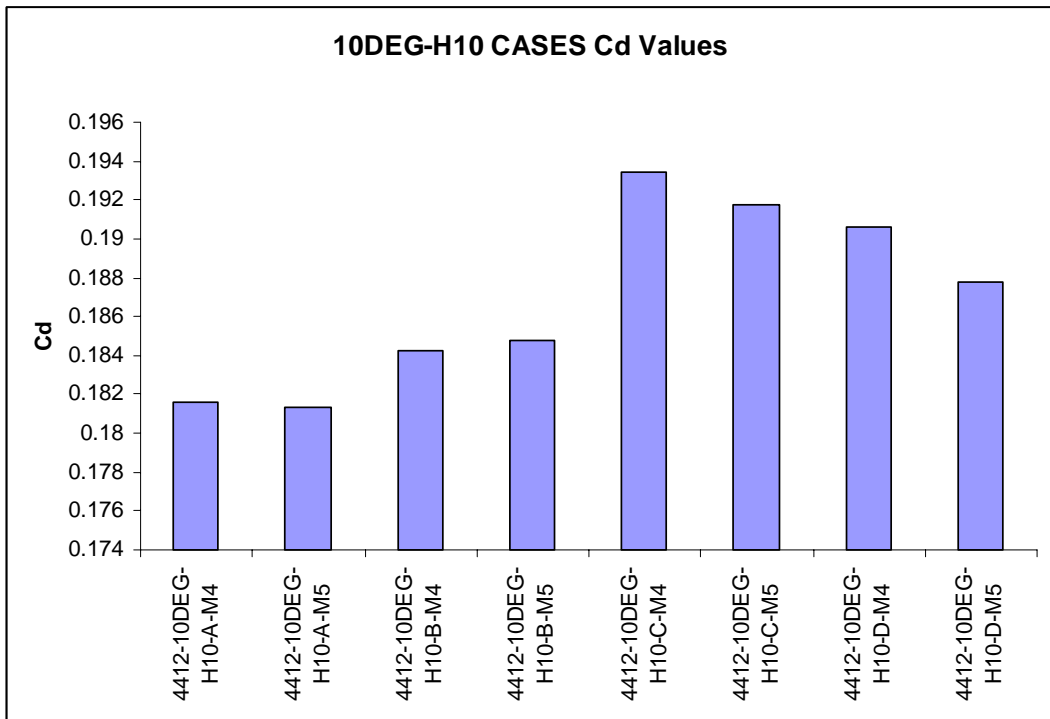


Figure 81: 10deg-h10 cases C_D Values ($h/c = 0.08$)

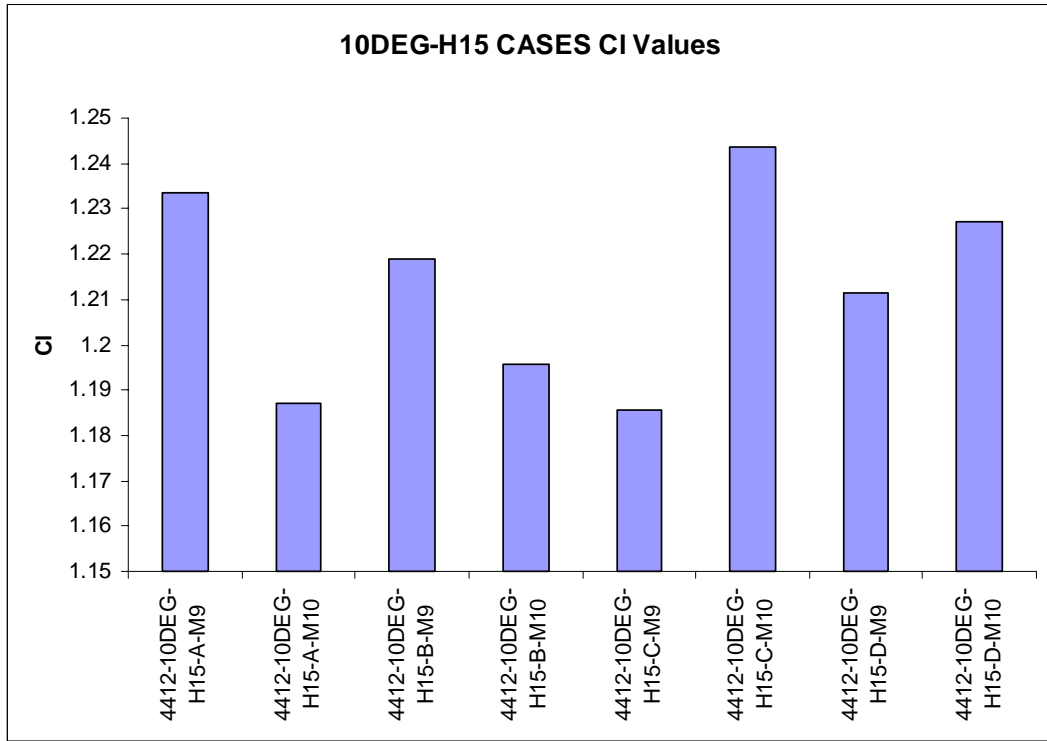


Figure 82: 10deg-h15 cases C_L Values ($h/c = 0.15$)

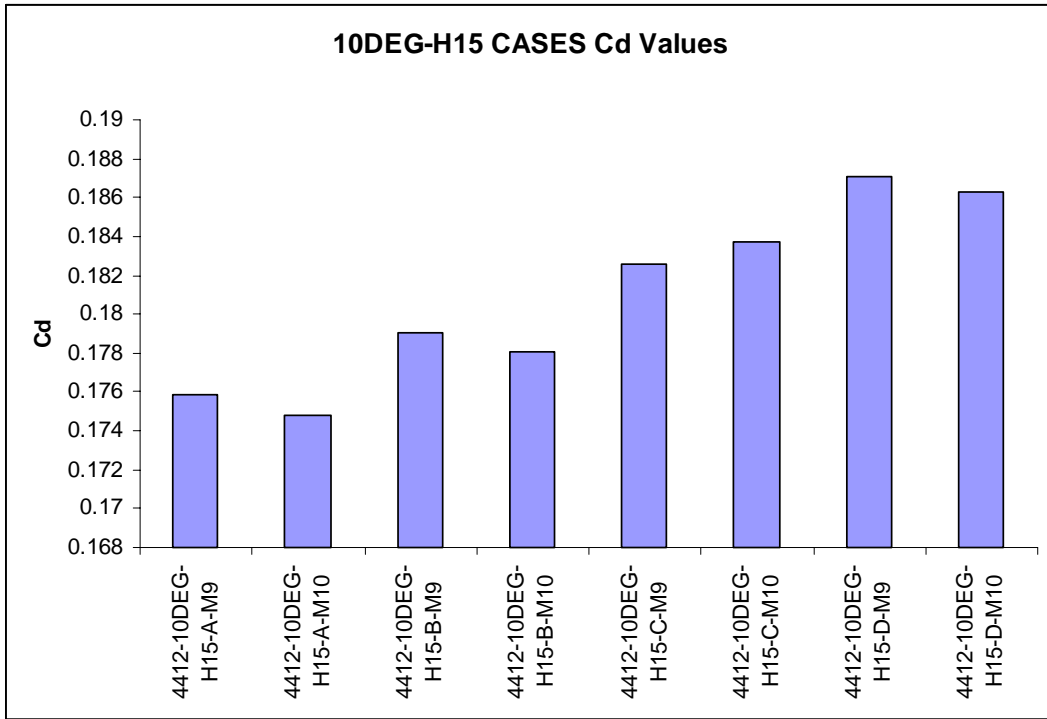


Figure 83: 10deg-h15 cases C_D Values ($h/c = 0.15$)

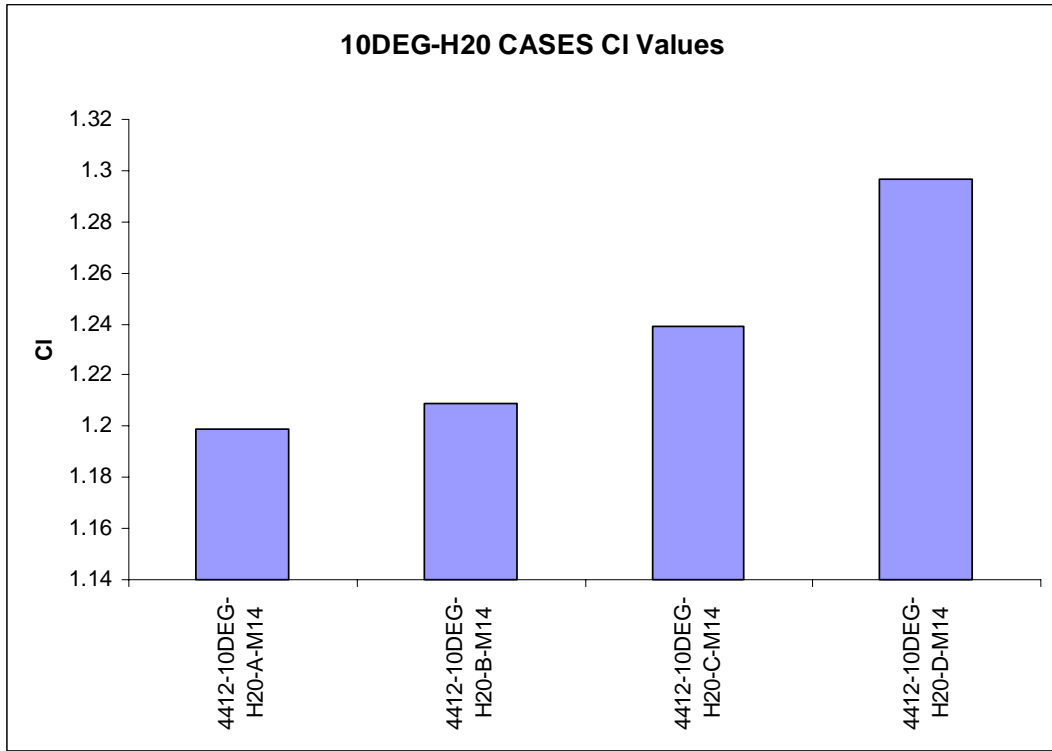


Figure 84: 10deg-h20 cases C_L Values ($h/c = 0.21$)

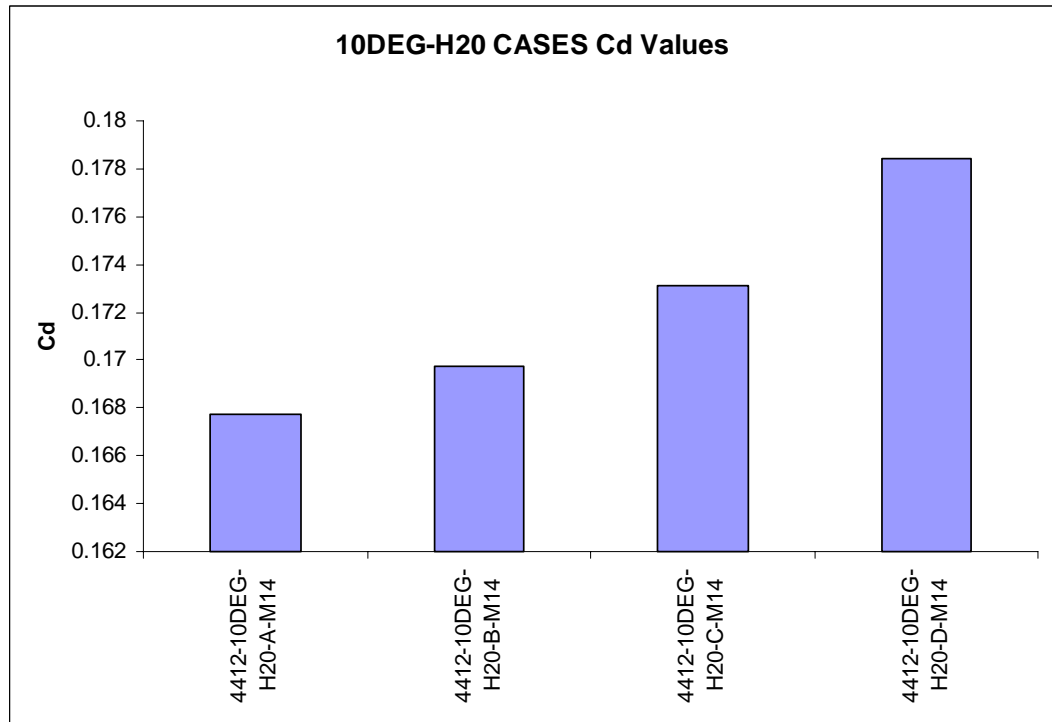


Figure 85: 10deg-h20 cases C_D Values ($h/c = 0.21$)

5.3.8 Comparison of C_L and C_D for All Test Cases

Table 4 shows the comparisons between all the cases. The maximum and minimum C_L and C_D , and the maximum L/D ratio are presented. As expected, the maximum C_L values are achieved when the inverted wing is closer to the ground, and with the higher incidence. The C_D values are much higher with the higher incidence. The maximum C_L/C_D (L/D) ratio of 8.31 was achieved with the 6deg-h20case. Note there are four points, not a line, for the 10deg-h20 cases.

Table 5 shows the corresponding heights for each point in figures 86 to 88. Figure 86 shows the C_L values in comparison to each case. The C_L values are not corrected for boundary disturbances. The trends between the high and low endplate configurations for the 6deg cases are very apparent, with the lower endplate cases having higher C_L values than the higher endplate cases. The 10deg cases show higher C_L values across the range of cases, as would be expected. What was not expected was the drop in C_L for endplates C and D in the h10 cases. This will be discussed later.

Figure 87 shows the C_D values in comparison to each case. Distinct differences in C_D values are present between the 6deg and 10deg cases. The general trend for all the configurations, except 10deg-h10, is that the C_D values increases with endplate size, indicating that the frictional drag force has a significant influence the overall drag. The addition of uncorrected boundary and wake forces will be discussed later. For the 6deg-h40 cases with endplate D, the effect of the endplate height can be seen as this difference is the most extreme.

Figure 88 shows the C_L/C_D (L/D) values in comparison to each case. For each set of cases, the general trend is higher L/D ratios for cases with smaller endplates.

Appendix B shows all the static pressure contours on the suction surface of the wings for the test cases. The endplates are shown for clarity. The results from these will be discussed in section 6.3.2.

	Maximum C_L	Minimum C_L	Maximum C_D	Minimum C_D	Maximum C_L/C_D
6DEG-H10	1.044	0.973	0.145	0.126	7.83
6DEG-H15	1.117	0.967	0.141	0.126	8.23
6DEG-H20	0.998	0.908	0.128	0.116	8.31
6DEG-H40	0.943	0.769	0.132	0.101	7.75
10DEG-H10	1.415	1.265	0.193	0.181	7.66
10DEG-H15	1.244	1.185	0.187	0.175	7.01
10DEG-H20	1.296	1.199	0.178	0.168	7.26

Table 4: Maximum and minimum C_L , C_D and C_L/C_D values for each case set

	1	2	3	4	5	6	7	8
6DEG-H10	2	4	2	4	2	4	2	4
6DEG-H15	4	9	4	9	4	9	4	9
6DEG-H20	9	14	9	14	9	14	9	14
6DEG-H40	28	34	28	34	10	34	10	34
10DEG-H10	4	5	4	5	4	5	4	5
10DEG-H15	9	10	9	10	9	10	9	10
10DEG-H20	14	N/A	14	N/A	14	N/A	14	N/A

Table 5: Endplate configuration, height vs case number

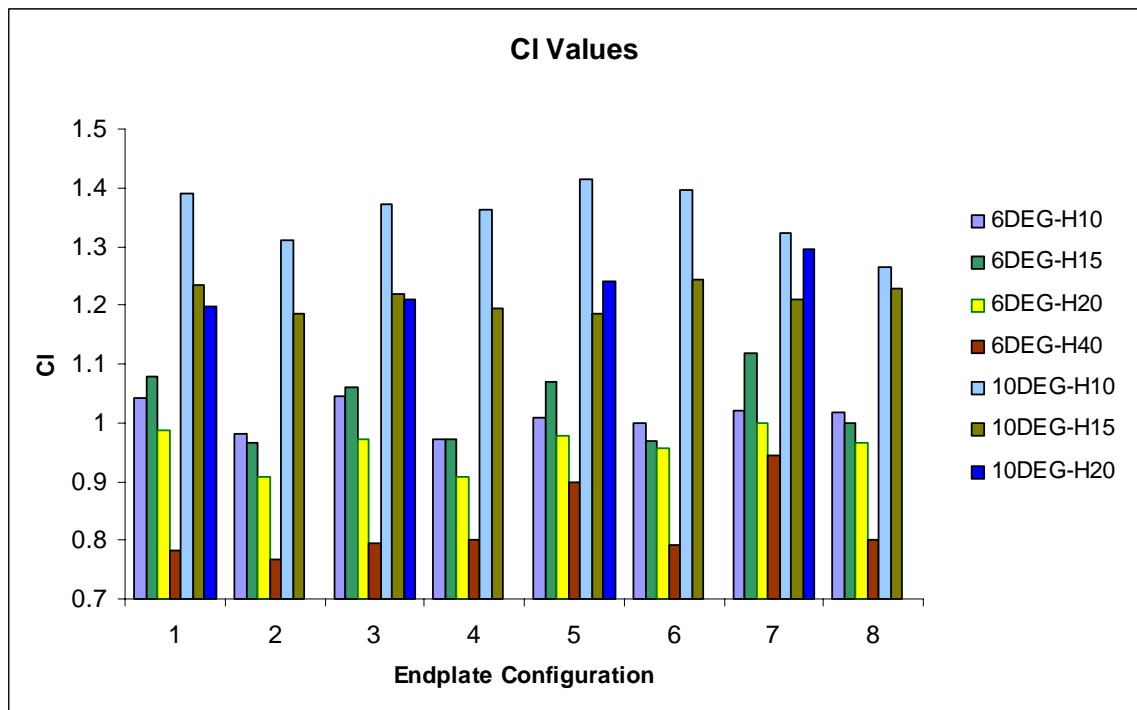


Figure 86: C_L comparison for Angle of Incidence and Height Cases

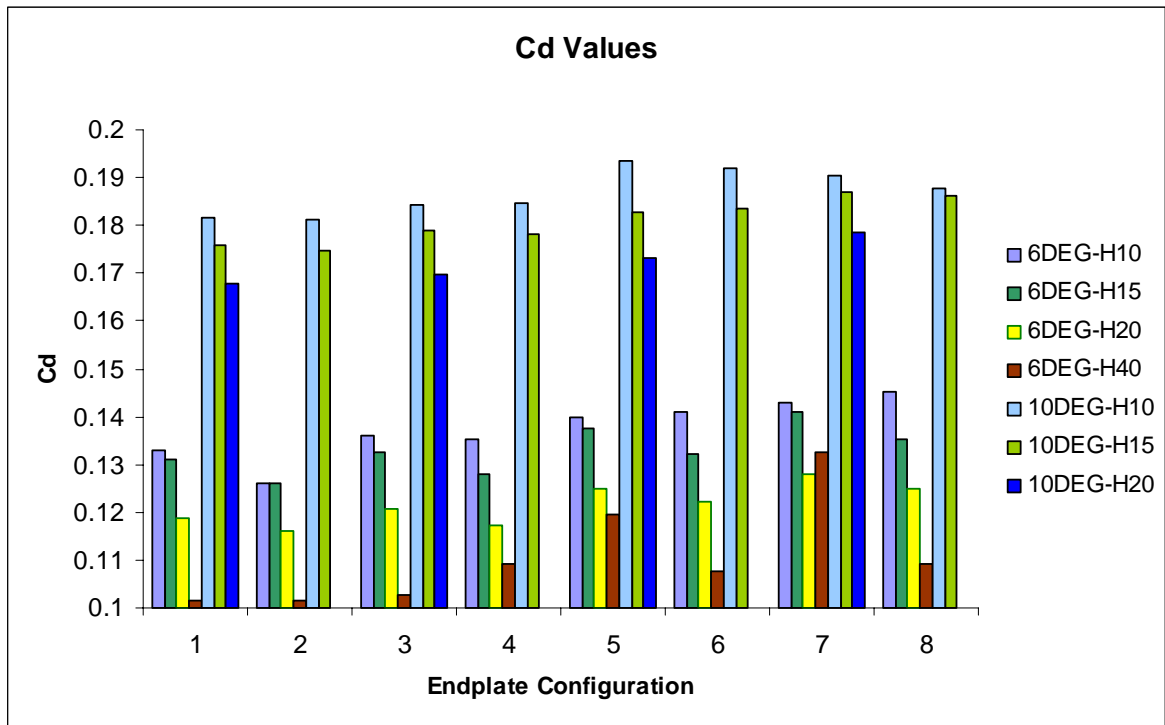


Figure 87: C_D comparison for Angle of Incidence and Height Cases

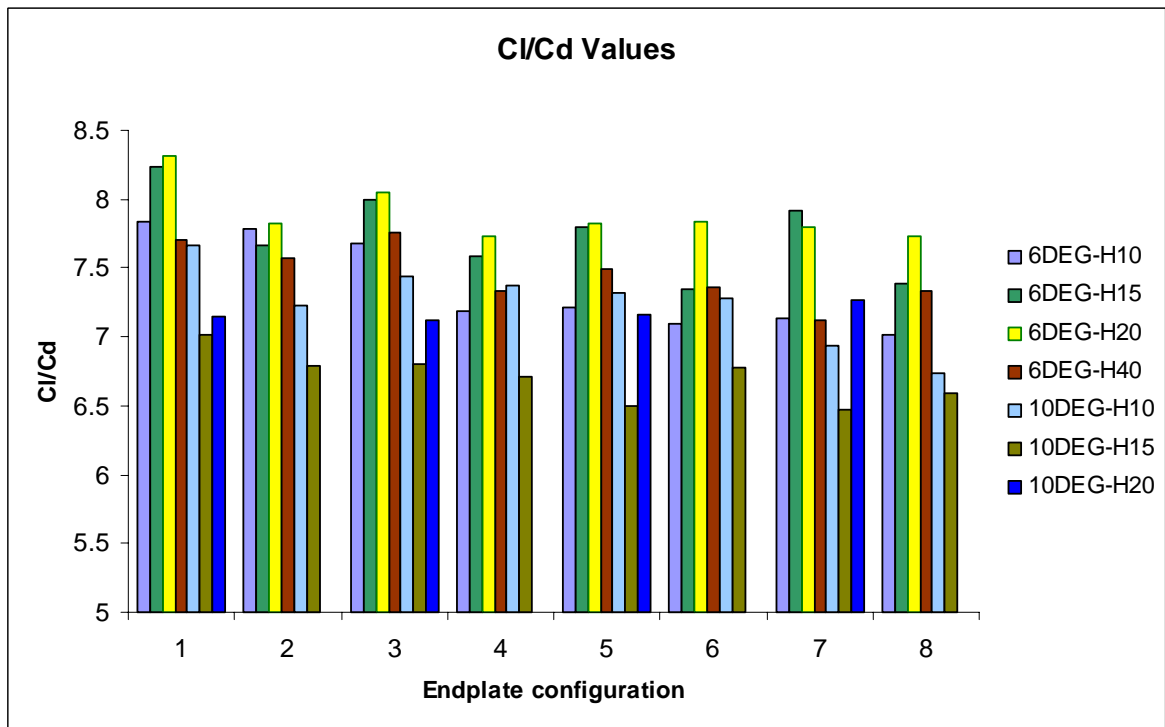


Figure 88: C_L/C_D comparison for Angle of Incidence and Height Cases

5.4 Laser Doppler Anemometry

One case was examined with LDA (laser doppler anemometry), 10deg-h20-C-m14. This case was chosen because it displayed quite a different flow field from very early observations, and further observations and analysis (flow visualisation and CFD) will be based on this case. Four planes were used to record the flow field, 0.067c, 0.267c, 1.333c and 2.667c. The data was recorded using BSA Flow software, and Tecplot 10TM software used for post processing. The LDA results were primarily vector values, and using Tecplot 10TM the vector fields were transformed into contour plots. The zero-zero coordinate corresponds to the point where the wing trailing edge joins the rear edge of the endplate, this point was chosen for its convenience when aligning the LDA traverse. The free stream velocity was set at 10ms⁻¹.

Figures 89, 91, 93 and 95 show the contour plots, figures 90, 92, 94 and 96 show the contour plots overlaid with the corresponding vector plots for distances of 0.067c, 0.267c, 1.333c and 2.667c respectively. Ideally a very small grid (1mm x 1mm) would be chosen, but due to time constraints (each point needed 30 seconds acquisition time plus traverse movement time, a fine 1mm x 1mm grid needed at least 6 hours for an adequate plane size, plus any other issues throughout the system), the following grid sizes were used for each plane, again, time was limited and no mesh sensitivity studies undertaken, the finest mesh size for each plane with given time constraints was applied:

- 2mm x 2mm grid for 0.067c plane
- 1.5mm x 1.5mm grid for 0.267c plane
- 3mm x 3mm grid for 1.333c plane
- 3mm x 3mm grid for 2.667c plane

In figure 89 the lower and upper vortices are clearly visible, the wake generated behind the wing is visible also, this region has velocities as low as 4.5ms⁻¹. There is a region of very high velocity to the right of the lower vortex, which would correspond to a very low pressure region. The upper vortex can be seen to the left of the endplate wake, as appears in the flow visualisation. The square edges on the endplate could create the relatively large wake behind the endplate, although the thickness of the endplate is 1mm. Figure 90 shows the vector plot for the 0.067c plane. The flow pattern on the suction side

of the wing shows the air moving towards the centre, away from the endplate. The flow just above the wing wake is flowing almost horizontal towards the endplate, the air on that region is migrating towards the area of lower pressure – the suction surface side of the wing.

Figure 91 shows the velocity contour plot at $0.267c$. The wake behind the wing is larger than at $0.067c$, and it also increases in size as it moves away from the endplate. The lower vortex is clear, while the upper vortex is much smaller and associated by a small region of higher velocity than the surrounding area. Overlaying the velocity vectors, in figure 92 clearly shows the locations of the vortices. The lower vortex is strong while the upper vortex has weakened. The flow above the wing wake is following the surrounding directions at this distance behind the wing. The velocity vectors indicate that the lower vortex has moved upwards and inwards from coordinates (y, z) $(4, 18)$ to $(7, 15)$, that is, 3mm inwards and 3mm upwards. The upper vortex appears to have dropped in height, but the resolution of the $0.067c$ plane restricts any accurate measurement.

Figure 93, 94, 95 and 96 shows the contours and velocity vector plots for $1.333c$ and $2.667c$ planes. The wake has thickened and moved upwards at both $1.33c$ and $2.667c$. In figure 93 the lower vortex has moved to $(20, 10)$, corresponding to 16mm across and 8mm upwards relative to the position at $0.067c$. In figure 95 the lower vortex has moved to $(24, 2)$, corresponding to 20mm across and 16mm upwards relative to the position at $0.067c$. The remnants of the upper vortex appears to be moving vertically downwards only, again, there are insufficient data points to obtain accurate data. In figures 93 and 95 a high velocity region located near the upper vortex path, unfortunately the LDA results did not capture data more to the left. This relatively high velocity region could be part of the upper vortex but without the full picture, a good analysis cannot be made.

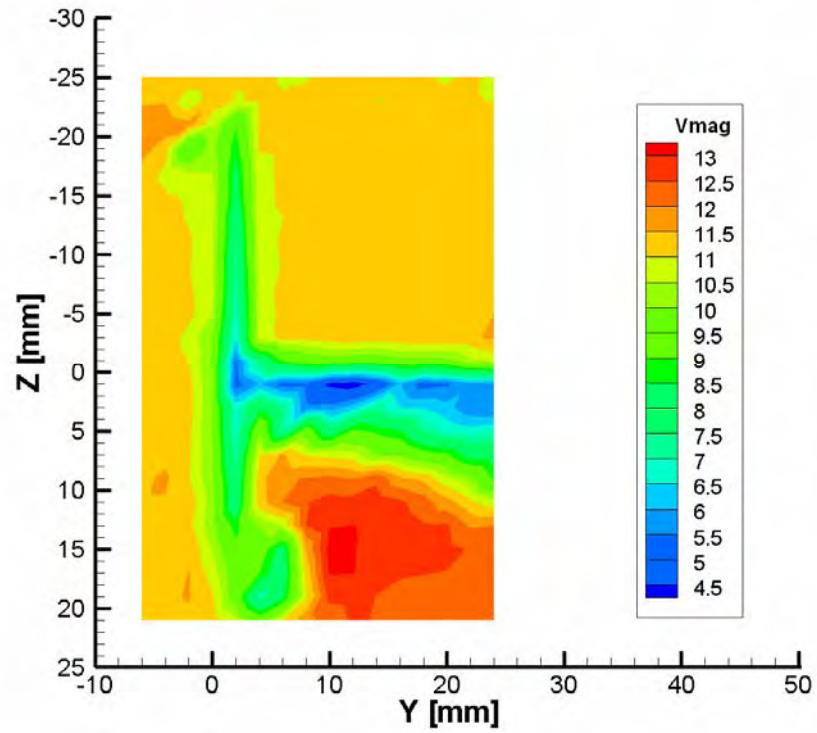


Figure 89: LDA velocity contours for case 10deg-h20-C-m14 at $0.067c$ (ms^{-1})

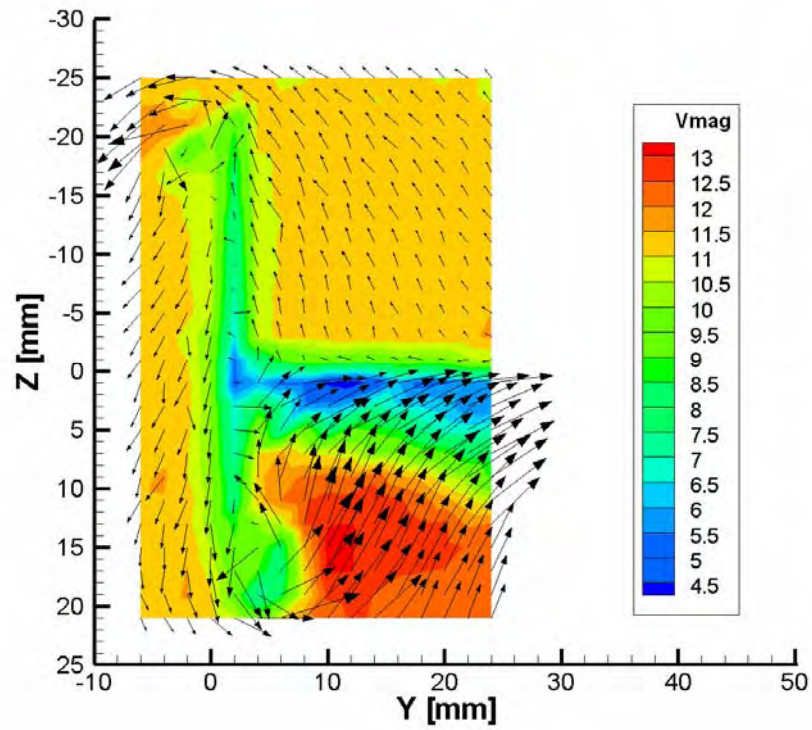


Figure 90: LDA velocity contours for case 10deg-h20-C-m14 at $0.067c$ with vectors (ms^{-1})

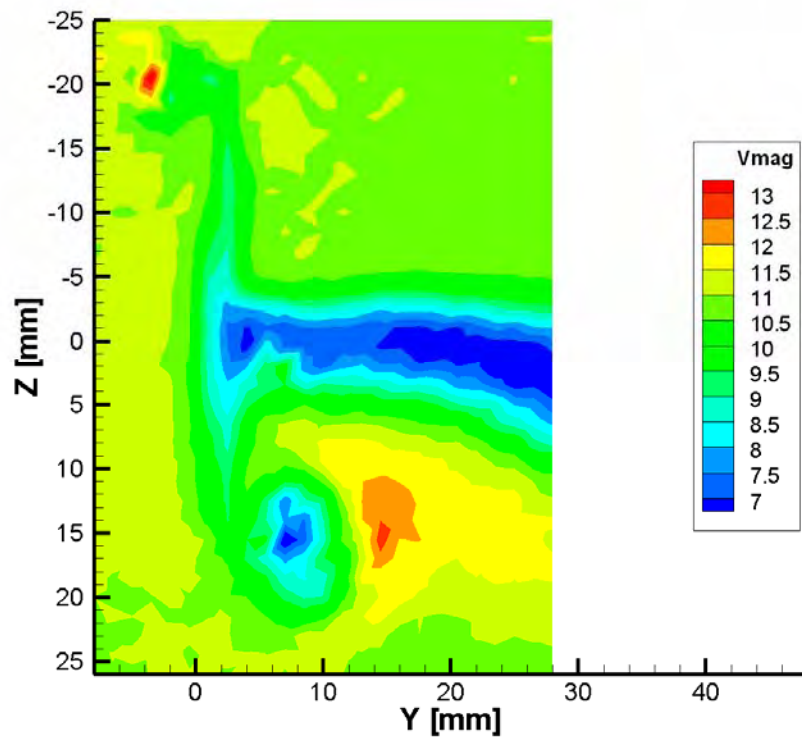


Figure 91: LDA velocity contours for case 10deg-h20-C-m14 at $0.267c$ (ms^{-1})

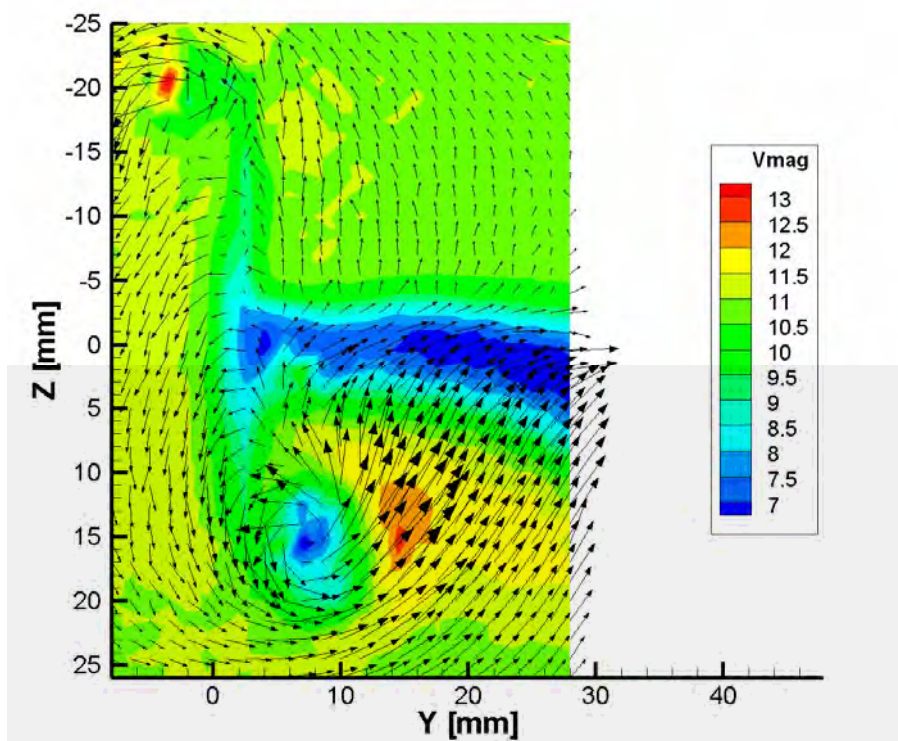


Figure 92: LDA velocity contours for case 10deg-h20-C-m14 at $0.267c$ with vectors (ms^{-1})

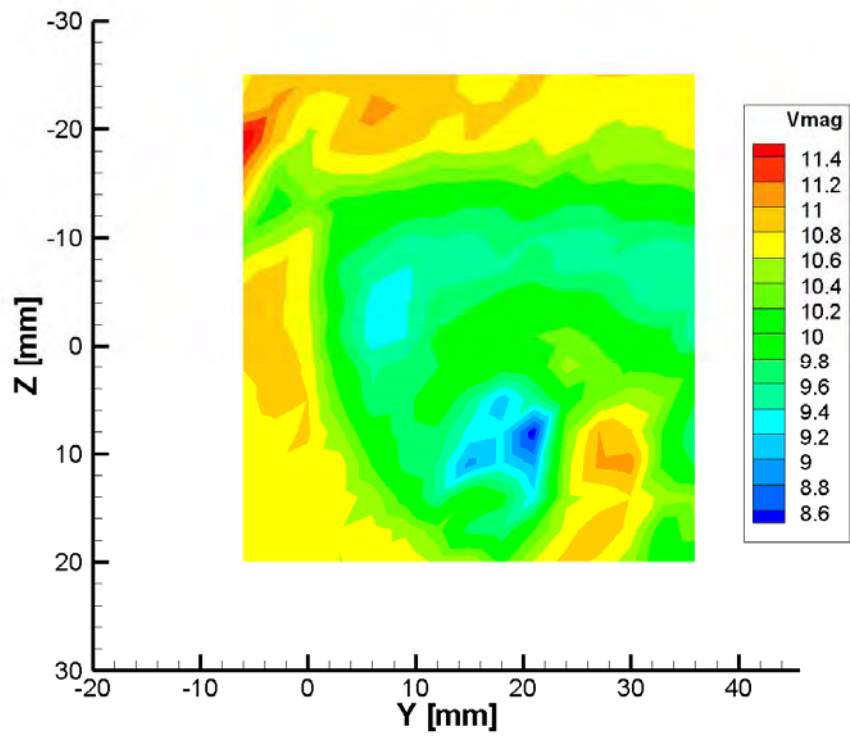


Figure 93: LDA velocity contours for case 10deg-h20-C-m14 at 1.333c (ms^{-1})

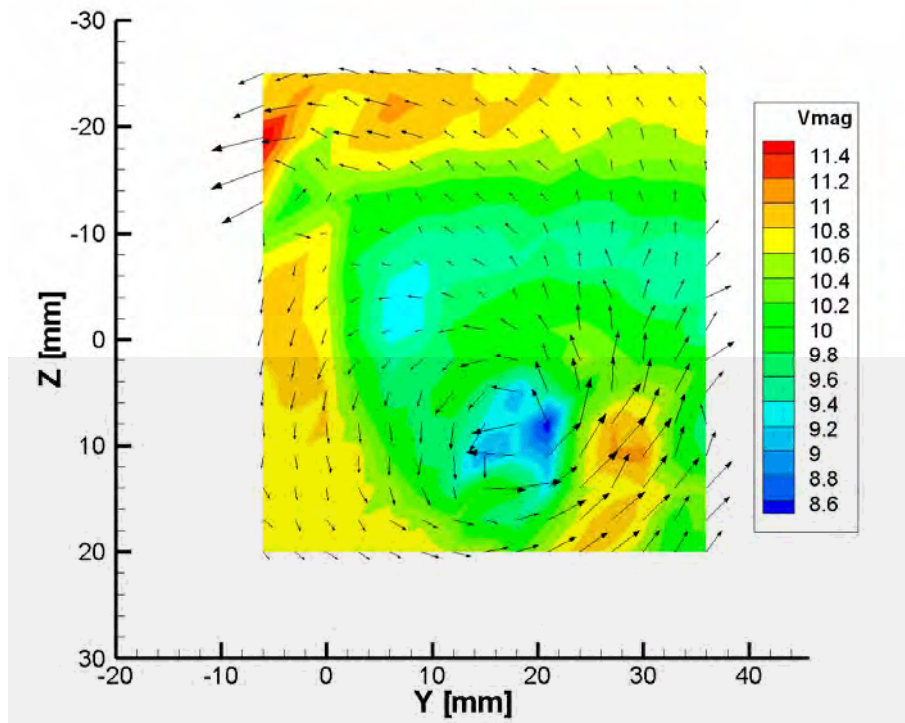


Figure 94: LDA velocity contours for case 10deg-h20-C-m14 at 1.333c with vectors (ms^{-1})

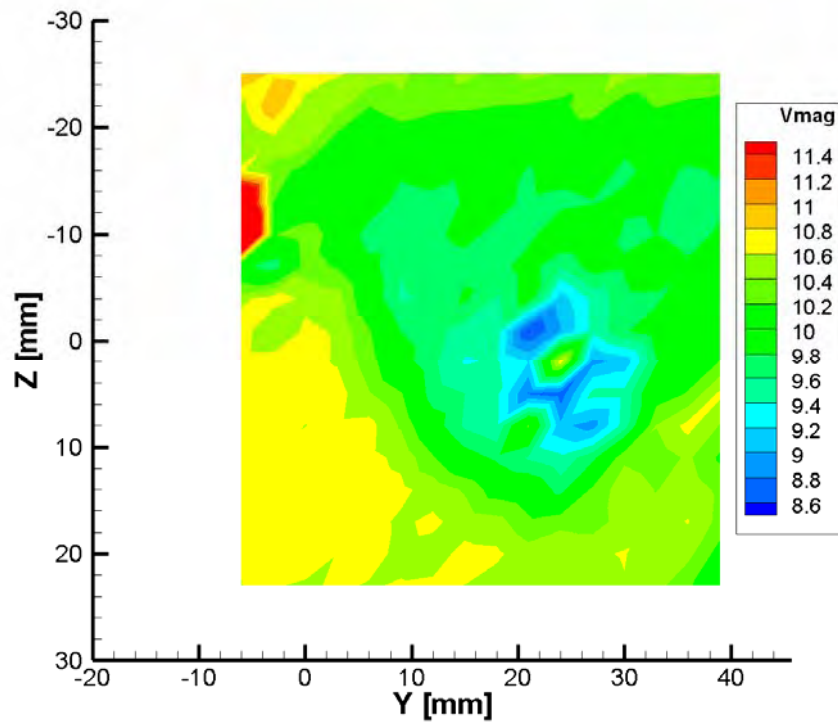


Figure 95: LDA velocity contours for case 10deg-h20-C-m14 at 2.667c (ms^{-1})

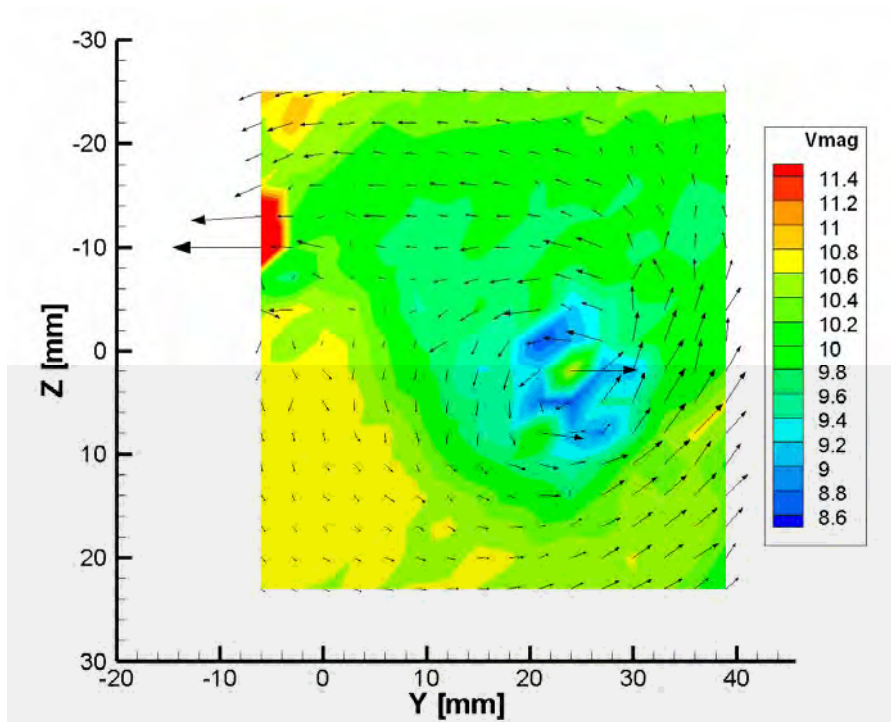


Figure 96: LDA velocity contours for case 10deg-h20-C-m14 at 2.667c with vectors (ms^{-1})

5.5 Summary

The flow visualisation results revealed a complex and interesting flow structure generated by inverted wings with endplates. Using different configurations of endplate sizes and positions, wing heights and angles of incidence, the complexities and interactions of the flow generated by the wing and endplate were recorded and examined.

The CFD analyses was used to quantify basically the effects of the different configurations, in a way that is related to the applications intended, motor sport. The C_L and C_D values extracted shows that by changing the endplate size or position, the C_L and C_D values can vary substantially.

The LDA results obtained were the only numeral results obtained from the actual wind tunnel, as force and moment measurements were unavailable. The data from the LDA experiments show detail that was not captured with the flow visualisation experiments, such as the possible intensities of the vortices.

6. DISCUSSION

6.1 Chapter Overview

This chapter discusses all the aspects of the work, from design and development of the moving ground to comparing results from flow visualisation, CFD and LDA analyses. Section 6.2 discusses the moving ground for the T1 wind tunnel, section 6.3 discusses the flow visualisation results, section 6.4 discusses the CFD results and section 6.5 discusses the LDA results. Section 6.6 compares the results obtained from the different methods and discusses any discrepancies between them.

6.2 Moving Ground

6.2.1 Material Choice for the Moving Ground

Constructing the entire moving ground structure from clear acrylic was very ambitious. An entirely clear structure would have provided unprecedented flow visualisation throughout the tunnel, but the value gained from such a feature would not be worth the effort and cost associated in making it work. The flow visualisation would have benefited comparisons to the CFD model. The main reason the entirely clear tunnel was not viable was that there was limited space between the top surface for the test section bed (belt on top of PTFE sheet) and the boundary layer duct for a tension control system which incorporated clear acrylic.

The lack of belt track control in the original design meant that each time a belt adjustment was made, the moving ground was disassembled – adjusted – reassembled, taking approximately 20 minutes each time. As expected, this process quickly lost its novelty value as many adjustments were needed to set the belt running straight. The multiple disassembly and reassembly of the moving ground caused the degradation of the threaded holes in the acrylic and the eventual fracture of one of the side walls. This was repaired but extra care was needed during the adjustment process.

The original belt from the first moving ground was 1mm thick insertion rubber. This material has superior flexibility, strength and resistance to elongation (creep). The join on the original belt was an overlap, approximately 5mm wide. This caused a ‘bump’ in the

flow as the belt rotated. From this observation the new belt needed to have a smooth surface.

Although the second attempt in manufacturing a belt was successful, it was not an ideal material and the construction was not durable enough for the conditions. The EPDM insertion rubber created static charge build-up problems when running for long periods of time, this was much more noticeable in the winter months when the air was cool and relatively dry. After many hours of continuous use the join showed signs of fatigue and the glue began to separate from the rubber. The operating environment was originally overlooked, as no consideration was taken in respect to the different flow visualisation fluids that were used. No data on any effects on the belt materials was available for the Dick Smith brand “Fog Juice”. Also no data was available on the effects of the vegetable oil used to seed the flow, on the belt materials.

The belt sourced by another student worked very well, but it was not the full width of the moving ground bed. A wider belt was tried but the edges curled up, along the length of the moving ground the edges of the belt were approximately 10mm off the bed. This was unacceptable as the airflow would be severely disturbed by the raised belt. The slightly narrower belt was reinstalled.

6.2.2 Moving Ground Drive System

The original drive system consisted of a brave person holding an angle grinder connected to the shaft of the drive roller. The next step of the moving ground drive development was to remove the brave person, as this was clearly an occupational health and safety issue. The angle grinder remained as it had the variable speed control and the maximum speed to run the belt at 15ms^{-1} , the highest free stream velocity. The angle grinder was suitable for the original moving ground as it was shorter in length (600mm) than the new moving ground (1000mm). The extra length required a more powerful motor as there was a higher friction force due to the longer bed length. It was noted too that the belt speed was not constant, the speed fluctuated as the motor did not have sufficient torque and control to adjust to the frictional forces. This fluctuation on belt speed would be detrimental to the wind tunnel free stream velocity profile. No analysis was attempted on the effects of the belt speed fluctuations on the velocity profile. The coupling system from

the angle grinder to the drive roller shaft was regularly changed, as the flexible nylon reinforced PVC tube degraded after approximately 10 hours continuous use. The drive system was eventually replaced with a controlled 3 phase motor, belt driven. This motor provided the necessary torque and control to run the belt.

Running the moving ground continuously brought many problems to light, the static charge build-up, drifting belt, insufficient belt tension and heat generation. The static charge build-up after running for long periods of time was so great that the friction force created between the belt and acrylic bed overcame the power supplied by the angle grinder, and the belt literally stopped. The two solutions to this issue was to use a PTFE (Trade name - Teflon) bed to reduce the friction, and to use a more powerful motor. The static charge build up was also a result of a mainly acrylic structure for the moving ground. The copper wires did help remove static charge build-up, but it was not fool-proof as the wires would break after a few hours continuous use. The updated moving ground base structure was constructed from aluminium, therefore allowing static charge to be 'earthed'.

To stop the belt drifting crown was added to the pulleys, this did not fix the problem completely as correct pulley alignment could not be guaranteed using fixed bearings. Insufficient belt tension caused the belt to rise at the rear of the test section, just before the belt wrapped around the drive roller. This would have adverse effects of the flow as it would partially block the wind tunnel.

All the reliability issues were gradually fixed over the course of the degree, the moving ground is now powered by a three phase motor, and the belt speed is synchronised to the free stream velocity in the test section. The belt in use was slightly narrower than the test section, but did remain flat. Belt tracking issues were resolved and the moving ground reliability was high enough to gain confidence in continual and multiple hour use.

6.2.3 Possible Causes of Error in the Moving Ground

The first possible cause of error in the moving ground was the width of the belt , as it did not extend the full width of the wind tunnel test section. Irregularities in the air flow near the corner of the wind tunnel ground and wall could have affected the flow as the wing was in close proximity to this region.

The second possible cause of error in the moving ground was the small gap between the leading edge and the belt. Although this gap was very small, 1 – 2mm, turbulent air from beneath the moving ground system could have been introduced into the free stream, thereby altering the velocity profile near the moving ground.

6.3 Flow Visualisation

6.3.1 Flow Visualisation Technique

The flow visualisation results obtained provide a large amount of detail on the flow patterns generated by inverted wings with endplates in ground effect conditions. Several attempts at obtaining results were tried before a reliable method was established. A film camera was originally considered, but quickly dismissed as soon as it was realised how many shots were required to capture a ‘good’ image.

The original attempts used an older smoke machine. Unfortunately this fog machine was not able to generate enough smoke for a period of time required to capture enough images of decent quality. The fog machine and liquid used was a Dick Smith brand machine and ‘Fog Juice’. This was the most reliable (and most readily available in case of failure) and generated enough smoke to capture clear images. The nozzle on this fog machine generated a strong turbulent jet of smoke, which was found to be detrimental to the flow if positioned incorrectly. If the nozzle pointed directly into the intake of the wind tunnel, the added velocity and turbulence affected the free stream velocity profile, if it was pointed too far away from the wind tunnel intake, not enough smoke would be captured resulting in a very weak smoke sheet flowing through the test section. Many trials were needed to find the optimum position of the fog machine. The length of each application of smoke also needed to be determined as too much flooded the test section with smoke and the flow patterns were covered beyond recognition.

Initially one laser was used, a 25mW Helium-Neon laser, this provided high enough power to highlight the plane of interest. After post processing the first set of results it was obvious that the wing and endplate needed to be highlighted for clarity, scale and identification purposes. Therefore a second, less powerful, laser diode was used to highlight

the endplate, and as an unexpected added bonus, it was found that if the laser was moved towards the wing slightly, the double sided tape reflected the laser light and provide a very clear presentation of the wing, as well as the endplate.

The digital camera was set to continuous shot mode and the photo was always focused on the highlighted plane, not the endplate. The photo capture technique was first to highlight the necessary plane and endplate, focus the lens where required, activate the smoke machine and press the camera trigger, taking as many photos before the camera buffer fills or smoke runs out, whichever came first. The photos were transferred to a computer for storage and post processing, and to free-up the memory card. Thousands of photos were captured and the first step was to cull the unusable images. Many decent photos remained and another benchmark was used to select the best photos, which were used in the results section. All the photos used were post processed in Gimp 2.2.8 software, the photos were converted to black and white, and the contrast improved. Many attempts were made in the post processing to suite the printing of the images on paper, as they initially looked good on the computer screen, but lacked contrast when printing. The post processing modified the images to be suitable for printing on paper.

6.3.2 Flow Visualisation Observations

The results show that the different endplates produce different flow fields. The cases at low h/c values and low angle of incidence produce a lower vortex which is much smaller than the cases with the same angle of incidence but larger h/c . This observation corresponds to a study by Zerihan [9]. Since only two heights (h10 and h20 cases) were studied with flow visualisation, the phenomenon of the lower vortex breaking down at very low h/c values was not observed. Cases with low h/c (h10 cases) were observed to have a weak lower vortex and a slightly smaller more distinct upper vortex, as the distance behind the wing and endplate increased the larger lower vortex dominated the flow field. The cases at a higher h/c (h20 cases) displayed relatively strong lower and upper vortices.

Comparing 6 degree angle of incidence cases (figures 31 to 45) to cases without endplates (figures 17 to 19), shows that the flow fields are obviously effected by the presence of the endplates, but illustrates the wide range of flows that are possible by changing the size of the endplate. Studying figures 17 to 19, shows that the single relatively

large vortex moves horizontally inwards, this observation can be made by comparing the horizontal distance from the vortex core to the laser used to highlight the endplate. Looking at figures 31 to 45, the main difference in vortex flow patterns is between cases using endplates A and B and endplate C and D. Endplates A and B produce flows that have two similar sized vortices, relatively close to each other, endplates C and D produce flows with vortices which are far apart, due to the endplate width. The lower vortex grows in apparent size, which includes the wake formed, and the upper vortex with wake remains relatively similar in size. In figure 44, the upper and lower vortices appear similar in size and strength, judging from the image.

Comparing the 10 degree angle of incidence h/c cases (figures 50 to 57) with a case without endplate (figures 46 to 49) shows as previously stated, that the addition of the endplates changes the flow patterns. Studying figures 46 to 49, the single vortex moves horizontally inwards more than the 6 degree case. Studying figures 50 to 57 shows the lower vortex is relatively weak in all cases, as is expected at the h/c of 0.08, and the upper vortex is stronger.

Studying figures 58 to 71, cases with an angle of incidence of 10 degrees, and $h/c = 0.21$, the cases with endplates A and B have slightly different flow fields near the wing and endplate, that is, at distances of $0.067c$ to $0.267c$, and at $2.667c$ the flow fields appear very similar. The flow generated by endplate A in the near field has a large lower vortex and a slightly smaller upper vortex, while the flow generated by endplate B in the near field has two very similar sized vortices. The flow in the near field generated by endplate C has a relatively much larger lower vortex and smaller upper vortex. The two vortices remain defined up to a distance of $2.667c$. The flow in the near field generated by endplate D has a large lower vortex and relatively small lower vortex, which remain distinctly separated at a distance of $2.667c$.

6.3.3 Possible Causes of Error in Flow Visualisation Experiments

The obvious errors in flow visualisation techniques are the experimental set up errors. Although utmost care was taken during experimental set ups, small discrepancies could have been present in measuring the height of the wing and endplate above the moving ground, the angle of the wing, and the orientation of the wing, that is, the endplate

parallel to the free stream flow direction, as a small angle could induce cross flow across the endplate.

Errors in the positioning of the laser sheet could have arisen, such as, the laser sheet not perpendicular to the free stream flow, or not located at the correct distance behind the wing and endplate.

Insufficient smoke in photos would not affect the results as such, but could cause the loss of an opportunity to obtain a complete set of results.

6.4 Computational Fluid Dynamics

6.4.1 Test Case Choice and Generation

The number of different test cases examined was mainly determined by the time available for solving and processing. The first step was choosing profiles that would have quite different effects on the flow, data was available from [9] [10] [11] [12] [17] [18] to help in choosing wing and endplate configurations. Originally three angles of incidence were chosen, 2°, 6° and 10° and 6 endplates, the current 4 endplates, A, B, C and D plus an endplate with a tapered top edge, with the wider vertical edge at the rear, and an endplate with radii on the top two corners.

There were ninety six different cases at first, but this was considered a little too ambitious, and the tapered endplate and curved endplate were not included in further analysis. The fifty six cases were therefore based on observations of motor sport vehicles, and simplified to suit the scope of the thesis. An emphasis was placed on testing similar wing configurations, with a variety of endplate sizes, thus the higher number of endplate variations rather than wing configurations. If more time was available a wider range of endplates and wing configurations would have been studied, but from the results shown, using a test method with relatively large iterations, could lead to missing interesting flow patterns. This was an initial study, as no studies of this kind were found in the public domain, and there were many unknowns, an attempt was made to study a wide range of cases, but with small variations between, to gain a large overall picture on the scope of flow phenomena generated by inverted wings with endplates.

Modelling the different cases was relatively simple, the problems arose during the mesh generation. The 2° cases proved very difficult to mesh using the similar style to the other cases, at an angle of incidence of 2° a larger surface was very close to the moving ground surface, and removing all the cells with high aspect ratios proved very time consuming. One cell with an aspect ratio too large would affect the solution, as the errors introduced would cause the local velocities to jump to incredible values.

6.4.2 Boundary Conditions

The boundary conditions used to model the test cases were set to match the wind tunnel test conditions. The main concern from the results was the wake generated from the wing and wall interface. Using the results to compare data from each set of cases, that is, cases with the same heights and angle of incidence, the wake generated is the same, from studying the CFD results, therefore can be excluded from case set comparisons. The effect of the wake can not be excluded from the comparisons across the range of results, as the wake generated for different angles of incidence, for example, is significantly different.

Using a solid wall for the boundary condition at the wing root produces substantially different flow patterns than if a full wing was used, or half wing with symmetry. Figures 97 to 108 shows the difference in flow patterns when the wall boundary condition at the wing root is replaced with a symmetry boundary condition. The case studied is 10deg-h20-C-m14. Looking at the velocity legend, the maximum velocities are different, the case with the stationary wall has a peak global velocity of 16.7ms^{-1} and the case using a symmetry wall condition has a peak global velocity of 18.3ms^{-1} . The global velocity is the peak velocity in the CFD domain, the peak velocity in both cases occurs beneath the suction surface of the wing, approximately $1c$ from the endplate, not shown in these figures. The convergence levels were similar for both cases.

Studying figures 97 and 98, velocity contours at $0.067c$ behind the wing and endplate, the absence of wake near the wall is the major difference in flow patterns. The lower vortex in the symmetry case is more prominent, this could be a result of the slightly higher pressure on the suction surface reducing the air flow from the free air side of the endplate, therefore reducing the roll-up of the vortex. The wake behind the endplate is stronger in the symmetry case than the wall case, this could be a result of the slightly

higher velocities in the symmetry case. Figures 99 and 100 are the velocity contours at $0.267c$ behind the wing and endplate. The wake is very strong near the wall in figure 99, and curves up, where the highest velocities were generated on the suction side of the wing. The wake in figure 100 is relatively horizontal, which would be a result of the more evenly distributed velocity profile on the suction side of the wing. Although there is no scale on these figures, the scale for each case presented is identical, the horizontal movement of the lower vortex is clear, the vortex movement in figure 100 appears greater than in figure 99, the wall case. Figures 101 to 104 show the velocity contours at $1.333c$ and $2.667c$ for the wall case and symmetry case. The wake from the wing and wall interface is present at $1.333c$ and $2.667c$. Although the vortex is not clearly defined by the unstructured mesh, it has moved horizontally more in the symmetry case than the wall case. This could be a result of the lower velocity and increased wake creating higher pressure relatively far downstream of the wing and endplate.

The paths of the upper and lower vortices are different for the wall and symmetry cases. Figures 105 and 106 shows the paths of the vortices of the wall case and symmetry case respectively, in plan view. The lower vortex in figure 105 does not move across as far as the vortex in figure 106, as discussed earlier, the distance between the upper and lower vortices is apparent in these two figures. With the symmetry case, the lower vortex path has a higher angle leading from the under side of the wing than the wall case, and straightens significantly at a distance of approximately $1c$, where as the lower vortex straightens in a larger radius.

The static pressure on the suction surface of the wing is affected by the presence of the wall as a boundary condition in the middle of the wing. A symmetrical boundary condition gives a more ideal representation of a wing in ground effect. Since the wall was real in the test cases, it was modelled in the CFD test cases. Figures 107 and 108 shows the pressure contours on the suction surface of the wing for the wall case and symmetry case respectively. The airflow is down the page, the leading edge of the wing is up. Looking near the endplate, the pressure contours shows the paths of the lower vortices, both are very similar. Studying the remainder of the static pressure contour plot on the wall case, the static pressure increases quite rapidly near the wall and towards the trailing edge of the wing. The pressure contours on the symmetry case are evenly distributed to the symmetry plane, as would be expected. The lowest pressures are -149Pa and -192Pa for the wall and

symmetry case respectively. This difference in static pressures would result in underestimated downforce in cases using a wall at the center line of the wing. It would also affect the drag force as more wake is generated.

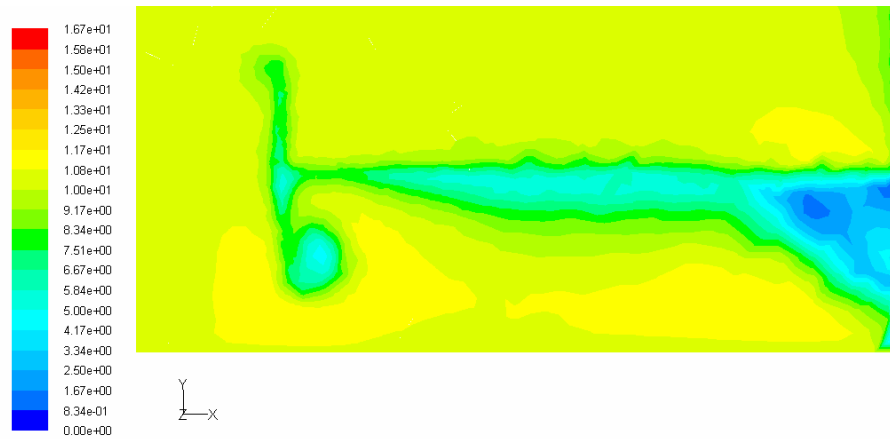


Figure 97: Velocity contours for 10deg-h20-C-m14 at 0.067c (ms^{-1})

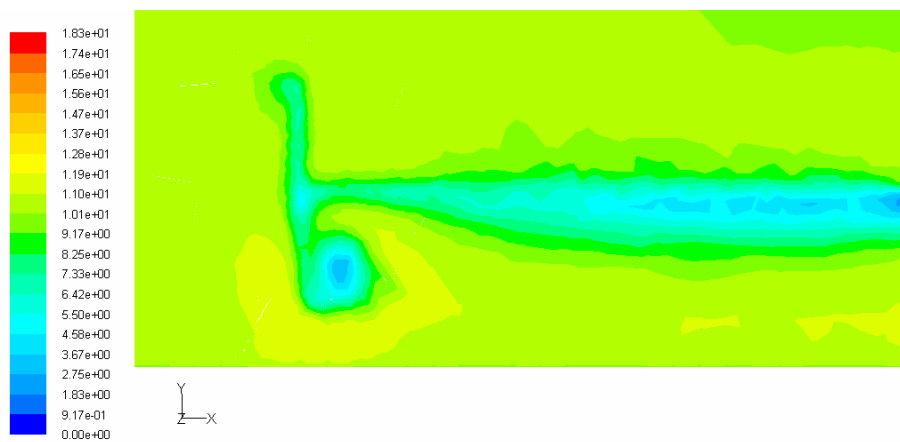


Figure 98: Velocity contours for symmetrical 10deg-h20-C-m14 at 0.067c (ms^{-1})

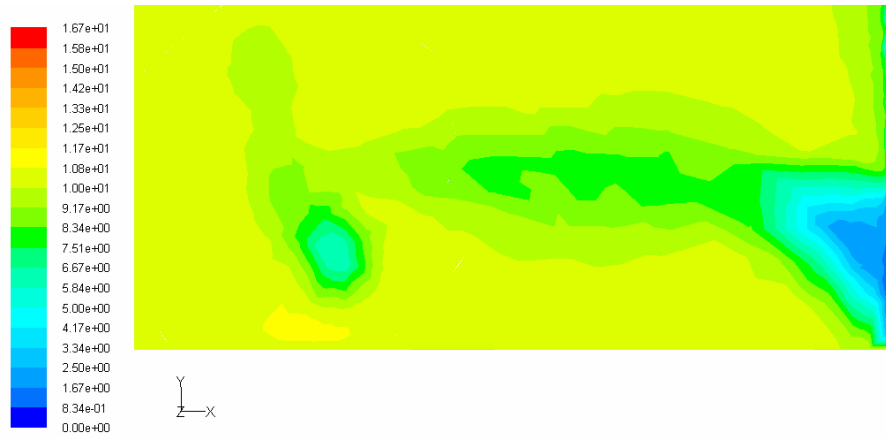


Figure 99: Velocity contours for 10deg-h20-C-m14 at $0.267c$ (ms^{-1})

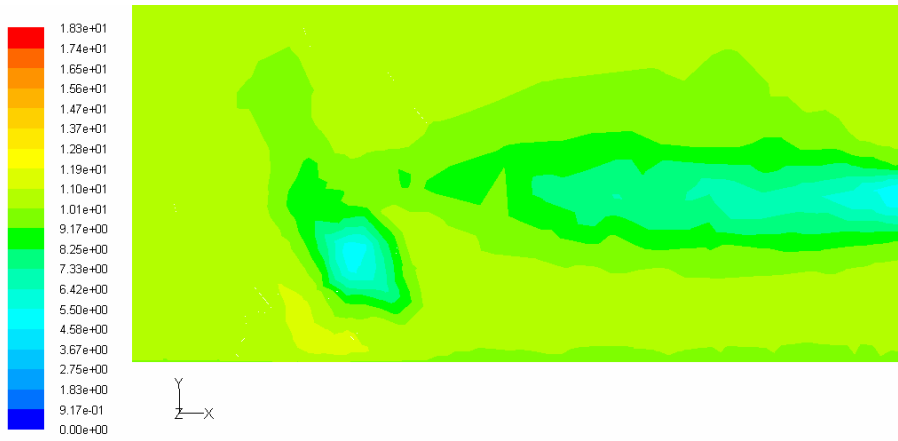


Figure 100: Velocity contours for symmetrical 10deg-h20-C-m14 at $0.267c$ (ms^{-1})

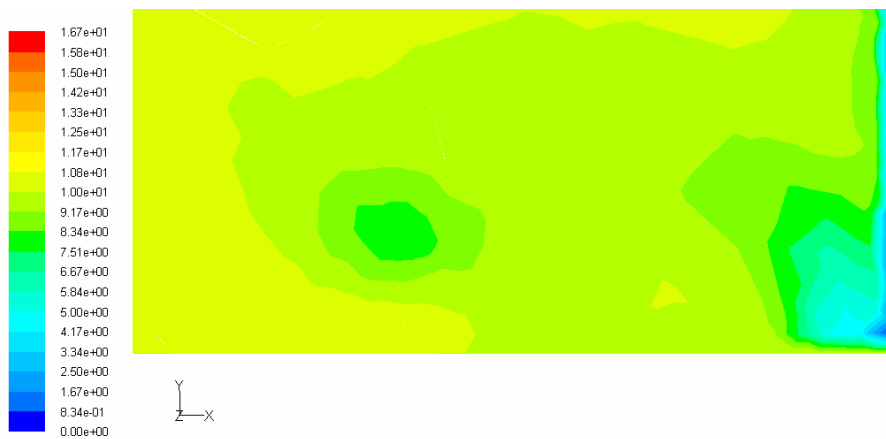


Figure 101: Velocity contours for 10deg-h20-C-m14 at $1.333c$ (ms^{-1})

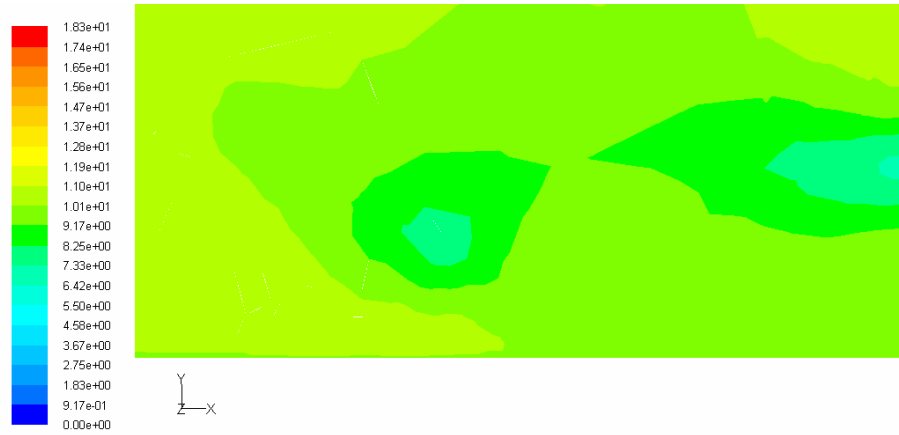


Figure 102: Velocity contours for symmetrical 10deg-h20-C-m14 at 1.333c (ms^{-1})



Figure 103: Velocity contours for 10deg-h20-C-m14 at 2.667c (ms^{-1})

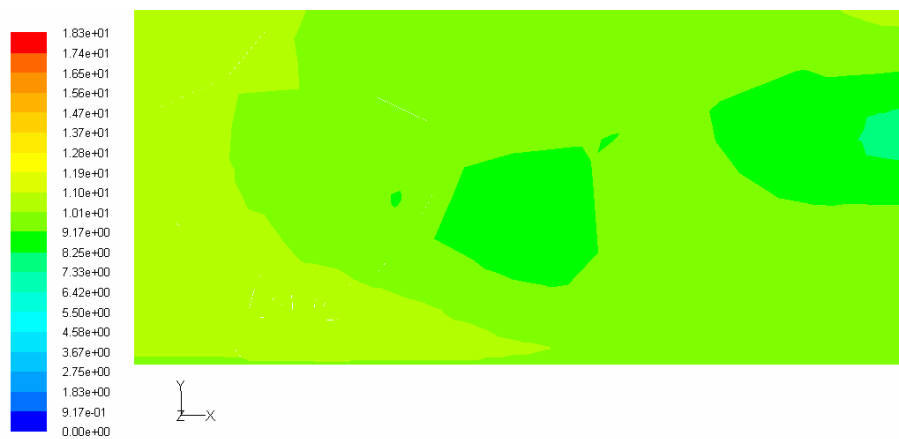


Figure 104: Velocity contours for symmetrical 10deg-h20-C-m14 at 2.667c (ms^{-1})



Figure 105: Upper and Lower Vortex path for 10deg-h20-C-m14, velocity path lines (ms^{-1})

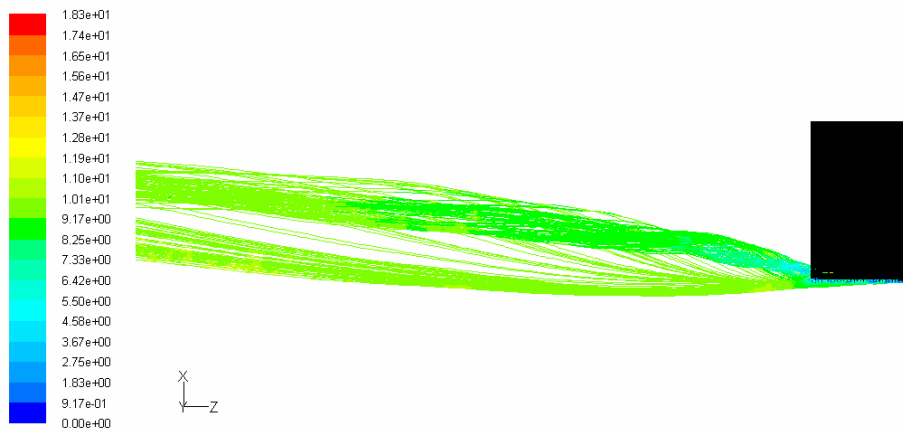


Figure 106: Upper and Lower Vortex path for symmetrical 10deg-h20-C-m14, velocity path lines (ms^{-1})

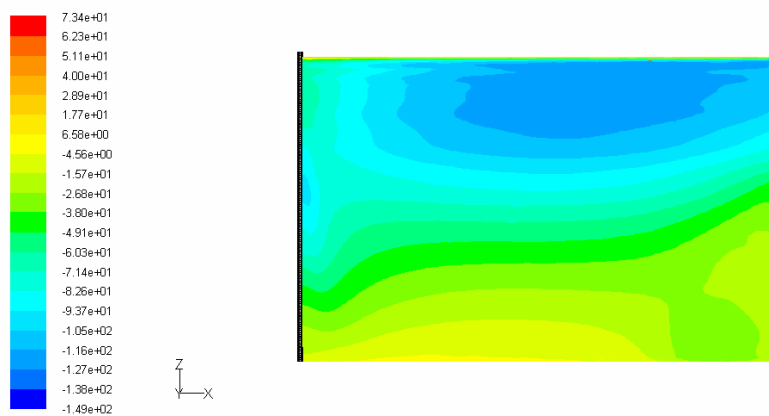


Figure 107: Suction surface static pressure contour plot for 10deg-h20-C-m14 (Pa)

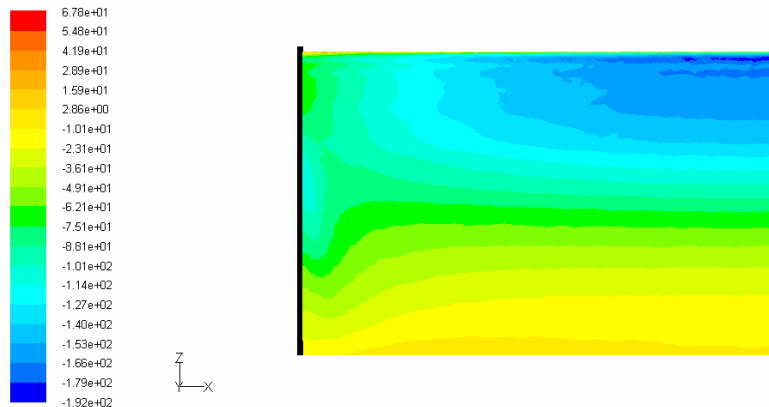


Figure 108: Suction surface static pressure contour plot for symmetrical 10deg-h20-C-m14 (Pa)

6.4.3 Static Pressures and Vortex Paths

The static pressure distribution and initial vortex path change with different endplates, and wing angle of incidence. The static pressure contours for all the CFD cases are shown in Appendix B. Figures B1 to B52 are for cases with endplates and figures B53 and B54 are for 6deg no endplate and 10deg no endplate cases respectively. All the figures in appendix B are looking at the lower surface (suction surface) of the wing which is closest to the moving ground.

Studying the cases without the endplates, figures B53 and B54, the vortex path on the suction surface is very clear. With the angle of incidence of 6° , the higher velocity created by the start of the vortex folding over is measured at approximately $0.5c$, compared to approximately $0.4c$ for the 10° case. The lowest static pressures were 93Pa and 107Pa for the 6° and 10° cases respectively.

The cases where the wing is closer to the ground, h10, h15 and h20 cases, show the wake effects from the wing/wall interface is significant, and the h40 cases, where the wing is much higher from the ground, the wake effect is less significant, see figures B25 to B32. Studying the cases with alternating endplate heights, that is, cases where the endplate position is the only different input, the path of the lower vortex wake generated from the endplate lower surface extends different distances. In figures B1 and B2, the difference in endplate height is $0.027c$, figure B1 has an endplate height of $0.027c$ and figure B2 has an

endplate height of $0.053c$. The length of the vortex wake is significantly longer, extending further down and across the wing suction surface. The case with the endplate closer to the ground has a greater negative pressure value of -222Pa , compared to -199Pa .

Looking at the first case set, $6\text{deg-h}10$ cases, figures B1 to B8, the configuration with the greatest negative pressure is with endplate B at a height of $0.027c$, with $p = -234\text{Pa}$. This corresponds with the maximum C_L value determined earlier. The vortex wake path angle are similar, but the starting positions vary slightly, the lower the endplate, the further along the wing/endplate edge the vortex wake starts.

Figures B9 to B16 show the $6\text{deg-h}15$ case set. The configuration with the greatest negative pressure is with endplate A at a height of 4mm , with $p = -220\text{Pa}$. This does not correspond to the case with the highest C_L , configuration D at $0.053c$ has the highest C_L in this data set.

Figures B17 to B24 show the $6\text{deg-h}20$ case set. The configuration with endplate A at a height of $0.12c$ has the greatest negative pressure, with $p = -130\text{Pa}$, again, this does not correspond to the case with the highest C_L , which is with endplate D and $0.12c$ height. In this case set, the effect of the wake against the wall is diminishing, as the lower pressure region has grown relative to case sets at lower heights.

Figures B25 to B32 show the $6\text{deg-h}40$ case set. The configuration with endplates A at $0.453c$ height and endplate C at $0.453c$ height have the greatest negative pressure, with $p = -114\text{Pa}$. This does not correlate to the case with the highest C_L , which is with endplate D at $0.133c$ height. The effect of the wake against the wall is almost non-existent at this height, as the pressure contours remain constant across the wing suction surface.

Figures B33 to B40 show the $10\text{deg-h}10$ case set. The configuration with endplate A at a height of $0.067c$ has the greatest negative pressure, with $p = -220\text{Pa}$. This does not correspond to the case with the highest C_L , which is with endplate C at $0.053c$. The effect of the wake against the wall has decreased the region of low pressure near the wall.

Figure B41 to B48 show the $10\text{deg-h}15$ case set. The configuration with endplate B at a height of $0.12c$ has the greatest negative pressure, with $p = -194\text{Pa}$. Endplate C at a height of $0.133c$ has the highest C_L for this case set. The effect of the wake against the wall is very clear, the low pressure region is significantly less near the wall.

Figures B49 to B52 show the 10deg-h20 case set. The configuration with endplate B at a height of $0.187c$ has the greatest negative pressure, with $p = -164\text{Pa}$. Endplate D has the highest C_L for this case set.

Comparing cases with 6° angle of incidence and 10° angle of incidence, the pressure distribution appears more spread over the suction surface for the 6° cases, the pressure distribution appears more concentrated towards the leading edge with the 10° cases.

In summary of the pressure distributions and vortex wake paths, the greatest negative pressure does not always indicate which case gave the best (highest) C_L coefficient. It does indicate that the particular case has the region of highest velocity. The position of the vortex path origin is effected by the size and position of the endplate, but does not necessarily correspond to an increase or decrease in C_L and C_D . The cases with 10° angle of incidence produced higher C_L and C_D coefficients than the cases at 6° angle of incidence. The position and size of the endplate does have an effect on the C_L and C_D values.

6.4.4 Possible Causes for Error in the Computational Fluid Dynamics Results

The first area of improvement for the CFD analysis would be to use a symmetry boundary condition instead of the solid wall. Although this would not represent the wind tunnel test section, it would remove the errors and irregularities generated by the wall boundary layer and wake. Although the vortex paths will be different if using a symmetry boundary, the general near field path would be similar, the path far from the wing trailing edge ($> 2c$) would deviate. This probably would not be a problem, as in automotive use another object or feature will certainly be within $2c$ distance from the trailing edge of the front wing. From [18] modelling cases very close to the ground requires a viscous model for more accurate results as the viscous forces are dominant in these conditions. The inviscid model is acceptable for cases with a medium to high h/c values, approximately $h/c > 0.4$.

All the CFD simulations used the Standard RNG $k-\varepsilon$ turbulence model with enhanced wall treatment activated. Various turbulence models were trailed (results not presented as the differences were small, and without an experimental benchmark),

including: Standard $k-\varepsilon$, Realizable $k-\varepsilon$, Standard $k-\omega$, SST (Shear Stress Transport) $k-\omega$ and the RSM (Reynolds Stress) turbulence models. Without a direct comparison to experimental work (and limitations of mesh construction) at the time of turbulence model trials, the Standard RNG $k-\varepsilon$ turbulence model was chosen as it was proven for the application with the wind tunnel work [3] [27]. No advantages were observed using the other turbulence models and without prior work or references to relate to, these turbulence models were not used. Also without any numerical data there was no means of knowing if the other turbulence models would over predict or under predict C_L , C_D and C_P coefficients. The T1 wind tunnel had very limited availability, therefore conducting any extensive experiments to help in the turbulence model choice, was not possible. The LDA system was not available until the end of the thesis, therefore experiments obtaining accurate velocities and turbulence levels were not possible. A detailed LDA analyses for turbulence model choice analysis is recommended for future work. The RSM turbulence model was not used as insufficient computing resources were available, and for other reasons stated above.

The use of an unstructured grid for the majority of the domain created a poor but indicative picture of the vortex flow fields. A structured mesh would be ideal but the time required to generate a structured grid for every case was not feasible considering the time available.

6.5 Laser Doppler Anemometry

6.5.1 Limitations of Laser Doppler Anemometry Experiments

Obtaining LDA results is time consuming, and time was limited, therefore only one case was investigated using LDA techniques. Preferably at least two cases would have been very beneficial, since the results can be used to directly compare to CFD results, and necessary corrections to the CFD simulation be made.

The LDA testing was performed to obtain the air velocity profiles at four planes behind the wing and endplate to capture the vortices. The planes were parallel to the test section inlet at distances of $0.067c$, $0.267c$, $1.333c$ and $2.667c$. These positions were determined earlier. The velocity vectors captured on each plane were converted into

contours using Tecplot 10 software, which are shown in figures 89 to 96. The larger the grid size used to capture the velocities, the less smooth the detail. In figures 93 and 95, a grid size of 3mm x 3mm was used. A finer grid would have captured much more detail in the flow, as there are traces of the upper vortex at the further distances behind the wing and endplate.

6.5.2 Possible Causes of Error in Laser Doppler Anemometry Experiments

Similar errors in LDA to flow visualisation experiments could have occurred, that is, errors in the experiment set up. Due to the time required to run LDA experiments, they were carried out over a series of non-consecutive days, and the set up was repeated for the same case a number of occasions.

Errors due to the physics of LDA and LDA system are present, but are beyond the scope of this thesis.

6.6 Comparisons and Observations

6.6.1 Experiments, Simulation and Analysis Techniques

Comparing and combining the flow visualisation, CFD and LDA results together provides a detailed analysis on the flow field generated by inverted wings in ground effect. The flow visualisation work can be used to obtain quick results and quickly determine the areas of interest in the flow. The CFD simulations can be used to investigate areas of interest which are not accessible via the wind tunnel experiments. Once confidence is obtained in the CFD simulations, these can be used to simulate many different wind tunnel cases, without the need to perform the wind tunnel tests. The LDA analysis can be used to measure the wind tunnel flow velocity and turbulence directly, and to serve as a CFD verification tool.

6.6.2 Comparing Results

Using one test case for comparisons, case 10deg-h20-C-m14, the accuracy of the CFD can be determined and investigated. Figures 109 and 110 show the LDA and CFD velocity contours at planes $0.067c$, $0.267c$, $1.333c$ and $2.667c$. The CFD results clearly show lack of detail at further distances. The upper vortex has all but disappeared in the CFD results, but in the LDA results, there are traces of it in all planes. The CFD has predicted the path of the lower vortex quite close to that of the LDA measurements, this was performed by aligning the images and measuring the distances, these are not shown. The wake from the wing is seems under predicted by the CFD simulations, as the velocities in the wake of the LDA results are generally lower than the CFD results.

Figures 111 to 113 show a comparison between flow visualisation, CFD and LDA results for case 10deg-h20-C-m14. The orientation and perspective of each picture do not exactly match, as the CFD and LDA pictures were rotated and positioned ‘free hand’, but they are very close and serve the comparison purpose well. Note that the sizes of the CFD and LDA velocity contour images are different sizes, The CFD images extend to the wing root wall, showing the boundary layer against the wall, and the LDA images show the contours of the grid envelope measured. As with figures 109 and 110, it is clear that the CFD results lack the vortex detail visible in the flow visualisation results. Examining the flow visualisation pictures in figures 111 to 113, insufficient smoke has failed to highlight all the interesting regions in the vortices. Due to the time constraints on LDA analyses, an examination of the upper vortices was not possible. Further LDA analysis is needed to determine the position and strength of the upper vortex.

Figures 114 to 117 show the velocity vector plots obtained from LDA measurements and CFD simulation. The vector plots extracted from the CFD results have vectors concentrated in certain areas, this is a result of the use of an unstructured mesh and consequent grid adaptation. Overall the CFD vector plots are reasonably close in magnitude to the LDA measurements, however there are some discrepancies. The vectors have been presented in black arrows as small coloured arrows are hard to distinguish on paper. As can be seen in figures 114 and 115 the upper vortex is under predicted. When comparing the CFD results to the flow visualisation results, this was a common discrepancy. This could be a result of using a mesh with too large cells, or insufficient adaptation in these regions.

Looking at figures 116 and 117 the vector plots are very close, but this could be that the LDA measurements were made with a relatively coarse grid size, which was close to the cell size in that region of the CFD domain. Comparing the vector plots to the flow visualisation indicates that the lower vortices and associated wake are relatively large at those distances from the wing.

6.6.3 Observations

Other observations in the flow patterns included the air flowing around the lower edge of the endplate to the outside before the maximum camber of the wing, then flowing back under the wing just after the maximum camber of the wing. No analysis was made in this area, but it was observed in several cases with the endplate lower edge near the suction surface of the wing. It was more prominent in cases with 10° angle of incidence. Figure 118 gives an example of the flow swapping sides of the endplate, the case is 4412-10deg-h10-D-m5 (the endplate and wing are not shown).

6.6.4 Scale Effects

Scale effect is a result of performing wind tunnel tests smaller (or larger) than the real life test. The test cases investigated in this thesis used a relatively small wing chord of 75mm, and low wind speed of 10ms^{-1} , with corresponding $Re = 53 \times 10^3$. Other studies [3] use a NACA4412 airfoil with a Re of 8,200,000. A full size representation of the test cases would have a chord of approximately 450mm and the free stream velocity could be assumed as 70ms^{-1} , giving $Re = 2.3 \times 10^6$.

The effect of the low Re would be the increase in boundary layer and earlier separation of the flow from the wing. No literature was found regarding effects of ground effect on low Reynolds Number flows, but it is known that the wake increases in thickness at very low h/c values [9]. Flow with relatively low Re increases the C_D values due to the increased boundary layer [25]. A trip wire can be used to fix the transition point from a laminar boundary layer to turbulent boundary layer. This technique is used to represent a 'full size' wing using a scaled model. No attempt was made to trip the flow as no measurements were possible to determine if the C_D value did in fact decrease. The C_L

value is known to decrease with low Re, therefore the C_L could be extrapolated to ‘full size’ values.

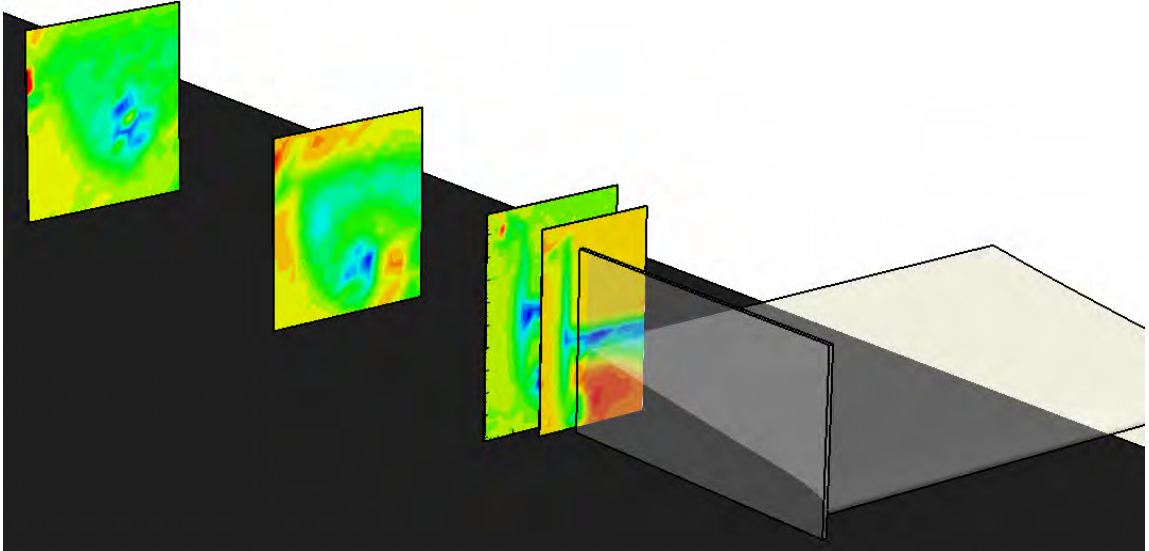


Figure 109: LDA velocity contours in 3D for 10deg-h20-C-m14

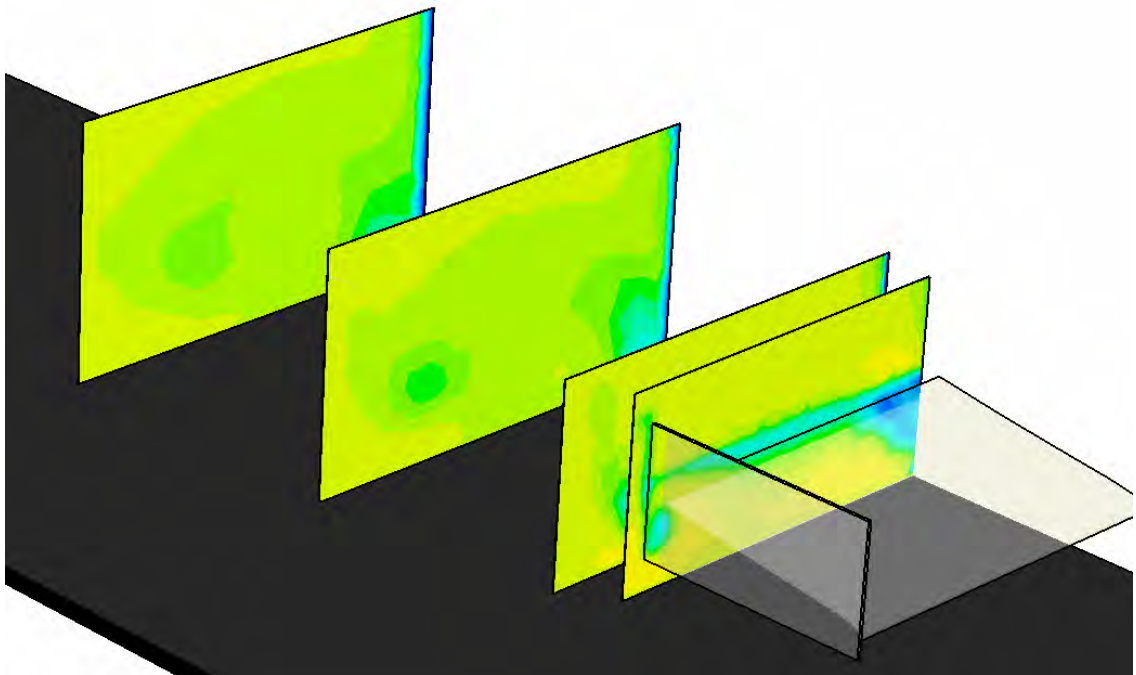
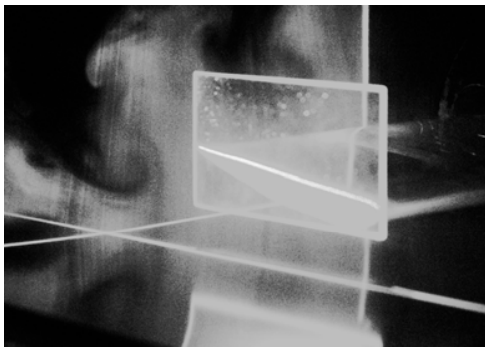
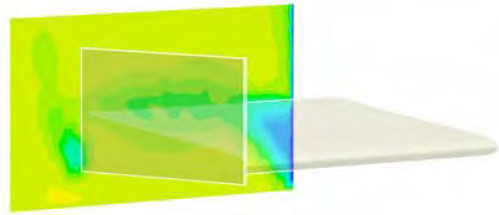


Figure 110: CFD velocity contours in 3D for 10deg-h20-C-m14



Flow visualisation

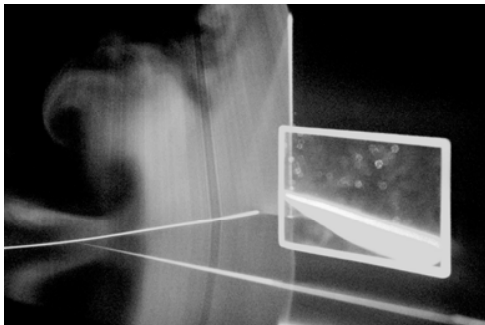


CFD



LDA

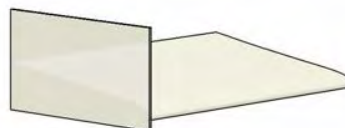
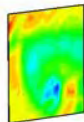
Figure 111: Comparison of 10deg-h20-C-m14 case at plane at 0.267c



Flow visualisation

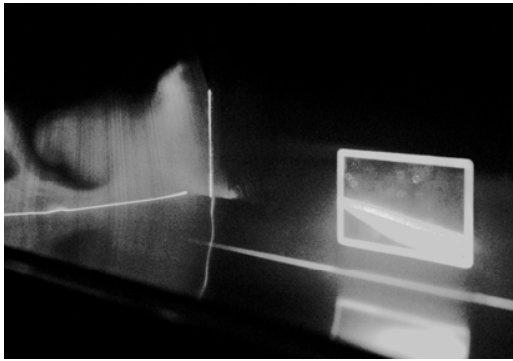


CFD

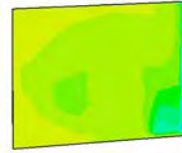


LDA

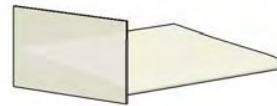
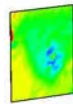
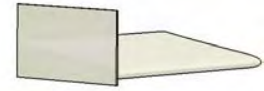
Figure 112: Comparison of 10deg-h20-C-m14 case at plane at 1.333c



Flow visualisation



CFD



LDA

Figure 113: Comparison of 10deg-h20-C-m14 case at plane at 2.667c

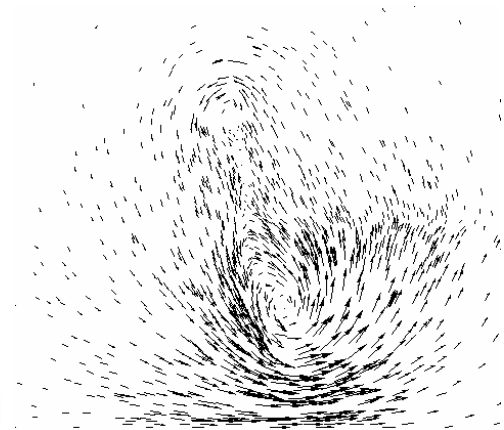
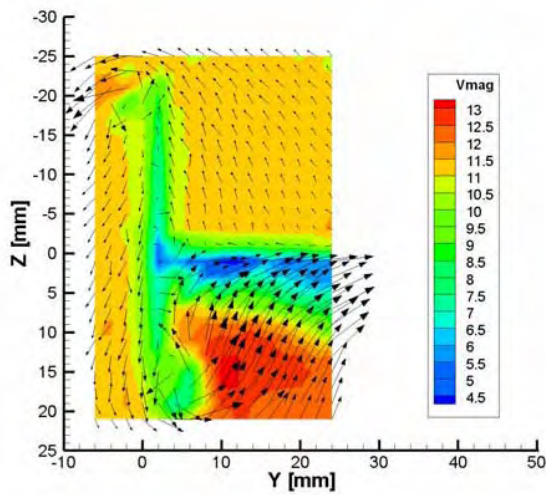


Figure 114: Velocity vector plots for LDA and CFD at 0.067c

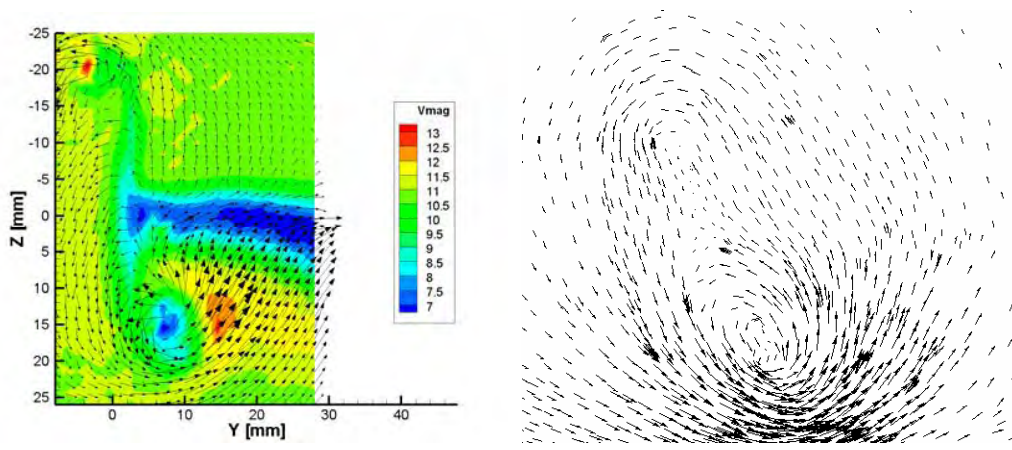


Figure 115 Velocity vector plots for LDA and CFD at 0.267c

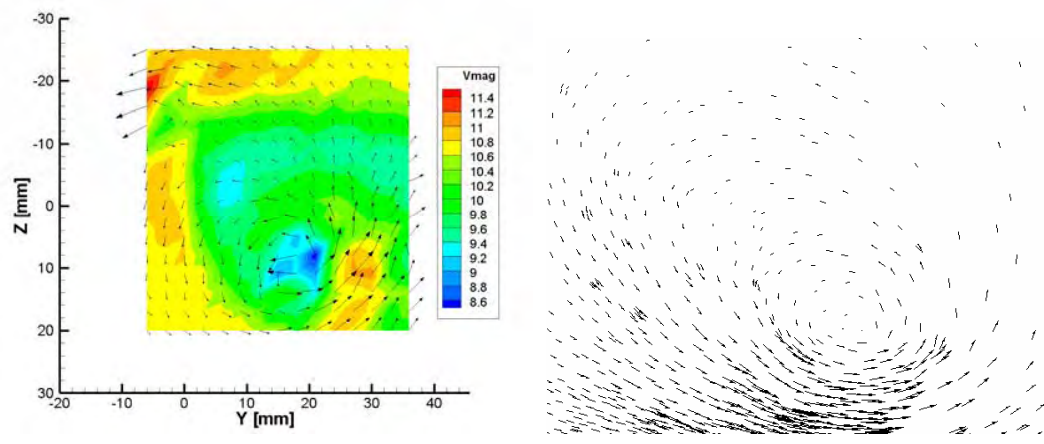


Figure 116: Velocity vector plots for LDA and CFD at 1.333c

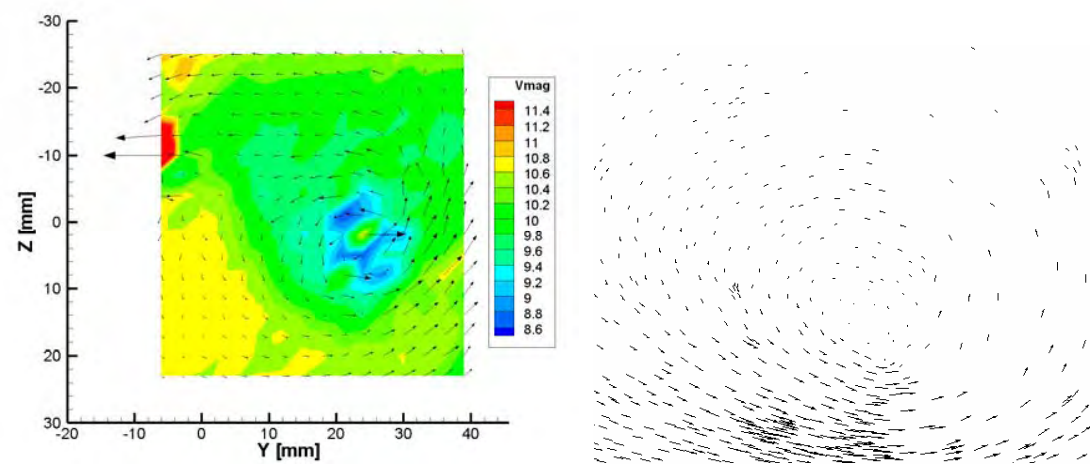
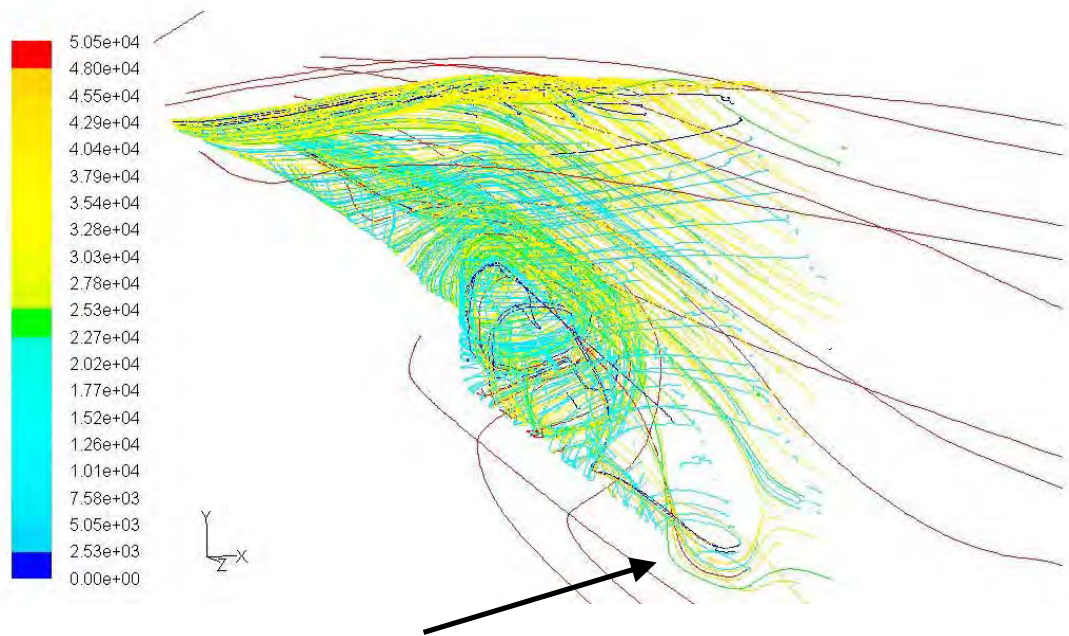


Figure 117: Velocity vector plots for LDA and CFD at 2.667c



Flow swapping sides across endplate

Figure 118: Flow swapping sides of endplate for case 4412-10deg-h10-D-m5 (units are particle ID)

7. CONCLUSION

7.1 Conclusion

Using different endplates on inverted wings in ground effect does affect the performance of the wing. The investigation found:

- Larger endplates can increase the downforce of the wing, but increase the drag force due to increased frictional drag forces.
- The height between the endplate and ground affects the downforce of the wing. A smaller height, or gap, generally increases the downforce for the same wing configuration, but can dramatically increase the downforce if the endplate 'gap' is reduced.
- Using endplates of different sizes has a smaller effect on downforce at higher ride heights, $h/c = 0.47$.
- Using an endplate dramatically changes the flow pattern from an inverted wing. An inverted wing without an endplate produces a single strong vortex. Using an endplate produces two vortices of different strengths.
- The paths of the vortices can be altered using different sized endplates.

Utilising all the available tools, such as Flow visualisation, CFD and LDA, the flow patterns generated by the different test cases could be studied by combining and comparing results. Both visual and numerical data can be obtained and analysed in great detail.

7.2 Suggestions for Future Work

Much emphasis was placed on obtaining CFD results, but there are many gaps in knowledge in regards to low Reynolds Number ground effect aerodynamics, which are the conditions of the UNSW T1 wind tunnel. Below are suggestions for future study:

- Research effects of flow visualisation fluids on belt materials.
- Capture the upper vortex and follow its path using LDA.

- Investigate the effect of the wall on the paths of the vortices.
- Investigate low Reynolds Number flow separation in ground effect.
- Use of LDA cases to compare to low Reynolds number flows in CFD analysis, using different turbulence models.
- Investigate flow patterns generated by the same geometry at various Reynolds numbers.

BIBLIOGRAPHY

Bibliography

- [1] Agathangelou, B., Gascoyne, M. Aerodynamic considerations of a Formula 1 racing car, 1998, S.A.E. paper 980399.
- [2] Katz, J. Aerodynamics of Race Cars, Annual Review of Fluid Mechanics, 2006.38:27-63.
- [3] Barber, T.J., Leonardi, E., Archer, R.D. Causes for discrepancies in ground effect analyses, The Royal Journal of the Aeronautical Society, December 2002.
- [4] Hucho, Wolf-Heinrich, Aerodynamics of Road Vehicles, 4th Edition, 1998
- [5] Wickern, G., Dietz, S., Luehrmann, L. Gradient Effects on Drag Due to Boundary-Layer Suction in Automotive Wind Tunnels, 2003 S.A.E. paper 2003-01-0655
- [6] Cooper, K.R., Rolling Road Technology for Automotive High Speed Testing, 2000 S.A.E. paper 2000-01-0353
- [7] Perkins, C. D., Hage, R. E., Airplane Performance Stability and Control, 1949
- [8] Zhang, X., Toet, W., Zerihan, J., Ground Effect Aerodynamics of Race Cars, Applied Mechanics Reviews, January 2006, Vol 59.
- [9] Zerihan, J., An Investigation into the Aerodynamics of Wings in Ground Effect, PhD dissertation 2001, University of .Southampton.
- [10] Riley, D.R., Wind-Tunnel Investigation and Analysis of the Effects of Endplates on the Aerodynamic Characteristics of an unswept Wing, NACA Technical Note 2440, 1951.
- [11] Zhang, X., Zerihan, J., Ruhrmann, A., Deviese, M., Tip Vortices Generated by a Wing in Ground Effect.
- [12] Barber, T. J., An Experimental Investigation of the Movement of Wingtip Vortices in Ground Effect, 5th Pacific Symposium on Flow Visualization and Image Processing, 2005, PSFVIP-5-202
- [13] Barber, T.J., Diasinos, S., Beves, C., Leonardi E., Ground Effect Aerodynamics, School of Mechanical and Manufacturing Engineering, University of New South Wales, 2005.

- [14] Chun, H. H., Chang, R.H., Turbulence Flow Simulation for Wings in Ground Effect with Two Ground Conditions: Fixed and Moving Ground, International Journal of Maritime Engineering, 2003.
- [15] McBeath, S., Competition Car Downforce – A Practical Handbook, 1998.
- [16] Anderson Jr, J. D., Fundamentals of Aerodynamics 2nd Edition 1991.
- [17] Thisse, E., Influence of End-plates on Tip Vortices in Ground Effect for a 2004 Formula One Front Wing, Cranfield College of Aeronautics, 2004.
- [18] Moryossef, Y., Levy, Yuval., Effect of Oscillations on Airfoils in Close Proximity to the Ground, AIAA Journal, Vol. 42, No. 9, September 2004
- [19] Makowski, F.T., Kim, S-E., Advances in External-Aero Simulation of Ground Vehicles Using the Steady RANS Equations, S.A.E. paper 2000-01-0484
- [20] Kim, T., Lee, B., Lee, D., A study on Vortex Shedding Around a Bluff Body Near the Ground, S.A.E. paper 2003-01-0652
- [21] Anderson Jr, J. D., Computational Fluid Dynamics The Basics with Applications, 1995.
- [22] Fluent Inc. Users Manual, Chapter 10. Modeling Turbulence, Fluent Inc 2003
- [23] Abbott, I. H., Von Doenhoff, A. E., Theory of Wing Sections, 1959
- [24] Ranzenbach, R., Barlow, J B., Cambered airfoil in ground effect – Wind tunnel and road conditions, AIAA Applied Aerodynamics Conference, 13th, San Diego, CA, Technical Papers. Pt. 2; US; 19-22 June 1995
- [25] Pope, A., Harper, J J., Low Speed Wind Tunnel Testing, 1966
- [26] Pope, A., Rae, W H., Low Speed Wind Tunnel Testing, 2nd Edition, 1984
- [27] Yangjun, Z., Zhenhua, L., Jinming, X., Shangrong, T., Incompressible Flow Computations Around Vehicle Bodies Using Unstructured Hybrid Grids, S.A.E. paper 2002-01-0598
- [28] Basara, B., Przulj, V., Tibaut, P., On the Calculation of External Aerodynamics: Industrial Benchmarks, S.A.E. paper 2001-01-0701

APPENDICES

Appendix A: CFD Test Case Details

CASE NAME	ANGLE	HEIGHT OF LEADING EDGE	HEIGHT 'h'	HEIGHT OF ENDPLATE	chord	h/c	Endplate AR	Wing AR	Test Case Re
	(degrees)	(mm)	(mm)	(mm)	(mm)				
4412-6DEG-H10-A-M2	6	10	5	2	75	0.07	3.75	3.1	53000
4412-6DEG-H10-A-M4	6	10	5	4	75	0.07	3.75	3.1	53000
4412-6DEG-H10-B-M2	6	10	5	2	75	0.07	5	3.1	53000
4412-6DEG-H10-B-M4	6	10	5	4	75	0.07	5	3.1	53000
4412-6DEG-H10-C-M2	6	10	5	2	75	0.07	1.88	3.1	53000
4412-6DEG-H10-C-M4	6	10	5	4	75	0.07	1.88	3.1	53000
4412-6DEG-H10-D-M2	6	10	5	2	75	0.07	2.5	3.1	53000
4412-6DEG-H10-D-M4	6	10	5	4	75	0.07	2.5	3.1	53000
4412-6DEG-H15-A-M4	6	15	10	4	75	0.13	3.75	3.1	53000
4412-6DEG-H15-A-M9	6	15	10	9	75	0.13	3.75	3.1	53000
4412-6DEG-H15-B-M4	6	15	10	4	75	0.13	5	3.1	53000
4412-6DEG-H15-B-M9	6	15	10	9	75	0.13	5	3.1	53000
4412-6DEG-H15-C-M4	6	15	10	4	75	0.13	1.88	3.1	53000
4412-6DEG-H15-C-M9	6	15	10	9	75	0.13	1.88	3.1	53000
4412-6DEG-H15-D-M4	6	15	10	4	75	0.13	2.5	3.1	53000
4412-6DEG-H15-D-M9	6	15	10	9	75	0.13	2.5	3.1	53000
4412-6DEG-H20-A-M9	6	20	15	9	75	0.20	3.75	3.1	53000
4412-6DEG-H20-A-M14	6	20	15	14	75	0.20	3.75	3.1	53000
4412-6DEG-H20-B-M9	6	20	15	9	75	0.20	5	3.1	53000
4412-6DEG-H20-B-M14	6	20	15	14	75	0.20	5	3.1	53000
4412-6DEG-H20-C-M9	6	20	15	9	75	0.20	1.88	3.1	53000
4412-6DEG-H20-C-M14	6	20	15	14	75	0.20	1.88	3.1	53000
4412-6DEG-H20-D-M9	6	20	15	9	75	0.20	2.5	3.1	53000
4412-6DEG-H20-D-M14	6	20	15	14	75	0.20	2.5	3.1	53000
4412-6DEG-H40-A-M28	6	40	35	28	75	0.47	3.75	3.1	53000
4412-6DEG-H40-A-M34	6	40	35	34	75	0.47	3.75	3.1	53000
4412-6DEG-H40-B-M28	6	40	35	28	75	0.47	5	3.1	53000
4412-6DEG-H40-B-M34	6	40	35	34	75	0.47	5	3.1	53000
4412-6DEG-H40-C-M10	6	40	35	10	75	0.47	1.88	3.1	53000
4412-6DEG-H40-C-M34	6	40	35	34	75	0.47	1.88	3.1	53000
4412-6DEG-H40-D-M10	6	40	35	10	75	0.47	2.5	3.1	53000
4412-6DEG-H40-D-M34	6	40	35	34	75	0.47	2.5	3.1	53000
4412-10DEG-H10-A-M4	10	10	6	4	75	0.08	3.75	3.1	53000
4412-10DEG-H10-A-M5	10	10	6	5	75	0.08	3.75	3.1	53000
4412-10DEG-H10-B-M4	10	10	6	4	75	0.08	5	3.1	53000
4412-10DEG-H10-B-M5	10	10	6	5	75	0.08	5	3.1	53000
4412-10DEG-H10-C-M4	10	10	6	4	75	0.08	1.88	3.1	53000
4412-10DEG-H10-C-M5	10	10	6	5	75	0.08	1.88	3.1	53000
4412-10DEG-H10-D-M4	10	10	6	4	75	0.08	2.5	3.1	53000
4412-10DEG-H10-D-M5	10	10	6	5	75	0.08	2.5	3.1	53000
4412-10DEG-H15-A-M9	10	15	11	9	75	0.15	3.75	3.1	53000
4412-10DEG-H15-A-M10	10	15	11	10	75	0.15	3.75	3.1	53000
4412-10DEG-H15-B-M9	10	15	11	9	75	0.15	5	3.1	53000
4412-10DEG-H15-B-M10	10	15	11	10	75	0.15	5	3.1	53000
4412-10DEG-H15-C-M9	10	15	11	9	75	0.15	1.88	3.1	53000
4412-10DEG-H15-C-M10	10	15	11	10	75	0.15	1.88	3.1	53000
4412-10DEG-H15-D-M9	10	15	11	9	75	0.15	2.5	3.1	53000
4412-10DEG-H15-D-M10	10	15	11	10	75	0.15	2.5	3.1	53000
4412-10DEG-H20-A-M14	10	20	16	14	75	0.21	3.75	3.1	53000
4412-10DEG-H20-B-M14	10	20	16	14	75	0.21	5	3.1	53000
4412-10DEG-H20-C-M14	10	20	16	14	75	0.21	1.88	3.1	53000
4412-10DEG-H20-D-M14	10	20	16	14	75	0.21	2.5	3.1	53000

Table A1: Test case details

CASE NAME	# OF CELLS	CONVERGENCE (x 10⁻⁶)	# OF ITERATIONS
4412-6DEG-H10-A-M2	1858855	6.7	1951
4412-6DEG-H10-A-M4	1956021	7.1	2105
4412-6DEG-H10-B-M2	1958522	10	1757
4412-6DEG-H10-B-M4	1957717	9.5	1572
4412-6DEG-H10-C-M2	2001871	9.5	1920
4412-6DEG-H10-C-M4	1943245	6.2	1937
4412-6DEG-H10-D-M2	1983997	7.6	1720
4412-6DEG-H10-D-M4	2029837	6.9	1915
4412-6DEG-H15-A-M4	2054148	6.9	2245
4412-6DEG-H15-A-M9	1954823	6.8	2693
4412-6DEG-H15-B-M4	1945051	6.8	2427
4412-6DEG-H15-B-M9	2097998	7.4	3118
4412-6DEG-H15-C-M4	2008009	6.9	1894
4412-6DEG-H15-C-M9	2106766	7.4	1835
4412-6DEG-H15-D-M4	1997905	6.9	1684
4412-6DEG-H15-D-M9	2029842	6.9	1765
4412-6DEG-H20-A-M9	2029825	10	1753
4412-6DEG-H20-A-M14	2087137	12	2517
4412-6DEG-H20-B-M9	2083143	8.6	1698
4412-6DEG-H20-B-M14	1999095	8.1	1923
4412-6DEG-H20-C-M9	1976175	8.1	2175
4412-6DEG-H20-C-M14	1926169	7.8	2048
4412-6DEG-H20-D-M9	1930739	8.1	1850
4412-6DEG-H20-D-M14	1965793	7.4	2928
4412-6DEG-H40-A-M28	1890293	12	2504
4412-6DEG-H40-A-M34	1935519	7.2	2014
4412-6DEG-H40-B-M28	1810418	6.9	1634
4412-6DEG-H40-B-M34	1772016	0.98	919
4412-6DEG-H40-C-M10	1944997	8	1736
4412-6DEG-H40-C-M34	1987060	6.4	2069
4412-6DEG-H40-D-M10	1935892	0.1	1122
4412-6DEG-H40-D-M34	1917146	8.3	1806
4412-10DEG-H10-A-M4	1941981	19	2019
4412-10DEG-H10-A-M5	2014490	24	2452
4412-10DEG-H10-B-M4	1851118	23	2447
4412-10DEG-H10-B-M5	1852518	31	2361
4412-10DEG-H10-C-M4	1832487	27	2247
4412-10DEG-H10-C-M5	1815136	36	3036
4412-10DEG-H10-D-M4	1532780	9.3	3248
4412-10DEG-H10-D-M5	1548737	7.6	1251
4412-10DEG-H15-A-M9	1503960	16	1918
4412-10DEG-H15-A-M10	1504433	16	2540
4412-10DEG-H15-B-M9	1485436	38	2354
4412-10DEG-H15-B-M10	1701320	56	2758
4412-10DEG-H15-C-M9	1697952	30	1697
4412-10DEG-H15-C-M10	1757331	30	2018

4412-10DEG-H15-D-M9	1847123	31	1536
4412-10DEG-H15-D-M10	1914474	25	2018
4412-10DEG-H20-A-M14	1665835	62	1980
4412-10DEG-H20-B-M14	1734910	63	1961
4412-10DEG-H20-C-M14	1761906	41	1643
4412-10DEG-H20-D-M14	1859876	31	1543

Table A2: CFD test case statistics

CASE NAME	Cl	Cd	Cl/Cd
4412-6DEG-H10-A-M2	1.0422	0.1330	7.8348
4412-6DEG-H10-A-M4	0.9810	0.1261	7.7805
4412-6DEG-H10-B-M2	1.0437	0.1359	7.6791
4412-6DEG-H10-B-M4	0.9731	0.1353	7.1927
4412-6DEG-H10-C-M2	1.0086	0.1398	7.2129
4412-6DEG-H10-C-M4	1.0007	0.1410	7.0992
4412-6DEG-H10-D-M2	1.0199	0.1430	7.1329
4412-6DEG-H10-D-M4	1.0187	0.1452	7.0154
4412-6DEG-H15-A-M4	1.0793	0.1311	8.2316
4412-6DEG-H15-A-M9	0.9671	0.1261	7.6675
4412-6DEG-H15-B-M4	1.0607	0.1326	7.9989
4412-6DEG-H15-B-M9	0.9716	0.1281	7.5829
4412-6DEG-H15-C-M4	1.0709	0.1374	7.7956
4412-6DEG-H15-C-M9	0.9699	0.1321	7.3421
4412-6DEG-H15-D-M4	1.1173	0.1410	7.9233
4412-6DEG-H15-D-M9	0.9982	0.1352	7.3816
4412-6DEG-H20-A-M9	0.9874	0.1188	8.3104
4412-6DEG-H20-A-M14	0.9076	0.1160	7.8233
4412-6DEG-H20-B-M9	0.9732	0.1208	8.0534
4412-6DEG-H20-B-M14	0.9083	0.1174	7.7360
4412-6DEG-H20-C-M9	0.9784	0.1251	7.8213
4412-6DEG-H20-C-M14	0.9572	0.1221	7.8381
4412-6DEG-H20-D-M9	0.9984	0.1281	7.7965
4412-6DEG-H20-D-M14	0.9651	0.1248	7.7333
4412-6DEG-H40-A-M28	0.7825	0.1016	7.7000
4412-6DEG-H40-A-M34	0.7686	0.1014	7.5763
4412-6DEG-H40-B-M28	0.7955	0.1026	7.7521
4412-6DEG-H40-B-M34	0.8006	0.1091	7.3357
4412-6DEG-H40-C-M10	0.8971	0.1197	7.4951
4412-6DEG-H40-C-M34	0.7915	0.1075	7.3646
4412-6DEG-H40-D-M10	0.9429	0.1324	7.1221
4412-6DEG-H40-D-M34	0.8001	0.1092	7.3287
4412-10DEG-H10-A-M4	1.3913	0.1816	7.6620
4412-10DEG-H10-A-M5	1.3110	0.1813	7.2308
4412-10DEG-H10-B-M4	1.3711	0.1843	7.4411
4412-10DEG-H10-B-M5	1.3622	0.1848	7.3725
4412-10DEG-H10-C-M4	1.4146	0.1934	7.3135
4412-10DEG-H10-C-M5	1.3961	0.1918	7.2794

4412-10DEG-H10-D-M4	1.3223	0.1906	6.9381
4412-10DEG-H10-D-M5	1.2649	0.1878	6.7364
4412-10DEG-H15-A-M9	1.2334	0.1759	7.0123
4412-10DEG-H15-A-M10	1.1869	0.1748	6.7891
4412-10DEG-H15-B-M9	1.2190	0.1791	6.8067
4412-10DEG-H15-B-M10	1.1958	0.1780	6.7163
4412-10DEG-H15-C-M9	1.1854	0.1826	6.4917
4412-10DEG-H15-C-M10	1.2437	0.1837	6.7706
4412-10DEG-H15-D-M9	1.2114	0.1871	6.4754
4412-10DEG-H15-D-M10	1.2273	0.1863	6.5868
4412-10DEG-H20-A-M14	1.1990	0.1677	7.1481
4412-10DEG-H20-B-M14	1.2087	0.1697	7.1212
4412-10DEG-H20-C-M14	1.2392	0.1731	7.1579
4412-10DEG-H20-D-M14	1.2963	0.1784	7.2645

Table A3: C_L , C_D and C_L/C_D values from CFD

Appendix B: Static Pressure Contours on Wing Suction Surface

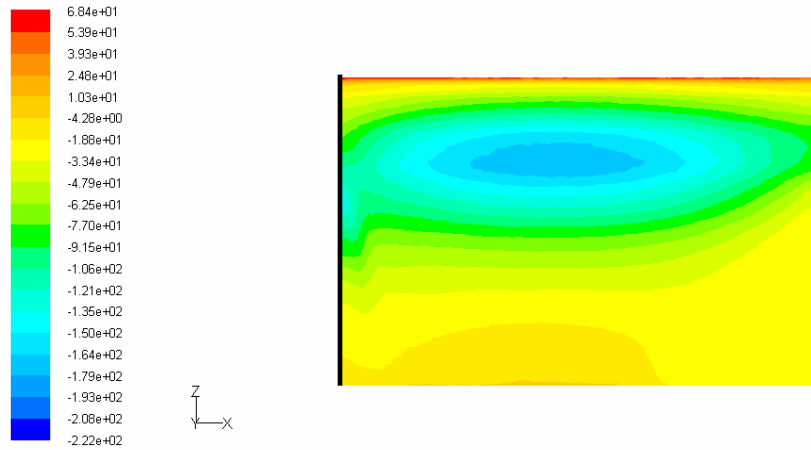


Figure B1: Suction surface static pressure contours for 6deg-h10-A-m2 (Pa)

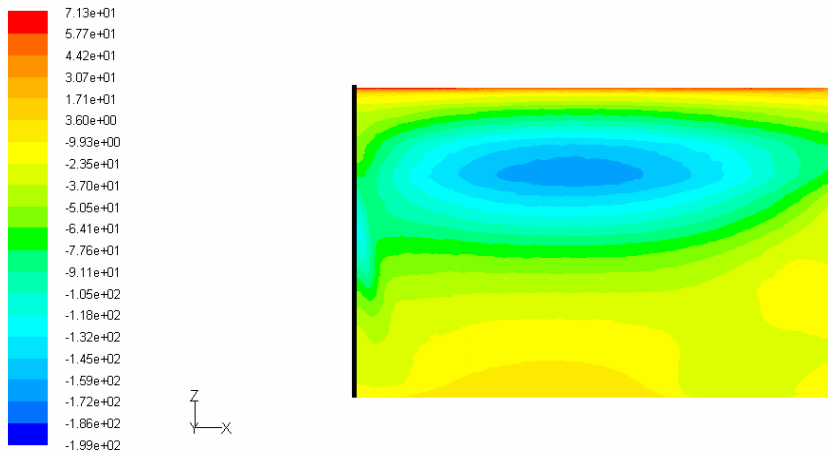


Figure B2: Suction surface static pressure contours for 6deg-h10-A-m4 (Pa)

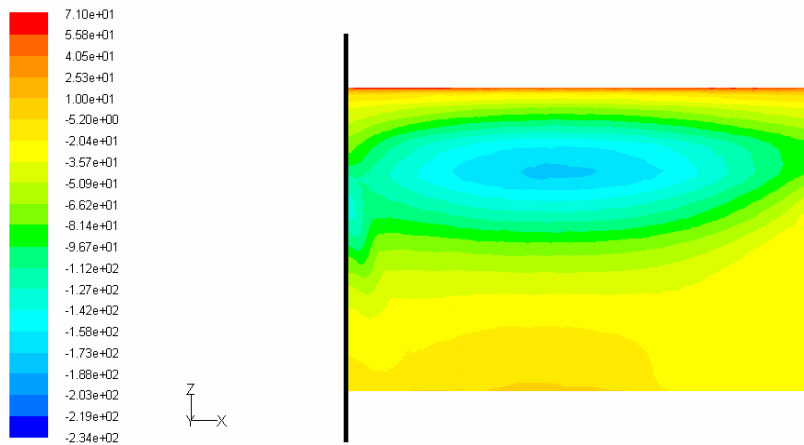


Figure B3: Suction surface static pressure contours for 6deg-h10-B-m2 (Pa)

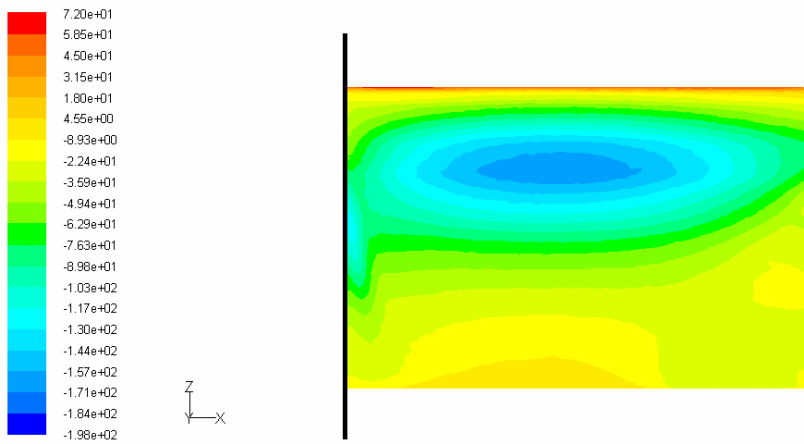


Figure B4: Suction surface static pressure contours for 6deg-h10-B-m4 (Pa)

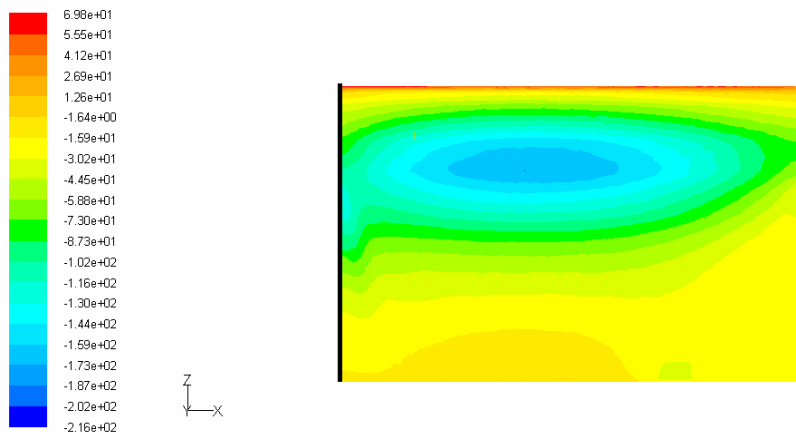


Figure B5: Suction surface static pressure contours for 6deg-h10-C-m2 (Pa)

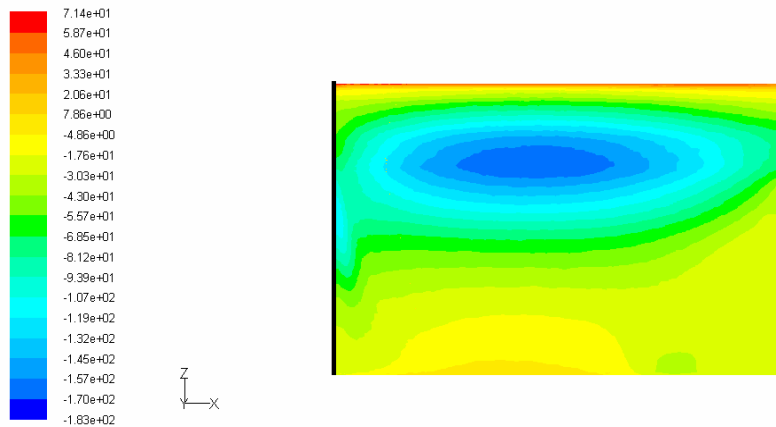


Figure B6: Suction surface static pressure contours for 6deg-h10-C-m4 (Pa)

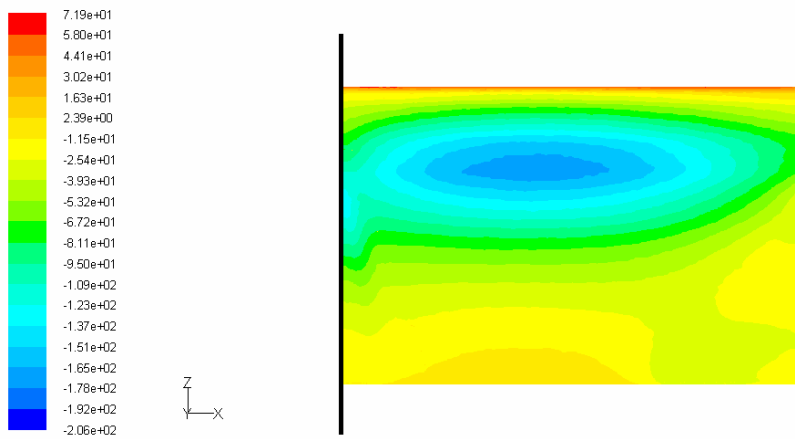


Figure B7: Suction surface static pressure contours for 6deg-h10-D-m2 (Pa)

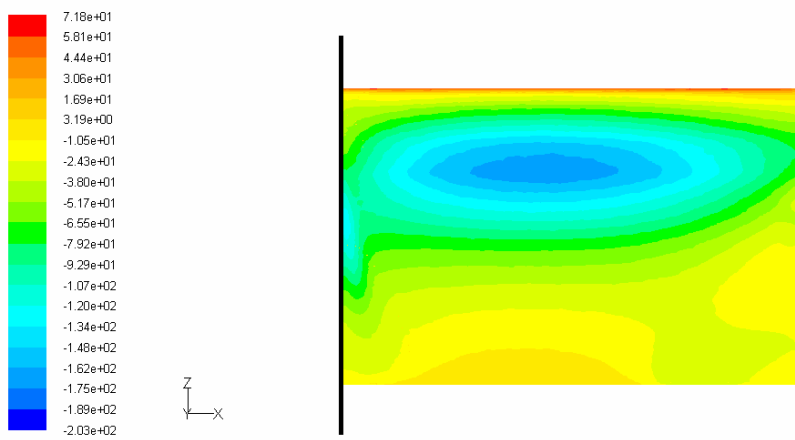


Figure B8: Suction surface static pressure contours for 6deg-h10-D-m4 (Pa)

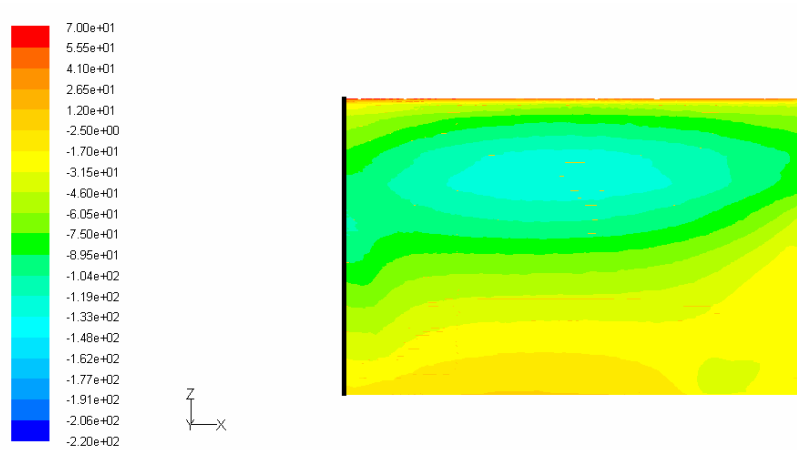


Figure B9: Suction surface static pressure contours for 6deg-h15-A-m4 (Pa)

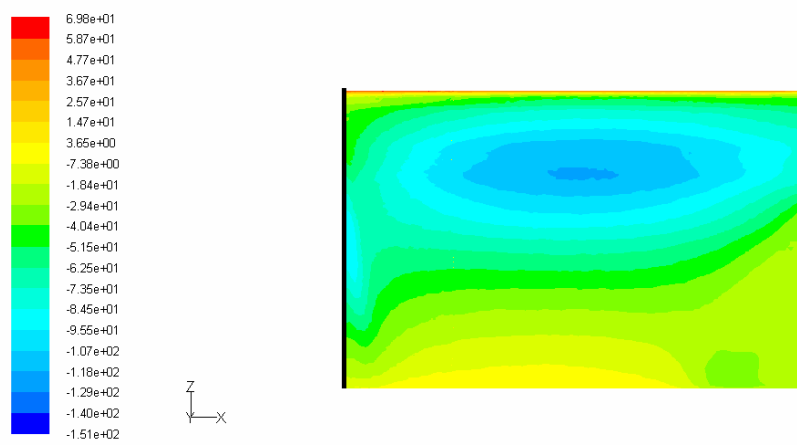


Figure B10: Suction surface static pressure contours for 6deg-h15-A-m9 (Pa)

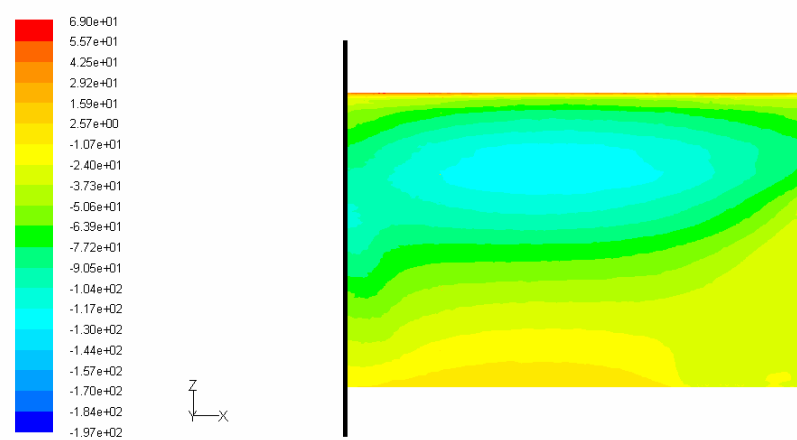


Figure B11 Suction surface static pressure contours for 6deg-h15-B-m4 (Pa)

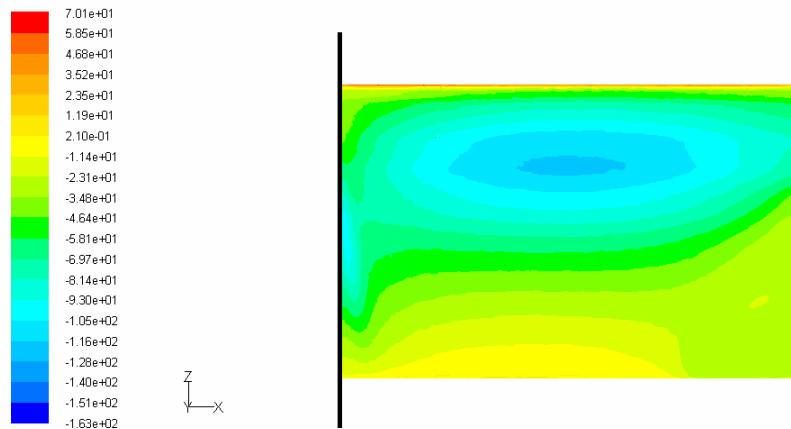


Figure B12: Suction surface static pressure contours for 6deg-h15-B-m9 (Pa)

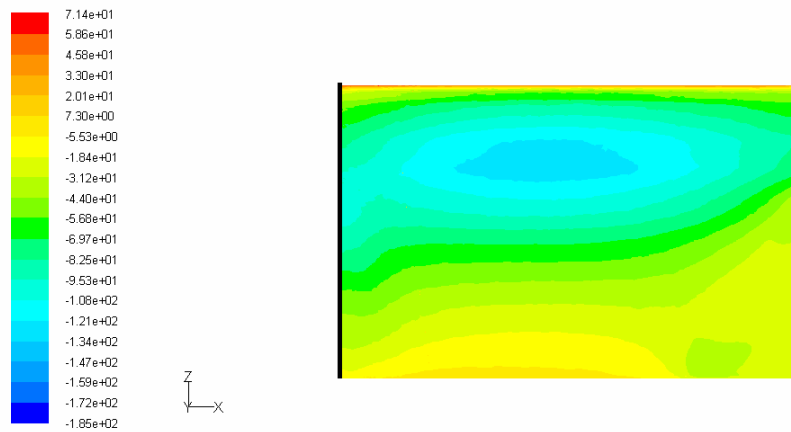


Figure B13: Suction surface static pressure contours for 6deg-h15-C-m4 (Pa)

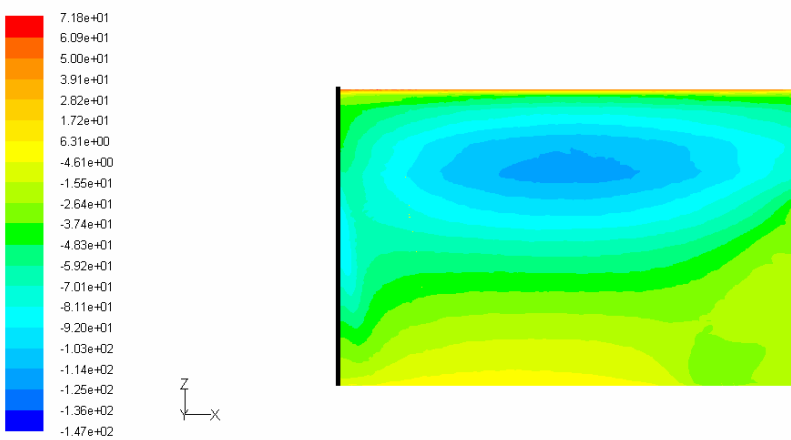


Figure B14: Suction surface static pressure contours for 6deg-h15-C-m9 (Pa)

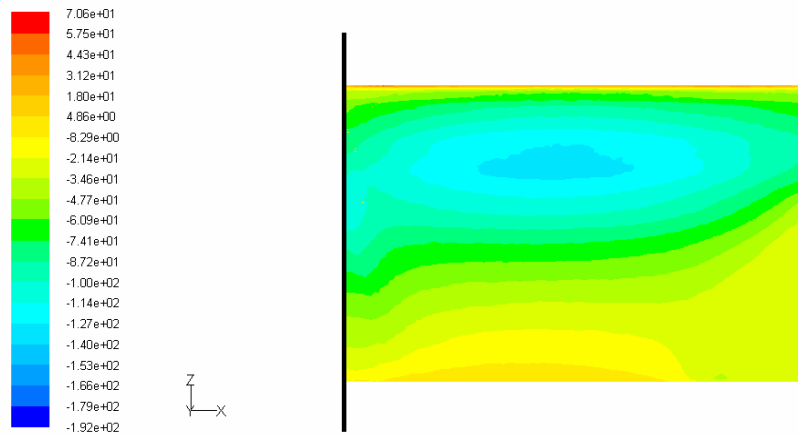


Figure B15: Suction surface static pressure contours for 6deg-h15-D-m4 (Pa)

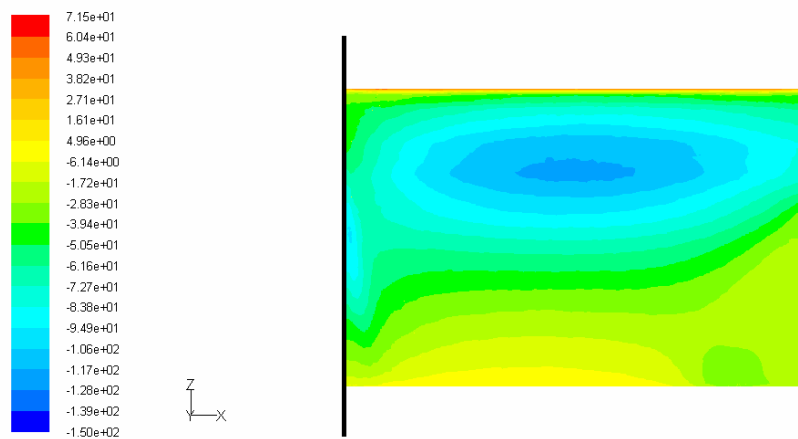


Figure B16: Suction surface static pressure contours for 6deg-h15-D-m9 (Pa)

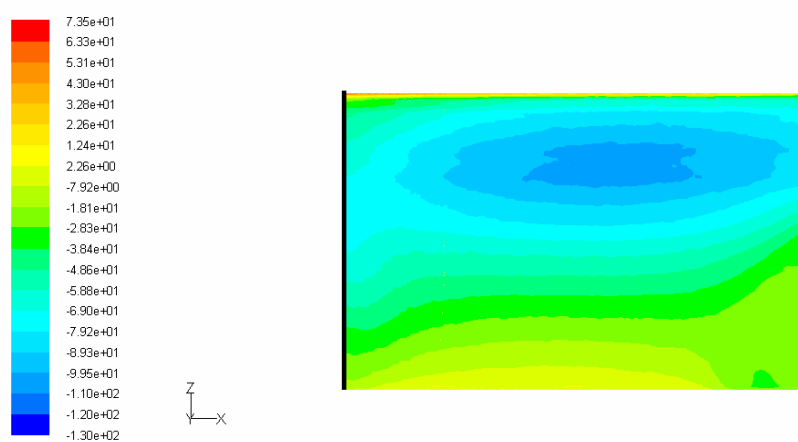


Figure B17: Suction surface static pressure contours for 6deg-h20-A-m9 (Pa)

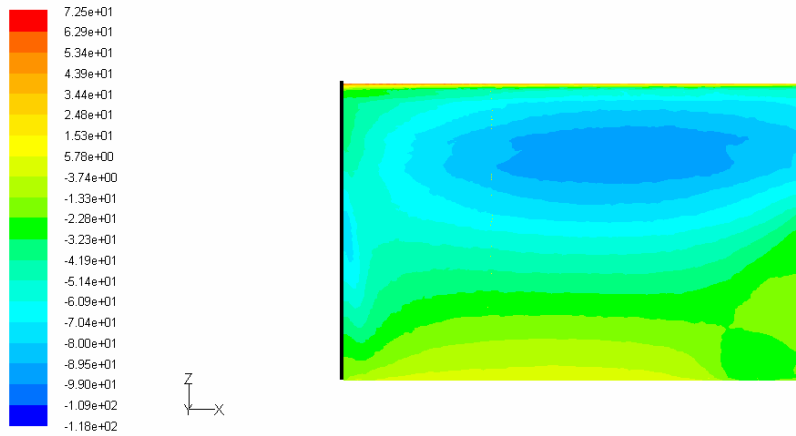


Figure B18: Suction surface static pressure contours for 6deg-h20-A-m14 (Pa)

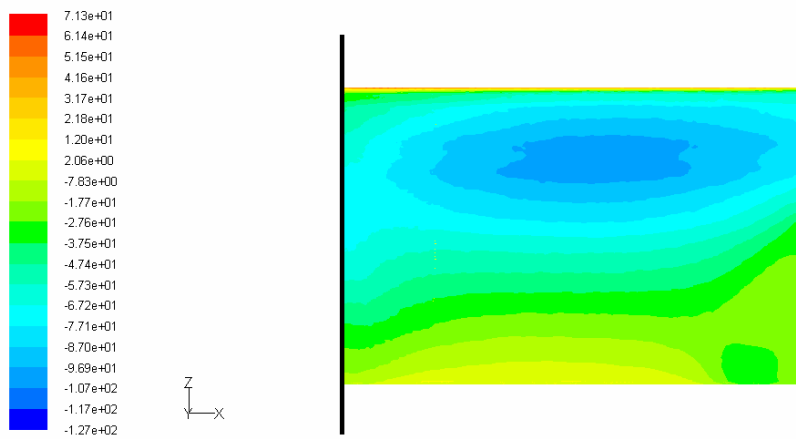


Figure B19: Suction surface static pressure contours for 6deg-h20-B-m9 (Pa)

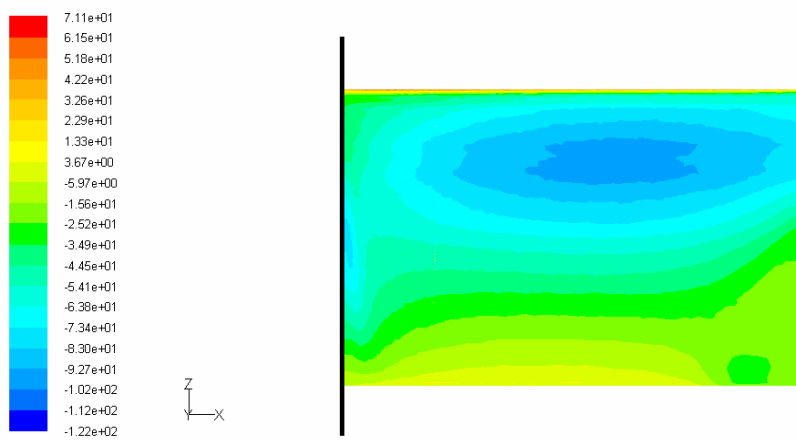


Figure B20: Suction surface static pressure contours for 6deg-h20-B-m14 (Pa)

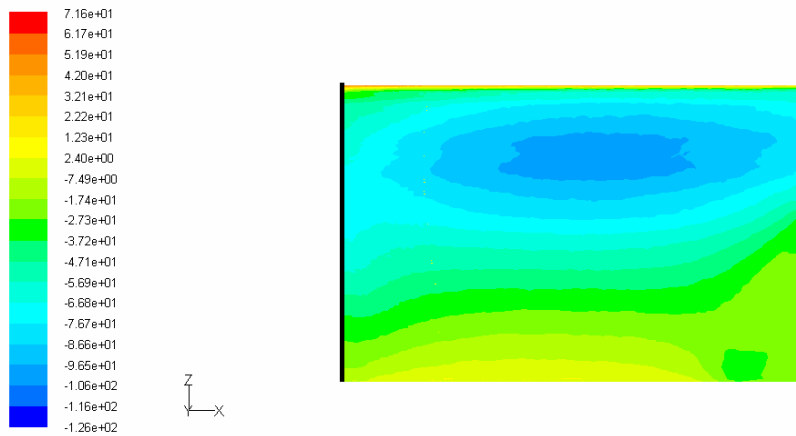


Figure B21: Suction surface static pressure contours for 6deg-h20-C-m9 (Pa)

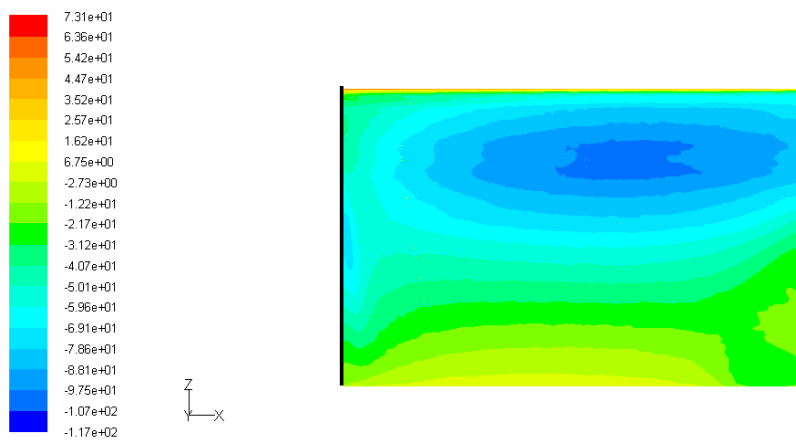


Figure B22: Suction surface static pressure contours for 6deg-h20-C-m14 (Pa)

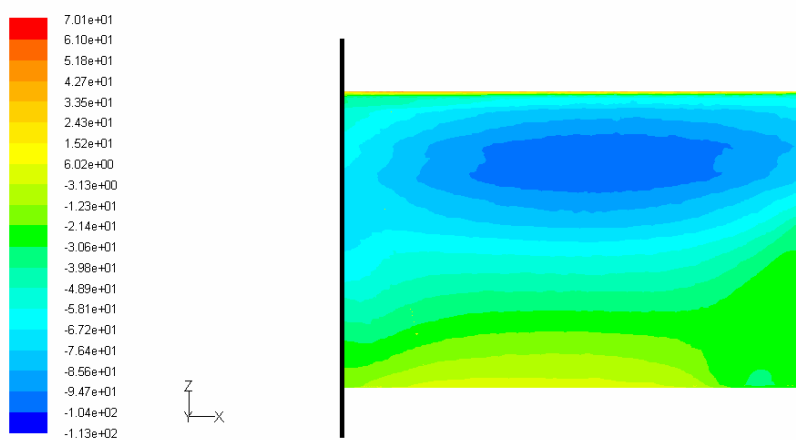


Figure B23: Suction surface static pressure contours for 6deg-h20-D-m9 (Pa)

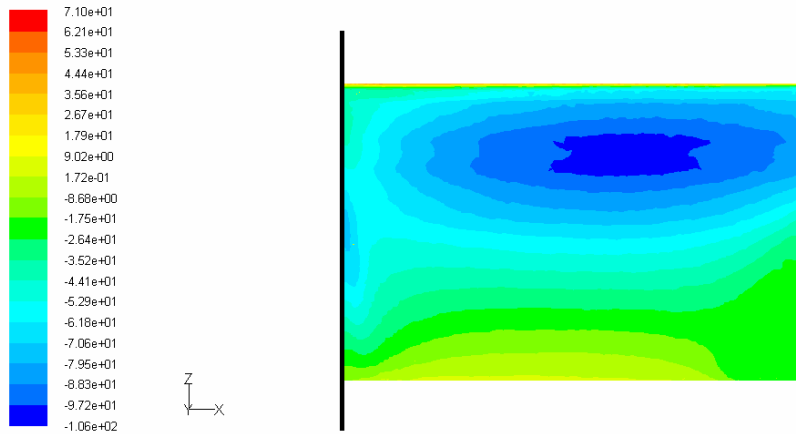


Figure B24: Suction surface static pressure contours for 6deg-h20-D-m14 (Pa)

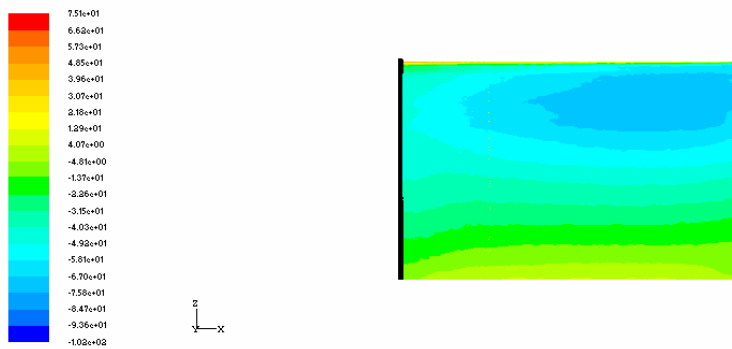


Figure B25: Suction surface static pressure contours for 6deg-h40-A-m28 (Pa)

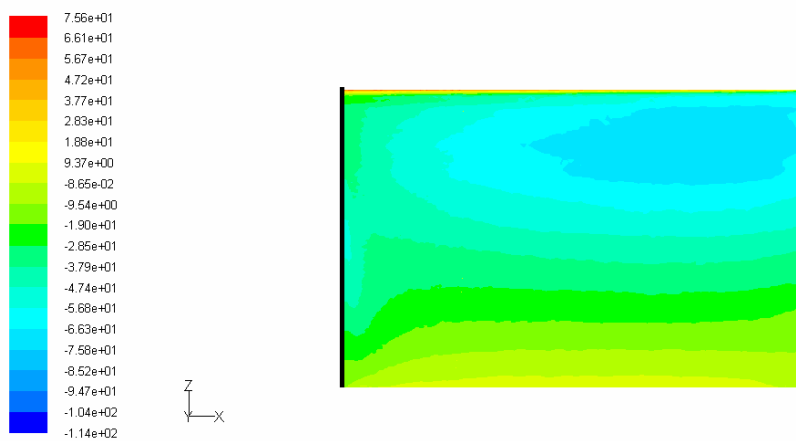


Figure B26: Suction surface static pressure contours for 6deg-h40-A-m34 (Pa)

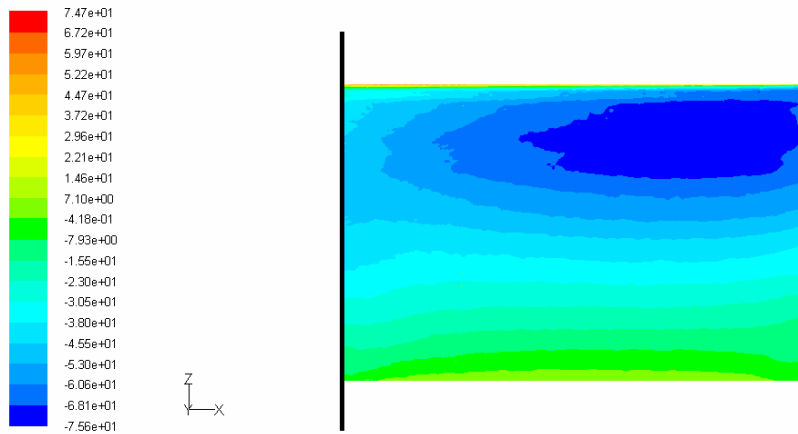


Figure B27: Suction surface static pressure contours for 6deg-h40-B-m28 (Pa)

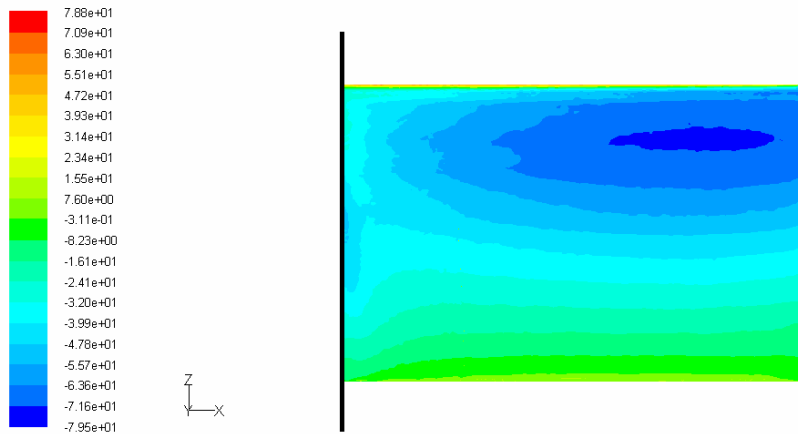


Figure B28: Suction surface static pressure contours for 6deg-h40-B-m34 (Pa)

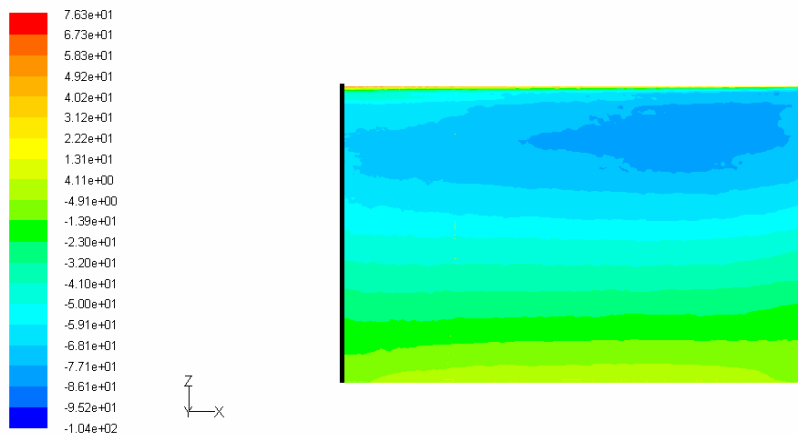


Figure B29: Suction surface static pressure contours for 6deg-h40-C-m10 (Pa)

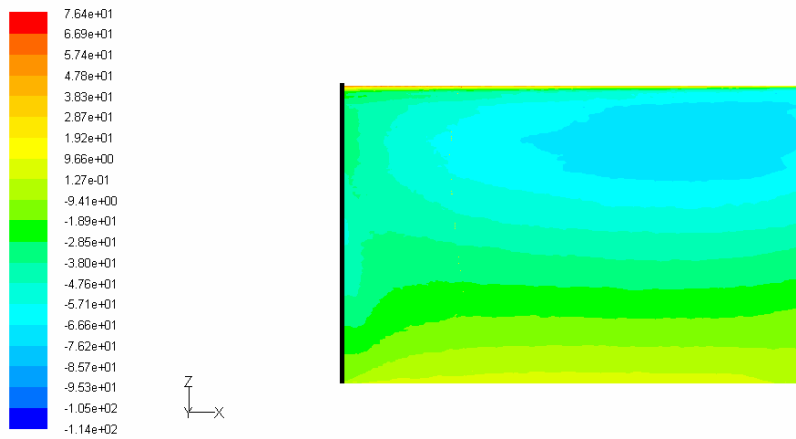


Figure B30: Suction surface static pressure contours for 6deg-h40-C-m34 (Pa)

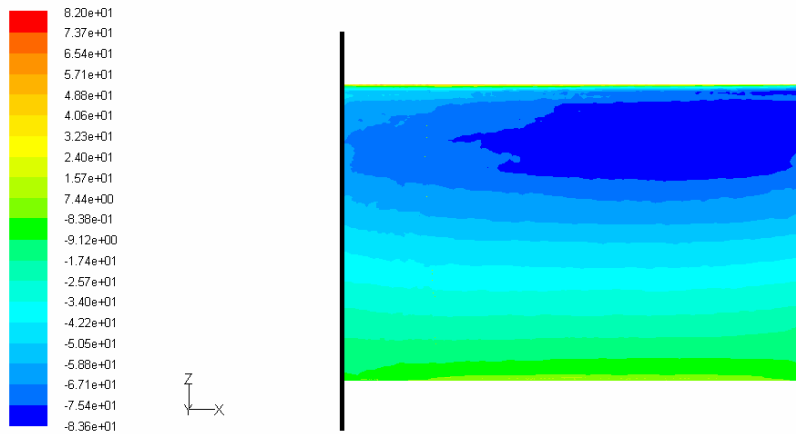


Figure B31: Suction surface static pressure contours for 6deg-h40-D-m10 (Pa)

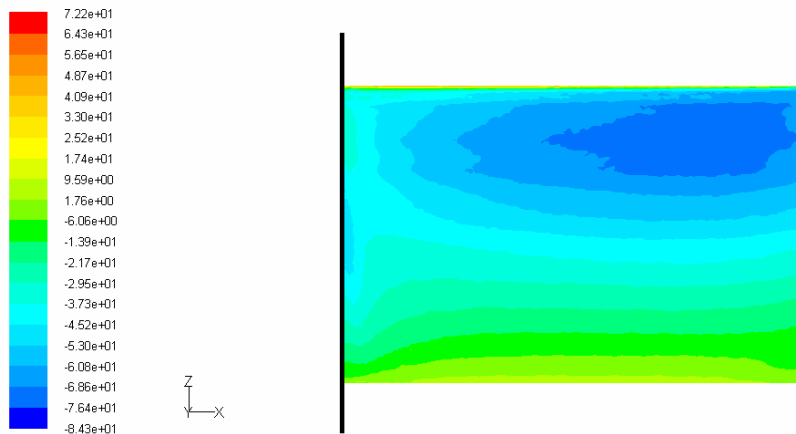


Figure B32: Suction surface static pressure contours for 6deg-h40-D-m34 (Pa)

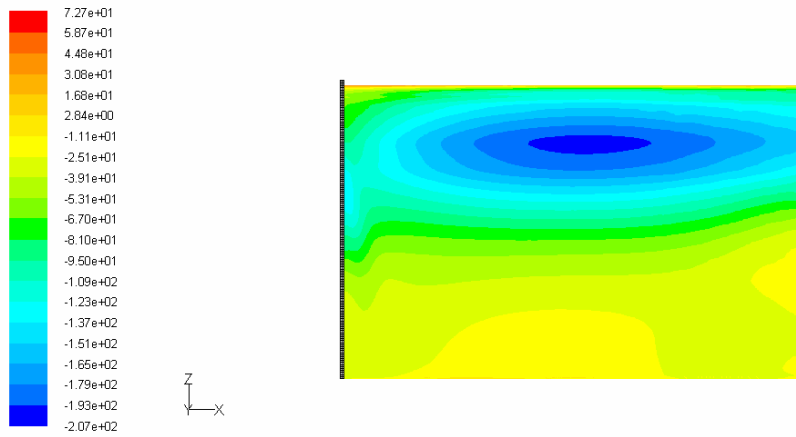


Figure B33: Suction surface static pressure contours for 10deg-h10-A-m4 (Pa)

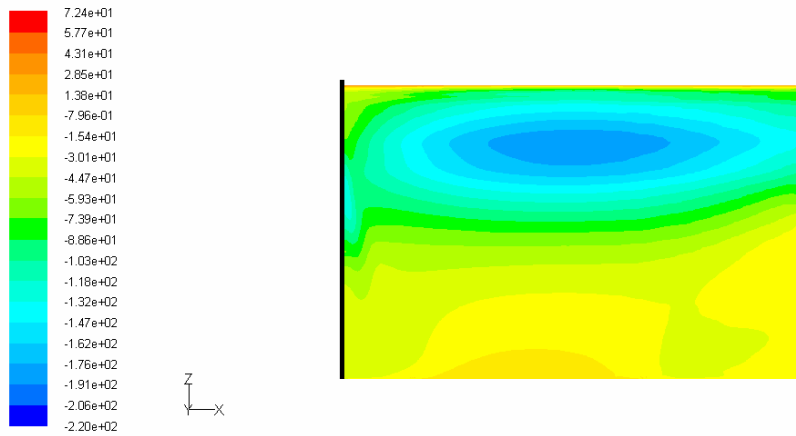


Figure B34: Suction surface static pressure contours for 10deg-h10-A-m5 (Pa)

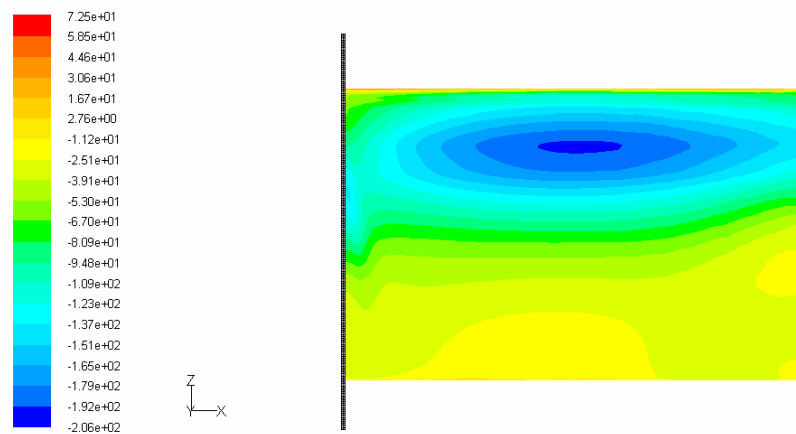


Figure B35: Suction surface static pressure contours for 10deg-h10-B-m4 (Pa)

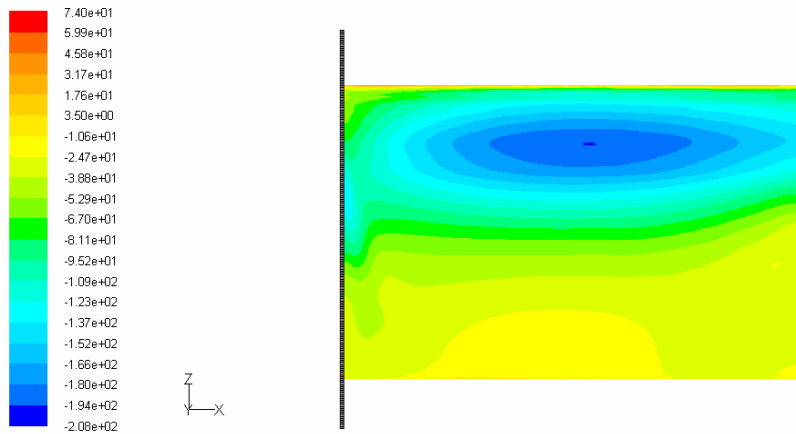


Figure B36: Suction surface static pressure contours for 10deg-h10-B-m5 (Pa)

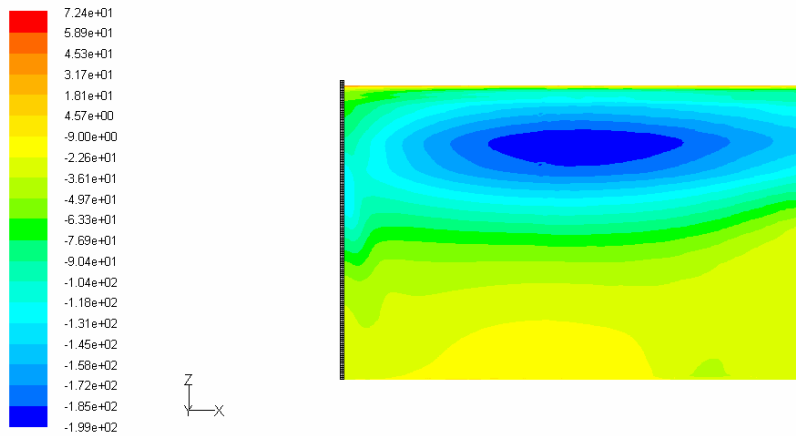


Figure B37: Suction surface static pressure contours for 10deg-h10-C-m4 (Pa)

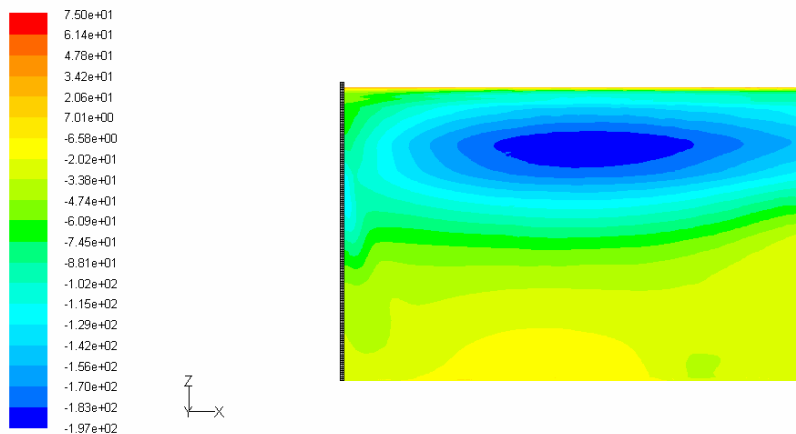


Figure B38: Suction surface static pressure contours for 10deg-h10-C-m5 (Pa)

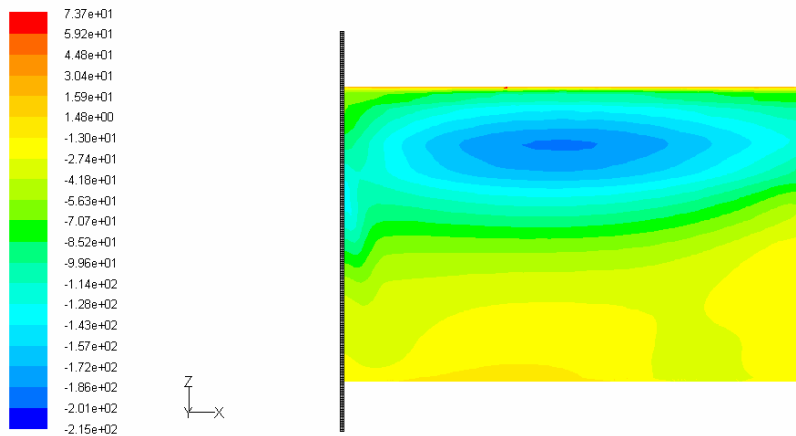


Figure B39: Suction surface static pressure contours for 10deg-h10-D-m4 (Pa)

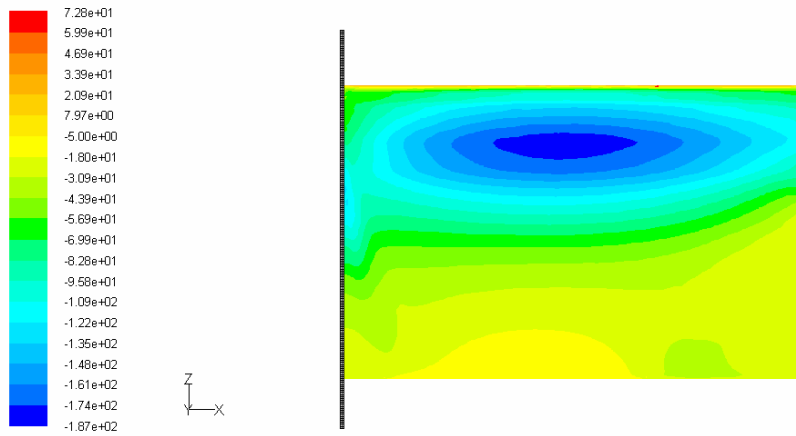


Figure B40: Suction surface static pressure contours for 10deg-h10-D-m5 (Pa)

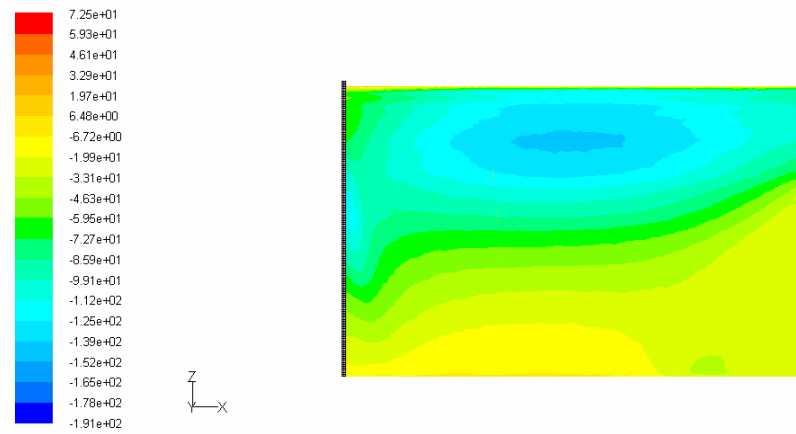


Figure B41: Suction surface static pressure contours for 10deg-h15-A-m9 (Pa)

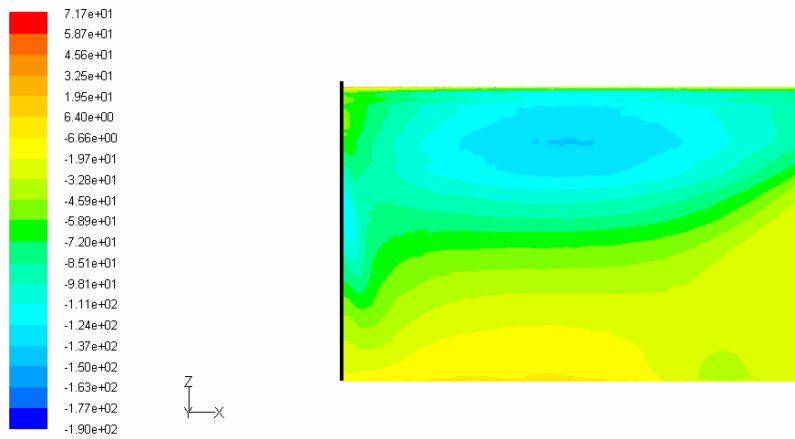


Figure B42: Suction surface static pressure contours for 10deg-h15-A-m10 (Pa)

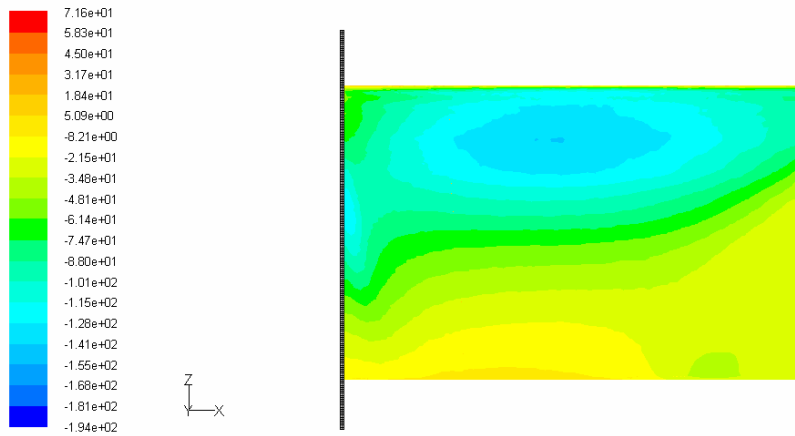


Figure B43: Suction surface static pressure contours for 10deg-h15-B-m9 (Pa)

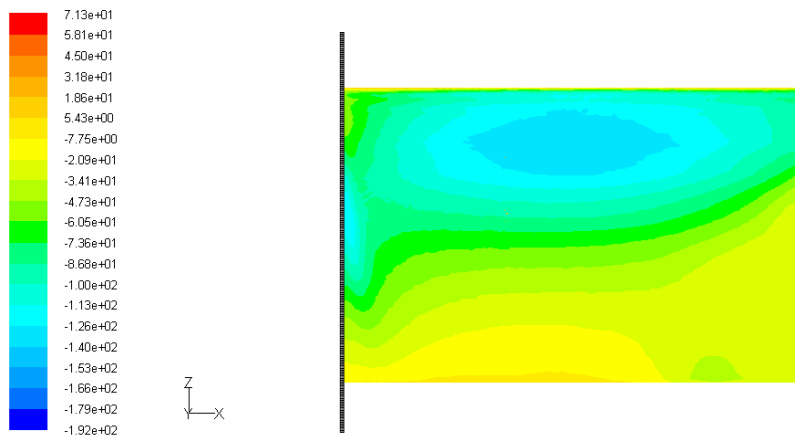


Figure B44: Suction surface static pressure contours for 10deg-h15-B-m10 (Pa)

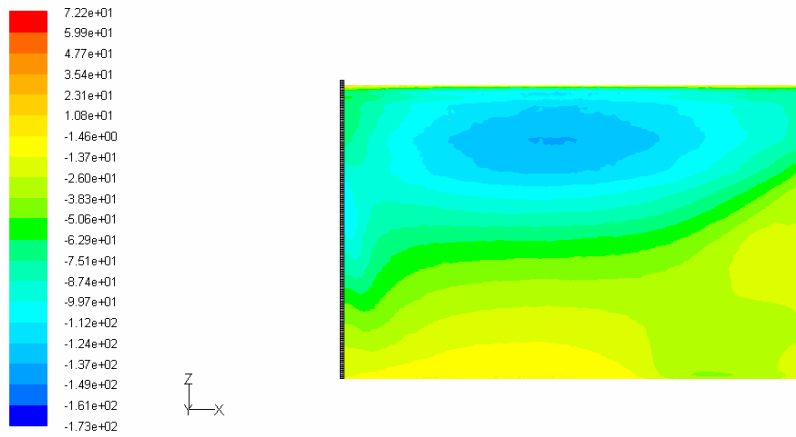


Figure B45: Suction surface static pressure contours for 10deg-h15-C-m9 (Pa)

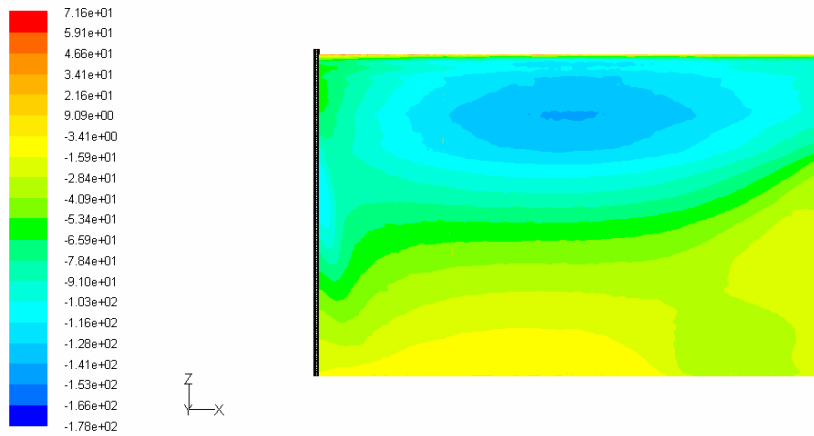


Figure B46: Suction surface static pressure contours for 10deg-h15-C-m10 (Pa)

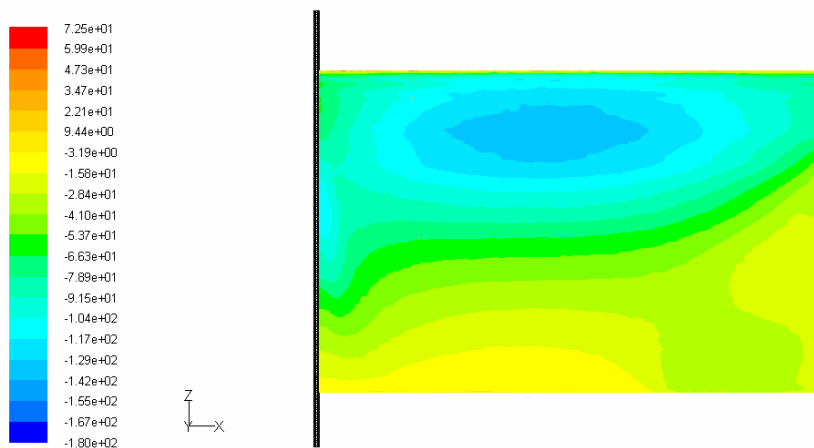


Figure B47: Suction surface static pressure contours for 10deg-h15-D-m9 (Pa)

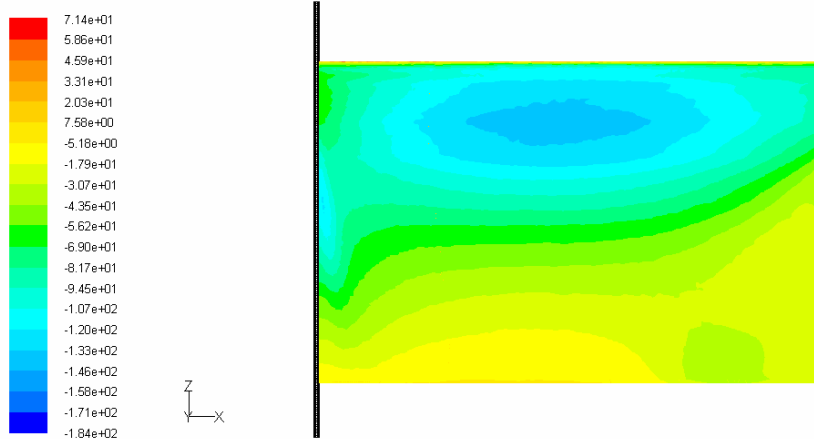


Figure B48: Suction surface static pressure contours for 10deg-h15-D-m10 (Pa)

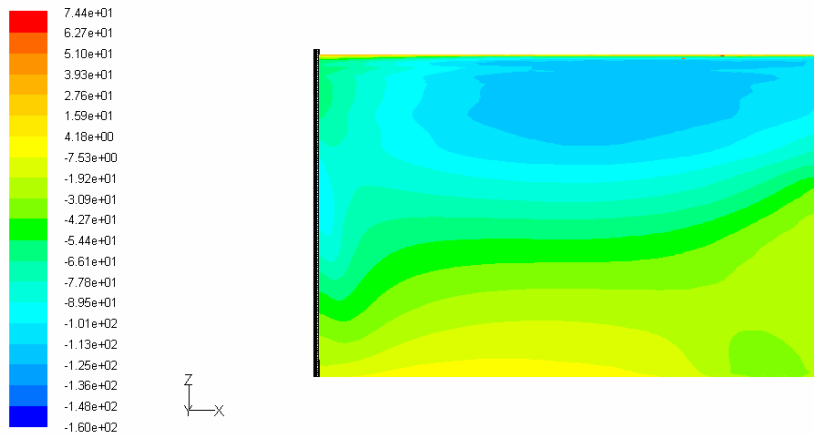


Figure B49: Suction surface static pressure contours for 10deg-h20-A-m14 (Pa)

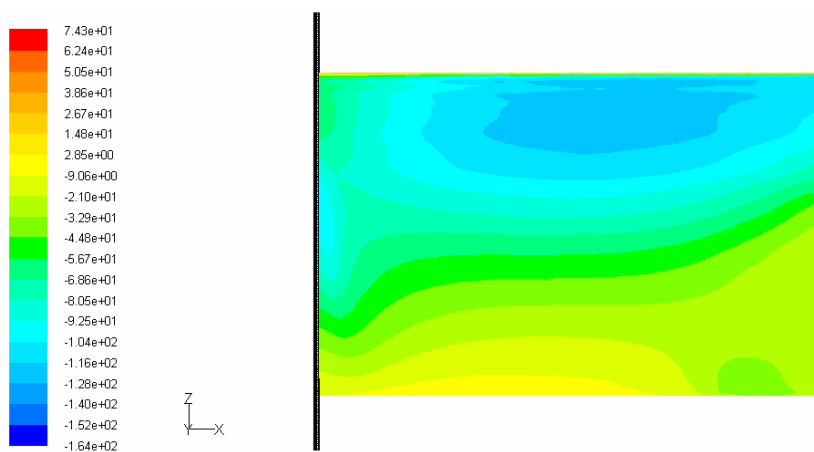


Figure B50: Suction surface static pressure contours for 10deg-h20-B-m14 (Pa)

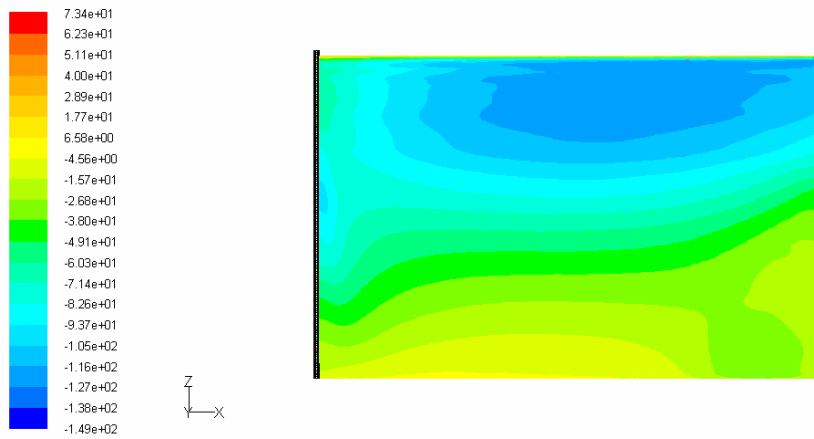


Figure B51: Suction surface static pressure contours for 10deg-h20-C-m14 (Pa)

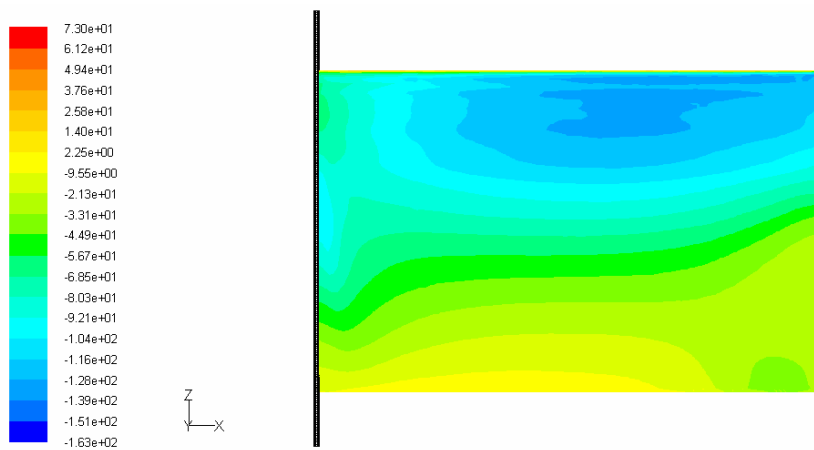


Figure B52: Suction surface static pressure contours for 10deg-h20-D-m14 (Pa)

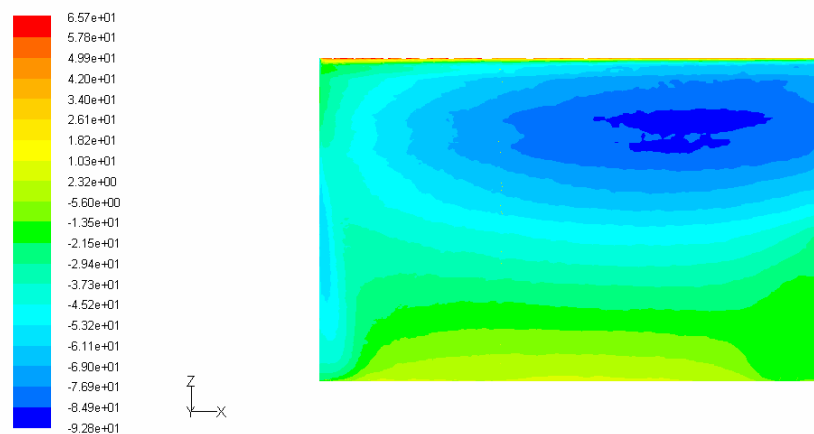


Figure B53: Suction surface static pressure contours for 6deg-no endplate (Pa)

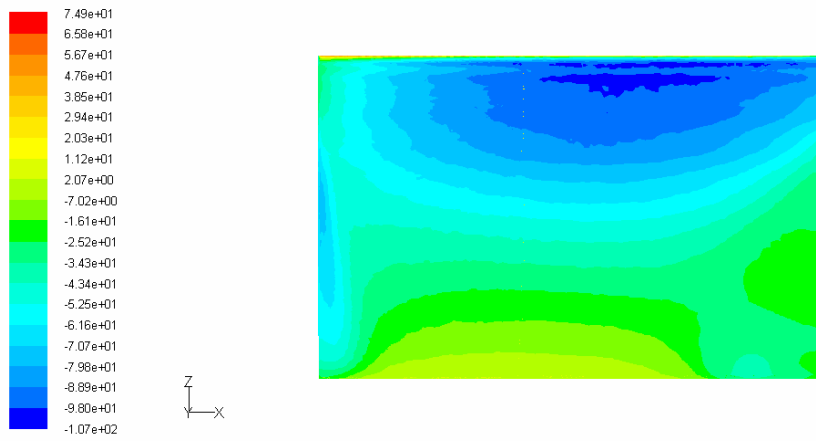


Figure B54: Suction surface static pressure contours for 10deg no endplate (Pa)

Appendix C: Drawings for Perspex Moving Ground Parts

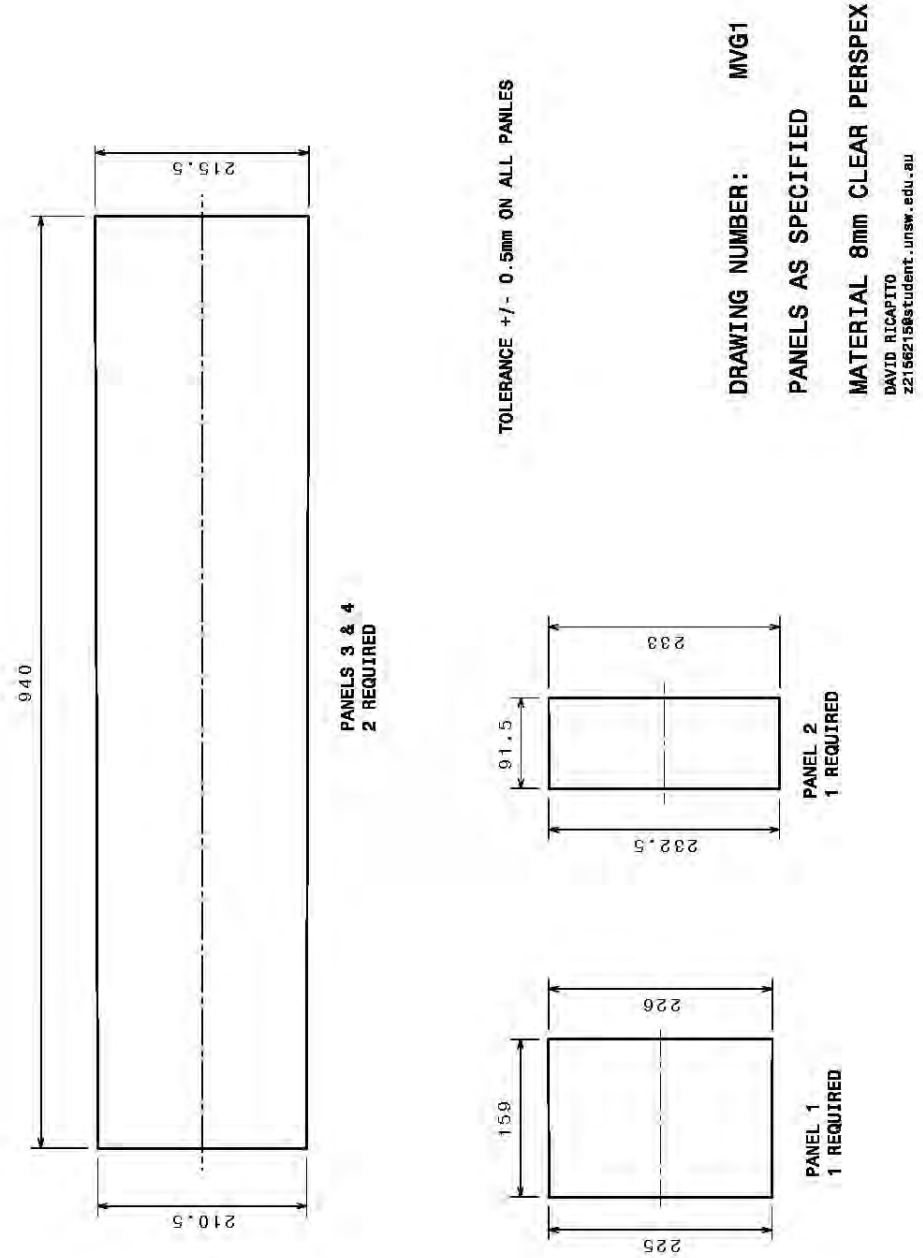
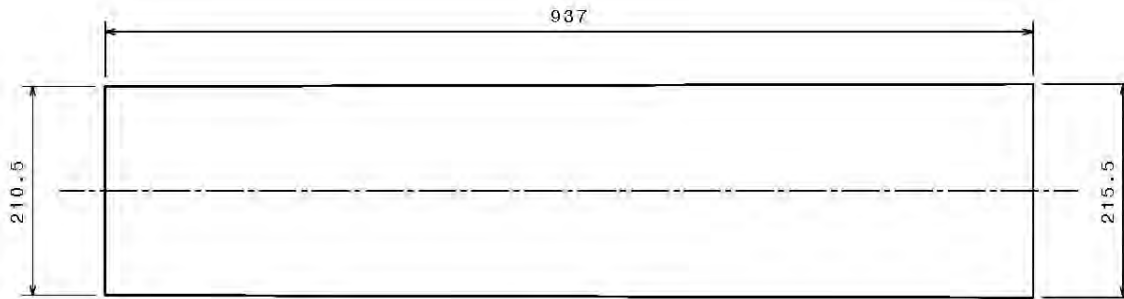
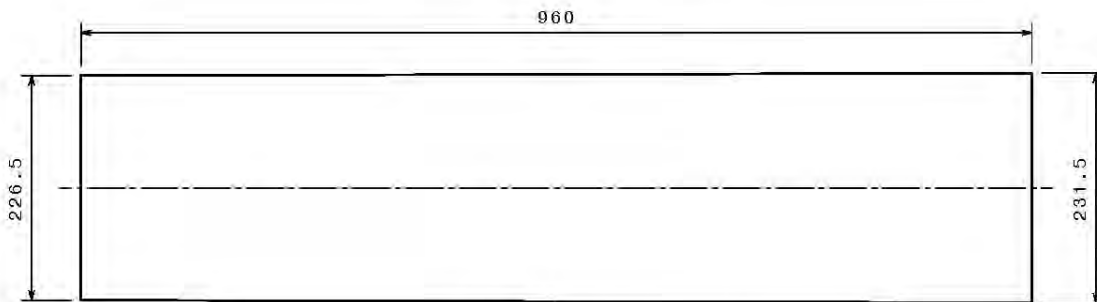


Figure C1: Moving ground drawing MVG1

Figure C2: Moving ground drawing MVG2



PANEL 5
1 REQUIRED
MATERIAL 8mm CLEAR PERSPEX



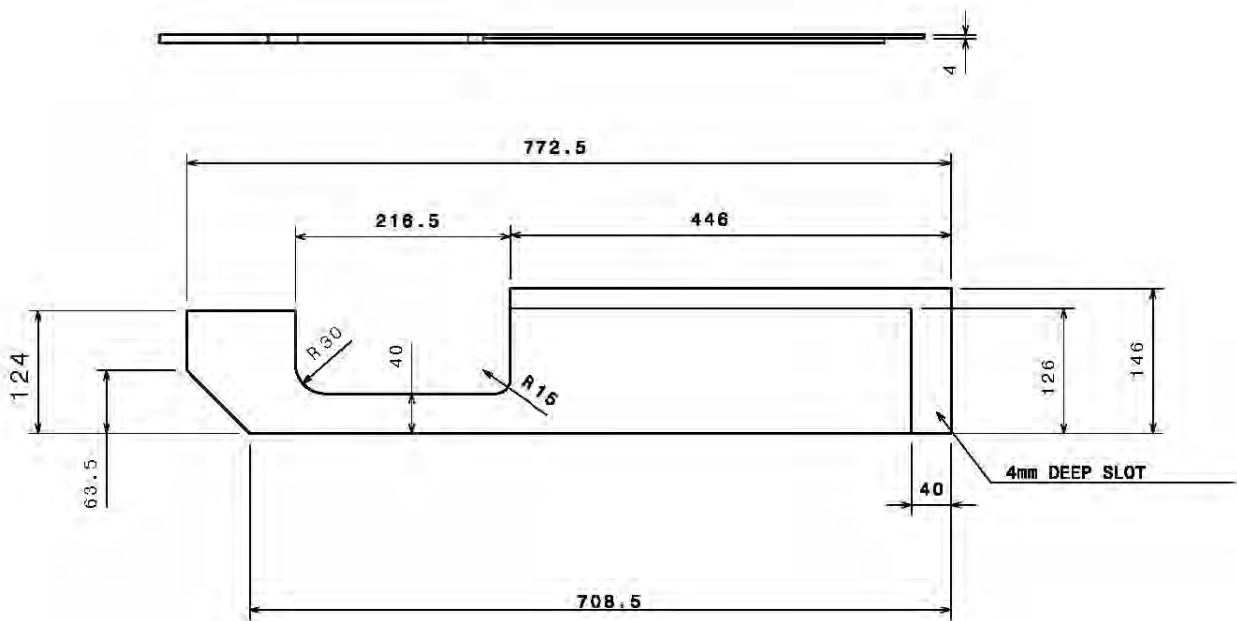
PANEL 6
1 REQUIRED
MATERIAL 3mm CLEAR PERSPEX

TOLERANCE +/- 0.5mm

DRAWING NUMBER: MVG2

MATERIAL AS SPECIFIED

DAVID RICAPITO
22156215@student.unsw.edu.au



TOLERANCE +/- 0.5mm

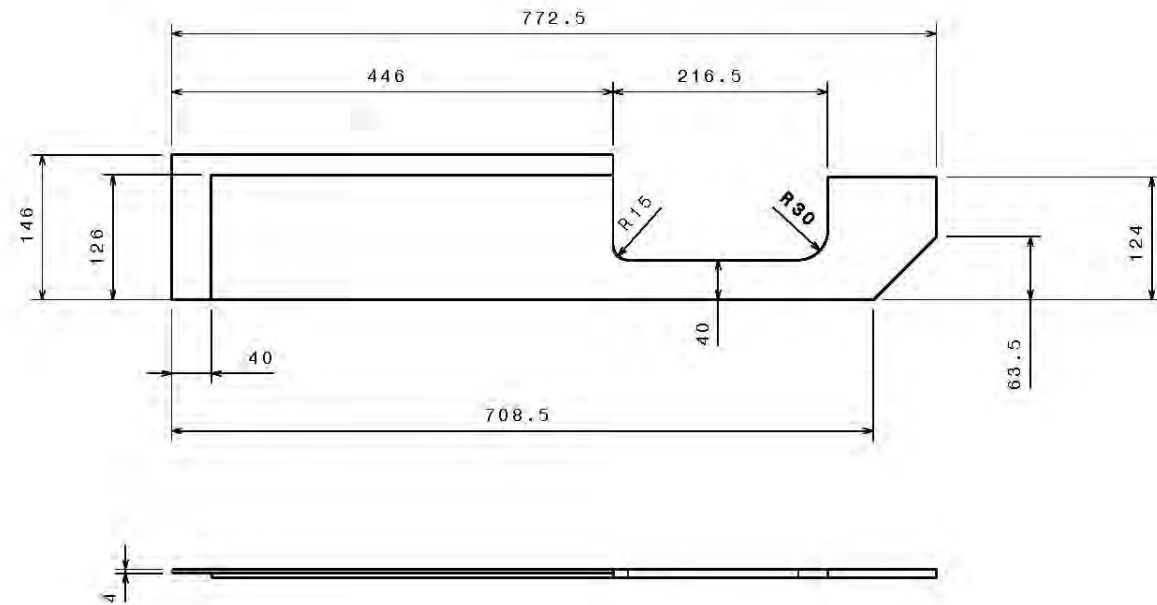
DRAWING NUMBER: MVG3

PANEL 7A

MATERIAL 8mm CLEAR PERSPEX

DAVID RICAPITO
z2158215@student.unsw.edu.au

Figure C3: Moving ground drawing MVG3



TOLERANCE +/- 0.5mm

DRAWING NUMBER: MVG5

PANEL 8A

MATERIAL 8mm CLEAR PERSPEX

DAVID RICAPITO
z2156215@student.unsw.edu.au

Figure C5: Moving ground drawing MVG5

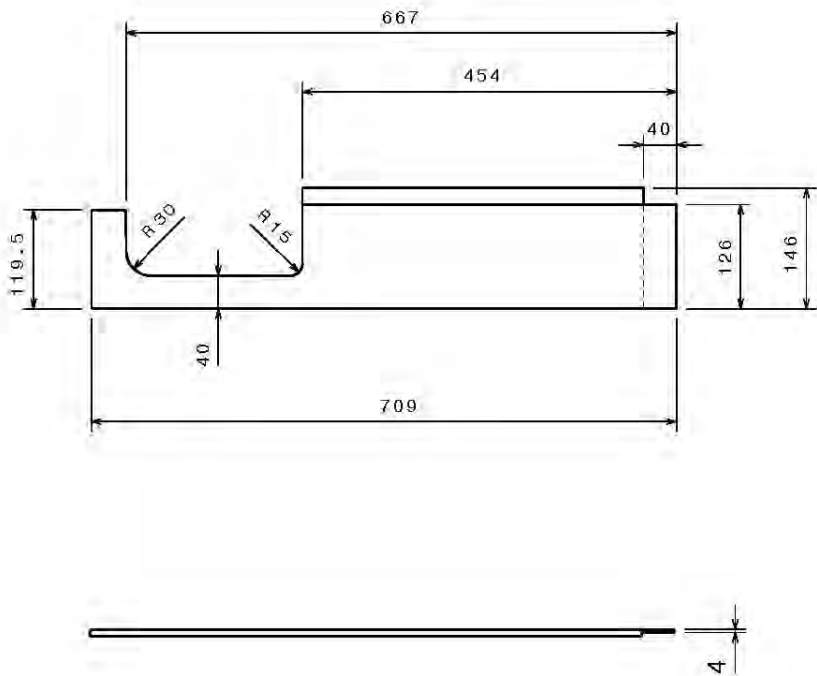


Figure C6: Moving ground drawing MVG6

TOLERANCE +/- 0.5mm

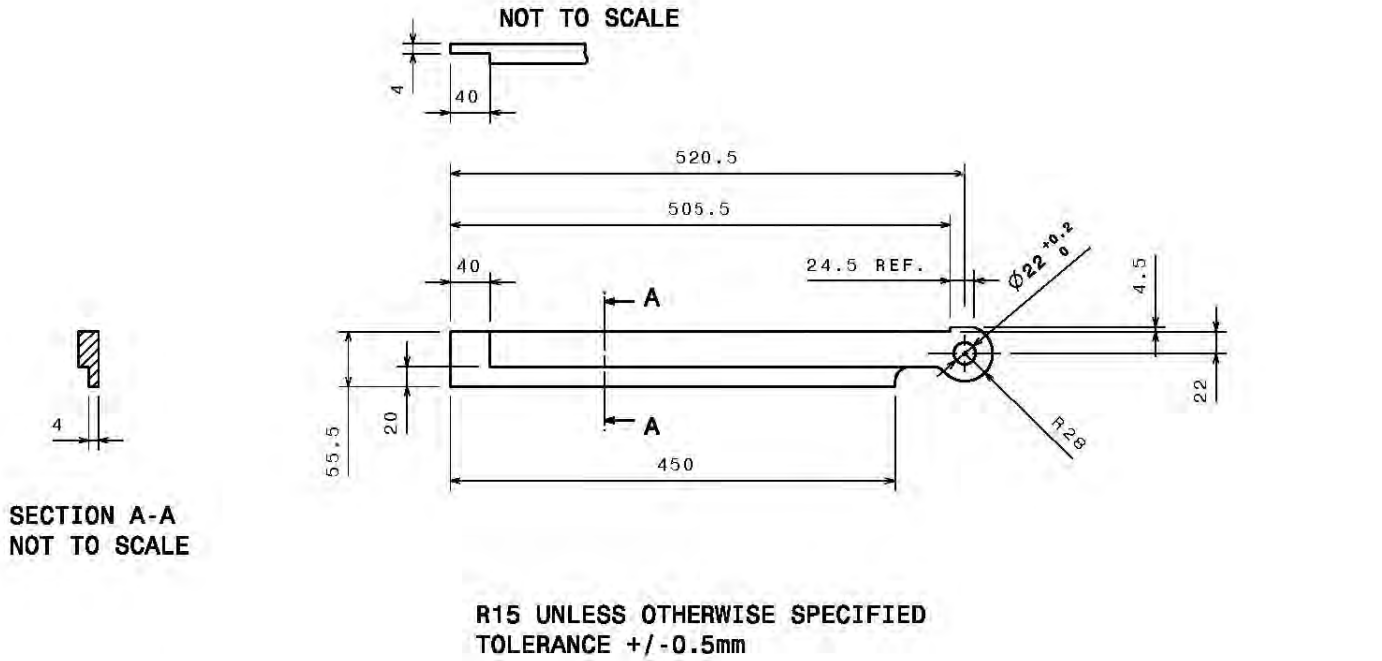
DRAWING NUMBER: MVG6

PANEL 8B

MATERIAL 8mm CLEAR PERSPEX

DAVID RICAPITO
z2158215@student.unsw.edu.au

Figure C7: Moving ground drawing MVG7



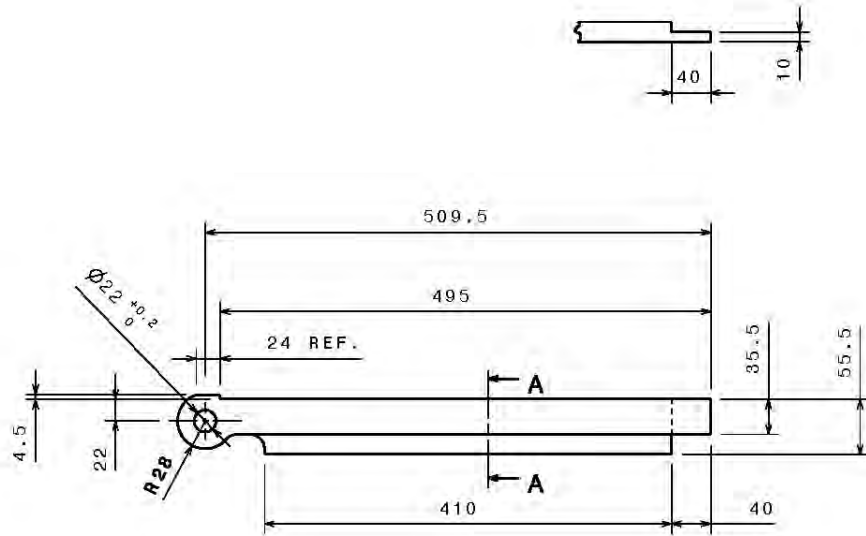
DRAWING NUMBER: MVG7

PANEL 9A

MATERIAL 8mm CLEAR PERSPEX

DAVID RICAPITO
z2158215@student.unsw.edu.au

Figure C8: Moving ground drawing MVG8



R15 UNLESS OTHERWISE SPECIFIED
TOLERANCE +/- 0.5mm

SECTION A-A
NOT TO SCALE

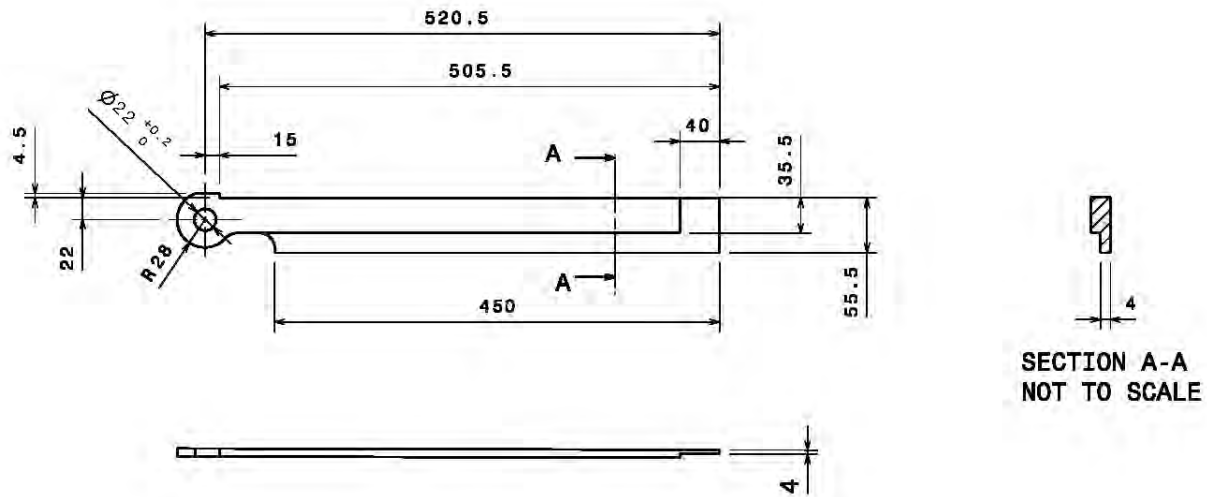
DRAWING NUMBER: MVG8

PANEL 9B

MATERIAL 8mm CLAR PERSPEX

DAVID RICAPITO
z2156215@student.unsw.edu.au

Figure C9: Moving ground drawing MVG9



R15 UNLESS OTHERWISE SPECIFIED
TOLERANCE +/- 0.5mm

DRAWING NUMBER: MVG9

PANEL 10A

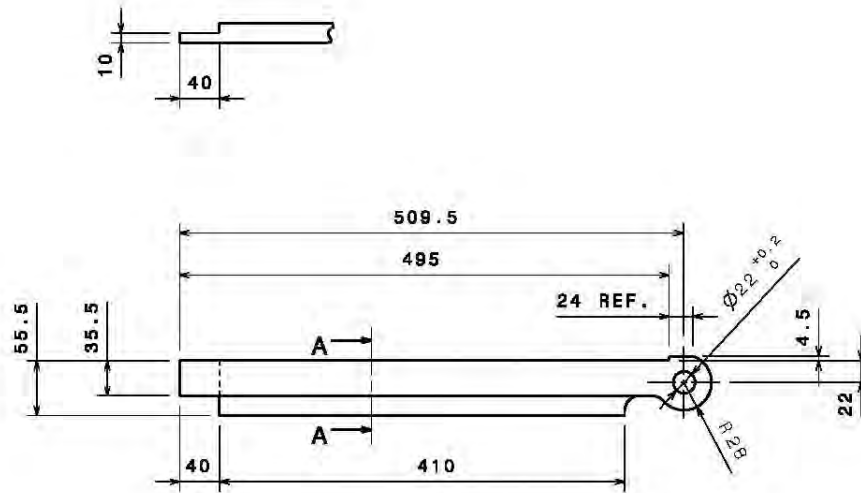
MATERIAL 8mm CLEAR PERSPEX

DAVID RICAPITO
z2156215@student.unsw.edu.au

Figure C10: Moving ground drawing MVG10



SECTION A-A
NOT TO SCALE



R15 UNLESS OTHERWISE SPECIFIED
TOLERANCE +/- 0.5mm

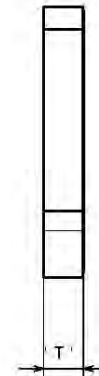
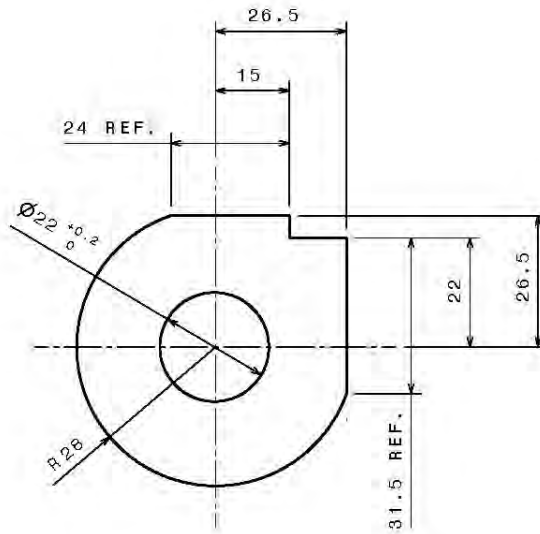
DRAWING NUMBER: MVG10

PANEL 10B

MATERIAL 8mm CLAR PERSPEX

DAVID RICAPITO
z2158215@student.unsw.edu.au

Figure C11: Moving ground drawing MVG11



PANEL 12	5.5	2
PANEL 11	3	2
PART No.	'T'	QTY

DRAWING NUMBER: MVG11

PANELS 11 & 12

MATERIAL CLEAR PERSPEX

DAVID RICAPITO
z2156215@student.unsw.edu.au